Design and Analysis of the Optical Beam Combiner and Corrugated Feed Horns for the QUBIC Instrument

Presented by

David Burke, B.Sc

A thesis submitted for the degree of

Doctor of Philosphy

Maynooth University

National University of Ireland Maynooth

Department of Experimental Physics

Maynooth University

National University of Ireland, Maynooth

Co. Kildare

Ireland

January 2021

Head of Department:

Dr. Créidhe O'Sullivan

Research Supervisor:

Dr. Créidhe O'Sullivan

Contents

Abstract

The next major step in Big Bang cosmology will be the detection of primordial B-modes in the polarisation pattern of the Cosmic Microwave Background (CMB). These primordial B-modes are extremely faint and unprecedented levels of sensitivity will be required to detect them. The QUBIC (Q & U Bolometric Interferometer for Cosmology) instrument, first proposed in 2008 and now on the verge of being commissioned, aims to detect them by using the novel technique of bolometric interferometry to combine the control of systematics provided by an interferometer and the sensitivity provided by an imager. QUBIC is a ground-based instrument that will be installed in Salta Province, Argentina.

This thesis describes the detailed optical analysis of the QUBIC instrument and, in particular, its quasi-optical beam combiner. Two variations of QUBIC are analysed: the full instrument (FI) and a technological demonstrator (TD). It was decided to develop the smaller optical combiner of the TD in 2015. The justification for and analysis of the TD are also presented.

The QUBIC FI will observe over two bands: 150 GHz (with a 25% bandwidth) and 220 GHz (with an 18% bandwidth). The operation of the QUBIC optical combiner across these bands was investigated using the techniques of physical optics and electromagnetic mode-matching for the feedhorns. This modelling also provided an insight into multimoded operation of QUBIC in the higher band, which will be useful for future instruments that aim to exploit the phenomenon.

The optical modelling in this thesis has been used in the calibration and testing phases of the instrument and will be also useful in the future when observations begin in Argentina.

Acknowledgements

I would first like to thank my supervisor, Dr. Créidhe O'Sullivan for agreeing to take me on as her student and imparting her knowledge. I greatly appreciate her understanding and support throughout my research as well as her patience with the correcting of this thesis, which was made more difficult due to the fact that this thesis was written predominantly during the COVID-19 pandemic.

I would also like to thank Dr. Marcin Gradziel for the upkeep of the Cluster and the MODAL software, allowing me to perform simulations without which the research presented would not have been possible. In addition I would like to thank Prof. Anthony Murphy, who was always willing to share his knowledge of quasi-optical systems and mode matching in waveguides, which has been invaluable for this research. Thanks also to Dr. Eimante Kalinauskaite, whose knowledge with mode matching techniques and software was of great benefit.

I also would like to thank all the staff in the Experimental Physics department, who all have aided me in my journey throughout my PhD research, and made the process of writing this thesis during the pandemic as easy as it could be.

A big thank you to all the postgraduate students that have been present in the department throughout my PhD, for both aiding me with my research and distracting me from it when necessary. A special mention to all the colleagues I have had who worked in the 'QUBIC office': Mr. Rory Sheridan, Mr. Donnacha Gayer, Dr. Stephen Scully, Mr. James Murphy and the honorary office colleague, Mr. Joe Brennan.

Thanks to the all the members of the QUBIC collaboration.

I would like to thank and acknowledge the funding I have received from the Irish Research Council, which made this research possible.

A huge thank you has to go to my family (My mum and dad – Mary and Derek, and my two siblings – Amy and Michael), who have always been there for me.

I am indebted to my partner Aisling, her unwavering support through the good times and bad has been instrumental, without which I could not have completed this research, thank you for everything Aisling.

I would like to dedicate this thesis to my mother Mary Burke. She was always there to support me, giving me a shoulder to cry or an encouraging word when she could see I was struggling. It has been incredibly difficult not having her here these past few years, but without doubt she gave me the skills necessary to succeed. I will always love you mum.

1 Introduction

The Big Bang theory is the most widely accepted theory for the origins of our universe. It theorises that the universe started from a small primordial seed and expanded into what we see today. The Cosmic Microwave Background (CMB) is the remnant radiation from the Big Bang that can still be observed; it exhibits a blackbody spectrum which peaks at millimetre wavelengths. The CMB is the key to understanding the universe as early physical processes have left an imprint on it that can be probed today.

There are two attributes of the CMB that can be observed: its temperature and its polarisation. Many experiments have observed the temperature of the CMB to incredible levels of detail showing the minor variations in the CMB which are a result of the structure in the early universe. What seeds this early structure is not known, that is where the polarisation pattern of the CMB becomes important and gives us an insight into this early structure.

There are two different types of polarisation pattern imprinted on the CMB, E-mode and B-mode (named for their structure that is analogous to that of electric (E) and magnetic (B) fields). The polarisation is caused by different phenomena and while the E-mode polarisation of the CMB has been detected, no measurement of the primordial B-modes has been made. Detection of the primordial B-mode polarisation will provide a fuller picture of the early universe and it will also be vital in testing the theory of inflation. It would be the first observational evidence of gravitational waves in the early universe – a key prediction of inflation. These gravitational waves create both E and B-mode polarisation patterns, but the E-modes they generate would be swamped by those from other sources. In essence, detection of the B-modes is the next step for cosmology and work designing an instrument that aims to detect these modes is the purpose of this thesis.

This chapter will introduce the background theory of the CMB and the history of its detection as well as providing a look at some of the more detailed temperature observations that have been performed. The theory of inflation and why it is necessary for Big Bang cosmology will be briefly explained as well as a description of the polarisation properties of the CMB and the motivation behind the drive for the detection of the aforementioned B-modes. The main polarisation measurements made so far are also summarised.

1.1 History of CMB observations and Big Bang cosmology

In the early 1900s it was found that galaxies had a noticeable radial velocity when observed from the Earth (Slipher, 1913), and this was the first indicator that the universe was not static but in fact, expanding. To try and explain this phenomenon, the 'Big Bang theory' was first proposed by Georges Lemaître in the 1920s (Lemaitre, 1927). A solid observational foundation for this theory was provided by Edwin Hubble (Hubble, 1929), who found many objects that were moving away from us. This theory was then taken much further by Alpher and Herman (Alpher and Herman, 1949), who described the universe expanding from a primordial atom out to the universe we see today (Figure 1.1) as well as Bethe and Gamow who accounted for the abundance of light elements using Big Bang nucleosynthesis (Alpher, Bethe and Gamow, 1948).

With such an energetic beginning to the universe it was theorised that there would be some remnant radiation permeating the universe that should still be observable today. This is now well documented as the CMB but was first theorised by a team at Princeton (Dicke *et al.*, 1965). At around the same time two scientists accidentally detected the CMB. A. Penzias and R.W. Wilson, from Bell labs were testing a horn

antenna (Figure 1.2) for observations at radio wavelengths. Initially they thought they were measuring noise in the system, but after eliminating all sources of noise it was found to be a background radiation with a uniform temperature of 3.5 ± 0.1 K (Penzias and Wilson, 1965) as seen in Figure 1.3. They worked in conjunction with the team at Princeton to combine the theory and the observations into the two papers mentioned that were inarguably the starting point for modern observational cosmology. Penzias and Wilson were awarded the Nobel Physics prize in 1978, for the observation of the CMB.

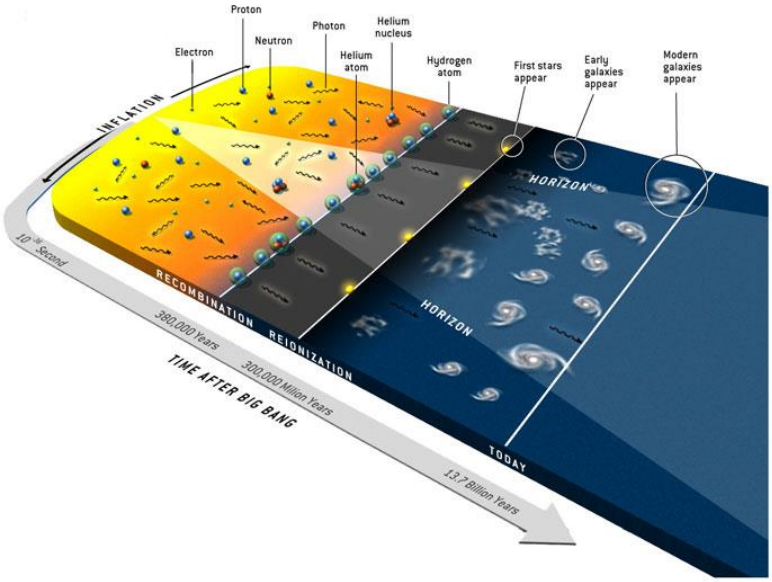

Figure 1.1: Artist interpretation of the expansion of the universe (credit: Bryan Christie Design).

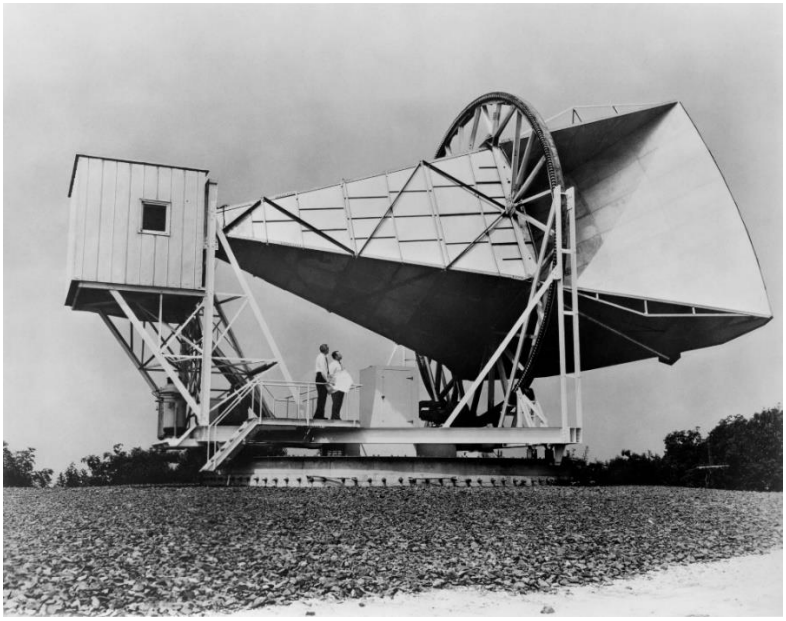

Figure 1.2: Horn Antenna used by Penzias and Wilson to observe the CMB (credit: NASA).

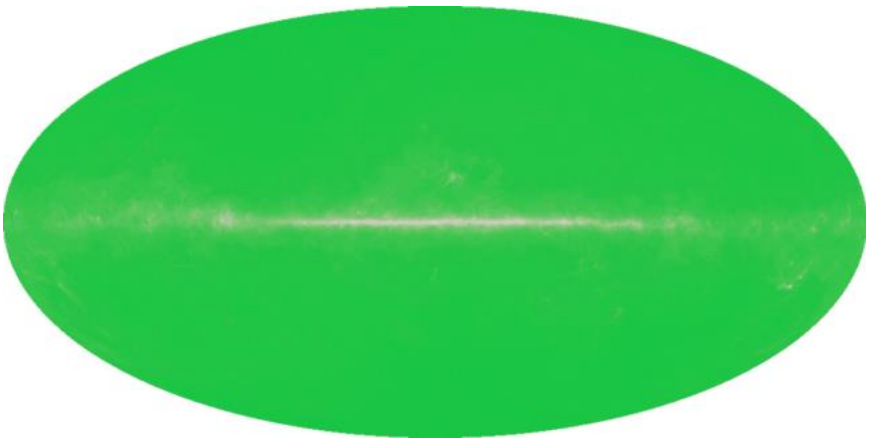

Figure 1.3: Simulated image of the full sky that would have been observed by Penzias and Wilson with their horn antenna (credit: NASA).

1.1.1 The surface of last scattering

Hydrogen (the lightest element) was abundant in the hot early universe when it was also filled with extremely energetic photons. These photons would have had enough energy to fully ionise the hydrogen and create a sea of free electrons. Free electrons have a large scattering cross-sectional area and the resulting scattering of photons from the high abundance of electrons essentially kept photons and matter coupled, making the early universe opaque. Eventually the universe cooled down enough (roughly 380,000 years after the Big Bang) so that the photons could no longer ionise the hydrogen, thus the protons and electrons could 'recombine' and form stable neutral hydrogen. This has a much smaller scattering cross section than the free electrons, thus the photons are said to have 'decoupled' from the matter and were free to travel unimpeded. These photons then travelled throughout the universe and can now be observed as the CMB. The CMB is the oldest observable source of EM radiation in the universe and thus an excellent probe into the early universe.

The photons we see today (the CMB) are considered to have originated from a surface that is known as the last scattering surface (LSS). This apparent source of the CMB was generated over the relatively short period over which recombination and decoupling occurred (roughly a redshift difference of $\Delta z \approx 195$ (Carroll and Ostlie, 2014)). Matter inhomogeneities present at this time imprinted temperature and polarisation inhomogeneities (anisotropies) in the CMB and it is these that we aim to observe today.

1.1.2 The standard cosmological model

One of the aims of cosmology is to develop a model that can describe and explain the entire universe. The current concordance Big Bang model (or standard cosmological model) is known as the Lambda-Cold Dark Matter (ΛCDM) model. This model parametrises a universe that contains three major components; dark energy (associated with a cosmological constant Λ), cold dark matter (CDM) and ordinary baryonic matter. This is a relatively simple model that can account for the properties of the universe and only requires six independent cosmological parameters (Table 1.1) to completely specify the model (Lahav and Liddle (2004) provide a very good overview of the cosmological parameters in the ΛCDM model) while the other parameters can be derived from the initial six. The model can also be extended to account for cosmological inflation.

Table 1.1: List of some cosmological parameters and their associated variables (Lahav and Liddle, 2004).

Parameter	Symbol
Hubble parameter	h
Total matter density	Ω_m
Baryon density	Ω_B
Cosmological constant	Ω_Λ
Radiation density	Ω_r
Neutrino density	Ω_ν
Density perturbation amplitude	$\Delta_R^2(k_*)$
Density perturbation spectral index	n
Tensor to scalar ratio	r
Ionisation optical depth	τ

1.1.3 Inflation theory

As cosmological observations and models became more advanced, it was found that there were observations that, although compatible with the Big Bang theory, could not be explained by it without fine tuning of initial conditions. This lead to the theory of inflation being developed (e.g. Guth, 1981) as an addition to the Big Bang theory. This section will briefly discuss three of these obvious problems, before introducing inflation theory.

Horizon problem

The horizon problem arises from the highly isotropic nature ($\frac{\Delta T}{T} \approx 10^{-5}$, explored further in Section 1.2) of the CMB. Due to the finite age of the universe in Big Bang cosmology, regions of the CMB that are separated by more than roughly 2° should not have been in causal contact (Liddle, 2015). Other than with the imposition of a uniform temperature (which will be maintained as the universe expands and cools) the Big Bang theory cannot explain the isotropy of the CMB.

The flatness problem

Hinshaw *et al.* (2013) show that the current total energy density of the universe Ω_o is very close to unity. However, the parameter (Ω-1) is an increasing function of time, as in equation [1] (Liddle, 2015), meaning that the total energy density at the beginning of the universe would have had to have been extremely close to one, e.g. $|\Omega_o - 1| \leq 10^{-18}$ at nucleosynthesis ($t \approx 1$ s), where the physics is well-understood. Cosmologists believe that there must be a reason for $\Omega_o = 1$ rather than imposing it as a coincidence of the Big Bang.

$$\Omega_{tot}(t) - 1 \propto \frac{|k|}{a^2 H^2} \qquad [1]$$

where k is the geometry of the universe, a is the scale factor of the universe and H is the Hubble time. Note that a^2H^2 decreases roughly linearly with time.

Existence of relic particles

Grand Unified Theories (GUTs) that describe the generation of the fundamental forces from a single force are compatible with the Big Bang theory, but all predict relic particles (e.g. magnetic monopoles) in relatively high abundance, which to date have not been detected.

To account for these and other observations the idea of inflation was proposed. This theory proposes that very soon after the beginning of the universe there was a very short period of time over which the universe expanded exponentially, from quantum to cosmological scales in a fraction of a second. This can be neatly explained using idea of false vacuums from Quantum Mechanics which is beyond the scope of this thesis. This idea of inflation is compatible with the Big Bang theories and bridges the gap between those theories and the observations, providing solutions to the problems mentioned above:

Resolution of the horizon problem

When inflation is accounted for the relationship between the size of the universe and time is non-linear and the size of its current horizon was actually much smaller than originally predicted at the surface of last scattering. It is possible for the entire observable universe to have been in causal contact.

Resolution of the flatness problem

Applying the exponential expansion of the universe from inflation to equation [1], the Hubble time H would remain constant while the scale factor a would increase exponentially. This would drive the right hand side of the equation to zero, thus providing $\Omega_o \approx 1$ in the early universe, explaining the flatness of the universe today.

Resolution of the existence of relic particles

The inflationary period diluted the density of the high energy relic particles (like magnetic monopoles) so that they cannot be detected today.

1.2 Understanding the observations of the Cosmic Microwave Background

This section will explore and explain some of the most important observations that have been made of the CMB, as well as giving a brief overview of the analysis of the data from these observations and how they provide answers to the questions posed by cosmologists.

Observations from more sensitive equipment than Penzias and Wilson had at their disposal have shown that the CMB temperature is not exactly uniform, which is expected since structure existed (matter inhomogeneities) at the time of decoupling, and these regions of differing density appear as hot or cold spots on the CMB due to the Sachs-Wolfe effect (Sachs and Wolfe, 1967).

To date the most comprehensive temperature studies of the CMB have been performed by observations from three satellites: COBE (the Cosmic Background Explorer) (Smoot *et al.*, 1992), WMAP (Wilkinson Microwave Anisotropy Probe) (Hinshaw *et al.*, 2013) and the Planck satellite (ESA and the Planck Collaboration, 2013). These satellites all made full sky maps of the CMB (Figure 1.4), which showed the temperature anisotropies of the CMB in ever increasing detail.

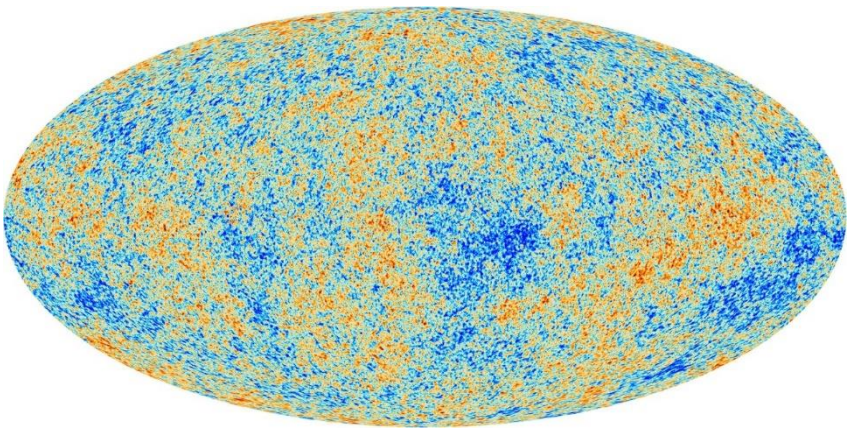

Figure 1.4: Full sky map of the CMB observed by the Planck telescope (credit: ESA).

1.2.1 Representing the data

Temperature anisotropies

The best way to represent the anisotropic temperature data from CMB observations is to express them as a sum of spherical harmonics as in equation [2] (see e.g. Smoot and Scott (1998)). The $l = 1$ dipole is omitted as this is obscured by the dipole resulting from the peculiar motion of the earth with respect to the reference frame of the CMB.

$$\frac{\Delta T}{T}(\theta, \varphi) = \sum_{l=2}^{\infty} \sum_{m=-l}^{l} a_{lm} Y_{lm}(\theta, \varphi) \qquad [2]$$

where, ΔT is the typical difference in the temperature of the CMB, T is the average temperature of the CMB (currently accepted to be 2.725 K), (θ, φ) are the spherical angles, l is the Legendre multipole which is related to angular separation across the sky by $l \approx \frac{180^{o}}{\text{angular sky separation}}$, m is the order of the Legendre multipole, a_{lm} is a spherical expansion coefficient, and Y_{lm} is the standard spherical harmonic.

Power spectrum and acoustics peaks

This decomposition can then be used to generate an angular power spectrum as in Figure 1.5, where $l(l+1)\frac{C_l}{2\pi}$ represents the power of the temperature deviations at given angular extents across the sky (with the amplitude of the multipole expressed as $C_l = \langle |a_{lm}|^2 \rangle$ (Coles and Lucchin, 2002)).

The peaks present in the angular power spectrum in Figure 1.5 are known as acoustic peaks and can be explained if the early universe (before recombination) is thought of as a photon-baryon plasma. Sound waves resulting from the scattering of photons off electrons caused compressions and rarefactions which in turn caused heating and cooling, respectively, of this primordial plasma. A detailed description of the formation of these peaks is provided by Hu and Dodelson (2002). At recombination, photons that were emitted from compressed or rarefied regions had different temperatures (energies) which resulted in a hot and cold spot pattern imprinted onto the CMB. The peaks represent the harmonic modes that ended in a compression or rarefaction at recombination, for example, the first peak was the result of the fundamental harmonic mode that could only complete one compression/rarefaction cycle before recombination.

The study of these peaks provides insights into our universe. For example, models that assume a flat universe predict the first acoustic peak at $l \approx 200$ (Hu and Dodelson, 2002), and the observed data agree

with this, indicating that the universe is in fact flat. Exploring the other peaks and comparing with models can provide information on other aspects of the universe, such as the dark matter and energy in the universe.

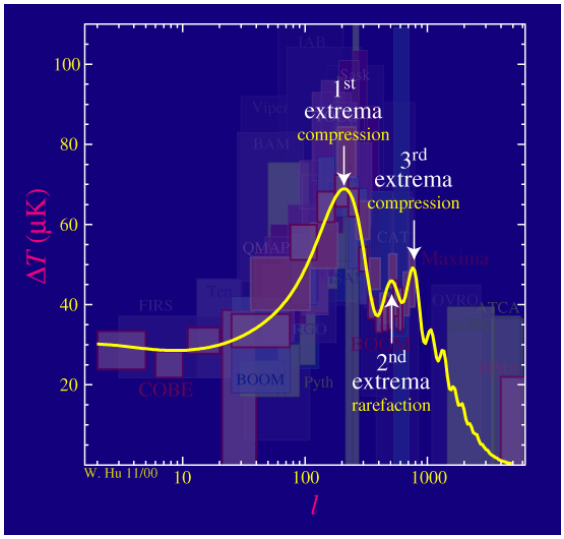

Figure 1.5: Example of an angular power spectrum showing the first three acoustic peaks (extrema) that resulted from compressions/rarefactions in the primordial plasma (Hu, 2001). Note that $\Delta T = l(l+1)\frac{C_l}{2\pi}$.

1.2.2 Satellite observations

COBE

The first full sky map of the CMB was obtained by the COBE satellite (Smoot *et al.*, 1992) which was launched in 1989, and provided the cleanest probe of the temperature anisotropies at that time (Figure 1.6). COBE made observations with an angular resolution of about 7° and found the anisotropies to be at a level of $\frac{\Delta T}{T} \approx 10^{-5}$.

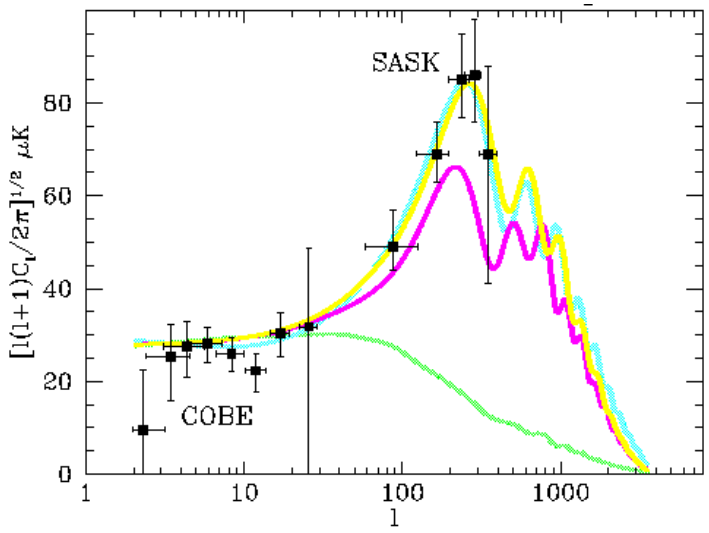

Figure 1.6: Angular Power spectrum models from COBE and other CMB observation missions (plot from Tegmark (1996)). The data from COBE and Saskatoon (Netterfield *et al.*, 1997) are compared with four variants of the standard CDM model of the universe from Sugiyama (1995) all with $n = 1$ and $\Omega_b = 0.05$. From top to bottom at $l = 200$, they are a flat model ($\Omega_\Lambda = 0.7$), a model with $h = 0.3$, the standard model with $h = 0.5$ and a model with a reionization optical depth $\tau \sim 2$.

Chapter 1: Introduction

WMAP

WMAP was launched in 2001 and had a much finer angular resolution than COBE (roughly 0.2º). This gave a much more precise understanding of the temperature anisotropies and the angular power spectrum. The WMAP data (Figure 1.7) provided a detailed measurement of the first and second peaks and some clear evidence of the third acoustic peak indicated by a rise in the data (a further study into the WMAP data provided a measurement of this peak (Hinshaw *et al.*, 2013) as seen in Figure 1.8).

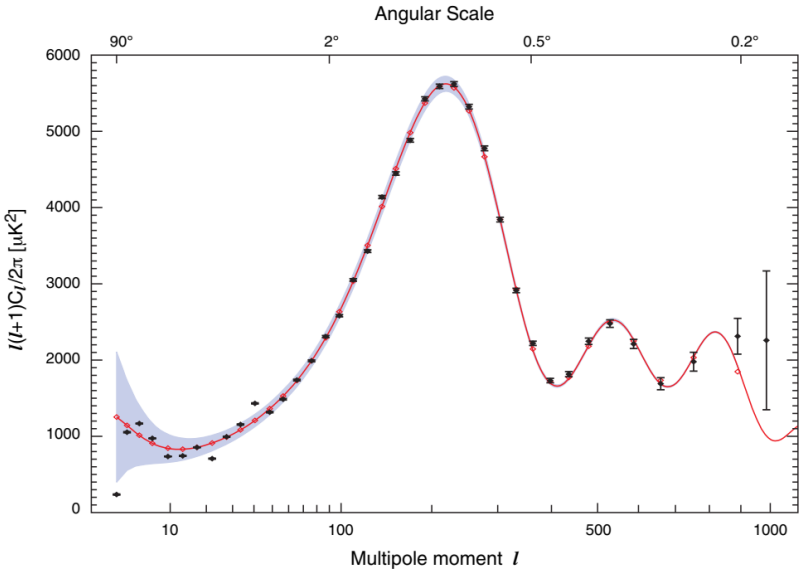

Figure 1.7: Angular power spectrum fitted to the WMAP data produced after 3 years of observations (Hinshaw *et al.*, 2007). The binned three-year angular power spectrum (in black) from $l = 2 - 1000$ is also shown. The points are plotted with noise errors only. The red curve is the best-fit ΛCDM model, fit to WMAP data only (Spergel *et al.*, 2007), and the band is the binned 1σ cosmic variance error. The red diamonds show the model points when binned in the same way as the data.

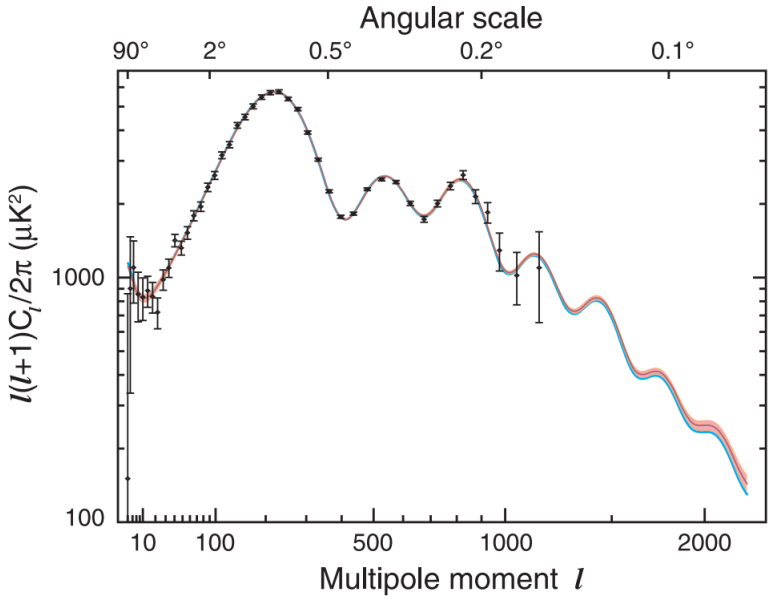

Figure 1.8: Angular power spectrum of 9 years of WMAP data compared with 6 parameter ΛCDM models. (Hinshaw *et al.*, 2013).

Planck

The most recent satellite to observe the CMB was the Planck instrument (Planck Collaboration I, 2014) which was launched in 2012 and had an angular resolution of between 0.08° and 0.16º. This was the most powerful probe of the CMB temperature and the angular power spectrum produced (Figure 1.9) shows very robust measurements of the 7 acoustic peaks present to $l = 2500$.

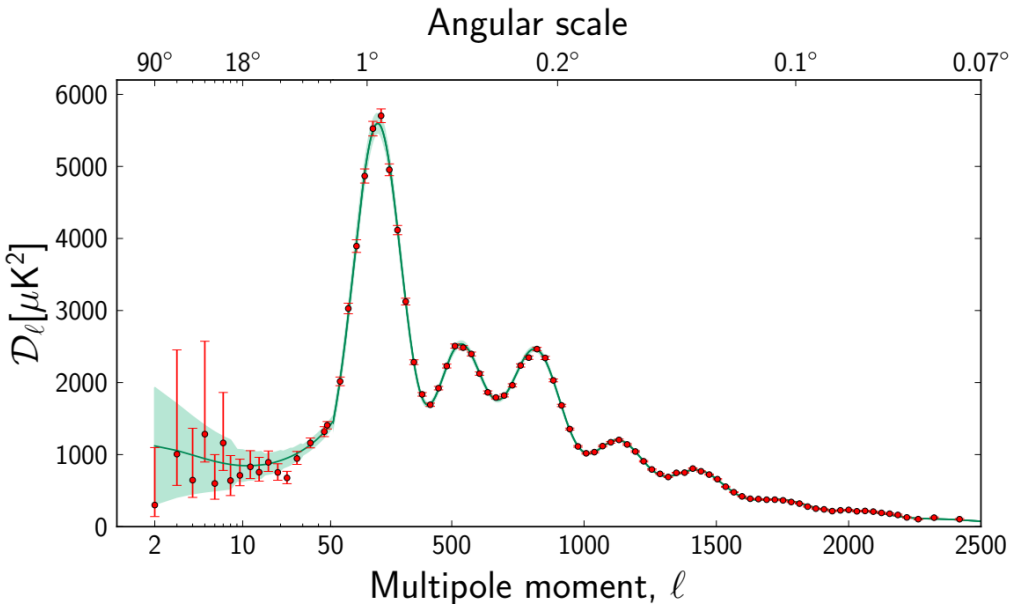

Figure 1.9: Temperature angular power spectrum of the primary CMB from Planck, showing a precise measurement of seven acoustic peaks that are well- fitted by a six-parameter ΛCDM model (the model plotted is the one labelled [Planck + WP + highL] in Planck Collaboration XVI (2014)). The shaded area around the best-fit curve represents cosmic/sample variance, including the sky cut used. The error bars on individual points also include cosmic variance. The horizontal axis is logarithmic up to $l = 50$, and linear beyond. The vertical scale is $l(l + 1)C_l = \pi$.

Planck has extracted essentially all of the information from the temperature anisotropy of the CMB, providing a good understanding of the parameters of the ΛCDM model. The next big step is to investigate its polarisation.

1.3 Polarisation of the CMB

The radiation from the CMB has a polarisation associated with it. This results from Thompson scattering from an electron of perpendicularly incident radiation at different temperatures (quadrupole anisotropy) as shown in Figure 1.10.

1.3.1 Describing the polarisation

The full polarisation state of a photon can be described by Stokes parameters (Stokes, 1880) as shown in Table 1.2 and seen in Figure 1.11. Since the polarisation of the CMB is only linear, the Q and U parameters are sufficient to describe its polarisation state.

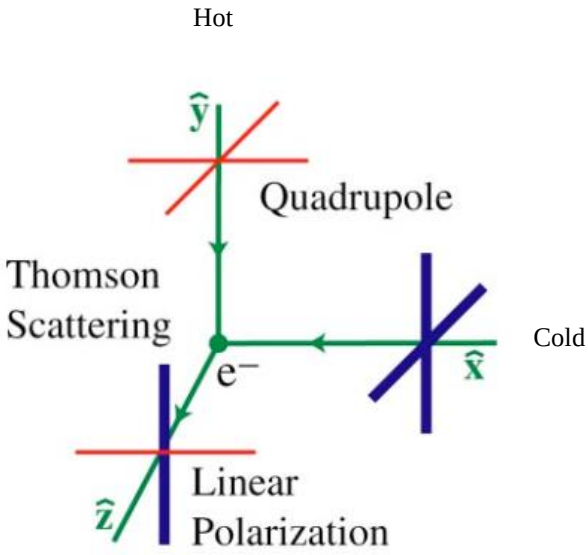

Figure 1.10:Quadrupole anisotropy incident on an electron will result in Thompson scattering that creates a linearly polarised photon (Image obtained from Hu and Dodelson, 2002).

Table 1.2: Descriptions of the four Stokes parameters

Parameter	Measures
I	Intensity
Q	Vertical/horizontal polarization level
U	Diagonal polarization level
V	Circular polarization level

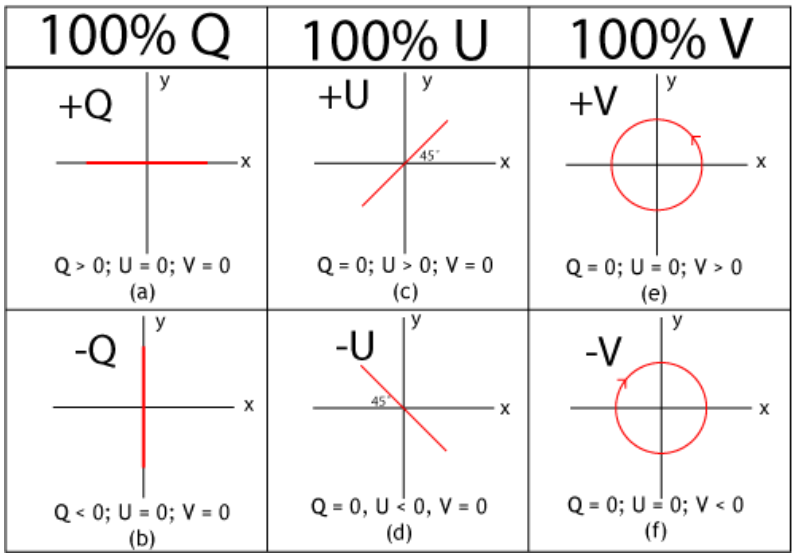

Figure 1.11: Schematic representation of stokes parameters for a beam travelling into the page (image available at https://en.wikipedia.org/wiki/Stokes_parameters)

An issue with using the Stokes parameters is that they are coordinate dependent (meaning that if the observer changed their orientation by 45°, the Q and U parameters would be swapped). Equations [3] and [4] show a pair of coordinate independent parameters that were derived from the Q and U parameters (Zaldarriaga and Seljak, 1997) expressed in a similar format to the temperature anisotropies above. These are the E- and B-modes and are the respective gradient and curl terms of the CMB polarisation pattern.

$$\tilde{E}(\hat{n}) = \sum_{lm} \left[\frac{(l+2)!}{(l-2)!}\right]^{\frac{1}{2}} a^{E}{}_{lm} Y_{lm}(\hat{n}) \qquad [3]$$

$$\tilde{B}(\hat{n}) = \sum_{lm} \left[\frac{(l+2)!}{(l-2)!}\right]^{\frac{1}{2}} a^{B}{}_{lm} Y_{lm}(\hat{n}) \qquad [4]$$

Taking a hot or cold spot in the CMB as the centre, the polarisation pattern present around that spot can be of two forms; E-mode or B-mode which are curl-free and divergence-free respectively (as seen Figure 1.12 and analogous to electric and magnetic fields). The present pattern is an indicator of the mechanisms which caused the quadrupole anisotropy (either a scalar or a tensor perturbation).

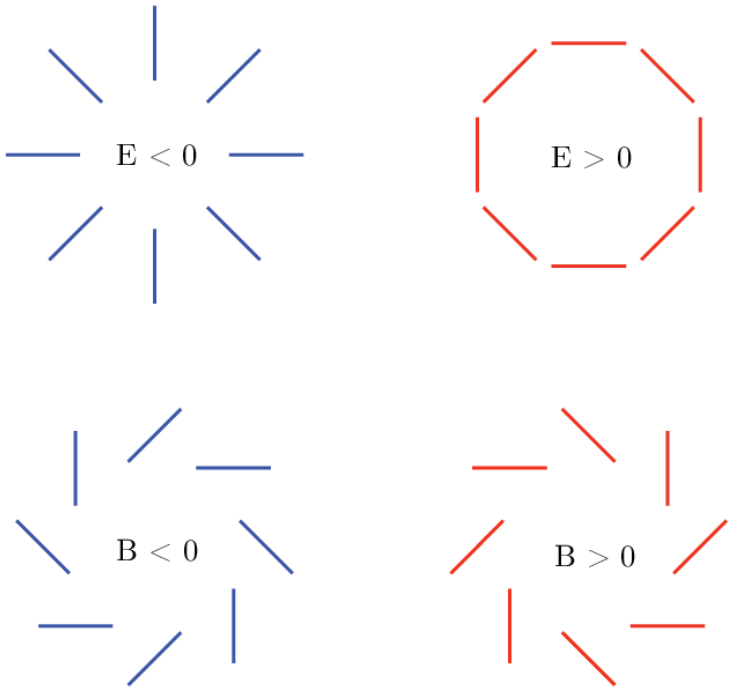

Figure 1.12: E modes (curl free) and B modes (divergence free). Image obtained from Baumann *et al.* (2009).

1.3.2 Scalar and tensor Perturbations

Hu and White (1997) describe how temperature perturbations on the CMB have three geometrically distinct sources: scalar ($m = 0$), vector ($m = 1$) and tensor ($m = 2$); the quadrupole variant ($l = 2$) of each of these can be seen in Figure 1.13. Vector perturbations are not compatible with inflation theory as they will decay as the universe expands unless they are continually generated (White and Cohn, 2002), hence that leaves two sources for the generation of the polarisation pattern of the CMB. From observing this pattern (Figure

1.14) it can be seen that the pattern produced by the scalar perturbations does not contain any of the asymmetric patterns expected of B-mode polarisation unlike what is observed for the pattern resulting from tensor perturbations. Thus, scalar perturbations only produce E-mode polarisation and tensor perturbations produce both E- and B-mode polarisation.

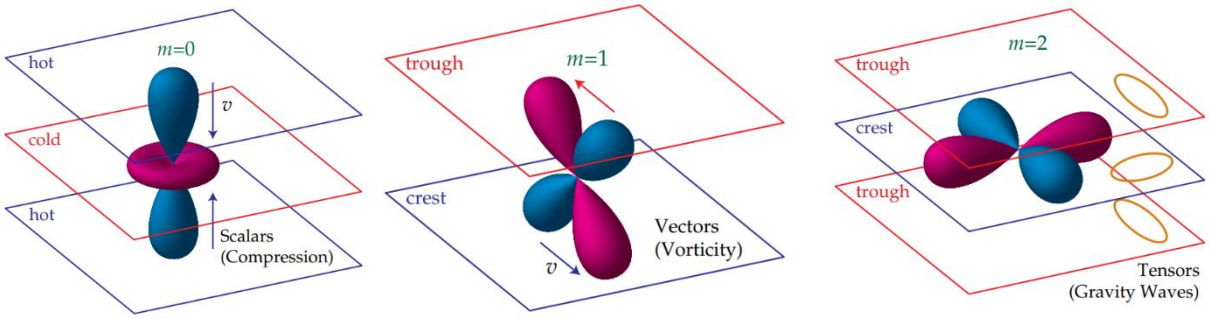

Figure 1.13: Representation of the polarisation pattern resulting from a scalar, vector and tensor perturbation (Hu and White, 1997).

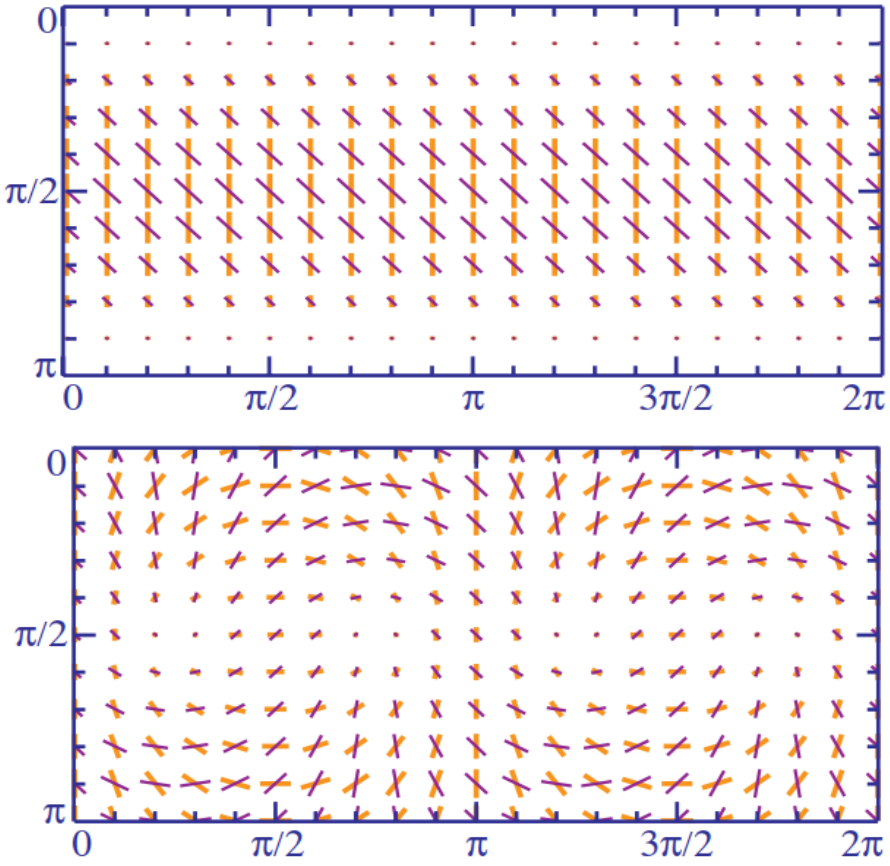

Figure 1.14: polarisation pattern resulting from scalar perturbations (top) and tensor perturbations (bottom). The yellow lines indicate the E-modes and the purple lines are rotated by 45° and represent the B-mode pattern if present (Hu and White, 1997).

The scalar perturbations are caused by density fluctuations (that also cause the hot and cold spots on the temperature maps) while the tensor perturbations are caused by gravitational waves, which can only result from the very energetic period of inflation. Gravitational lensing of the E-mode polarisation by intervening matter can result in a B-mode pattern, but these are not considered 'primordial' B-modes. Hence primordial B-modes are the 'smoking gun' of inflation theory and detection of these is the next big step in observational cosmology and the goal of the QUBIC (Q & U Bolometric Interferometer for Cosmology) instrument on which this thesis is based.

Since the polarisation of the E and B-modes can be decomposed into spherical harmonics, the coefficients $a^E{}_{lm}$ and $a^B{}_{lm}$ can be obtained in a similar way to the temperature anisotropies and an angular power spectrum can be generated for the E and B modes as in Figure 1.15. Since the E-modes originate from scalar (density) perturbations the acoustic peaks are also present in its spectrum. It can also be seen that the E-mode spectrum is orders of magnitude lower than that of the temperature anisotropies, both the density oscillations and the low power levels of the E-modes have been verified with the DASI (Degree Angular Scale Interferometer) instrument (Kovac *et al.*, 2002). The B-mode spectrum has not been directly detected but is predicted to be orders of magnitude lower again, hence an instrument with unprecedented levels of sensitivity will be required for its detection. It can also be seen where the E-mode spectrum can be gravitationally lensed to appear as B-modes, this is restricted to higher multipoles (smaller angular resolution). An instrument that is restricted to lower multipoles (larger angular resolution) can avoid detection of these lensed modes and will only detect primordial B-modes.

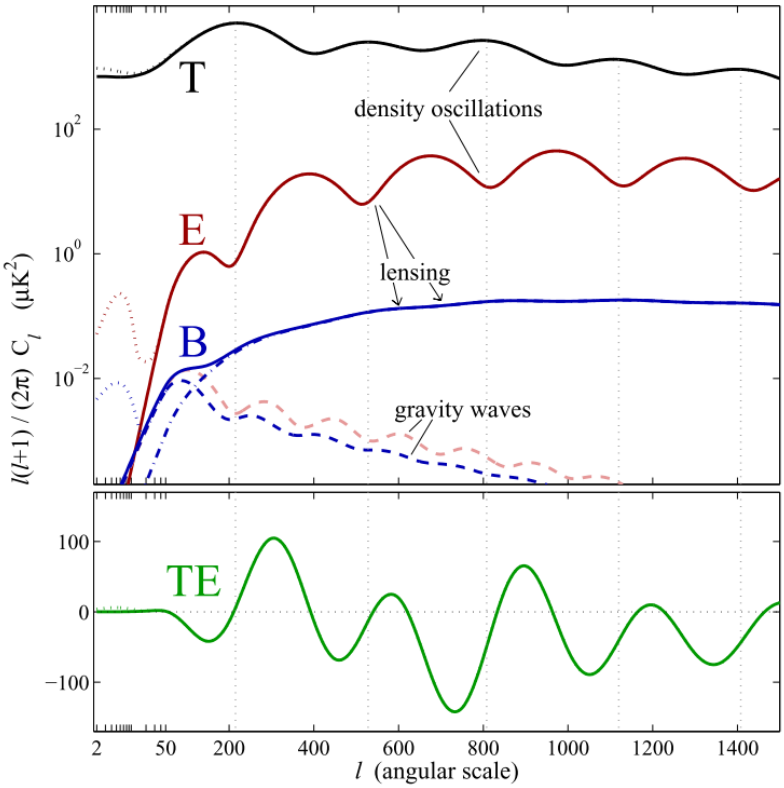

Figure 1.15: Simulated angular power spectrum of the temperature anisotropies, E-modes and B-modes (Carlstrom *et al.*, 2003). TE represents the cross power component of the temperature and E-mode spectra, TB and EB do not exist as the B-mode field has opposite polarity to the E-mode field and the temperature field.

1.3.3 Tensor to scalar ratio

Detection of the B-modes would constrain the tensor to scalar ratio r, which can be thought of as the ratio of the power of the B-modes (resulting from tensor perturbations) to the E-modes (resulting from scalar perturbations) such that $r = C_l^B / C_l^E$, at $l = 2$ (see e.g. Tartari *et al.*, 2016). This can be used to determine the energy scale of inflation, V by equation [5] (see e.g. Planck Collaboration XVI, 2014).

$$V^{\frac{1}{4}} \approx 1.06 \times 10^{16}\text{GeV}\left(\frac{r}{0.01}\right)^{\frac{1}{4}} \quad [5]$$

This energy scale is massive and observations of the tensor perturbations (as well as furthering our knowledge of cosmology and the parameters of ΛCDM models of the universe) can provide a probe into high energy physics at levels that are orders of magnitude greater than what is available at the LHC and Baumann *et al.* (2009) propose compelling arguments for the observation and detection of the B-mode polarisation for the field of high energy physics as well as general relativity and string theories. If high-energy physics theories are used in conjunction with the concordance model of the universe it can estimated that the inflation scale would be of the order of 10^{16} GeV, which would provide a value of $r = 0.01$ (from equation [5]). This is just an estimate however, all the current data can currently only constrain the tensor-to-scalar ratio as $r < 0.06$ with a 95% confidence level (Ade *et al.*, 2018). To refine this constraint further more sensitive measurements are required.

1.3.4 Polarised foregrounds

Detection of the faint B-mode signal requires a very sensitive instrument, but it also requires accurate correction for the polarised foreground. When observing the CMB, you also observe radiation from any intervening source, these are known as the foregrounds and need to be corrected for to obtain an accurate CMB map. Table 1.3 (Dickinson, 2016) shows that the polarisation levels vary considerably for the different foregrounds, but both Galactic synchrotron radiation and the different forms of Galactic dust radiation have considerable levels of polarisation (combined they would present a polarisation level of at least 10%) that occur at the angular scales of the primordial B-modes. Being able to separate the B-mode polarisation and the foreground polarisation components from the observations is vital in ensuring accurate detection of the B-modes and is the reason why CMB experiments make observations at multiple frequencies.

Table 1.3: Examples of different types of CMB foregrounds, with the associated angular scale across the sky at which they are present as well as the estimation of the level in which they are present. Adapted from Dickinson (2016).

Foreground	Angular Scale	Polarisation level
Atmosphere	Large scale	$\approx 0\%$
Ground	Large scale	Varies
Radio Frequency Interference	All	$0 - 100\%$
Sun/Moon	All	Low
Planets/Solar system	Small scale	Low
Zodiacal light	Large scale	Low
Galactic synchrotron radiation	Large scale	$\approx 10 - 40\%$
Galactic free-free radiation	Large scale	Low
Galactic thermal dust radiation	Large scale	$\approx 2 - 20\%$
Galactic spinning dust radiation	Large scale	Low
Galactic magnetic dust radiation	Large scale	$\approx 0 - 35\%$
Galactic line emission	Large scale	Low
Radio Galaxies	Small scale	Few %
Sub-mm/IR Galaxies	Small scale	Low
Infrared Background (CIB)	Small/Intermediate scale	Low

1.3.5 Polarisation measurements to date and the current state-of-the-art

As mentioned above, the E-mode polarisation was measured by the DASI instrument and provided some promising results. Since then, the E mode polarisation has been measured by the Planck instrument (Figure 1.16) which provided very good agreement between the model and the observations.

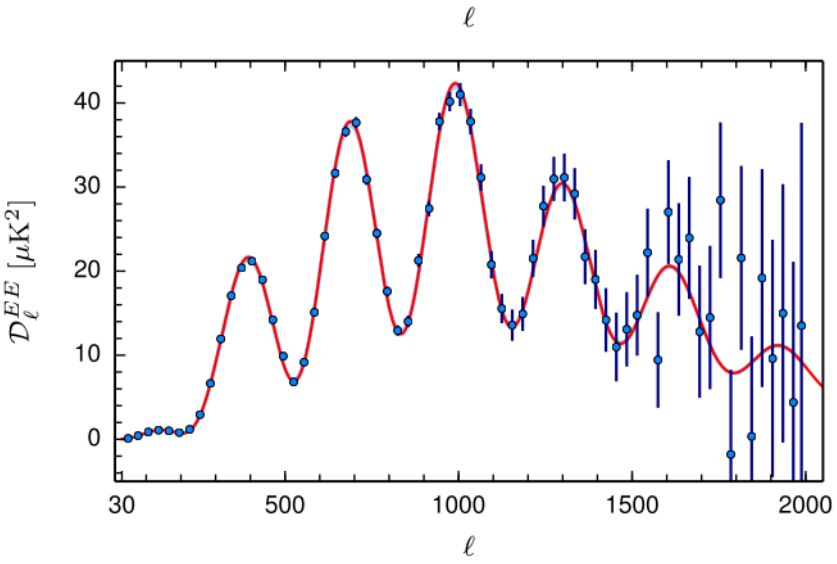

Figure 1.16: EE angular power spectrum. The red line shows the theoretical EE spectrum from the Planck high l (> 30) ΛCDM model and make use of the Planck temperature and polarisation data. Image obtained from Planck Collaboration XX. (2016).

As mentioned, there has been no detection of the primordial B-modes. There are many instruments hoping to provide this (Table 1.4). The most notable and advanced of these is BICEP3 (Background imaging of Extragalactic Polarisation). BICEP has been through two iterations (conveniently named BICEP (Yoon *et al.*, 2006) and BICEP2 (Ogburn IV *et al.*, 2010)), and now it has joined with the Keck array and there is a plan to expand the instrument array further (Schillaci *et al.*, 2020). For an overview of the BICEP iterations- more papers are available at http://bicepkeck.org/.

BICEP (at the time of writing) is the leader in the race to detect the primordial B-mode polarisation. In 2014 primordial B-modes were reportedly detected by BICEP2, however after a joint BICEP2/Keck Array/Planck study (Ade *et al.*, 2015) it was found that this measurement was actually more consistent with the polarised foreground from cosmic dust. This measurement was important as it showed the levels of sensitivity required for B-mode detection could be achieved and also it cemented the importance of accurate modelling and understanding of the polarised foreground so that it could be corrected. This is a big area of research for the CMB community and was a leading area of discussion in the 'B mode from space' conference in late 2019. Extensive refining of the Planck results has provided a detailed full sky map of the polarised foreground (Planck Collaboration IV, 2018) which has helped significantly in this area.

Even though detection of the primordial B-modes is the main goal of QUBIC, detecting the B-modes at higher multipoles from the gravitational lensing of E-modes is still important as it can provide information on the gravitational structures present in the universe. A promising instrument that aims to do this is the Simons Array. This will consist of 3 POLARBEAR2 type instruments which are an expansion of the successful POLARBEAR instrument (Arnold *et al.*, 2010). POLARBEAR observed the multipole range $500 \leq l \leq 2100$ and has observed lensed B-mode polarisation that matches well with the theoretical predictions (The POLARBEAR Collaboration, 2017) as seen in Figure 1.17. High levels of sensitivity were obtained to observe these B-modes and this will be expanded in the Simons Array to lower multipoles to try and detect the primordial B-modes.

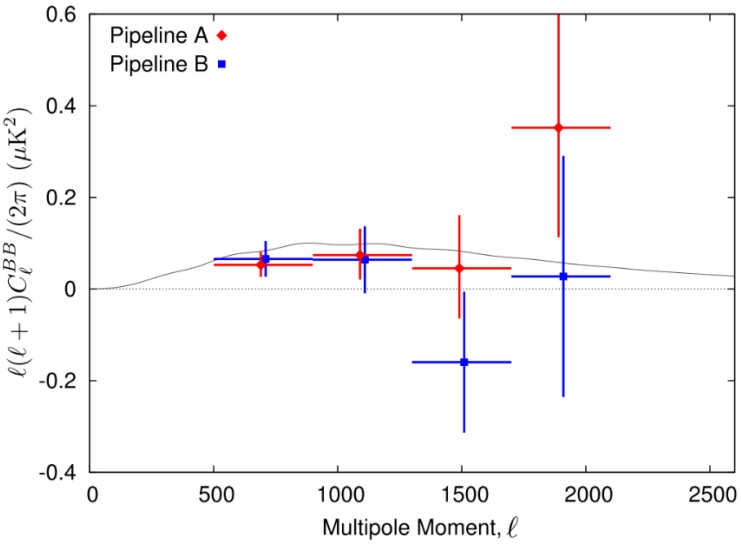

Figure 1.17: POLARBEAR B-mode angular power spectrum from two seasons of data (The POLARBEAR Collaboration, 2017). The datapoints show the measured band powers form each pipeline. The error bars correspond to the 68.3% confidence intervals of the statistical uncertainty only (no systematic uncertainties) the black curve is a theoretical ΛCDM model of the lensed B-spectrum from the Planck data.

It is a very exciting time in the CMB community, LiteBIRD (Sugai *et al.*, 2020) the first satellite solely for CMB polarisation observations is being studied and developed. This is a joint venture between Japan, North America and Europe. It will have a range between $2 \leq l \leq 200$ with a planned launch in 2027 if funded.

Table 1.4: A non-exhaustive list of current and proposed CMB instruments representing the current state of the art in CMB B-mode instruments with the aim of observing the B-mode polarisation signal (results or proposals for most of these instruments were presented at the 'B-mode from Space' conference held in the Max Planck Institute for Astrophysics, Garching from December 16-19, 2019 that this author attended).

Instrument	Reference	Observation	Type	Frequency (GHZ)	Status
Simons Array	Stebor *et al.*, 2016	Primordial and lensed B-modes (expansion of POLARBEAR)	Ground	95, 150	Deployed (continually improved with more receivers)
BICEP3	Grayson *et al.*, 2016	Primordial B-modes	Ground	95, 150, 220	Deployed
GroundBIRD	Oguri *et al.*, 2016	Primordial B-modes	Ground	145, 220	Under construction
QUIJOTE	López-Caniego *et al.*, 2014	Primordial and lensed B-modes	Ground	10, 20, 30, 40	Deployed
South Pole Telescope (SPTpol)	Austermann *et al.*, 2012	Primordial and lensed B-modes	Ground	90, 150	Deployed
Keck Array	Sheehy *et al.*, 2010	Primordial B modes	Ground	150	Deployed
SPIDER	Gualtieri *et al.*, 2018	Primordial B-modes	Baloon	90, 150	Launched
Ali CMB project	Li *et al.*, 2019	Primordial B-modes	Ground	95, 150	Under construction
LiteBIRD	Sugai *et al.*, 2020	Primordial B-modes	Satellite	40, 50, 60, 68, 78, 89, 100, 119, 140 166, 195, 235, 280, 337, 402,	Proposal being studied
CMB-S4	Abazajian *et al.*, 2019	Primordial and lensed B-modes	Ground	7 bands from 20 – 278 GHZ	Proposal being studied

1.4 QUBIC site

QUBIC itself will have a field of view of 12.9°, which is defined by the horns that will be used at the aperture of the instrument (these will be discussed more later in the thesis). This allows it to observe large angular extents on the sky and restrict the instrument to lower multipole moments. QUBIC will observe at the Alto Chorillos site in Argentina (24°11′11.7″ S; 66°28′40.8″ W, altitude of 4869 m above sea level), which has been shown to have low atmospheric opacity at the frequencies at which QUBIC will observe (150 and 220 GHz) as seen in Figure 1.18. The instrument will use an alt-azimuth mount to allow it to point to the desired region on the sky. The region on the sky it will observe will require low dust foregrounds to minimise the polarisation contamination mentioned earlier.

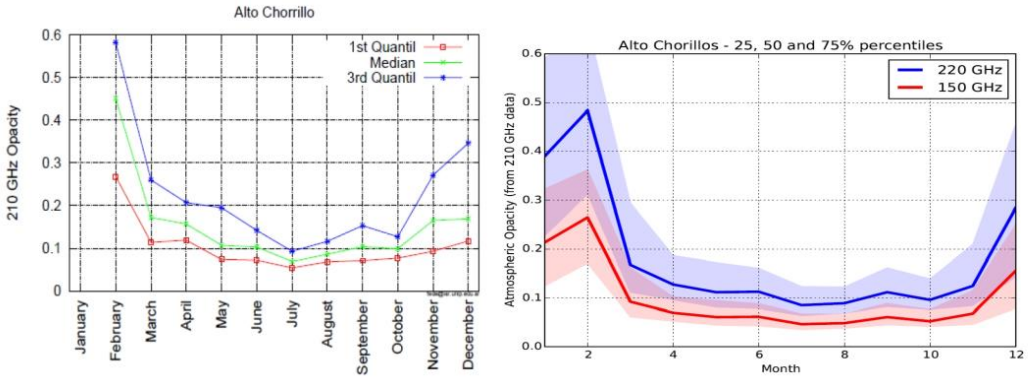

Figure 1.18: Left: atmospheric opacity at 210 GHz as measured in Alto Chorrillos for each month. Right: extrapolations to 150 GHz and 220 GHz. Image obtained from Garc *et al.* (2020).

1.5 Outline of Thesis

The current state of the art of the CMB B-mode instruments is very impressive, and this thesis focusses on one such experiment: the QUBIC instrument. This instrument is different from those mentioned above because it will use the novel technique of bolometric interferometry to act as a synthetic imager, allowing it to exploit the benefits of both interferometry and imaging in order to achieve the sensitivity levels required for primordial B-mode detection. It will also operate over two frequency bands, to allow for foreground separation.

Chapter 2 introduces the optical modelling techniques and software that will be used to analyse the quasi-optical combiner of the QUBIC instrument. There are two techniques explored in detail, Gaussian beam mode analysis and physical optics. Both of these methods model the diffraction effects of the instrument, with physical optics being more accurate and providing a full vector analysis. This chapter also introduces the optical modelling software MODAL that was used extensively throughout this thesis in the analysis of the QUBIC instrument.

Chapter 3 discusses the QUBIC instrument, providing the overall aims and a brief description of the history of QUBIC. The instrument itself and its systems is described in this chapter, providing insight into how the instrument will operate and how all the systems will combine to create a novel instrument with the sensitivity levels required to detect the primordial B-modes. It was decided that a technological demonstrator be constructed and this instrument will be introduced with the differences between this and

the full instrument highlighted. This chapter will finish with some optical modelling results, using the MODAL software to predict the point spread function and the synthetic beam of the instrument.

Chapter 4 provides the results of modelling the technological demonstrator, with a particular focus on the modelling of the test and calibration setup of the instrument. It investigates the effects of different components on the instrument's performance and calculates the tolerance of the positions of the mirrors in the combiner to misalignments. Some comparisons with measured results obtained in the lab are also be discussed in this chapter.

Chapter 5 is concerned with the performance of the horns in the QUBIC horn array. Mode matching techniques that were used to analyse the individual horns are detailed along with the results of that modelling in both operating frequency bands of the instrument. This chapter finishes with some comparisons between the results of the simulations of realistic horn geometries to the results of a Vector Network Analysis of the real horns carried out by collaborators in Milan, Italy.

Chapter 6 focuses on future instrument modelling, including the modelling of the full QUBIC instrument, in both operating bands using physical optics. An investigation of spectro-imaging and its viability as a means for distinguishing between signals at different frequencies is presented.

Chapter 7 summarises the conclusions to the research presented in this thesis.

2 Optical modelling software

2.1 Introduction

This chapter will discuss the theory behind both Gaussian Beam Modes (GBM) and Physical Optics (PO) modelling techniques and will describe how to use the in-house Maynooth Optics Design and Analysis Laboratory, or MODAL software (Gradziel *et al.*, 2007) using a simple multi-slit interferometer as an example to provide some context for the QUBIC modelling performed later.

Throughout this thesis the modelling of the optical combiner of the QUBIC instrument (Figure 2.1) will be presented – note that any modelling performed for the QUBIC optical combiner in this chapter will only use the most basic setup, consisting of two mirrors and a focal plane. A geometric (ray) optical (GO) analysis is not enough to model the instrument since it will observe at two bands centred on 150 GHz (λ=2 mm) and 220 GHz (λ=1.4 mm) whose wavelengths are of the same order of magnitude as the size of the optical components (a 'quasi optical' system). This means that there will be diffraction and aberration of the beams as they interact with the optical elements, making GO inadequate. Thus, to model this instrument, the in-house software MODAL was used. This is a robust software that can utilise both PO and GBM to analyse a system.

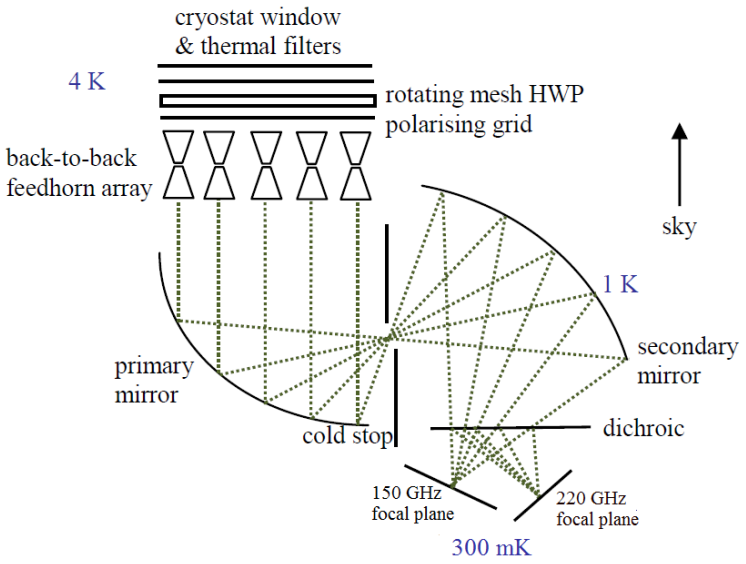

Figure 2.1: Simple schematic of the offset-Gregorian design for the optical combiner of the QUBIC instrument (image adapted from (Scully *et al.*, 2016)).

2.1.1 Physical optics

PO analysis is a computationally expensive but accurate vector method for analysing electromagnetic (EM) radiation in a system. It uses the wave interpretation for EM radiation which also includes the phase component. This allows for the modelling of more complex phenomena such as diffraction, interference and polarisation.

To perform a PO analysis of radiation from a surface on which there is incident radiation, the surface must be sampled. Each sample position is known as a PO point. In PO analysis it is assumed that the surface is a perfect conductor and this allows for the electric field radiated by it to be calculated using a surface current

induced from incident radiation. For these perfectly conducting surfaces, the induced current at each PO point is assumed to be equal to the current of an infinite plane that is tangential to the surface at the PO point. This does present some limitations with PO for very curved surfaces or at the edge of surfaces. The induced electric (J_e) and magnetic (J_m) current densities on these surfaces give rise to the vector potentials (Collin and Zucker, 1969)

$$\boldsymbol{A_e} = \frac{\mu_o}{4\pi}\iint_S \boldsymbol{J_e}(\mathbf{r}')\frac{e^{-jkR}}{R}dS \quad [6]$$

$$\boldsymbol{A_m} = \frac{\varepsilon_o}{4\pi}\iint_S \boldsymbol{J_m}(\mathbf{r}')\frac{e^{-jkR}}{R}dS \quad [7]$$

where A_e is the electric vector potential and A_m is the magnetic vector potential, μ_o is the permittivity of free space, ε_o is the permeability of free space, r' is the integration variable, R is the radial propagation distance given by $|\mathbf{r} - \mathbf{r}'|$ (where r is the observation point), k is the wavenumber, and S is the scattering surface.

The electric and magnetic potential each give rise to both an electric and magnetic field, resulting in equations [8] and [9] (see e.g Balanis, 2005).

$$\mathbf{E} = -j\omega\left(\boldsymbol{A_e} - \frac{\nabla(\nabla.\boldsymbol{A_e})}{\omega^2\mu_o\varepsilon_o}\right) - \frac{1}{\varepsilon_o}\nabla\times\boldsymbol{A_m} \quad [8]$$

$$\mathbf{H} = -j\omega\left(\boldsymbol{A_m} - \frac{\nabla(\nabla.\boldsymbol{A_m})}{\omega^2\mu_o\varepsilon_o}\right) - \frac{1}{\mu_o}\nabla\times\boldsymbol{A_e}. \quad [9]$$

If the surface is a perfect conductor then the scattered field ($\boldsymbol{E_S}$) is generated from the induced current due to the incident field ($\boldsymbol{E_I}$), with the total radiated field ($\boldsymbol{E_T}$) being the sum of the two fields (TICRA, 2005)

$$\boldsymbol{E_T} = \boldsymbol{E_I} + \boldsymbol{E_S}. \quad [10]$$

The scattered field can be obtained using the PO approximation of infinite conducting planes so that

$$\boldsymbol{E_S} \approx \boldsymbol{E_{PO}}. \quad [11]$$

Considering the scattered electric field using only PO can cause some inaccuracies at the edge of a surface, the infinite plane assumption cannot always capture some of the special behaviour at these points. So, another method, known as the Physical Theory of Diffraction (PTD), can be used. PTD calculates the field in nearly the same way as PO, except it assumes an infinite half plane (Johansen, 1996). Hence the scattered electric field would be given by equation [12]

$$\boldsymbol{E_S} \approx \boldsymbol{E_{PO}} + \boldsymbol{E_{PTD}}. \quad [12]$$

MODAL uses the PO approximation only, this is sufficient for the modelling of the QUBIC instrument, and when compared with GRASP (TICRA, 2005), the industry standard that can utilise PTD for large

beams (in which the incident field would strike the edges of the reflectors and the benefits of PTD would be seen) it can be seen that both provide very similar results for QUBIC simulations, a full verification of MODAL against GRASP was performed by S. Scully (Scully, 2015). An example can be seen in Figure 2.2 (the setup for this simulation is explored in much more detail in Section 6.2). MODAL provides other benefits, e.g. it allows for the generation of complex element shapes, and for the modelling of accurate horn geometries within an optical system so Gaussian approximations do not need to be utilised (this will be discussed in more detail in Section 2.2.3). Other benefits of MODAL will be highlighted throughout this thesis.

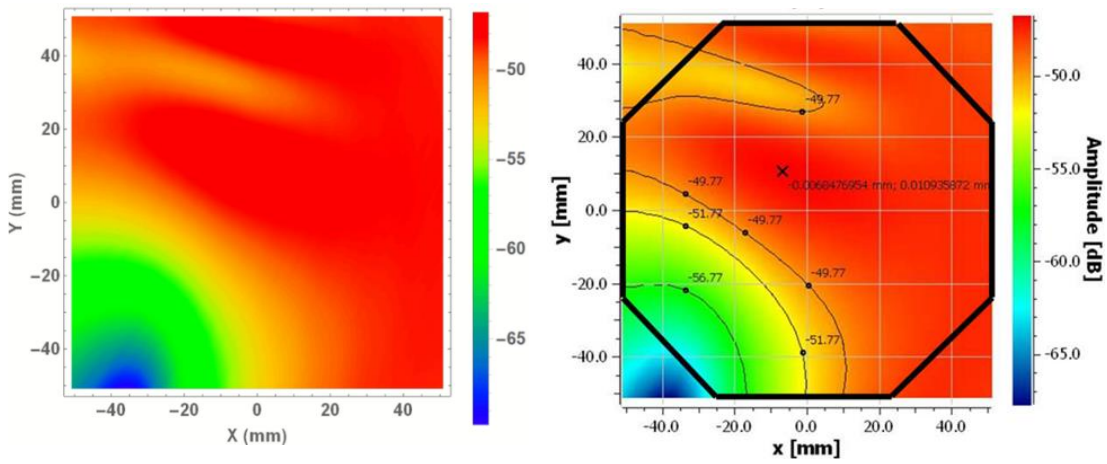

Figure 2.2: Beam pattern on the focal plane of the QUBIC instrument resulting from the propagation of a 50° Gaussian beam through the QUBIC optical combiner simulated in MODAL (left) and GRASP (right). The GRASP plot was provided by M. De Petris of the Sapienza University of Rome, the black outline in the GRASP pattern indicates the approximate shape of the focal plane in the QUBIC instrument. Both patterns are normalised to the peak of the input beam in both models.

2.1.2 Gaussian Beam Mode analysis

GBM analysis is a less computationally expensive method of analysis, and it also takes diffraction into account, so it can be an ideal alternative in some cases. To use this approach, we have to make some assumptions to simplify the situation (Lesurf, 1990).

Paraxial approximation: This assumes that the beam is collimated, i.e. its cross sectional area is not large enough so that it can be treated as an infinite parallel plane wave, and that it is moving along a given axis, however there is some diffraction taking place so the beam spreads out into a small opening angle (the divergence of the beam is typically within 10° of the axis).

Scalar field: The beam must be represented by a scalar field; to account for the polarisation of the field the beam must be represented as two separate independently propagated scalar fields (Goldsmith, 1998).

Field variation: The transverse variation of the beam compared to the wavelength is small.

With these approximations the Gaussian Beam modes are solutions to the wave equation in free space. We can show this by first considering EM waves in free space that satisfy the Helmholtz equation as expressed in equation [13] (Siegman, 1986; Goldsmith, 1998)

$$(\nabla^2 + k^2)\Psi = 0. \quad [13]$$

where Ψ represents any component of the electric or magnetic field. Considering an electric field propagating in the z direction, its transverse profile can be expressed in terms of a complex scalar function $u(x, y, z)$:

$$E(x, y, z) = u(x, y, z)\exp[-jkz] \quad [14]$$

where k is the wavenumber, $2\pi/\lambda$, of the EM radiation. This can then be inserted into equation [13], along with the assumptions above and, expressed in cartesian coordinates, gives equation [15] (Siegman, 1986). This is known as the reduced wave equation or paraxial wave equation.

$$\frac{\partial^2 u}{\partial x^2} + \frac{\partial^2 u}{\partial y^2} + k^2\frac{\partial u}{\partial z} = 0. \quad [15]$$

Goldsmith (1998), for example, provides a derivation of a general solution to the paraxial wave equation:

$$u(r, z) = A(z)\exp\left[\frac{-jkr^2}{2q(z)}\right] \quad [16]$$

where $r = \sqrt{x^2 + y^2}$ and $q(z)$ is known as the complex beam parameter and can be expressed in terms of the radius of curvature, $R(z)$, and the beam radius, $w(z)$ (Figure 2.3), as in equation [17].

$$\frac{1}{q(z)} = \frac{1}{R(z)} - \frac{j\lambda}{\pi w(z)^2} \quad [17]$$

where

$$R(z) = z + \frac{1}{z}\left(\frac{\pi}{\lambda}{w_0}^2\right)^2 \quad [18]$$

and

$$w = w_0\left[1 + \left(\frac{\lambda z}{\pi {w_0}^2}\right)^2\right]^{0.5} \quad [19]$$

and w_0 is the beam radius at $z = 0$

Equation [20] (see e.g. Goldsmith, 1998) gives the dispersion angle, θ_o in Figure 2.3. The FWHM angle, which is used throughout this thesis to express the size of gaussians beams, is given in equation [21].

$$\theta_o = \frac{\boldsymbol{\lambda}}{\pi w_o} \quad [20]$$

$$\theta_{FWHM} = 1.18\theta_0. \quad [21]$$

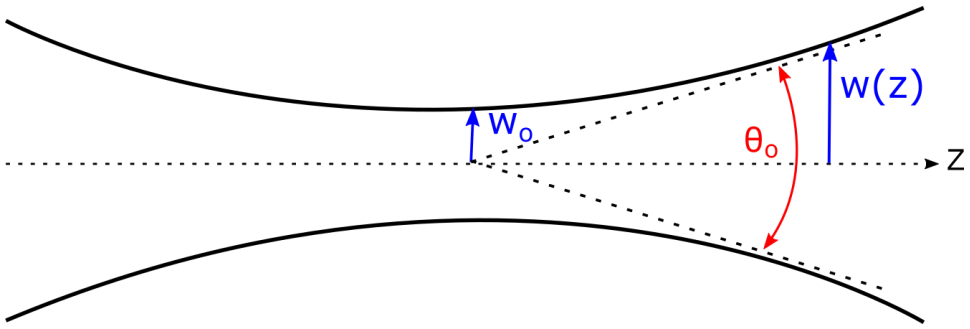

Figure 2.3: Geometric description of a Gaussian beam that is propagating in the z-direction, with a full dispersion angle θ_o.

The complex amplitude term A(z) in equation [16] can be expressed as:

$$\frac{A(z)}{A(0)} = \frac{w_0}{w}\exp[j\phi_0] \qquad [22]$$

where ϕ_0 is the Gaussian phase shift given by:

$$\phi_0 = \tan^{-1}\left(\frac{\lambda z}{\pi {w_0}^2}\right). \qquad [23]$$

Assuming that the amplitude of the beam at the beam waist is unity then equations [17] and [22] can be inserted into equation [16] to provide the complete expression for the fundamental Gaussian beam mode:

$$u(r,z) = \frac{w_0}{w}\exp\left[\frac{-r^2}{w^2} - \frac{j\pi r^2}{\lambda R} + j\phi_0\right]. \qquad [24]$$

Using the relation in equation [14], the complete electric field expression for a fundamental gaussian beam can be expressed as

$$E(r,z) = \frac{w_0}{w}exp\left[\frac{-r^2}{w^2} - jkz - \frac{j\pi r^2}{\lambda R} + j\phi_0\right]. \qquad [25]$$

These equations model the evolution of a paraxial Gaussian beam through free space. The ABCD matric method, described next, is used to model its interaction with optical components.

2.1.3 ABCD matrix

ABCD matrices are traditionally used in describing the propagation of rays through an optical system (Figure 2.4). Given a beam with an offset position Y and an incident angle ϕ, the equivalent output parameters can be obtained with equation [26].

$$\begin{bmatrix} Y_{out} \\ \phi_{out} \end{bmatrix} = \begin{bmatrix} A & B \\ C & D \end{bmatrix}\begin{bmatrix} Y_{in} \\ \phi_{in} \end{bmatrix}. \qquad [26]$$

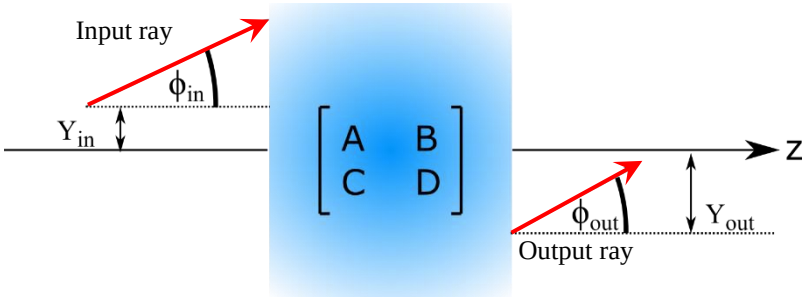

Figure 2.4: Arbitrary optical system described with some ABCD matrix that can be used to model the output of an input ray.

Different optical elements and free space have their own unique ABCD matrix (see Table 2.1). Piecewise matrix multiplication can be utilised to determine a single ABCD matrix for a multi-element system, where the matrices must be multiplied in reverse order. For example if there is a system with three separate regions each with its own matrix, and the optical beam interacts with region 1 first, then the combined matrix is obtained with the piecewise multiplication $M = M_3 \cdot M_2 \cdot M_1$.

Table 2.1: Example of ABCD matrices for a sample of optical elements

Region	**Matrix of the form** $\begin{bmatrix} A & B \\ C & D \end{bmatrix}$
Free space	$\begin{bmatrix} 1 & L \\ 0 & 1 \end{bmatrix}$ where L is the length of the medium
Thin lens	$\begin{bmatrix} 1 & 0 \\ -\frac{1}{f} & 1 \end{bmatrix}$ where f is the focal length of the lens
Curved mirror	$\begin{bmatrix} 1 & 0 \\ -\frac{2}{R} & 1 \end{bmatrix}$ where R is the radius of curvature of the mirror

Equation [27], detailed by Goldsmith (1998), shows how the ABCD matrix elements for an optical system can be used along with the complex beam parameter to model a system

$$q_{out} = \frac{A \cdot q_{in} + B}{C \cdot q_{in} + D} \qquad [27]$$

where q_{in} is the complex beam parameter of the input beam, q_{out} is the complex beam parameter of the output beam and equation [17] can be used to calculate the beam width from them as given in the following example for QUBIC.

To use this method for the QUBIC combiner, it must be reduced to an idealised on-axis system. In its most basic form the QUBIC combiner consists of the source (one of the horns in the array), a primary mirror, a

secondary mirror and a focal plane. This can be idealised as a simple dual thin lens combiner system as in Figure 2.5. In this setup there are two types of optical regions to be modelled with the ABCD matrices from Table 2.1, free space and lenses.

The beam from one of the downward facing horns (FWHM of 12.9° at 150 GHz) can be approximated as a Gaussian beam of waist $w_0 = 3.329$ mm, $R = \infty$ at the waist position. The beam parameter is calculated from these using equation [17]. The ABCD matrix for the first step (free space 1) is constructed using Table 2.1 and equation [27] and can then be used find the complex beam parameter after this step (i.e. at the primary lens).

The new R and w can be obtained using q_{out} and equations [28] and [29].

$$R_{out} = \left(\mathrm{Re}\left[\frac{1}{q_{out}}\right]\right)^{-1} \quad [28]$$

$$w_{out} = \left(\frac{\lambda}{\pi \times \mathrm{Im}\left[-\frac{1}{q_{out}}\right]}\right)^{0.5} \quad [29]$$

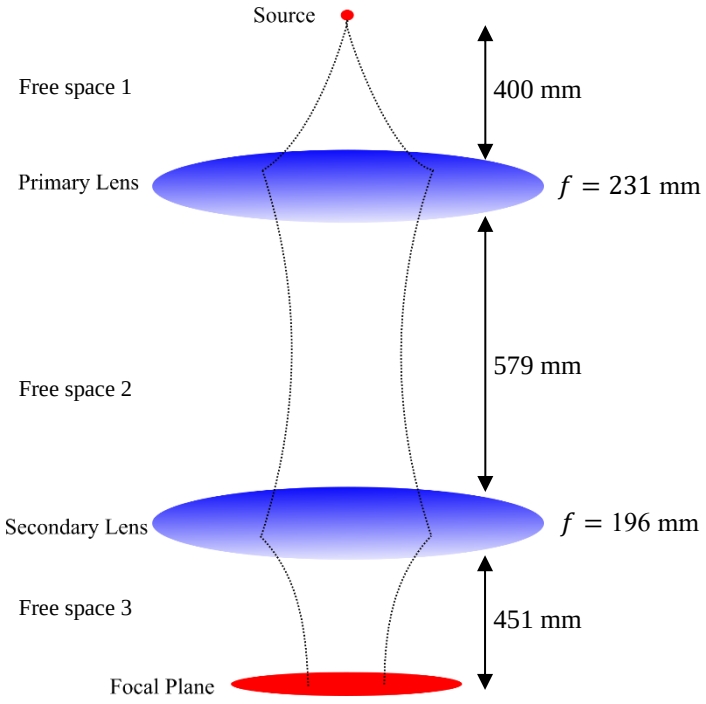

Figure 2.5: Simple schematic of the propagation of a Gaussian beam through the idealised QUBIC model.

This beam parameter is then used as input to the next step with the ABCD matrix of the primary lens. Table 2.2 gives w and R for the beam calculated at each optical component.

Table 2.2: Approximate values for the ideal lens model of the QUBIC instrument in Figure 2.5, values for the distances and focal lengths obtained from (Scully, 2015). w_{out} and R_{out} are calculated using equations [28] and [29] respectively.

Optical region	Parameter	w_{out} (mm)	R_{out} (mm)
Source	FWHM = 12.9°	3.329	∞
Free space 1	Distance = 400 mm	76.56	400.76
Primary lens	Focal length = 231 mm	76.56	-545.34
Free Space2	Distance = 579 mm	6.75	64.69
Secondary lens	Focal length = 196 mm	6.75	96.57
Free space 3	Distance = 451 mm	57.22	489.59

This simple model proved extremely useful in the early stages of the project. For example it can be used to approximate the power that is captured by the focal plane of the instrument. Equation [30] shows the power falling on some circular surface, of radius r from an incident Gaussian beam of radius w.

$$P = 1 - \exp\left(-2\left(\frac{r^2}{w^2}\right)\right) \qquad [30]$$

where P is the proportion of total power captured. If $r = w$, then 86% of the power will be captured. Since Gaussian beams are infinitely wide, it is convention to assume that if $r = 2w$ (>99% of the total power) then effectively the entire beam is captured. The QUBIC focal plane can be approximated by a 60 mm radius disc, meaning that it captures more than 86 % of the total power incident on it. This is just a rough estimate for an on-axis system of course, in reality QUBIC has an off-axis design, but it is a good starting point with a much more robust analysis for refinements possible with the PO analysis software in MODAL, described next.

2.2 MODAL

This section describes the MODAL software, explaining the different parameters that have been used in the modelling of QUBIC. To illustrate how the software is used, a multi-slit interferometer model will be detailed. This model approximates the QUBIC interferometer, and provides some preliminary results for later comparison to more detailed models.

MODAL is a very robust software which allows for the modelling of complex optical systems such as the QUBIC instrument. It provides a basic CAD model for a visual description of the optical system that is being modelled (Figure 2.6) and can also be used for a simple GBM analysis of the system. The size of the beam in Figure 2.6 follows the formulation shown Section 2.1.2. MODAL also provides a scaling factor for these Gaussian beams, where the diameter of the beam can be quickly altered so that the power displayed changes according to equation [30]. This is useful as it provides a rough estimate for the path and size of the beam as it passes through the system, and will quickly determine if optical elements can capture enough power.

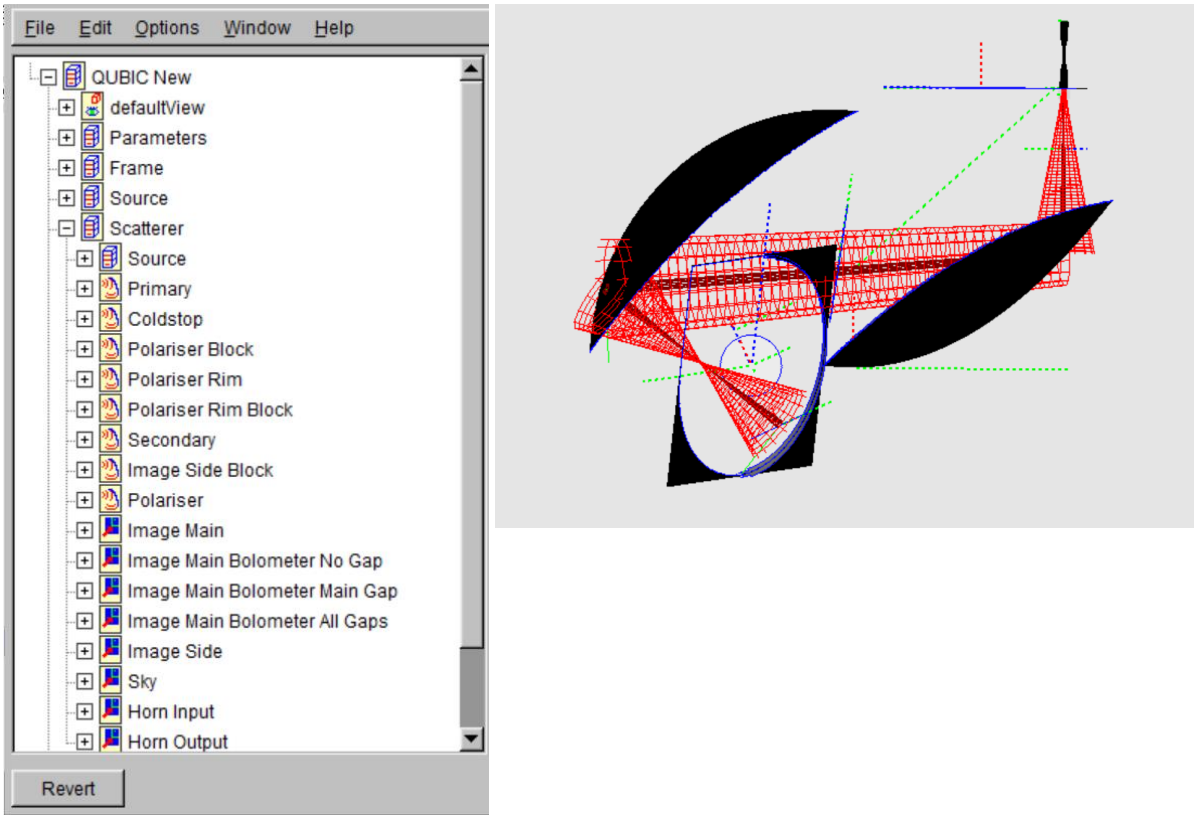

Figure 2.6: MODAL UI showing a list of some of the optical elements (left) and accompanying CAD model of the QUBIC optical combiner (right) in MODAL, the red beams are obtained using GBM analysis and the red mesh shows a width of $r = w$.

2.2.1 Optical elements in MODAL

MODAL has a variety of optical elements that can be implemented into a model (Figure 2.7). When implementing an element in MODAL the shape has to be defined using the parameters in Figure 2.8,

Frame: Sets the position for the reference frame of the object (see Section 3.3.3.1 for more detail on the reference frames for the QUBIC elements)

Centre: Sets the centre of the reference frame, defaults to the origin of the frame

N, *U* and *V*: the Normal (*N*) and two orthogonal (*U* and *V)* axes of the frame. default corresponds to the *z*, *x* and *y* axes respectively

WidthU and *WidthV*: The size of the element in the *U* (*x*) and *V* (*y*) direction.

Default mapping: Defines the mapping of the object. This is explained in greater detail in Section 2.3.1

Bounding volume: Usually used to define the outer rim but it can be used to develop some more complex shapes as detailed when setting up the multi-slit model later in this chapter. Note that when defining the bounding volume it must be within the sizes set by *WidthU* and *WidthV*.

Surface: This setting allows for the surface of the component to be defined by the quadratic equation [31].

$$Ax^2 + By^2 + Cz^2 + Dxy + Eyz + Fxz + Gx + Hy + Iz + J = 0 \qquad [31]$$

This equation is how the collaboration defines the shape of the off-axis mirrors in QUBIC thus this is used in the modelling performed in MODAL. Note that the 'mirror' option shown in Figure 2.7, is a suitable reflector option in MODAL for QUBIC as it allows for the quadratic definition of the surface (Figure 2.9).

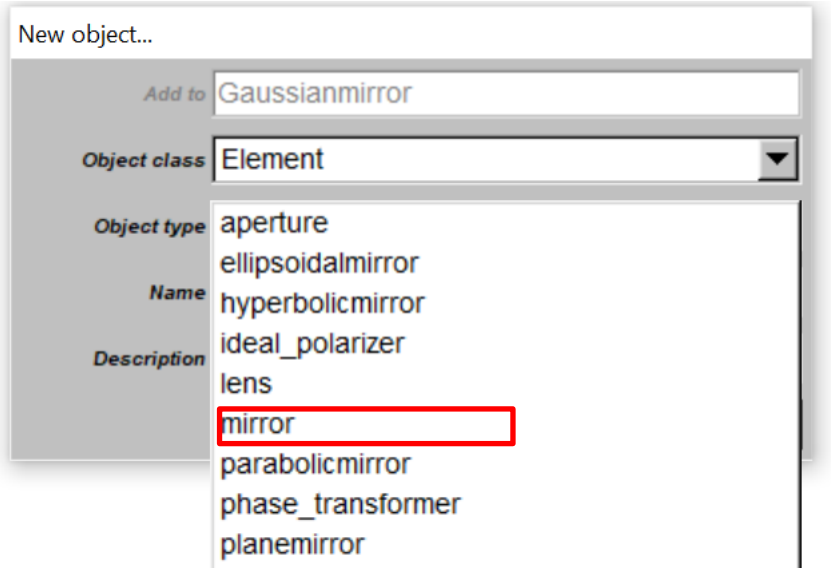

Figure 2.7: Options for the optical elements in the MODAL software. The QUBIC mirrors are defined with the highlighted mirror option.

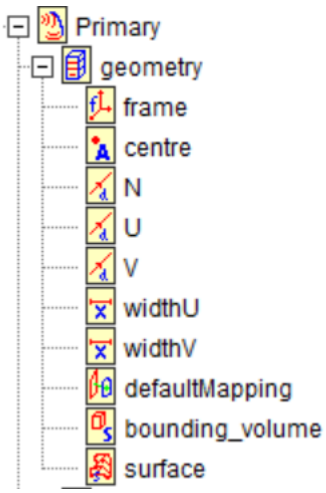

Figure 2.8: Geometry options for element definition within MODAL. Note that this is for the primary mirror in the QUBIC model.

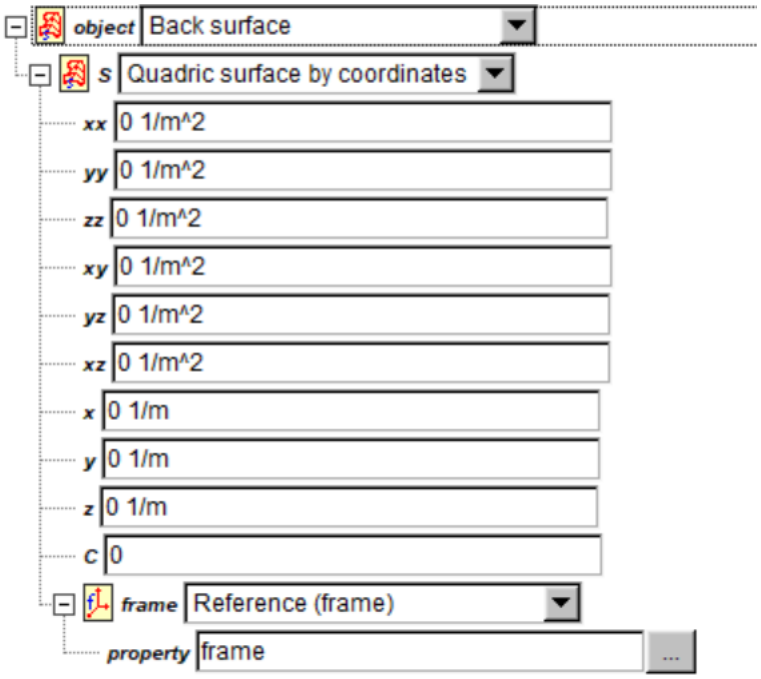

Figure 2.9: Surface description option for describing quadratic shapes in MODAL. Each entry corresponds to the variables A-J in equation [31].

2.2.2 Description of sources in MODAL

Figure 2.10 shows the different source options available in MODAL. Throughout this thesis there will be three different sources used within MODAL: plane waves, illuminated apertures and Gaussian beams. One of the most powerful tools in MODAL is that it allows for the use of horn geometries in the model (network source in Figure 2.10), which is vital in the QUBIC models.

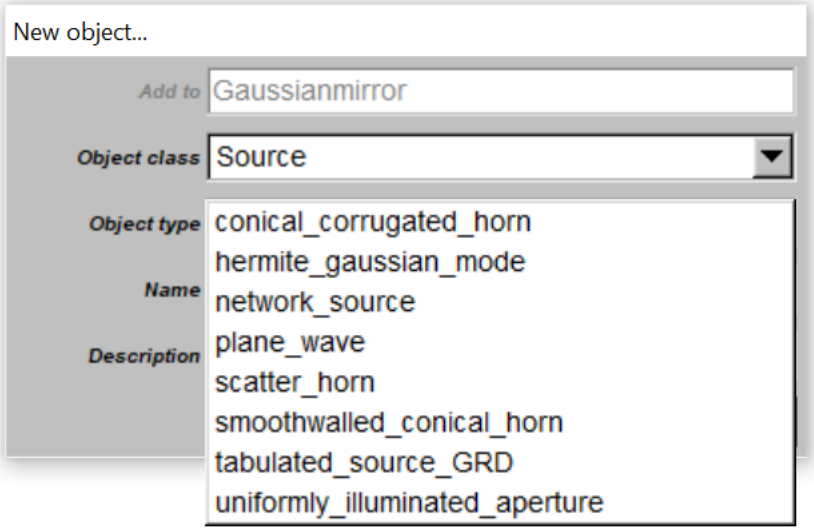

Figure 2.10: Source options within MODAL.

Plane wave

The modelling of the point spread function (PSF) of QUBIC (this will be described in more detail in Chapter 3) is vital to understanding the response of the instrument. To replicate the observation of a point source the optical model in MODAL can use a plane wave from the sky as a source. A plane wave is an infinite plane of constant phase and amplitude (Figure 2.11) which mimics what the radiation from a far-field point source would be over the relatively small opening aperture of the QUBIC instrument. Off-axis observations can be modelled by rotating the plane wave about an axis, which introduces a phase slope onto the radiation incident on the QUBIC aperture while keeping the amplitude constant as seen in Figure 2.12.

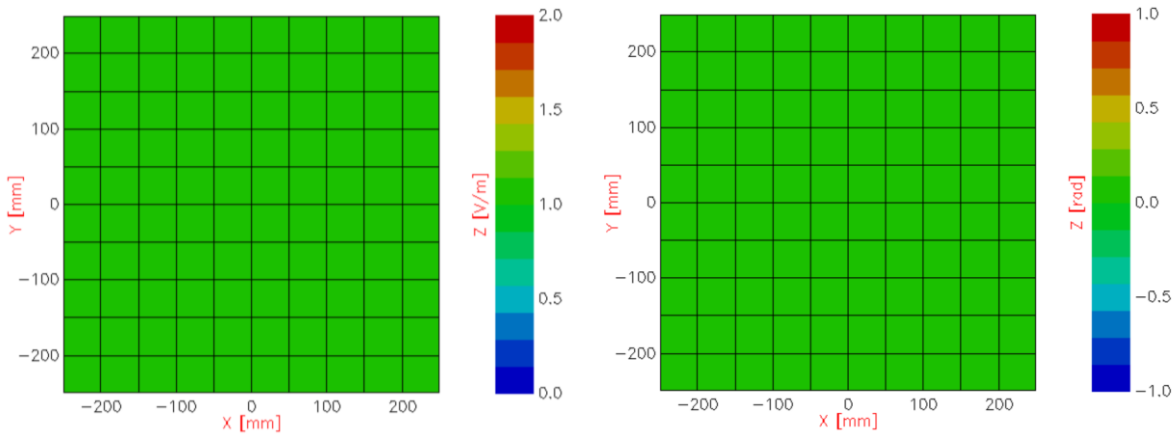

Figure 2.11: Amplitude (left) and phase (right) of plane wave at 150 GHz.

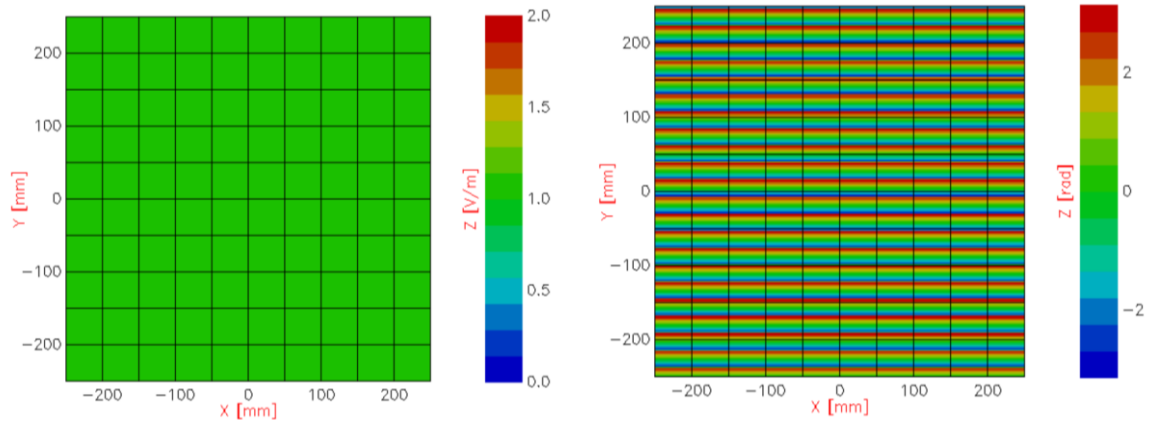

Figure 2.12: Amplitude (left) and phase (right) of a 5° off-axis plane wave at 150 GHz (the phase is wrapped between $\pm\pi$).

Illuminated aperture

As will be discussed in Chapter 4, the QUBIC instrument is also modelled by propagating a point like source from the focal plane onto the sky to simulate the response at that specific position on the focal plane to different source positions on the sky. To accurately model this it would be ideal to have a point-source on the focal plane and propagate its beam back up through the optical combiner. However, a point source is un-physical; a good alternative is to use the illuminated aperture in MODAL. An illuminated aperture can be modelled by creating a very small aperture (one of the optical elements seen in Figure 2.7) in a surface and exciting this with a plane wave source (Figure 2.13). However, in MODAL the 'uniformly-

illuminated-aperture' option does all this automatically as a single element in the model, making it less complex. As the aperture size is reduced the beam approximates the uniform amplitude and spherical phase front of a point source (Figure 2.14).

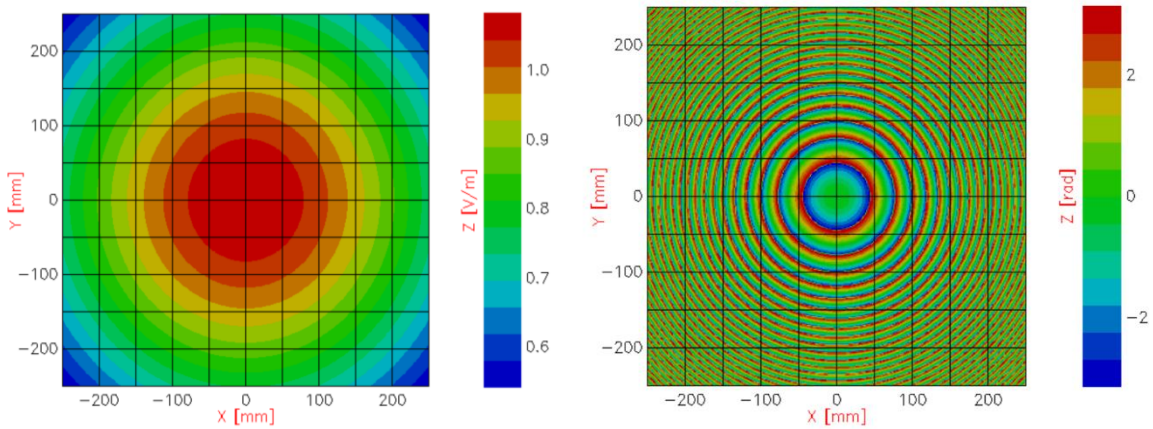

Figure 2.13: amplitude (left) and phase (right) produced by an illuminated aperture of radius 2 mm at 150 GHz source propagated onto a screen 1 m away. The phase is wrapped between ± π.

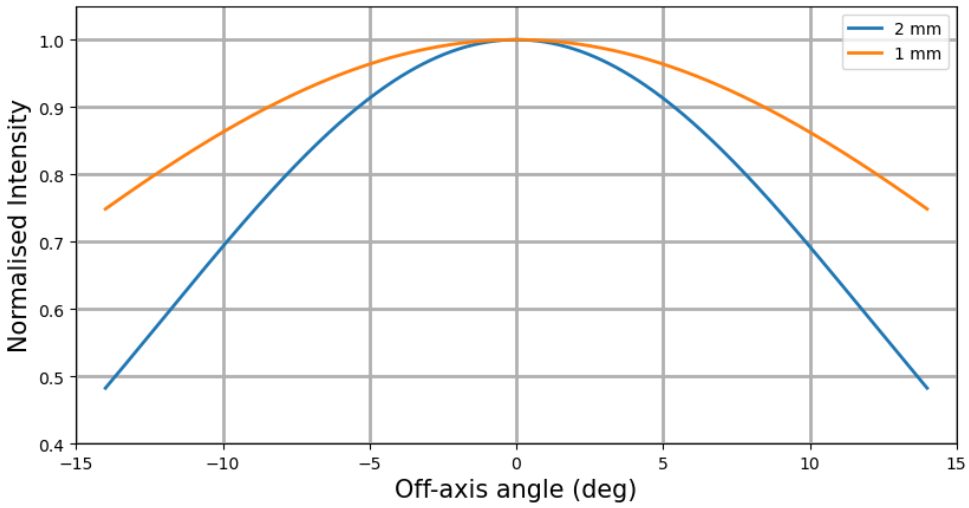

Figure 2.14: Normalised intensity profile of the beam produced by 150 GHz illuminated aperture of radius 1 mm and 2 mm.

Gaussian like source

A simple Gaussian-like source can be simulated in MODAL ('hermite_gaussain_mode' in Figure 2.10). The frequency and beam waist radius of the source can be set by the user which dictates the size of the beam from the source. One parameter to be aware of here is the physical size of the source, which must be set (i.e. the source is a truncated beam). If it is not big enough the beam will become truncated at too high a level and will develop sidelobes as it propagates to the far-field. A reasonable option is to set it to twice the size of the beam waist (using that $r = 2w$ will capture >99% of the power from equation [30]). The QUBIC horns can be approximated by a 12.9° Gaussian beam (corresponding to a waist of 3.329 mm at 150 GHz) as in Figure 2.15. In this thesis I will also describe calibrator sources that can be modelled as ideal Gaussian beams for which this type of source will also be used (see Chapter 4).

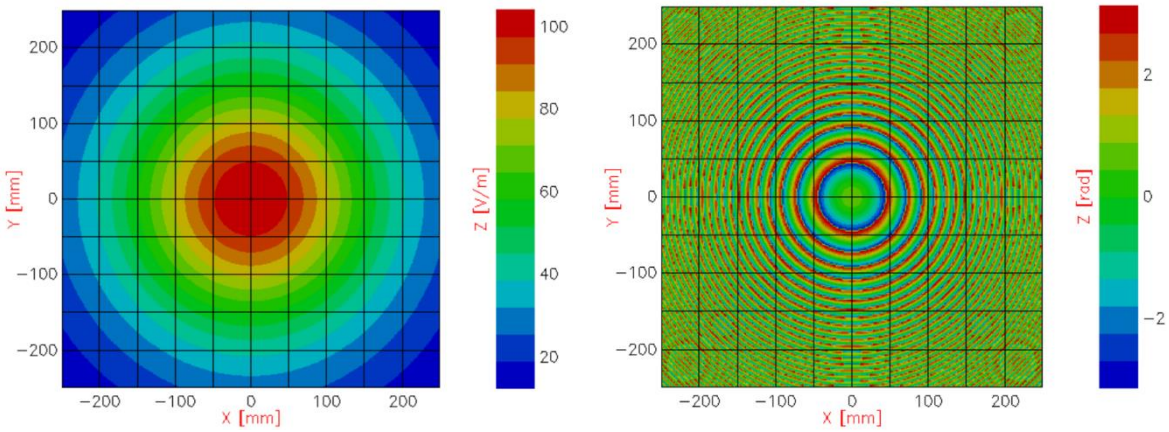

Figure 2.15: Amplitude (left) and phase (right) of a 12.9° Gaussian beam on a screen 1 m away.

2.2.3 Horn geometries

Horn antennas are used to control and direct radiation at millimetre wavelengths. One benefit of MODAL is that it allows for a horn's geometry to be implemented into an electromagnetic model (Figure 2.16) which uses mode matching techniques (which will be discussed in detail in Chapter 5) to model the output from the horn. These horns are not in themselves sources, and they need to be excited with some form of electromagnetic source. The most common way to test the horn geometry is to use a plane wave excitation as it mimics an ideal far-field observation. The QUBIC horn is a scaled version of the CLOVER horns, which were originally designed to operate at 90 GHz, when scaled they operate optimally at 150 GHz and satisfied all the criteria for QUBIC. As detailed by Scully (2015) the profile of the QUBIC horns was further modified to its current design (which will be discussed more in Chapter 3 and Chapter 5) so that they could also be used optimally at the higher operating band. The operation of the horns at these frequencies will be discussed in Chapter 5. Each side of the QUBIC horn consists of 176 corrugation nearly all of which have a thickness of 0.3 mm but the flanges at the throat (nominal radius of 0.953 mm) and aperture (nominal radius of 6.167 mm) of the horn have a thickness of 0.9 and 3 mm respectively which gives and overall length of 56.1 mm. Figure 2.17 shows the beam from a QUBIC horn, showing that the beam from the horn is not an exact 12.9° Gaussian beam as has been mentioned, this was merely an approximation (a reasonably accurate one as seen in the figure with very good agreement to about -15 dB). The real beam from the horn contains side-lobes at high off-axis angles (note that due to the size of the focal plane these side lobes will not be seen by the instrument). This use of an accurate description of the horn beam makes MODAL a powerful modelling tool. It can also be seen from Figure 2.17 that the level of the cross-polarisation pattern is much lower than that of the co-polar, this is a characteristic of corrugated horns and why they were chosen for QUBIC (the co and cross-polarisation characteristics of the horn will be discussed in more detail in Chapter 5).

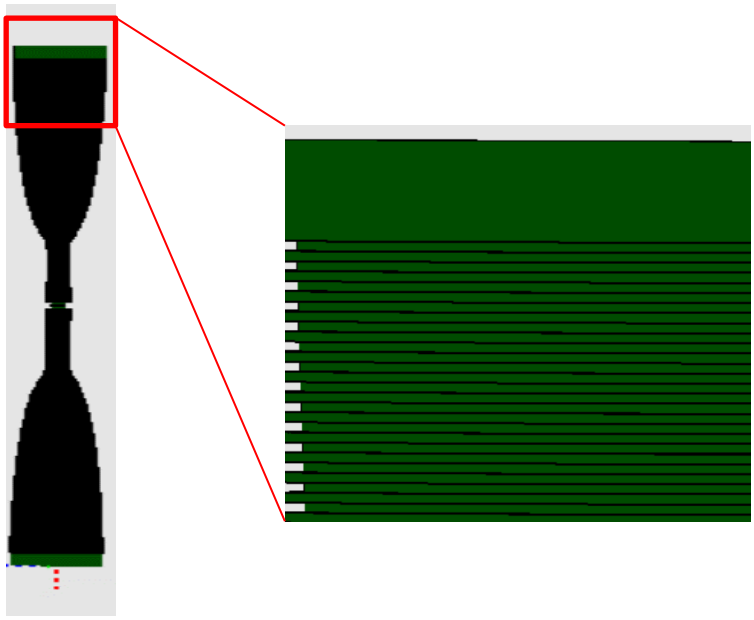

Figure 2.16: Horn geometry of the back-to-back QUBIC feedhorn in MODAL. The image on the right is zoomed in to show the corrugations that are modelled accurately in MODAL.

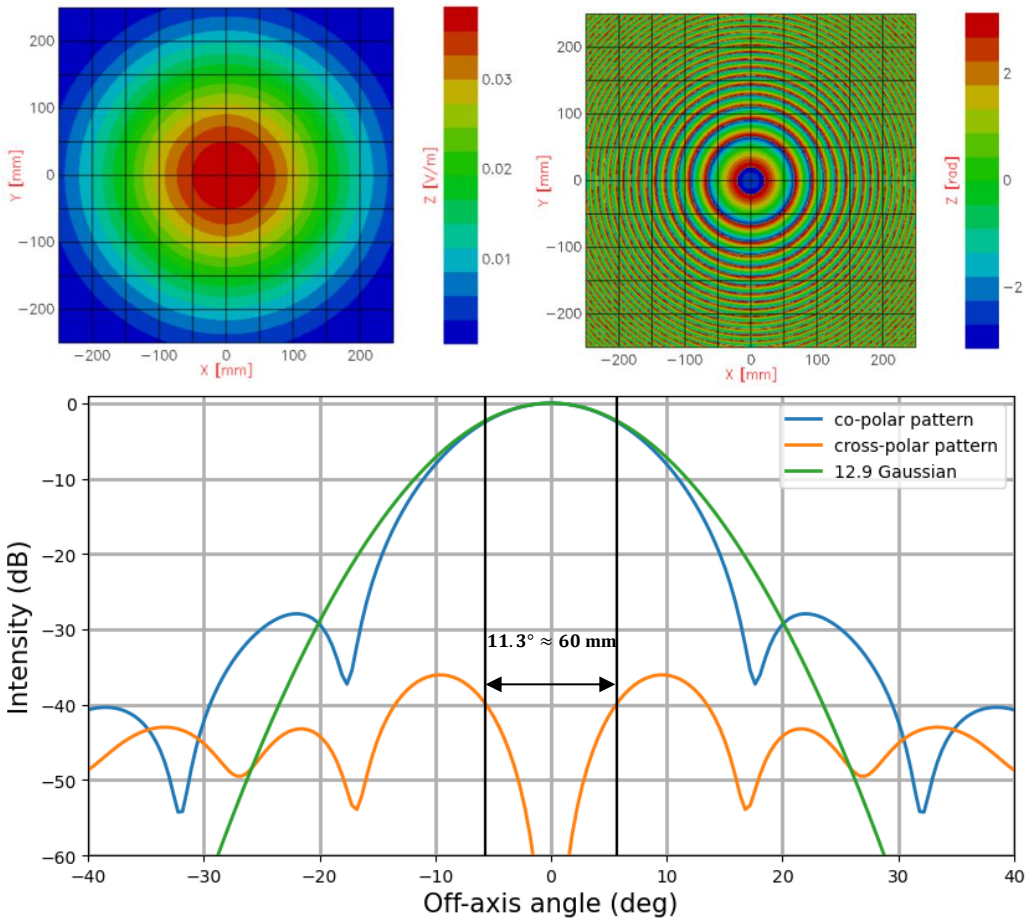

Figure 2.17: È-plane co-polar Amplitude (top left) and phase (top right) of beam produced by the horn when excited by a 150 GHz plane wave and propagated onto a screen 1 m away. The bottom shows the profile of the horn beam compared with the profile of a 12.9° Gaussian beam with the black lines indicating the apporximate size of the QUBIC focal plane. Note that the co and cross polar patterns are normalised to the peak of the co-polar pattern.

2.2.4 Reference frames in MODAL

In MODAL, every element and source in a model has its own reference frame (RF) with the axes as in Figure 2.18. The direction of propagation of the radiation in MODAL is along the *z*-axis. The origin of these reference frames can be positioned anywhere in the model with the options available in Figure 2.19.

Global: This places the object at an arbitrary position in space. It is usually used to define a starting RF often called a Global Reference Frame (GRF), relative to which all other frames in the model are positioned.

Transformed: Allows the RF of an element to be defined relative to a previously defined RF in the model. This is the command that allows for the use of the GRF. Figure 2.20 shows the available options for the transformation of reference frames. The QUBIC model utilises the GRF method of frame positioning. The original frame for all elements is the Global frame and to position the other elements, the Euler $ZY'Z''$ method of frame definition is used (see Section 3.3.3.1 for a full breakdown of the positioning of the QUBIC elements).

Origin and two vectors: allows the user to define the position of the origin and then the orientation of the *x* and *y* axes are defined with vectors.

reference (frame): allows the user to use the same reference frame for an object that has already been defined within the system. Note that this will use the exact same reference frame and does not allow for relative positioning between frames like the *transformed* command.

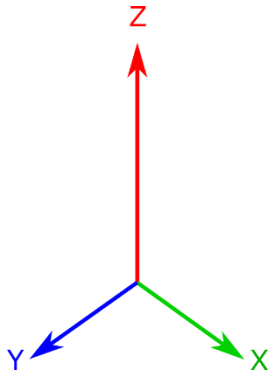

Figure 2.18: Reference frame of an object in MODAL. Green represents the *x*-axis, blue represents the *y*-axis and red represents the *z*-axis.

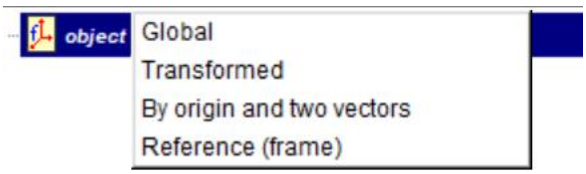

Figure 2.19: Reference frame options within MODAL.

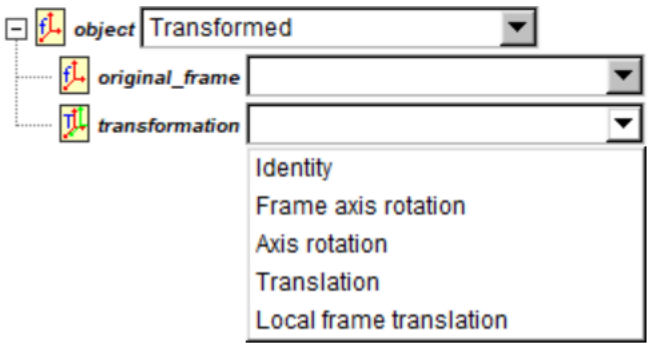

Figure 2.20: Options for a transformation of a reference frame in MODAL. 'Frame axis rotation' allows for rotations about the local axes and 'Axis rotation' allows for rotations about a different set of axes (this is the same for translation and Local frame translation).

2.2.5 Propagators

Defining and positioning the frames sources and optical elements in MODAL merely places them into the model and allows for them to be visualised in the CAD description. To analyse the setup, every object in the model requires a 'propagator'. This in itself can be thought of as a command that tells the model to perform the PO analysis. There are scalar and vector propagators within MODAL. Only vector propagators have been used in the modelling shown in this thesis. There are source and element propagators in MODAL, each have different options (as seen in Figure 2.21) with the element propagator clearly being more complex.

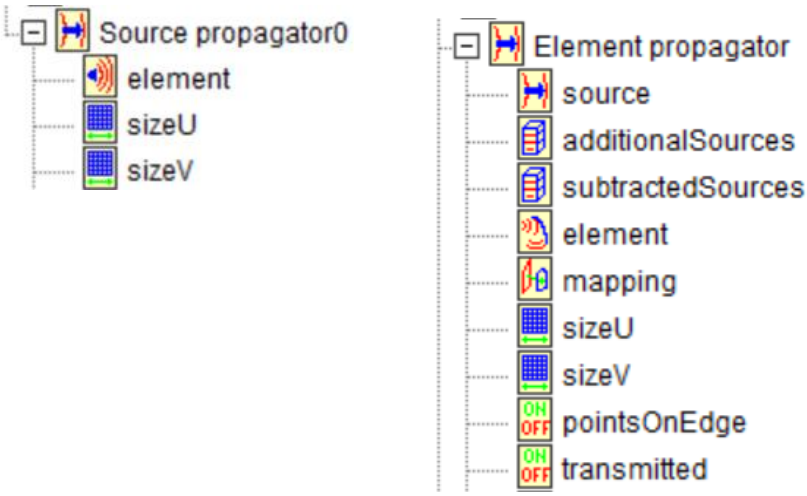

Figure 2.21: Source propagator options (left) and element propagator options (right) used in this research.

Element (source and element): Links the propagator to a particular object in the optical model.

SizeU/V (source and element): This determines the number of PO points in the *U* and *V* directions. Note that the number of points will be evenly spaced along the *WidthU* and *WidthV* of the element defined in the previous section. The number of PO points is very important when modelling, this will be explained with examples for the multi-slit model in Section 2.3.2.

Source (element only): This defines the source that is incident onto the element; this can be a source or an element propagator. For example, in the QUBIC model the primary mirror could be illuminated with a Gaussian beam (a source propagator), hence this is its source. However, the secondary mirror is illuminated by radiation reflected from the primary mirror, thus the primary mirror (with an element propagator) is its source.

Additional and Subtracted source (element only): Allows for the addition of other sources in a multi-source system, or for the subtraction of a source (useful if there was some blockage to be modelled in the system).

Mapping (element only): Determines the area over which the element is sampled. This is detailed with examples in the next section.

Points on edge (element only): This settings was still in development at the time of writing and was not utilised in this thesis.

Transmitted (element only): If there is an aperture in a reflector this setting determines whether to utilise the transmitted or the reflected radiation.

2.3 Modelling Optical systems in MODAL

To illustrate the use of the modelling software MODAL and some of its intricacies, this section will detail the modelling of a simple system with MODAL: generating the elements, running the simulation and outputting the data. It was decided that a multi-slit experiment would be a good system to model, due to its simplicity and the fact that it can also act as a basic approximation the QUBIC interferometer. In the first instance, a double slit model will be analysed (approximating a single baseline of QUBIC), which will produce an interference pattern on a screen with

$$d \sin\theta = m\lambda \qquad [32]$$

where d is the distance between the slits, m is the fringe order, λ is the wavelength of the radiation and θ is the off-axis angle of the fringe.

QUBIC uses an array of feedhorns with a 14 mm separation to generate an interference pattern. Using this distance between the slits will produce a very simple approximation of the interference pattern produced by a single baseline in the QUBIC instrument (the QUBIC baselines will be discussed further in Chapter 3). Including more slits with the same distance between them will generate an even closer approximation to the QUBIC interferometer.

2.3.1 Setting up the propagation chain

When modelling a system the first thing that needs to be decided upon is the propagation chain, that is what elements are required, the order in which the radiation interacts with them, and the position of their reference frames in the system. For the double slit experiment this was relatively simple and only required the optical elements in MODAL aligned as in Figure 2.22. In MODAL the z-axis defaults as the propagation direction and for simplicity, every element was centred along this axis meaning there were no offsets to account for. Hence the only parameter that needed to be defined when positioning the objects was the distance between them.

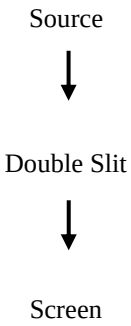

Figure 2.22: Propagating chain for the double-slit experiment.

Source

The source chosen was an on-axis plane wave at 150 GHz (this is the design frequency of the QUBIC feedhorns, is close to the peak of the CMB spectrum and in an atmosphere window). The reference frame for this was set as the global frame and the other elements were positioned relative to it.

Diffraction Grating

The most important part of this model was the definition of the diffraction grating; this was the most complex element in the system as it is what produces the interference pattern on the screen. To show the difference between a transmitting and reflecting propagator, a plane mirror was chosen as the element from which our diffraction grating will be made.

As mentioned previously the bounding volume option gives a lot of control to the user. Figure 2.23 shows a list of shapes and Constructive Solid Geometry (CSG) commands available. The shapes would be used to simply define a boundary rim (for example, if an infinite cylinder was selected, this would cut out a disc from the plane mirror, or in the case of the QUBIC mirror a section of an ellipse as shown in Section 3.3.3.5). Each option has its own reference frame so offset sections can be defined. CSG allows complex shapes to be defined. The CSG difference command was used to define the slits in the grating. CSG difference allows the user to define and position a shape and then subtract that from the surface, generating the double slit grating seen in Figure 2.24.

In a multi-slit interferometer the width of the slits should be comparable to the wavelength ($\lambda = 2$ mm), hence in this model they were made to be 0.5 mm wide. For this model interference was only desired in the *x*-direction. To achieve this the diffraction grating should be infinite in length (the *y*-direction), an approximation for this is to have it much larger than the wavelength of the incident radiation. Thus, the diffraction grating was set to a height of 3000 mm. The full width of the grating was set to 30 mm.

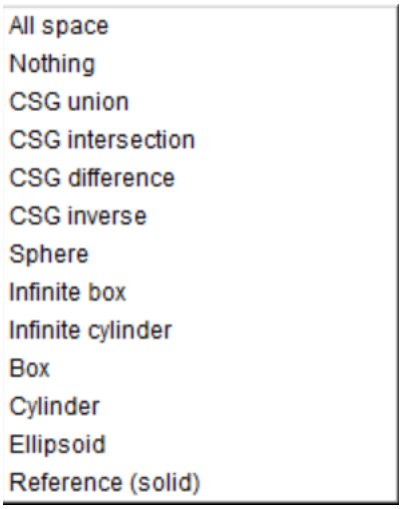

Figure 2.23: options for the bounding volume of the optical elements in MODAL.

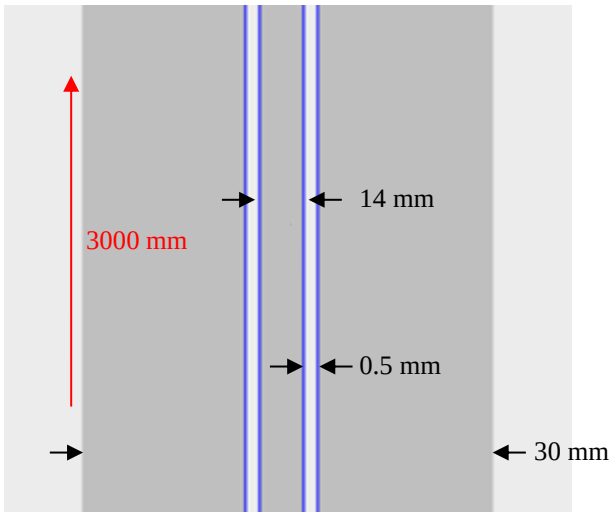

Figure 2.24: Two slits on the plane mirror obtained utilising the CSG difference command in MODAL. Two infinite boxes positioned ±7 mm from the centre along the *x*-axis were used to subtract material from the surface and create the gaps to transmit radiation. Note that the slits are made larger for display purposes.

It is important to set the correct number of PO points. Without enough points it is possible to under sample the element, which would result in incorrect results. Too many points would result in oversampling, which will provide the correct result, but also increases the computation time. Sometimes, this is a trade-off that must be accepted.

In the *x*-direction; the width of the grating is 30 mm with the 0.5 mm wide slits centred on ±7 mm from the centre. There will be an even distribution of PO points from ±15 mm on the diffraction grating, e.g. for 11 PO points there will be one point every 3 mm, thus the slits will not actually be sampled at all, and the diffraction grating will act as a blank screen. It was decided to oversample the grating. The number of PO points was set to 301 × 2001 (because the grating was longer int the *y*-direction the sampling along this direction had to be much larger) for this model (a breakdown of the results from different sampling is included in Section 2.3.2).

Mapping

The mapping defines how an element is sampled, in terms of the direction and the extent. Figure 2.25 shows the default options for the mapping of objects in MODAL, and it can be seen that normally the mapping is centred on the origin of the reference frame of the element and along the *z*-direction. The extent defaults to the physical extent in the *U* and *V* as mentioned previously. When plotting the propagator for the improvised diffraction grating (Figure 2.26) with the default settings, it can be seen that it is centred on the point (0 mm, 0 mm). This is in contrast to when the position of the centre of the mapping is shifted (for illustration purposes only). This option is not vital for the multiple slit experiment, however it can be used when modelling the QUBIC mirrors which have an ideal shape that is an offset section of an ellipse (this will be discussed further in Chapter 3, where the mirrors are described in detail).

Figure 2.25: Default mapping options within MODAL.

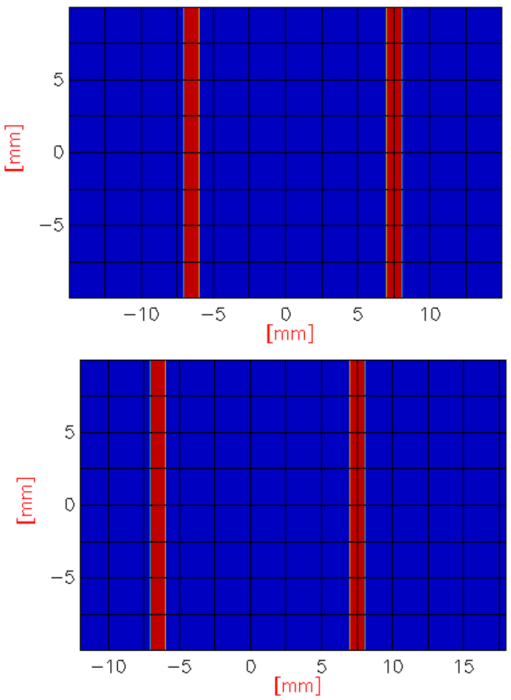

Figure 2.26: Propagator for the diffraction grating with the default mapping (top) and with mapping offset by 3 mm in the *x*-direction (bottom). Red shows transmission and blue shows reflection.

Observation Screen

The final element for this model is the observation screen. Since the interference pattern will only form in the far-field, this needs to be placed sufficiently far away. MODAL has a simple option for an output plane. The shape can be further modified with the CSG commands shown previously, allowing for the generation of any shape (useful when modelling the focal plane of an instrument that has a peculiar shape). For this model a simple 150×150 mm^2 square was positioned 300 mm away (an adequate distance for a double slit separation of 14 mm and the focal length of the QUBIC combiner is 300 mm equivalent) from the diffraction grating, with 301×301 PO points.

When performing a simulation every PO point from the previous propagator is propagated onto every PO point of the next element. For example let us examine the electric field component on the observation screen. This has 63,001 PO points in total, and there are 90,601 PO points on the diffraction grating. The electric field from each point on the diffraction grating will be transmitted onto each point on the observation screen, with the total electric field at each point resulting from the summation of all the contributing constituent points. In complex optical systems with multiple elements along the propagation chain this effort will add up and the simulation time can increase rapidly.

2.3.2 Data output

MODAL has an object called a 'dataset' (Figure 2.27) that must be implemented to store the data from a propagator defined in the optical model (in fact all the images shown so far in this section have utilised this dataset command) meaning that radiation on every object can be modelled, not just on the focal plane. This dataset object is required for files to be exported after a simulation in MODAL. Figure 2.28 shows the options available for columns that can be assigned to the dataset. The model utilises vector propagators and the phase component of the electric field can be obtained (Figure 2.29), which is vital when investigating the interference pattern.

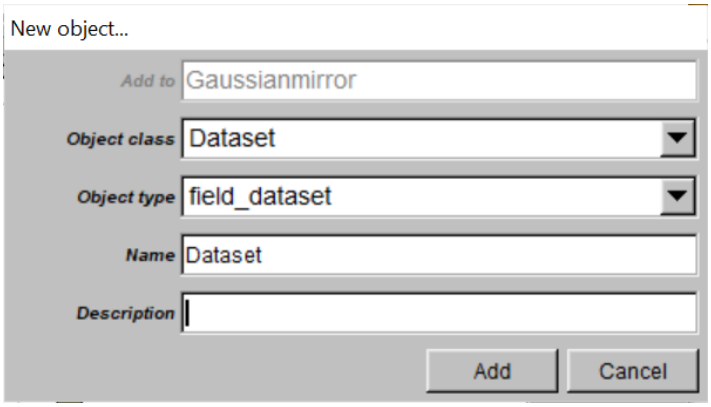

Figure 2.27: Dataset options in MODAL.

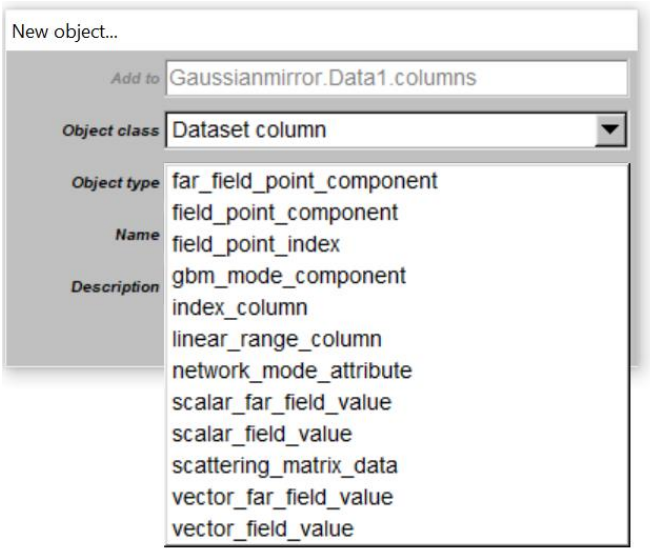

Figure 2.28: Example of variables that can be recorded and stored in a dataset.

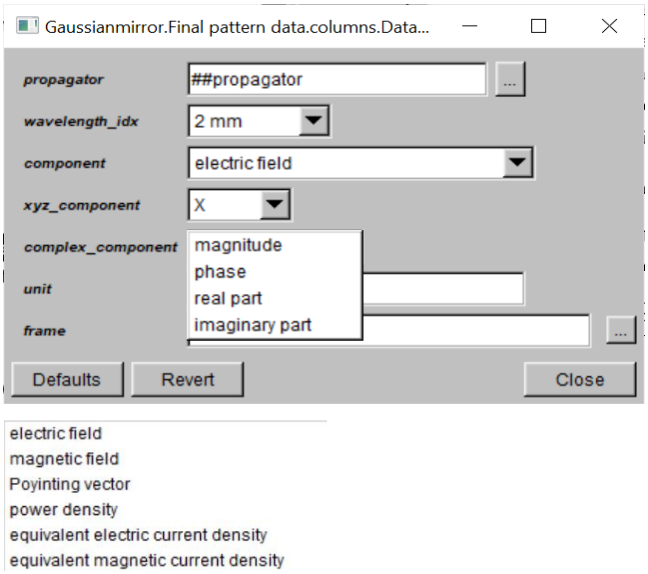

Figure 2.29: Vector field component options in MODAL. Note that different field components can be selected (such as electric or magnetic field – seen at the bottom of the figure) as well as a choice in whether or not to output the field point in polar form as magnitude and phase or in cartesian form with the real and imaginary components.

The dataset is structured where each row contains the requested information for a particular PO point, with each column having a header defined by the user. Table 2.3 shows the components (and the headers) that were obtained for this model. These are the same components that were obtained for the simulations of the QUBIC instrument. The dataset can be exported into a suitable file format, defined by the user and, once exported, the data can then be plotted, as seen in Figure 2.30 in which there is a clear interference pattern. The angular position of the first order peak occurs at $\pm$ 8.2°, which corresponds with the position predicted by equation [32].

Table 2.3: list of columns used in the dataset for the output of the double slit experiment, note the phase and amplitude directions correspond to the X and Y components of the electric field.

U-position (mm)	V-position (mm)	X-amplitude (V/m)	X-phase (rad)	Y-amplitude (v/m)	Y-phase (rad)

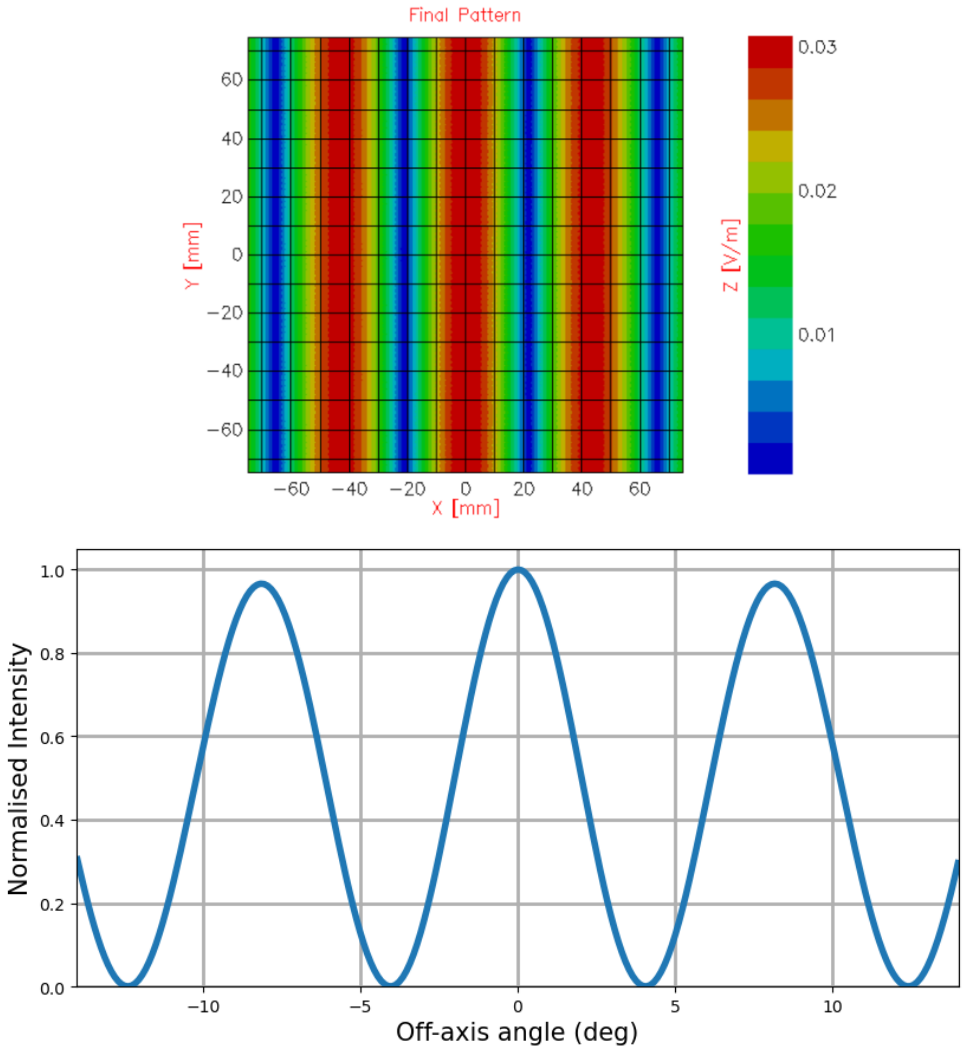

Figure 2.30: 2d plot of the *x*-component magnitude of the electric field on the screen resulting from the excitation of double slits separated by 14 mm by a 150 GHz on-axis plane wave (top) and 1d horizonal cut (at $y = 0$) where the amplitude and position have been converted to intensity and off-axis angle respectively.

Effects of sampling

Figure 2.31 shows the effect on the interference pattern when the PO sampling size of the observation screen is varied. This highlights the importance of accurate sampling size, under-sampling can create unrealistic structure in the pattern. There is no difference in the structure of the pattern between the 301×301 grid and the 1001×1001 patterns, meaning that there is no benefit to excessive over-sampling, in fact there is a major drawback as the computation time increases.

Sampling of an optical element in a system can also have serious effects on the results (it has been mentioned drastic under-sampling could cause the slits to not be sampled and hence the grating acts as a screen blocking the radiation). Figure 2.32 shows varying levels of sampling of the double slit, with some

very unrealistic structure arising when under-sampling the double slits. This is obvious if modelling a well understood system such as the double slit, but with unknown systems ensuring adequate sampling is important, a sampling of roughly 1 PO point per every half-millimetre ($\lambda/4$ at 150 GHZ) on the optical elements in the QUBIC system is sufficient.

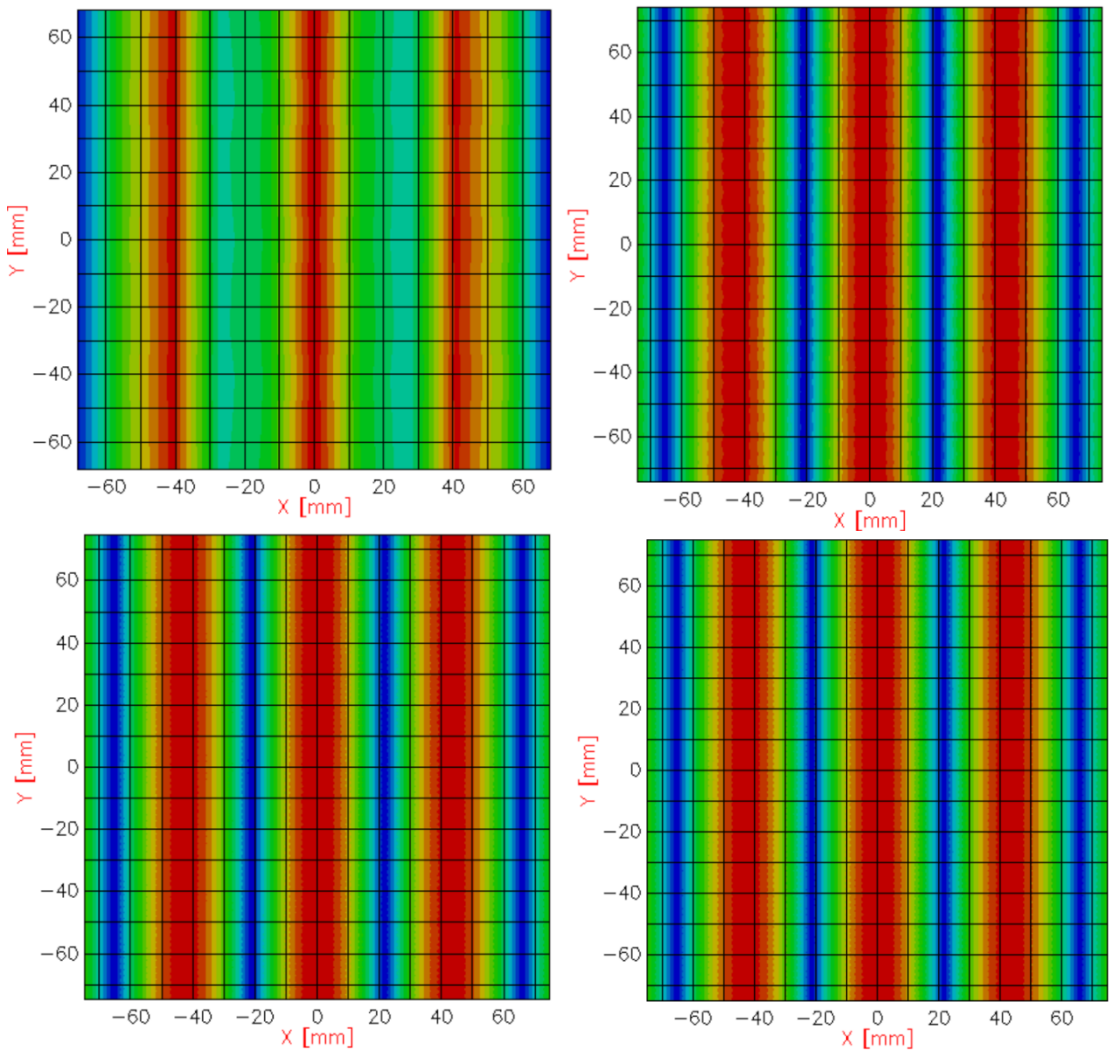

Figure 2.31: two slit interference pattern on an observation grid with a PO sampling grid size 11×11 (top left), 101×101 (top right), 301×301 (bottom left) and 1001×1001 (bottom right).

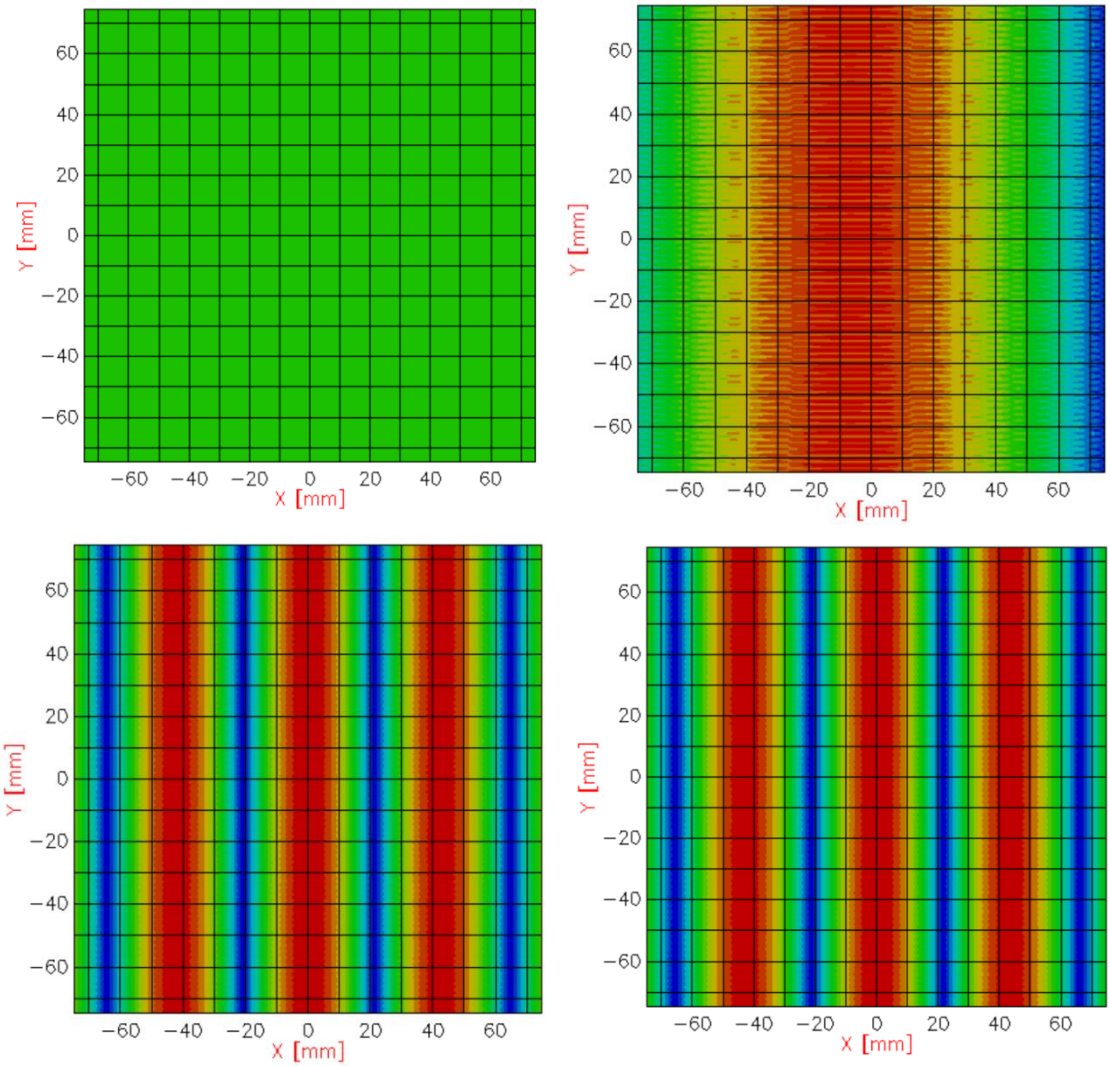

Figure 2.32: Two slit interference pattern (the observation screen sampling grid size is fixed at 301×301) resulting from varying sampling sizes (in the *x*-direction) of the double slit grating: 31 (top left), 41 (top right), 61 (bottom left) and 301(bottom right).

Modelling on the computing cluster

When there is an increase in the complexity of the model, there is usually an increase in the number of PO points, which in turn causes an increase in the computation time of the simulation, sometimes to a level where it becomes unfeasible to simulate the model on a standard PC. In MU there is an in-house computing cluster that was assembled and is currently maintained by Dr. M. Gradziel. This cluster is comprised of 30 computers which provides a possible total of 124 nodes (equivalent to cores on a traditional computer) which allows for drastically increased computation speeds. This allows for the analysis of complex models and also stops the software from crashing when modelling these systems (which can occur if there is insufficient RAM, typical on a single machine- this is very noticeable when modelling the full QUBIC instrument).

To investigate the benefits of the cluster let us look at the pattern observed with 1001×1001 PO points from Figure 2.31. Table 2.4 shows the substantial decrease in the computation time when running on the cluster (roughly 19 times quicker). This cluster was used for all of the modelling performed for the QUBIC

instrument that will be shown throughout this thesis. Due to the complexity of the QUBIC model, without this cluster, the MODAL software could not have been used for this research.

Table 2.4: Time taken to simulate and output the pattern on the observation screen for the double slit model on a single octo-core computer and the cluster.

Computational device	Time taken (seconds)
Single computer (octo-core)	660
Cluster (running 120 cores)	35

2.3.3 Expanding the model

The real QUBIC instrument uses an 8×8 and a 20×20 input feedhorn array at the aperture of the technological demonstrator and full instrument, respectively (this will be discussed in much more detail in Chapter 3) with an inter-horn separation of 14 mm. As a very simple approximation of these, the double-slit model can be modified by increasing the number of slits to 8 and 20, with their separation remaining at 14 mm. The width of the grating needed to be increased requiring an increase in the number of PO points and thus the computation time increased. Figure 2.33 shows that increasing the number of slits to approximate the QUBIC instruments generated the peaks in the same position as previously, however the width of the peaks is narrower, with the FWHM of the peaks shown in Table 2.5 (note that the FWHM is inversely proportional to the number of slits). This narrowing of the peaks is a phenomenon that was expected with the increasing size of the diffraction grating, this will be explored in further detail when the QUBIC model is investigated.

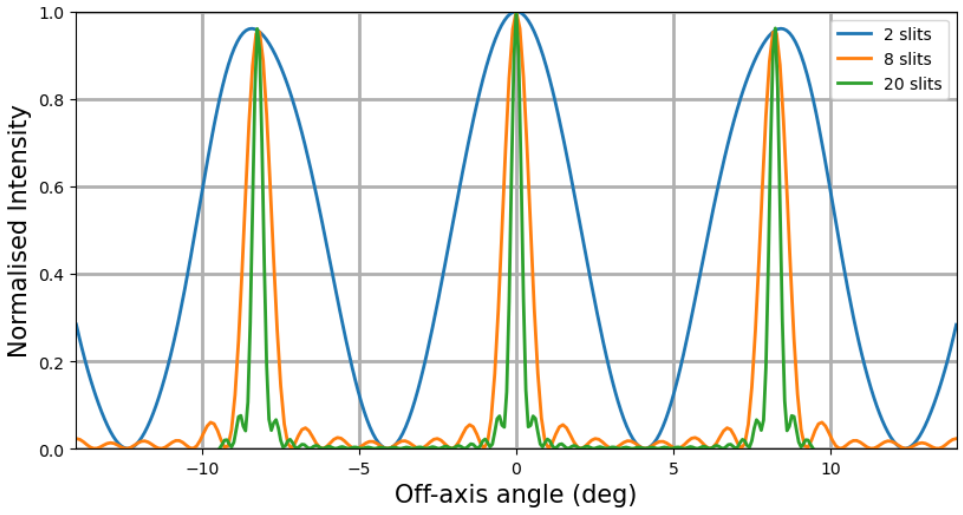

Figure 2.33: Horizontal cut of the intensity pattern for three multi-slit models in MODAL.

Table 2.5: FWHM of the central peak for the multi-slit models simulated in MODAL.

Number of slits	FWHM (degrees)
2	4.06°
8	0.91°
20	0.37°

The full theoretical model of the intensity on a screen resulting from a diffraction grating can be described with

$$I = I_o \frac{\sin^2\left[N\frac{\delta}{2}\right]}{\sin^2\left[\frac{\delta}{2}\right]} \quad [33]$$

where N is the number of slits in the grating and

$$\delta = \frac{2\pi}{\lambda} b \sin(\theta) \quad [34]$$

where λ is the wavelength of the incident radiation and b is the separation between the slits in the grating. Figure 2.33 shows that the MODAL model and this theoretical model (for N =20) agree very well. This model shows that MODAL gives a baseline for what to expect with the QUBIC instrument, and verifies that it can model the complex physics that accompanies the interference of coherent sources, with the results agreeing very closely with the theoretical predictions. This is in addition to the verification against the industry standard GRASP software shown previously, as well as the in depth verification performed by S. Scully (Scully, 2015).

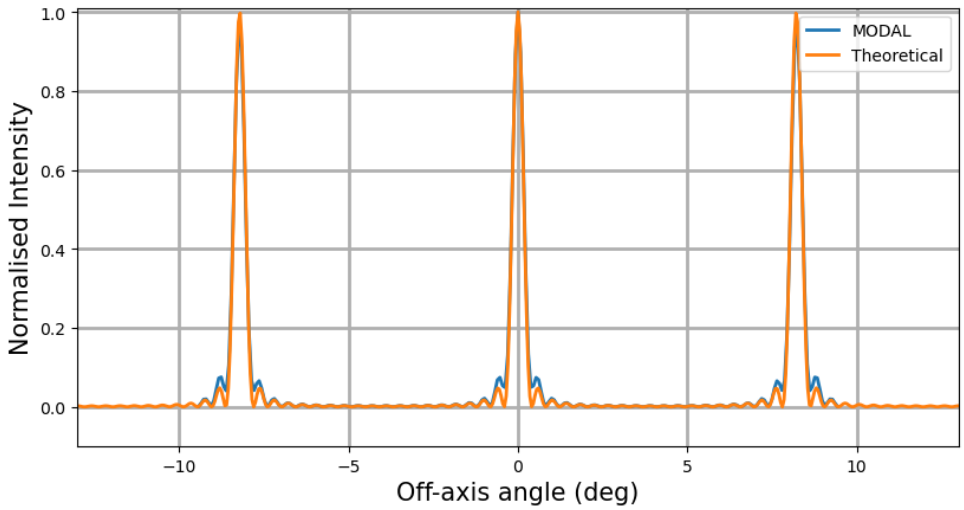

Figure 2.34: Comparison between the theoretical interference pattern resulting from equation [33] and the horizontal cut through the 20 slit interference pattern from MODAL (with a grating sampling of 301 in the *x*-direction and a sampling grid of 301×301 on the observation screen). In these models $\lambda = 2$ mm and $b = 14$ mm.

Since QUBIC will utilise horns that emit Gaussian-like beams, a better approximation of the instrument can be obtained in MODAL by placing pure Gaussian sources at the centre of each slit location and propagating them onto the observation screen. Performing this with eight 12.9° Gaussian sources placed at the centre of each slit location in the 8-slit model from above result in Figure 2.35. The central peak is identical to that of the multi-slit pattern and the off-axis peaks are in the same locations. However the height of these off-axis peaks is attenuated by the beam profile (a 12.9° Gaussian). This attenuation is expected and will be seen throughout the analysis of the QUBIC instrument.

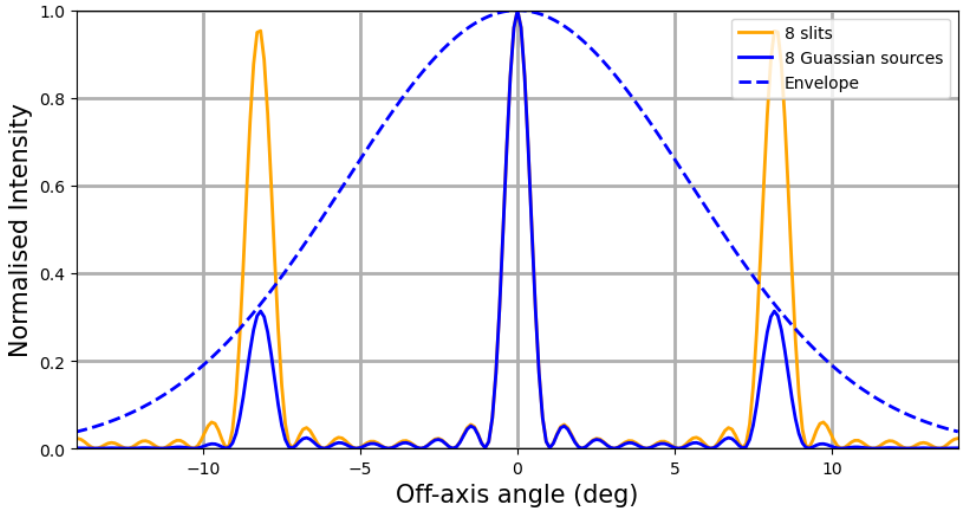

Figure 2.35: Interference pattern resulting from an 8-slit diffraction grating and 8 Gaussian sources placed at the centre of each slit location. The dashed blue line represents the envelope of the Gaussian interference pattern (a 12.9° Gaussian beam).

2.4 Model data output with MODAL

Two QUBIC models were analysed for this thesis. The full instrument with 400 feedhorns and the technical demonstrator with 64 (see Chapter 3 for more information on the two models of QUBIC). In both models, the horn geometry modelling capabilities of MODAL is utilised. This tool is powerful, but each horn requires its own object in MODAL, unlike the single object for the diffraction grating element shown previously. Thus, a MODAL model that has all of the horns included in one simulation would be very cumbersome, at a minimum, the primary mirror propagator would then have 64 sources using the additional source command from Figure 2.21. Making changes to the model would then become very difficult and confusing for the user. However, running MODAL on the cluster allows the user to run it in a batch mode using a '.bash' script. In this mode a series of simulations can be performed where parameters (i.e. horn position) can be changed between the simulations. This was used for the QUBIC model so a data file was obtained for the field on to focal plane from each horn in the input array. The combined intensity (and hence the interference) pattern of all of the horns was then generated mathematically using the real and imaginary components (equation [35]).

$$I = \left(\sum_{i=1}^{N} Re_i\right)^2 + \left(\sum_{i=1}^{N} Im_i\right)^2 \qquad [35]$$

where i is the horn index up to a total of N horns, Re is the real component of the electric field and Im is its imaginary component. Since the output is usually given in terms of magnitude and phase the real component can be obtained with $\text{mag} \times \cos(\text{phase})$ and the imaginary component with $\text{mag} \times \sin(\text{phase})$.

2.5 Fourier transform analysis

The multi-slit experiment is a nice verification of the MODAL software, but Fourier transforms can be used as a very simple and extremely computationally inexpensive model of the idealised QUBIC instrument. Before the full physical optical model is introduced this method will be explored as it can be a useful way

of thinking about the QUBIC instrument. The Fourier transformation of a beam gives its far-field distribution. QUBIC is an imager such the pattern that on the focal plane (for an ideal system) is the Fourier transform of the horn aperture fields.

In 1D the horn aperture can be thought of as an infinite comb function (of 14 mm spacing) multiplied by a top hat function (to define the width of the array) convolved with the Gaussian pattern of a horn beam as seen in Figure 2.36. The Fourier transform of this pattern (see Bracewell (2000) for a description of the properties of Fourier transforms) is therefore a comb function with a spacing that is inversely proportional to the aperture comb spacing (horn separation) convolved with the Fourier transform of a top hat function (a sinc() function with a width that is inversely proportional to the width of the top hat, i.e. the extent of the horn array) and multiplied by the Fourier transform of the horn beam (a 12.9° Gaussian). We can therefore easily appreciate how it is the individual horn beams that determine the focal plane envelope, the extent of the horn array that determines the width of the peaks and the horn separation that determines the separation of the peaks.

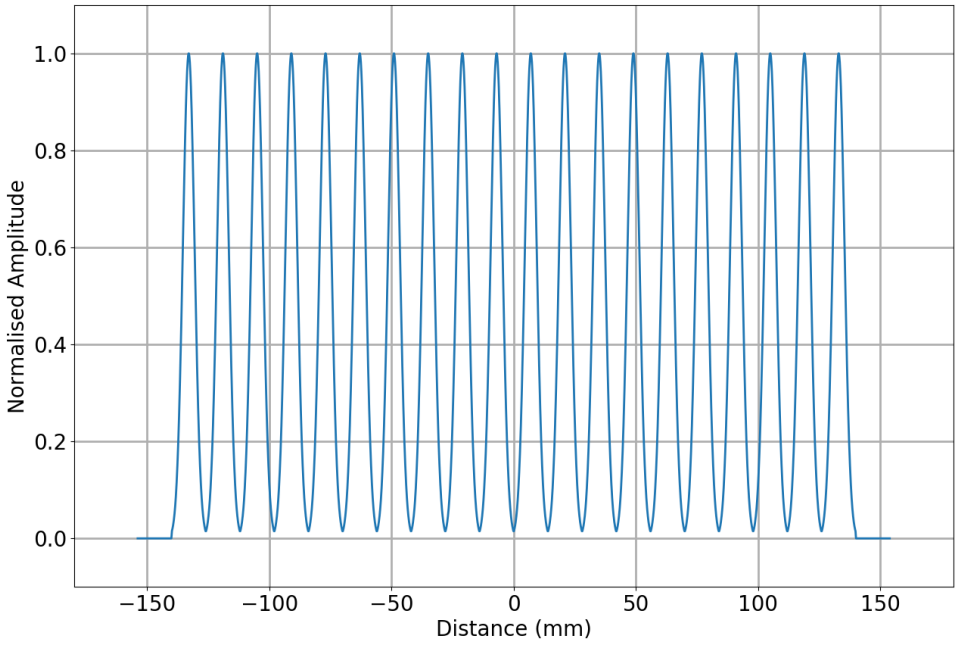

Figure 2.36: Input of Gaussian as a model for the field at the QUBIC horn aperture array.

Performing the Fourier transform on the aperture pattern of Figure 2.36 resulted in the expected pattern as seen in Figure 2.37. Even though this method is very straightforward, it is very robust, the positions of the off-axis peaks are located at the expected position of $\pm 8.2^{o}$, the locations of the peaks from the multi slit model (based on equation [32]). As mentioned QUBIC has a 300 mm focal length and the focal plane can be roughly approximated by a 60 mm radius disc, which gives rise to an angular extent of $\tan^{-1}\left(\frac{60}{300}\right) = 11.3°$, meaning that the focal plane can capture the peaks. It can be seen that the resulting pattern is attenuated as expected by the 12.9^{o} Gaussian beam as expected. This gives a good basis against which to compare the results from the more sophisticated optical modelling.

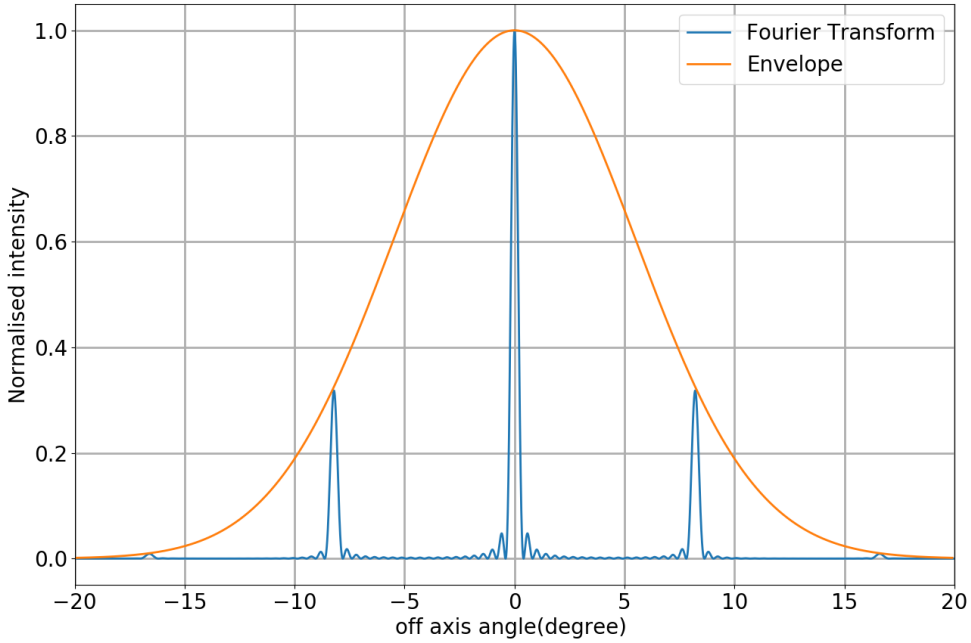

Figure 2.37: Fourier transform of the input array with a 12.9º Gaussian envelope.

The power of this method is that some of the different physical properties of the instrument can be explored easily. Modelling a smaller 8 Gaussian input field (analogous to the technological demonstrator detailed in Chapter 3) provides a beam pattern with wider peaks than the full instrument (Figure 2.38) as seem with the multi slit model, and changing the distance between the horns changes the position of the peaks of the beam as seen in Figure 2.39.

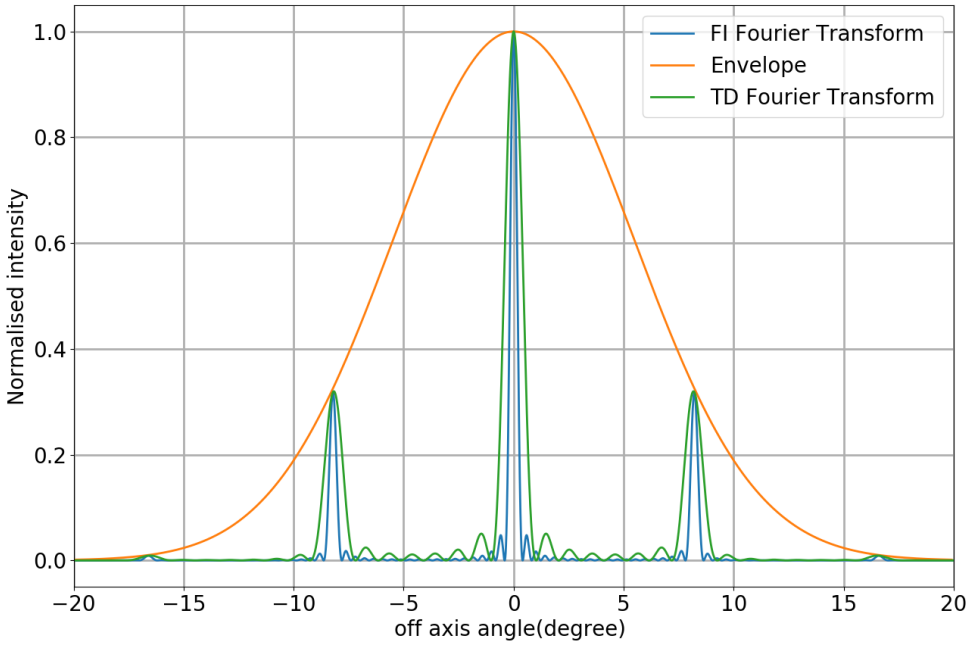

Figure 2.38: Comparison of the Fourier transformations of the TD input array and the FI input array.

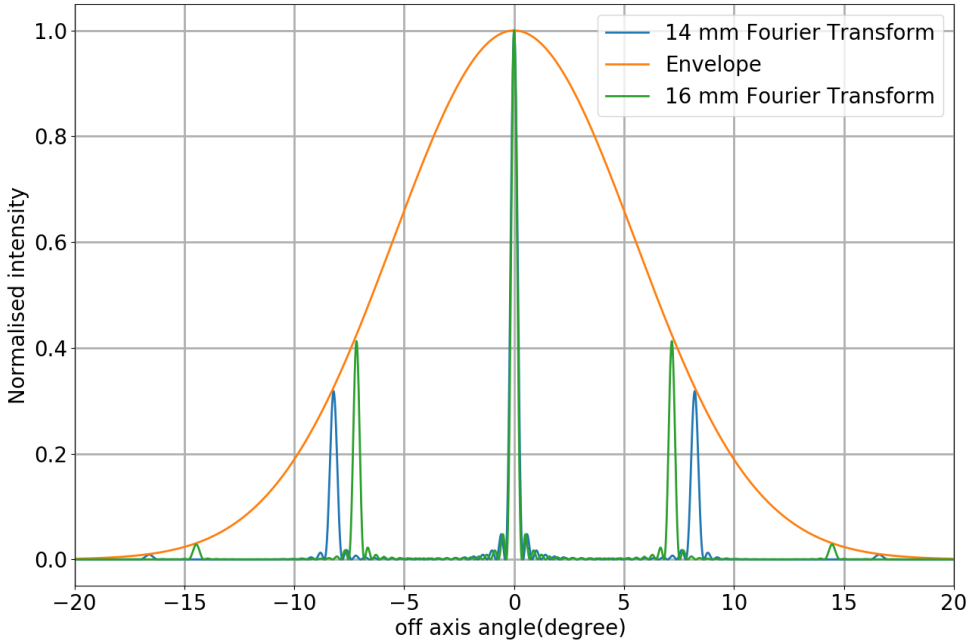

Figure 2.39: Comparison of the Fourier transformation of the input horn array with a 14 mm separation and a 16 mm separation.

2.6 Summary

In this chapter the theoretical concepts of physical optics and Gaussian beam mode analysis were introduced along with ABCD matrix analysis and its application to a simplified model of the QUBIC instrument.

The in-house software MODAL was then introduced. It was shown that this software can utilise both GBM and PO analysis. GBM works well for beams that obey the paraxial approximation, however PO provides a full vector analysis of the optical system, hence this was used as the main method of analysis throughout this thesis. This chapter provided an insight into how to use the MODAL software, detailing how optical components are modelled in systems. Some of the benefits of MODAL were shown, its CSG implementation means that complicated geometries can be modelled very easily. Another benefit is that multiple EM sources can be defined within the MODAL software, allowing the modelling of multiple observations (e.g. near-field and far-field observations). One of the most powerful and unique modelling tools that MODAL provides is that it can read in horn geometries and model the accurate horn beam and coupling between a free-space beam and the horn, which is very useful for QUBIC and instruments that operate at millimetre wavelengths.

Next, the modelling of a simple multi-slit interferometer in MODAL was described and its results were examined and compared with theoretical predictions. It was shown that MODAL gave results that agreed with the theoretical predictions. In this section, even though the power of PO was shown, it is very computationally expensive, and it was also shown that to avoid spurious results, adequate sampling of the elements was required. In complex optical systems this can drastically increase the computational load. Hence, the MODAL software was run on a cluster that is managed in-house in MU.

Finally it was shown that a very simple but effective model of QUBIC can be implemented with Fourier transforms, that allows for rapid investigation into the effects of some of properties of the optical combiner on the focal plane pattern (such as the horn array size and inter-horn separation).

The next chapter will focus on the QUBIC instrument itself. Detailing its aims and describing the different systems in the instrument, with a particular focus on the optical systems and operation, which is the focus of this research.

3 QUBIC

3.1 Introduction to QUBIC and its Aims

In this Chapter I will detail the aims of the QUBIC instrument and provide some history on its development. The current design of the QUBIC instrument will then be explained. The optical combiner was the focus of the research for this thesis so I will concentrate on its design in particular. The components that most directly impact on this work are discussed in detail, along with modelling results. When this research started it was decided that a technological demonstrator (TD) would be built first and an expansion to the full instrument (FI) – the planned phases of the QUBIC deployment will be discussed further in Chapter 6 – would be performed in the future. The development and redefinition of the optical combiner for the smaller demonstrator instrument was a significant part of this research and will be presented in this chapter.

3.1.1 Aim of QUBIC

As mentioned in Chapter 1, QUBIC is a ground-based instrument that aims to detect the primordial B-modes imprinted onto the CMB. These can be used, alongside the E-mode amplitudes, to determine the tensor-to-scalar ratio (Hamilton and Charlassier, 2010). To achieve this detection, QUBIC will operate over two frequency bands: 150 GHz, where the signal of the CMB is most prominent (Figure 3.1) and 220 GHz, which allows for the detection and subsequent correction for the polarised foreground contamination in the CMB (as discussed in Section 1.3.4) which peaks over this band (Ade *et al.*, 2015). Using the higher band to correct for the contamination (along with other data that can be used for foreground correction) it is envisioned that after three years of observation an upper limit on the sensitivity of $r \approx 0.021$ with a 68% confidence level can be achieved (Hamilton *et al.*, 2020). QUBIC can also be used as a spectro-imager where it has multiple sub-bands in the physical bands (this will be explored more in Chapter 6). This is unique to QUBIC and affords it the opportunity to be a very powerful probe of the foreground contamination as explained in Hamilton *et al.* (2020).

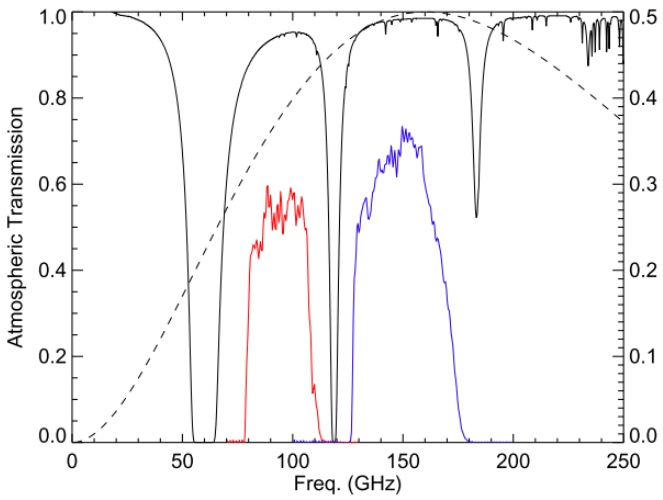

Figure 3.1: Atmospheric transmission as a function of frequency at Antarctica (Hinderks *et al.*, 2009). The dashed line shows the CMB spectrum. This is for the QUaD instrument (the red and blue bands indicate its spectral bands) but provides a good idea for the atmospheric transmissions possible for ground-based instruments.

3.1.2 QUBIC predecessors

QUBIC is the work of many researchers from collaborators in Argentina, France, Italy, Ireland, the UK, and North America. The current QUBIC collaboration formed from the pathfinding MBI (Tucker *et al.*, 2003) and BRAIN (Masi *et al.*, 2005) missions.

The Millimetre-wave Bolometric Interferometer: MBI

MBI was a collaboration between US and European researchers. Its aim was to test the validity of bolometric interferometry at millimetre wavelengths. MBI was a Fizeau interferometer consisting of a Cassegrain design with 4 back-to-back feed-horns and a cryogenically cooled array of bolometer detectors (Figure 3.2). An optical analysis of the MBI instrument was performed by Curran (2010).

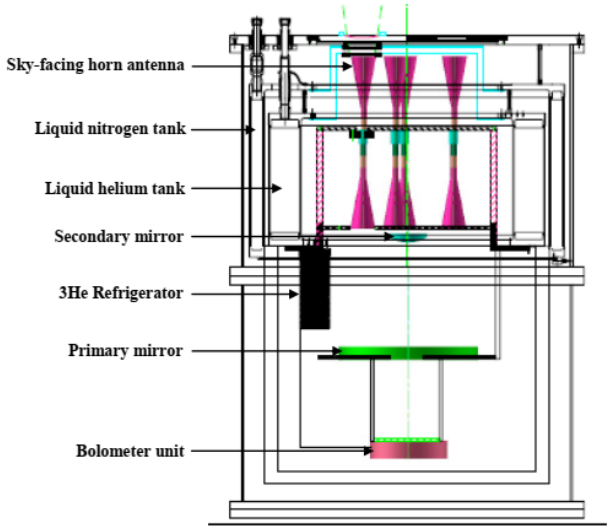

Figure 3.2: Schematic of the MBI instrument. Image obtained from Curran (2010).

Background Radiation Interferometer: BRAIN

BRAIN was the direct precursor to the QUBIC instrument. It was developed by a combined group of researchers from Italy, France and the UK. BRAIN was a bolometric interferometer that observed from the Dome C Concordia station in Antarctica (Figure 3.3), which provided suitable atmospheric conditions for observing all year round.

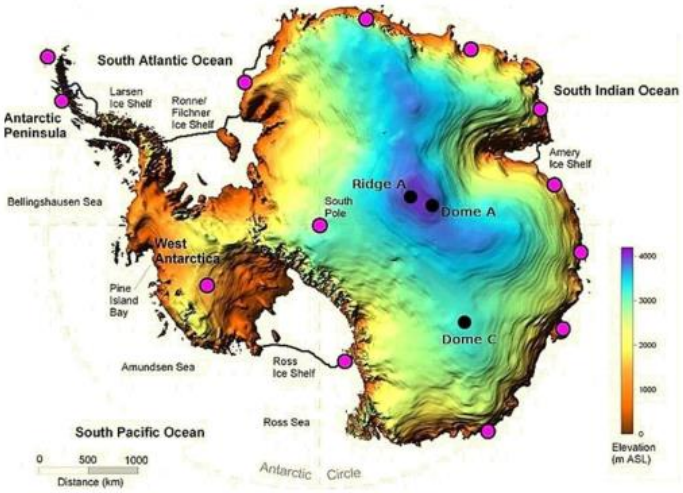

Figure 3.3: Elevation map of Antarctica (Spencer, 2013), Dome C is the location of the site for BRAIN.

BRAIN was a pathfinder mission which was to investigate conditions for future missions. Specifically, it tested the operation of a cryogenic system operating in the hostile environment in Antarctica, and also investigated the atmospheric conditions at the operating frequency of 145 GHz (Polenta *et al.*, 2007).

In 2008 after the fruitful research using both the MBI and BRAIN instruments it was decided to combine all aspects into a new instrument, QUBIC.

3.2 Interferometry with QUBIC

As discussed in great detail in Scully (2015), QUBIC is a Fizeau interferometer (similar to MBI), which has a focal plane consisting of pixels of Transition Edge Sensor (TES) bolometers that can image interference fringes, hence QUBIC is a 'bolometric interferometer'.

To achieve the sensitivity required to detect the B-mode polarisation QUBIC will operate as a synthetic imager. Even though QUBIC is an interferometer, when radiation from a large enough number of baselines are summed together on a focal plane they result in an image of the source (convolved with the synthesised beam – discussed in Sections 3.2.3 and 3.6). This presents the unique opportunity to allow QUBIC to exploit both the high levels of sensitivity provided by imagers as well as the control over systematics that an interferometer provides. In this section the theory of bolometric interferometry and synthetic image generation will be discussed in relation to the QUBIC instrument.

3.2.1 Interference

An example of a simple interferometer was provided in Chapter 2 along with some preliminary results on what to expect from QUBIC. As shown, for interference to occur, two or more sources with phase coherence, need to be incident on a detector. There are two types of phase coherence to consider in interferometry: spatial (defined phase relation along the spatial extent of the wave) and temporal (defined phase relation along the wave at any two points in time). The QUBIC instrument is an example of a spatial interferometer, similar to the multi-slit model.

Temporal interferometry

A simple example of temporal interferometry is when two sources have a phase delay between them, this is achieved by a Michelson interferometer (Figure 3.4). In this instrument, a source (typically a laser) is incident on a semi-silvered surface, where roughly half of the radiation is transmitted and the other half is reflected, creating two sources (coherent as they originate from the same source) that are incident on fully reflecting mirrors, one of which is moving. These sources are then recombined and observed on a screen and by using the moving mirror the phase relation between them can be altered by changing the path length of one of the beams. This phase difference then creates interference at the observation screen. By combining two identical beams that have travelled different distances we measure the correlation of the phase of the source at different moments in time.

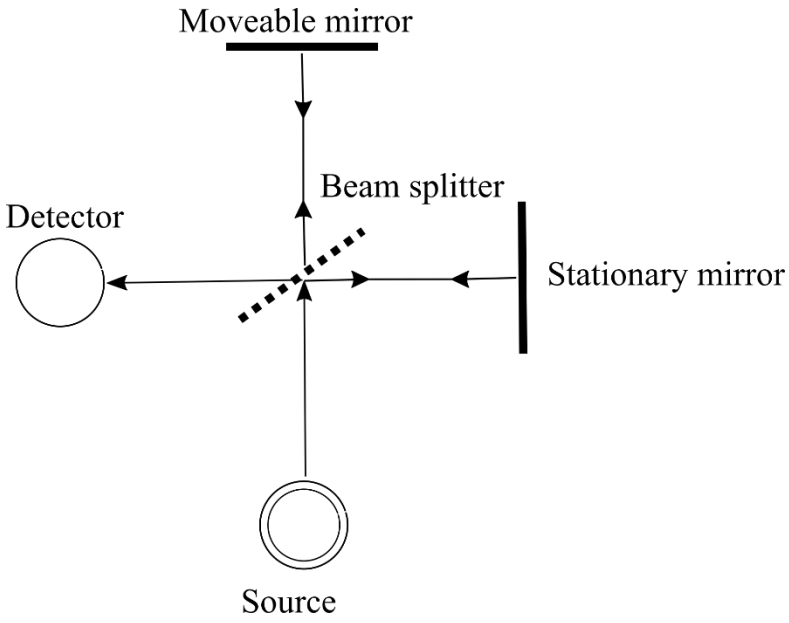

Figure 3.4: Simple schematic of a Michelson interferometer.

Spatial interferometry

Spatial interferometers are different in that they measure the phase correlation across a wavefront. Looking back at the multi-slit interferometer example presented in Section 2.3, the sources were all combined after travelling to the same observation screen and interference occurs due to phase differences in the wave fronts.

In particular QUBIC is a spatial Fizeau interferometer. There is a feedhorn array at the aperture of the instrument that can be considered analogous to the slits in the multi slit interferometer shown previously. When excited with radiation, each horn propagates a beam into an optical combiner and they are recombined at the focal plane producing a spatial interference pattern. Spatial interference can be used to determine the visibility of a source with the Van-Cittert Zernike theorem (van Cittert, 1934) as in equation [36].

$$V(u,v) = \mathrm{F}\big(I(\alpha,\beta)\big) \qquad [36]$$

where $V(u,v)$ is the fringe visibility as a function of spatial coordinates, u and v, I is the intensity distribution of the observed source as a function of angle, α and β, and F is the Fourier transform operator. To fully understand this theorem the idea of baseline interferometry needs to be discussed.

3.2.2 QUBIC baseline interferometry

The TD instrument will be discussed in detail later in this chapter but it will be modelled in this section with GBM as it is useful to explain the operation of the QUBIC interferometer and synthetic image generation. The TD has an array of horns as in Figure 3.5. Every pair of horns in the array can be thought of as a baseline. Each baseline then generates a spatial interference pattern on the focal plane of the instrument. In this section baselines will be indicated using the term 'baseline *a_b*' where *a* and *b* are just horn numbers from Figure 3.5

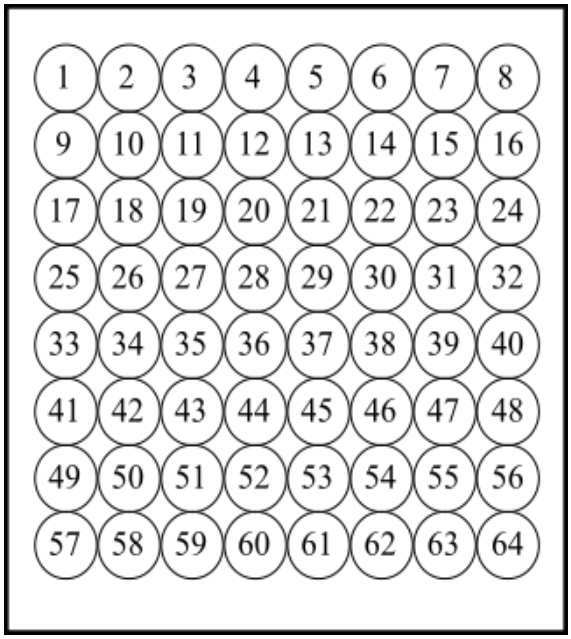

Figure 3.5: Simple top-down schematic view of the QUBIC horn array. Note that numbering is arbitrary and the spacing between the horns is not representative of the real array.

The pattern from each baseline depends on the distance between the horns. This is evident when modelling an idealised version of the QUBIC instrument using ABCD matrices with the optical regions and parameters from Table 2.2 to simulate the transmission of the beam from each horn all the way through the combiner. Figure 3.6 clearly shows that the interference pattern observed was dependent on the separation between the horns, d, the far-field angle between the fringes is roughly given by equation [37], derivative of the previous equation [32].

$$\theta = \sin^{-1}\left(\frac{\lambda}{d}\right) \qquad [37]$$

where $\lambda = 2$ mm (150 GHz), d is the size of the baseline, which has a value of 14 mm for both horizontally and vertically adjacent horns (i.e. the inter-horn distance, which will be discussed more in Section 3.3.3.4).

As was shown in Chapter 2, it can be seen that the envelope (a 12.9°FWHM Gaussian – i.e. the far-field pattern of a QUBIC horns) attenuates the interference pattern observed by different baselines. The fringe peaks for all baselines cannot be higher in intensity than this envelope.

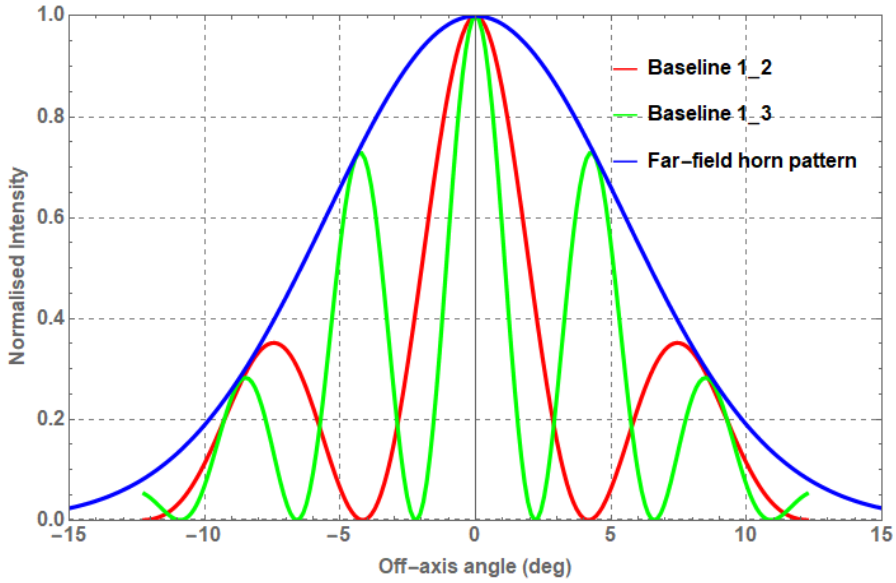

Figure 3.6: Interference pattern of two baselines (baseline 1_2 and baseline 1_3) when the sources are modelled as 12.9° Gaussian beams at 150 GHz with the distance between horn centres set to 14 mm.

In this 2D model the orientation of the baseline determines the orientation of the fringes on the focal plane (Figure 3.7). Thus, when combining multiple baselines at different orientations complex interference patterns will be generated. With this idealised model of QUBIC, identical baselines (i.e. baselines of the same orientation and separation, also known as redundant baselines) will produce identical patterns on the focal plane. It does not matter about the position within the horn in the array, i.e. baseline 1_2 will produce the same pattern as baseline 62_63. Redundant baseline pairs can be used to perform a novel rigorous self-calibration procedure that allows for unprecedented control over the systematic errors in the instrument (see Bigot-Sazy *et al.* (2013)).

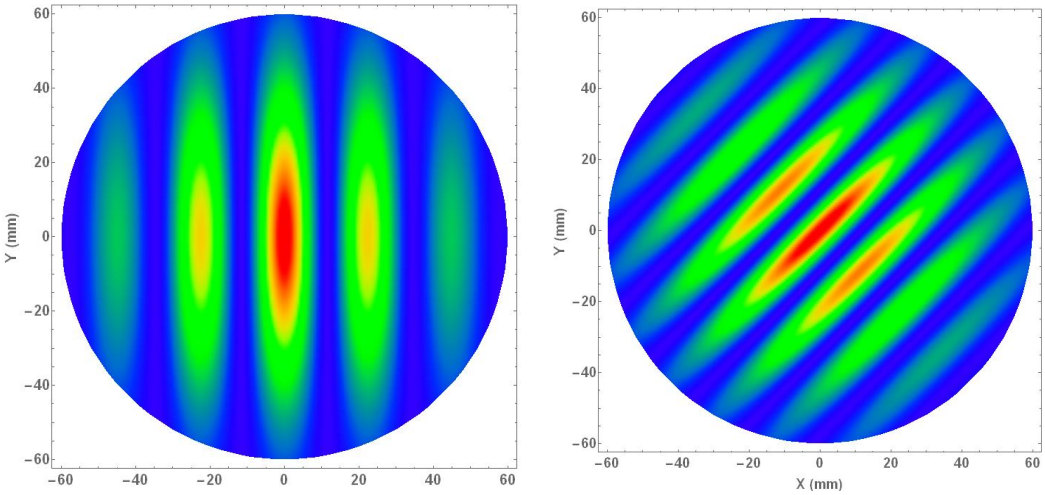

Figure 3.7: interference pattern for baseline 1_3 (left) which has a 28 mm horn separation and baseline 1_19 (right) which has a 39.6 mm horn separation and is at 45° to baseline 1_3, which results in the interference patterns being at 45° with respect to each other. Also it should be noted that the number of fringes increases with the increase in baseline separation as expected.

3.2.2.1 QUBIC as a synthetic imager

The Van-Cittert Zernike theorem (equation [36]) shows that the fringe visibility from a source as function of baseline (length/λ) can be obtained with a Fourier transform of the intensity distribution of the source being observed. Unique baselines will provide unique Fourier components of the source intensity distribution. Therefore, if QUBIC had an infinite number of baselines then it would be able to obtain an infinite number of Fourier components, and since each component is just the Fourier transform of the intensity distribution of the sky, the full intensity profile (or image) of the sky could be obtained. Hence an interferometer can be a synthetic imager if there is a sufficiently large enough number of baselines.

Obviously, there is not an infinite number of baselines. However, a large subset of baselines is enough to provide a synthetic image of the sky. The total number of baselines is given by equation [38] meaning that there are 2016 baselines for the QUBIC TD with its 64 feedhorn array. When the FI with its 400 feedhorn array, gets deployed there will be 79800 baselines (which includes identical baselines). The full instrument will be able to provide great detail on the sky.

$$\text{Number of baselines} = \frac{N(N-1)}{2} \qquad [38]$$

where N is the total number of horns in the array.

The ability to operate QUBIC as a synthetic imager can be shown simply by adding up the interference patterns from all the baselines produced with the ABCD matrices. Figure 3.8 shows that when more baselines are combined, the pattern is much more complex than for the single baseline. When accounting for all the baselines, the pattern produced resembles a traditional Point Spread Function (PSF) that an imager would obtain when observing a point-like source, with additional off-axis peaks occurring at a position that depends on the horn separation (equation [37]). Similar to a real imager, the convolution of this PSF with the sky will be recorded. It should be noted that this is for an idealised on-axis instrument, the PSF for the real QUBIC optical combiner will be shown later in this chapter.

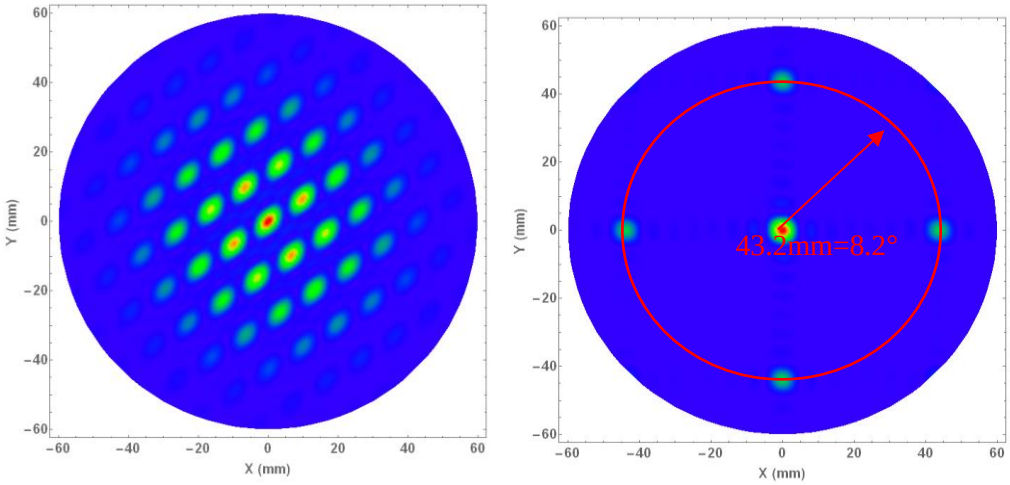

Figure 3.8: Patterns resulting from the addition of baselines with a length of 13 horn separations for the TD (left) and the beam pattern for the combination of all baselines in the FI (right); this was simulated utilising the same Gaussian beam for all horns in the array simulating the observation of a plane wave (i.e. a point source). The off-axis peaks occur at 43.2 mm from the centre of the focal plane which corresponds to 8.2° for a 300 mm focal length (agreeing with the peak separation seen in the multi-slit model shown in Chapter 2).

3.2.3 The window function

The window function is a measure of the response of the instrument to multipoles on the sky, and allows for a sensitivity analysis of the instrument to be performed. To derive and explain the window function, the idea of 'bolometric interferometry' must be looked at. The focal plane of QUBIC consists of an array of TES bolometers (see Section 3.3.2). Each TES in the focal plane has a unique synthetic beam, which is similar in structure to the PSF. The synthetic beam describes the response of the bolometer to radiation at different positions across the sky. For an ideal instrument the PSF shown above is equivalent to the synthetic beam for an on-axis bolometer. It should be noted that for the real combiner, due to aberrations introduced by its design, they are not exactly the same and this will be explored more in Section 3.6. The synthetic beam will be convolved with the intensity distribution of the sky, and thus every TES will record a synthesised image as given in equation [39] (Battistelli *et al.* (2011)).

$$S_I(p, \bar{n}_0, \theta_0) = \int I(\bar{n}) B_s^p(\bar{n} - \bar{n}_0, \theta_0) d\bar{n} \qquad [39]$$

where S_I is the synthesized image in intensity I (a similar equation holds for the other Stokes parameters), P is the TES number, $\bar{n}_0$ is the telescope direction, $\bar{n}$ is the source direction, $\theta_0$is the pitch angle of the telescope, $I(\bar{n})$ is the intensity of the source and $B_s^p$is the synthesised beam of the bolometer being investigated.

The intensity of the sky can be decomposed into spherical harmonics as in equation [40] (just as the angular power spectrum for the anisotropies could be obtained from the decomposition into spherical harmonics shown in Section 1.2.1).

$$I(\bar{n}) = \sum_{lm} a_{lm} {Y^*}_{lm}(\bar{n}) \qquad [40]$$

where Y_{lm} is the standard spherical harmonic function as before and a_{lm} is the sky spherical expansion coefficient for the CMB. In addition, for the CMB,

$$\langle a_{lm} {a^*}_{l'm'} \rangle = C_l \delta_{ll'} \delta_{mm'} \qquad [41]$$

where C_l is the coefficient of the angular power spectrum of the CMB introduced before.

We introduce $\beta_{lm}(p, \bar{n}_o, \theta_o)$ from Battistelli *et al.* (2011):

$$\beta_{lm}(p, \bar{n}_0, \theta_0) = \int B_s^p(\bar{n} - \bar{n}_0, \theta_0) Y_{lm} d\bar{n} \qquad [42]$$

so that the synthesised beam can be written

$$B_s^p(\bar{n} - \bar{n}_0, \theta_0) = \sum_{lm} \beta_{lm}(p, \bar{n}_o, \theta_0) Y_{lm.} \qquad [43]$$

Combining equations [39] and [43] and using the orthogonal nature of the spherical harmonics $Y_{lm}$the synthetic image can be expressed as:

$$S_I(P, \bar{n}_0, \theta_0) = \sum_{lm} a_{lm}\beta_{lm}(p, \bar{n}_o, \theta_0). \quad [44]$$

Using this expression, the covariance matrix of two bolometer signals (from bolometers numbered p and q) can then be expressed as:

$$\langle S_I(p, \bar{n}_k, \theta_i) {S_I}^*(q, \bar{n}_l, \theta_j)\rangle = \sum_{lm}\sum_{l'm'} a_{lm}\beta_{lm}(p, \bar{n}_k, \theta_i)\ \ {a^*}_{l'm'}{\beta^*}_{l'm'}(q, \bar{n}_l, \theta_j). \quad [45]$$

Using [41] this can be reduced to:

$$\sum_l C_l \sum_m \beta_{lm}(p, \bar{n}_k, \theta_i)\ \ {\beta^*}_{l'm'}(q, \bar{n}_l, \theta_j) \quad [46]$$

where the right side of the expression is the newly termed window function:

$$W_l(p, q, \bar{n}_k, \bar{n}_l, \theta_i, \theta_j) = \sum_m \beta_{lm}(p, \bar{n}_k, \theta_i)\ \ {\beta^*}_{lm}(q, \bar{n}_l, \theta_j). \quad [47]$$

Thus equation [45] can be expressed as in equation [48] and allows the image on the sky to be expressed in terms of the window function.

$$\langle S_I(p, \bar{n}_k, \theta_i) {S_I}^*(q, \bar{n}_l, \theta_j)\rangle = \sum_l C_l W_{lm}(p, q, \bar{n}_k, \bar{n}_l, \theta_i, \theta_j)\,. \quad [48]$$

Hence the window function can be used as a means of describing the sensitivity of individual detectors or the entire instrument to multipoles on the sky (Figure 3.9). The window function is used as a figure-of-merit in Chapter 4 when I investigate the tolerance of the instrument to mirror alignment (Section 4.2).

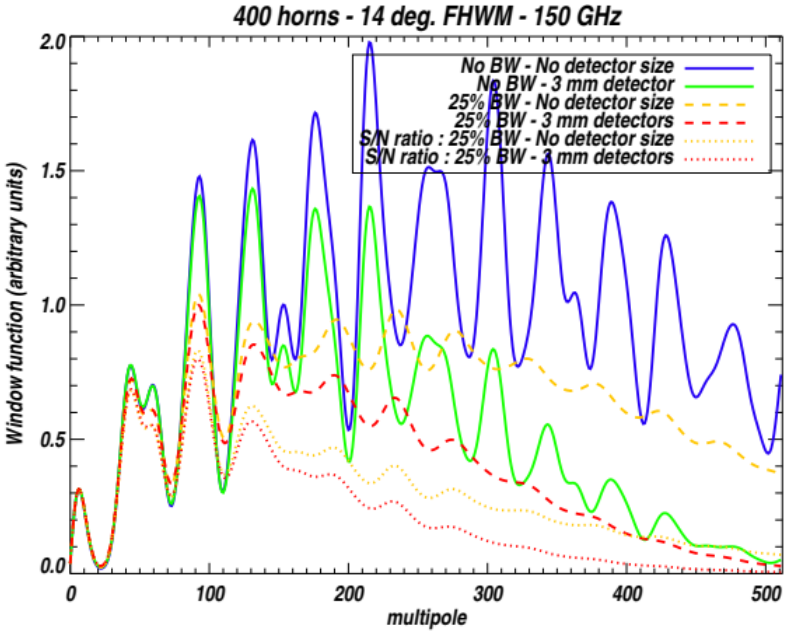

Figure 3.9: Window function for a variety of setups of the original QUBIC instrument (described briefly below). Image obtained from Battistelli *et al.* (2011). When the finite size of the detector is included the synthetic beam smears out and drops in peak intensity which leads to the drop in the window function.

3.2.4 The design of the optical combiner

So far the QUBIC instrument has only been modelled as an idealised on-axis combiner, however as seen in Figure 2.1 its combiner has an offset Gregorian (also known as compensated Gregorian) design. Different aspects of the QUBIC instrument – such as the overall combiner design, the horn profile and individual element designs within the combiner – have undergone multiple iterations. The current design of the combiner is based on the results of in depth modelling and refinements performed by Bennet (2014). The original design of the combiner was based on a horn geometry that emitted a 14° Gaussian beam, with a horn separation of 10 mm. The requirement to Nyquist sample interference fringes (which dictates that for a baseline to be sufficiently sampled, there must be at least two bolometers per fringe for that baseline) with our 3 mm^2 bolometers resulted in the short 300 mm focal length. This is described in greater detail by Bennet, but here I explain the basic reasoning behind these design decisions.

Figure 3.6 showed that the fringes of the interference pattern narrow as the inter-horn spacing increases. The baseline $\left(u = \frac{d}{\lambda}, \text{ where } d \text{ is the length of the baseline}\right)$ represents the Fourier component on the sky and determines the multipole, l, that can be detected by the instrument (equation [49] (e.g. White *et al.*, 1999)).

$$l \approx 2\pi u. \qquad [49]$$

In this original design it was envisioned that the instrument would detect the multipoles $30 < l < 200$ (Hamilton *et al.*, 2008).

Table 3.1 shows that for integer multiple increases in the baseline separation, a 3 mm wide bolometer will be able to sample the fringes for baselines that correspond up to a maximum multipole of 314 (this is higher than desired, but this description does not account for any gaps that would be present between the bolometers, meaning that in reality this maximum would be lower), hence justifying the design chosen. It should also be noted that many different focal lengths were tested by Bennet, however due to physical restrictions of the cryostat (volume of roughly 1 m^3), the focal length was limited. A focal length of 300 mm was the largest feasible value that could be obtained with these restrictions.

Table 3.1: Multipole and fringe size corresponding to a particular baseline separation (the minimum baseline separation is 10 mm).

u	Multipole	Fringe separation for a 300 mm focal length instrument (mm)
5λ	31	60.0
10λ	63	30.0
15λ	94	20.0
20λ	126	15.0
25λ	157	12.0
30λ	188	10.0
35λ	220	8.6
40λ	251	7.5
45λ	283	6.7
50λ	314	6.0

The above reasoning is not dependent on any specific type of optical combiner, merely a general overview for ideal interferometers. It was decided that the best design for the optical combiner was an offset Gregorian design as shown previously. The size of the cryostat caused mechanical restrictions and the offset Gregorian design allowed for the necessary focal length and TES size to be achieved within the cryostat, as well as allowing for an opening aperture that would encompass the horn array. The aberrations introduced by this design will be shown later in the chapter, but it was found that they introduced, roughly a 10% drop in the sensitivity of the window function compared to an ideal instrument as seen in Figure 3.10. The offset Gregorian design does minimise the decrease in sensitivity when compared with other designs (the large unobstructed aperture means the beam from the horns are able to pass through this combiner) and this drop was deemed to be acceptable.

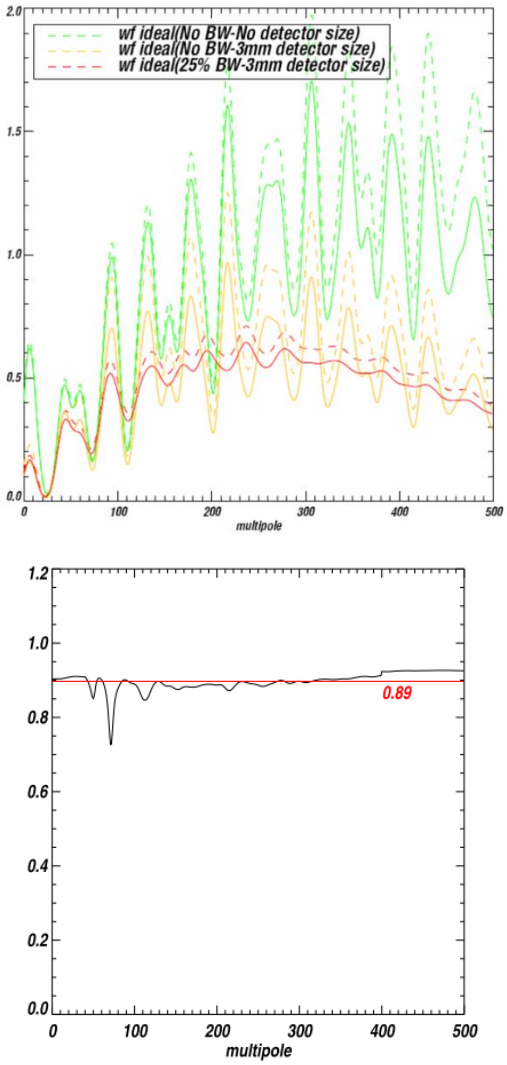

Figure 3.10: The top plot shows the window function for the offset Gregorian combiner with the bolometer size and bandwidth accounted for. The y-axis units are arbitrary. The dashed lines indicate an ideal aberration free combiner and the solid lines account for the aberrations introduced by the combiner, this image was provided by M.A Bigot-Sazy of APC Paris and taken from Bennet (2014). The bottom shows the window function of the real (aberrations included) instrument divided by that of the ideal one as a function of multipole number (taken from Bigot-Sazy (2013)).

3.3 QUBIC current Full Instrument (FI) description

The current plan is to the install the TD in the observation site in the region of Alto Chorillos in Argentina and then upgrade to the FI at a later date. The introduction of the TD is a relatively new concept which was first conceived in 2015 (when this research started) as a proof of technology for the novel systems that are being utilised. The FI was designed first and the TD is derivative (de-scope) of this. For this reason this section will introduce the full QUBIC instrument as well as its optical design before describing the TD later in the section.

3.3.1 Cryogenic systems

It has been shown that the B-mode polarisation signal in the CMB is very faint, and an instrument with unprecedented levels of sensitivity will be required to detect it. The novel techniques that QUBIC utilises will aid in detecting the signal. As well as this, any noise must be reduced. QUBIC will utilise a multi-stage cryogenic system to cool down the optical elements and minimise any thermal fluctuations and noise, as well as cooling the detectors to their operating temperature. A very detailed analysis of the cryogenics system and the operation of the different cooling stages is provided by May *et al.* (2018) and Masi *et al.* (2020).

The QUBIC optical combiner (Figure 2.1), which will be fully detailed in Section 3.3.2, is placed in a cryogenic system with a volume of approximately 1 m^3. This system is then placed inside a shell (the cryostat) as seen in Figure 3.11 that allows the instrument to operate under the high vacuum conditions required to reach the desired low temperatures. This shell also supports the internal elements and provides a gap that allows for thermal insulation around the cryogenic systems. The incident radiation enters into the system through a window in the cryostat. From the diagram it can be seen that there are different stages to the cooling process of the instrument (the 40 K and 4 K stages are specifically shown), for these stages two pulse tube coolers (PTCs) are used to reach the desired temperatures.

To further minimise the thermal fluctuations, some elements in the optical combiner (from the horn array to the focal planes) are placed in what is called the 1 K box (Figure 3.12). This box is attached to the 4 K stage and is initially cooled to this temperature with the PTCs. It is then further cooled down to 1 K with a helium-4 fridge. For the bolometers to act as Transition Edge Sensors (TESs), they must be cooled down further to 350 mK; this is achieverd with a further cooldown provided by a helium-3/helium-4 combination fridge. There are multiple stages to the cool down and in total it takes an estimated 15 days to complete (The QUBIC collaboration, 2016).

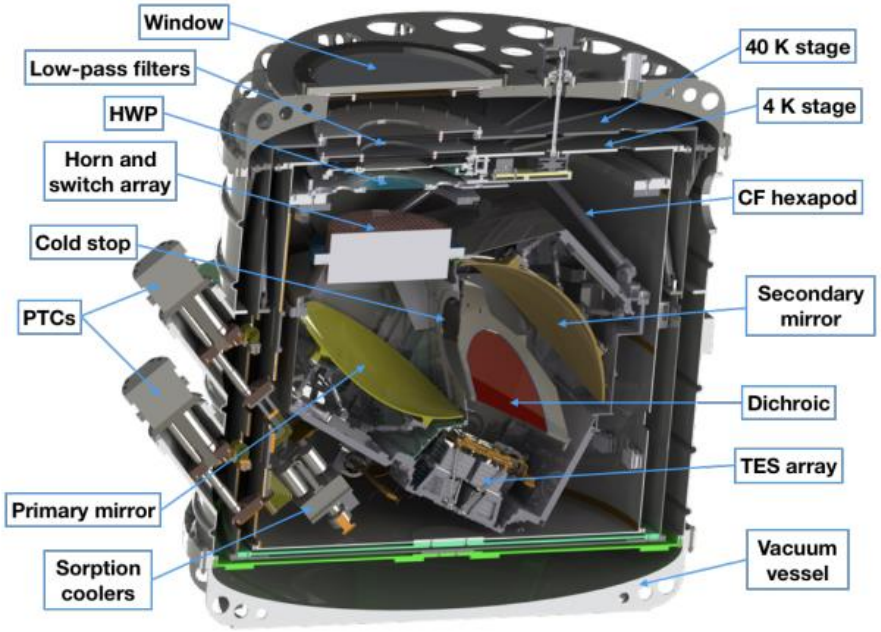

Figure 3.11: CAD model of the full instrument optical combiner inside the cryostat Image obtained from May *et al.* (2018).

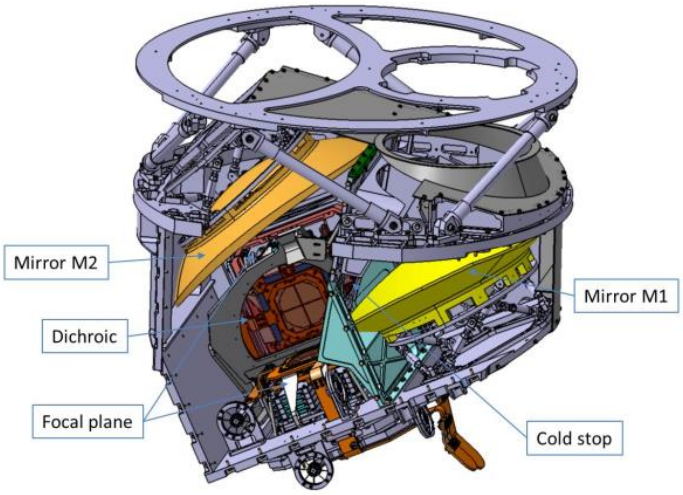

Figure 3.12: 1 K box housing the optical combiner. Image obtained from the Technical Design Report (The QUBIC collaboration, 2016).

3.3.2 QUBIC detector pixels

Bolometers

As mentioned, QUBIC utilises an array of bolometers as pixels on the focal plane. Bolometers have an excellent track record and have been successfully used on previous CMB missions such as the Planck satellite (Holmes *et al.*, 2008). Figure 3.13 shows the schematic of a simple lumped element bolometer detector, similar to what is used in QUBIC: an absorber of heat capacity C is connected to a heat sink at temperature T_s by a connector with thermal conductance G. Any incident radiation of power P increases the absorber temperature. This temperature increase is measured as a change in resistance R of a

semiconductor biased with constant current I_b. QUBIC bolometers are TESs cooled to their superconducting temperatures as presented next

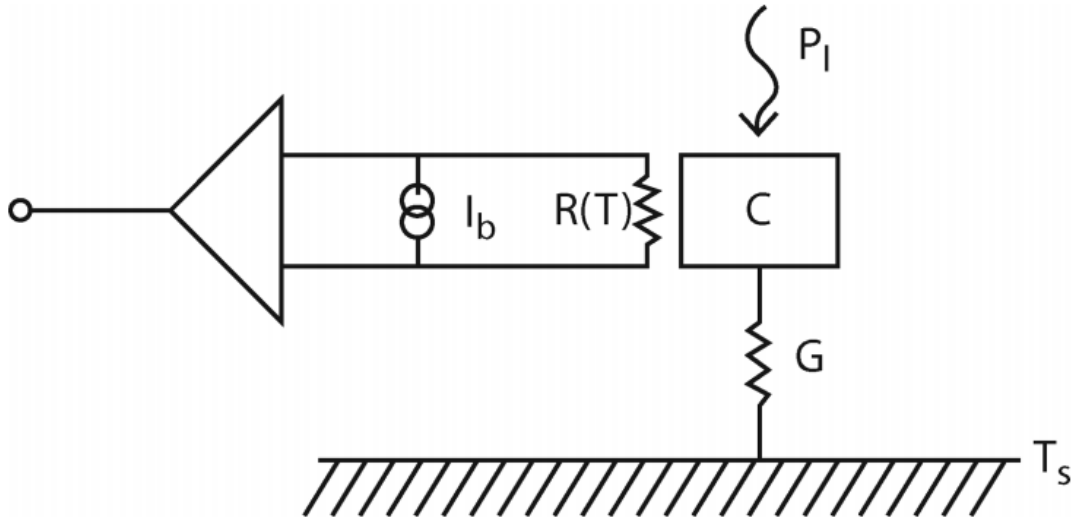

Figure 3.13: Bolometer Schematic (image obtained from Holmes *et al.*, 2008).

Transition edge sensor

Once a conductor is cooled down sufficiently to be considered a superconductor, its resistance drops sharply. While in this superconducting range if the temperature is increased so that it transitions back to the 'normal' conducting range there is a sharp nonlinear increase in the resistance which can be seen in Figure 3.14. The temperature range for this transition from superconducting to normal is very narrow, thus making it very sensitive to small changes in temperature. Cooling the bolometers so that they are just at the superconducting level (or the 'transition edge'), will mean that even the smallest change in radiation will induce a large resistance change, meaning they are very sensitive.

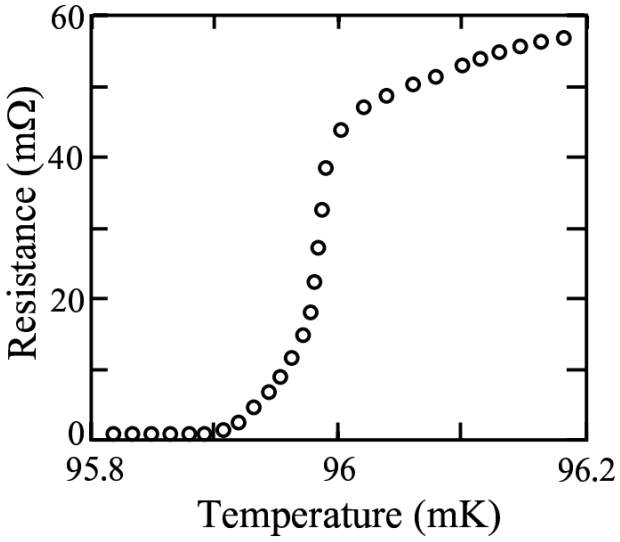

Figure 3.14: Transition edge of a superconducting Mo/Cu proximity bilayer (image obtained from Irwin, Hilton and Ed, 2005).

The focal plane of QUBIC will consist of an array of 992 NbSi TES pixels and the signal from each pixel will be read out with a superconducting quantum interface device, or SQUID (Figure 3.15), which is a very sensitive magnetometer. 128 signals from the SQUIDs are then passed to a single SiGe ASIC (Application-Specific Integrated Circuit) that will both control the multiplexing of the signals and also amplify them, generating the data required. A full detailed report on the performance of the readout of the QUBIC TESs has been performed by Bélier *et al.* (2018) and Piat *et al.* (2020).

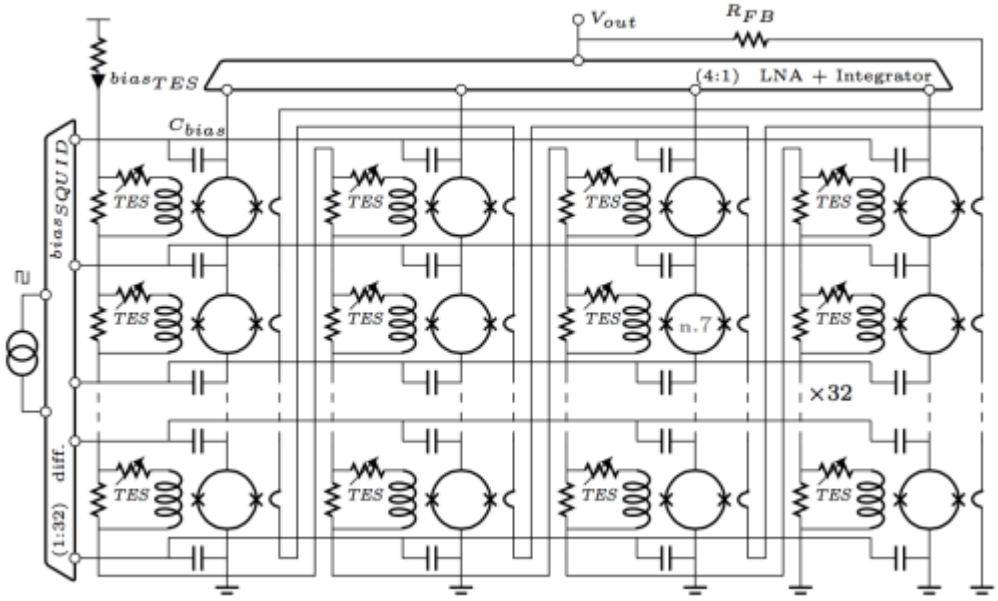

Figure 3.15: Layout of a collection of pixels coupled with a SQUID (image obtained from Piat *et al.*, 2020).

It was shown how bolometers of 3 mm^2 are suitable for an instrument of 300 mm focal length. In reality the active area of the pixels is not quite that large (2.7 mm × 2.7 mm), with Figure 3.16 showing the layout of the actual focal plane for the FI. The full surface of the focal plane is not sensitive to radiation due to the gaps between the sensitive area of each of the pixels. As well as this, the horns were redesigned from the original 14° beam emitters to 12.9° emitters (this reduces truncation in the combiner), and there was also a change in the inter-horn (baseline) separation from 10 to 14 mm. Taking this into account it can be seen from Table 3.2 that even with these separations the performance of the instrument remains similar to before; the multipoles to which the instrument is sensitive are within the range $44 < l < 352$ (assuming the Nyquist sampling restriction of 2 bolometers per fringe in a baseline).

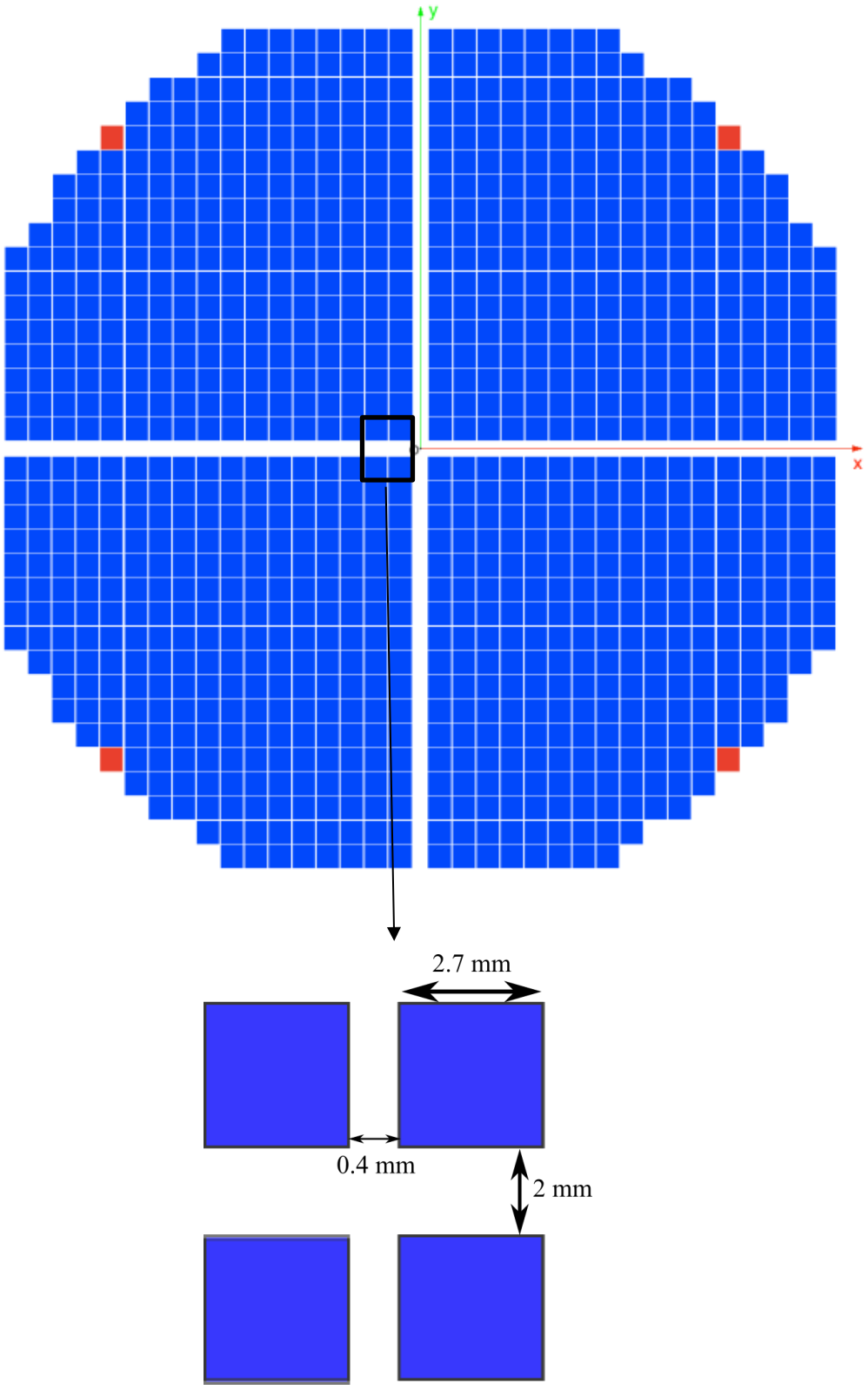

Figure 3.16: Focal plane layout; there are four quadrants each consisting of 248 active bolometers, providing a total of 992 bolometers, the active bolometers are shown in blue. The lower figure shows a zoomed in section of the top image.

Table 3.2: Baseline separations and their corresponding fringe size and multipole for the current QUBIC design.

Baseline separation (mm)	Baseline Separation (horns)	Baseline separation, *u*	Fringe separation(mm), *r*,	Multipole, *l*
14	1	7	42.86	44
28	2	14	21.43	88
42	3	21	14.29	132
56	4	28	10.71	176
70	5	35	8.57	220
84	6	42	7.14	264
98	7	49	6.12	308
112	8	56	5.35	352
126	9	63	4.76	396

Initially the focal plane was modelled in MODAL as a disc with a radius corresponding to the full width of the actual focal plane as seen in Figure 3.17. To ensure that all the bolometers were captured, it was decided to increase the MODAL focal plane to a disc of radius 60 mm. It is important to ensure that all the bolometers are covered by this focal plane, particularly when modelling the synthetic beams for specific TES (this will be discussed further in Section 3.6). The MODAL focal plane will capture more power than the real one, but the power falling on each pixel can be calculated from it, if required. It was also assumed that it was a perfect absorber.

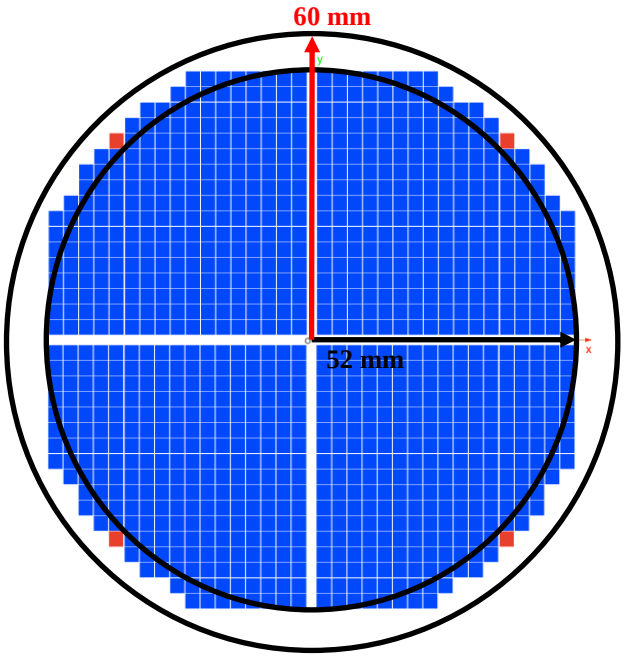

Figure 3.17: In MODAL a focal plane approximated by a disc with a radius corresponding to the width of the actual focal plane (52 mm), does not capture the full power, while a focal plane of 60 mm does.

3.3.3 Layout of optical combiner

In this section the optical combiner (Figure 2.1) will be discussed for the FI, with the TD differences outlined later in the chapter. The optics in the system have two main goals for the instrument: to allow the desired bands (150 GHz with 25% bandpass and 220 GHz with 18% bandpass) into the system and to direct the radiation from all the input feed horns so that they are combined on the focal plane.

3.3.3.1 Reference Frames

As mentioned in Chapter 2, we define a global reference frame (GRF) for QUBIC and every object is positioned relative to that frame, thus having its own local reference frame (RF). The GRF is located at the centre of the horn array in the plane of the output (downward-facing) apertures, note that there is no actual horn centred at this position (Figure 3.18).

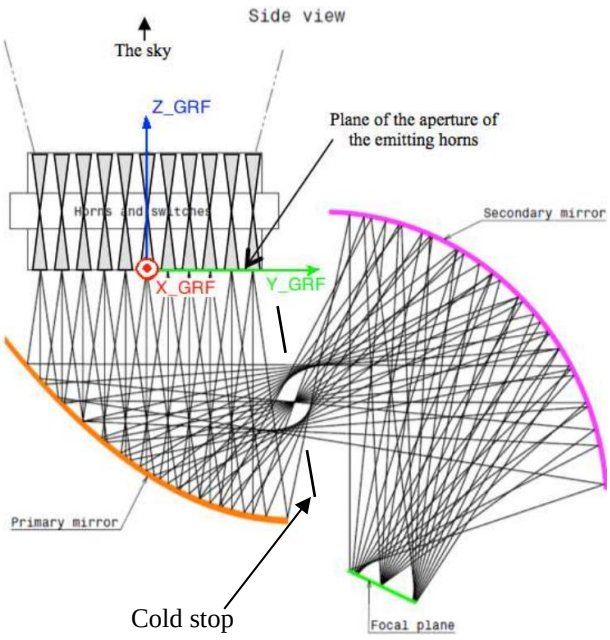

Figure 3.18: Side view of the QUBIC combiner model with the GRF x, y and z axes shown (image adapted from the Technical Design Report (The QUBIC collaboration, 2016)).

Table 3.3 shows the parameters that are used to define the other optical element local frames relative to the GRF: dx, dy and dz are translations in the x, y and z direction respectively, and the α, β, γ, angles are used to determine the orientation of the element reference frame. Euler $ZY`Z``$ rotations are used; after the frame origin has been determined with the translation (dx, dy, dz) a rotation of α rad is performed around the local z-axis (Z), then a rotation of β rad is performed around the newly oriented y-axis ($Y`$) generating another newly oriented frame, then a final rotation of γ rad is performed around the z-axis of this frame ($Z``$), thus creating the correct orientation of the local frame for the element. Note that in Table 3.3 Δz is the distance of the horn phase centre from the horn aperture. For a corrugated horn the phase centre of the beam is not actually at the aperture of the horn, it is in fact some distance behind the aperture. This has been calculated as -2.5 mm at 150 GHz (Scully, 2015) for the QUBIC horns.

Table 3.3: Local RF positions relative to the GRF for all the optical elements that will be placed in the QUBIC instrument.

Element	Frame	*dx* (m)	*dy* (m)	*dz* (m)	*Alpha* (rad)	*Beta* (rad)	*Gamma* (rad)
Cryostat window	Win_RF	0	0	0.48000	0	0	0
IR blocking filter 1	IRB1_RF	0	0	0.46005	0	0	0
IR blocking filter 2	IRB2_RF	0	0	0.45255	0	0	0
IR blocking filter 3	IRB3_RF	0	0	0.34210	0	0	0
IR blocking filter 4	IRB4_RF	0	0	0.33500	0	0	0
IR blocking filter 5	IRB5_RF	0	0	0.32710	0	0	0
IR blocking filter 6	IRB6_RF	0	0	0.28550	0	0	0
Low-pass filter	12cm-LPE_RF	0	0	0.27630	0	0	0
Half wave plate	HWP_RF	0	0	0.23780	0	0	0
Polariser	Pol_RF	0	0	0.18360	0	0	0
GRF	QUBIC_GRF	0	0	0	0	0	0
Horn array (downward facing)	Secho_ARF	0	0	0	π/4	0	0
Horn array (beam waist of horns)	Secho_BWP	0	0	Δz	π/4	0	0
Primary mirror	M1_RF	0	2.09576	-0.466757+ Δz	0	π	- π/2
Cold stop	CS_RF	0	0.231103	-0.26564+ Δz	- π/2	-1.42768	0
Secondary Mirror	M2_RF	0	0.209576	-0.302273+ Δz	π/2	-2.40253	0
On-axis Focal plane	ONA_FPRF	0	0.331210	-0.563118+ Δz	- π/2	-0.44377	0
Off-axis Focal plane	OFA_FPRF	0.11	0.378428	-0.463773+Δz	0	- π/2	-1.12702
Dichroic	PG_RF	0	0.378438	0.463773+Δz	0.40555	0.87800	1.38033

3.3.3.2 Filters

The QUBIC instrument has a cryostat window that is 560 mm in diameter, this acts as the instrument aperture. There will be a collection of filters after the window (Table 3.4). The specific details of these filters are given in the QUBIC Technical Design Report (The QUBIC collaboration, 2016): the IR filters will block most of the unwanted IR radiation, the low-pass edge (LPE) filter will block out-of-band far IR radiation, and has a high in-band throughput. The combination of these filters ensures a low thermal load inside the system, as well as ensuring that the desired frequency bands are measured by the combiner.

Table 3.4: Sizes of the different filters just after the cryostat window for the TD instrument (at the time of writing the FI sizes are still to be confirmed). Values provided by M. De Petris of the Sapienza University of Rome.

Component	Diameter (mm)
IR blocker 1	278
IR blocker 2	278
IR blocker 3	225
IR blocker 4	225
IR blocker 5	225
IR blocker 6	200
12cm-LPE	200

3.3.3.3 Half wave plate and polarising grid

After the filters there is a rotating half-wave plate (HWP) (Figure 3.19) that will modulate the polarisation of the incident radiation. This device covers a total of 90° in rotation, achieved by rotating between 7 positions separated by 15° (a full description and analysis of this subsystem is provided by D'Alessandro *et al.* (2020)). After the HWP is a polarising grid that transmits one polarisation direction. The bolometers are not polarisation sensitive, hence the HWP and polarising grid are vital for QUBIC to modulate the polarised sky signal and allow for the recovery of the I, Q and U maps (as per equation [50] (Mele *et al.*, 2020)) that are required in order to measure the polarisation anisotropies, this is described in much more detail in the Technical Design Report (The QUBIC collaboration, 2016). Hamilton *et al.* (2020) also provide some preliminary results of the analysis of the focal plane radiation when using the half wave plate and polariser combination during the testing phase of the instrument.

$$I(p,v,\theta) = \frac{1}{2}[S_I(p,v) + S_Q(p,v)\cdot\cos(4\theta) + S_U(p,v)\cdot\sin(4\theta)] \qquad [50]$$

where I is the intensity, p is a bolometer number, v is the frequency, θ is the orientation of the HWP and S_I, S_Q, and S_U are the stokes components of the sky convolved with the synthetic beam for the bolometer.

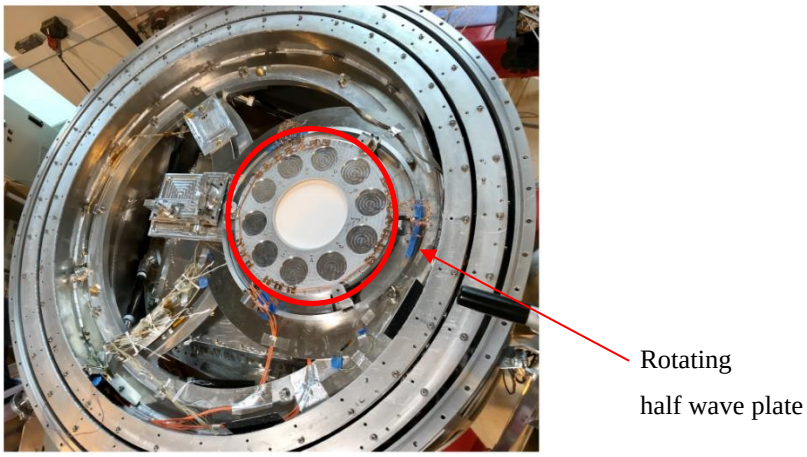

Figure 3.19: The rotating half wave plate installed in the QUBIC instrument (image adapted from D'Alessandro *et al.* (2020)).

3.3.3.4 Back-to-back feedhorn array

Following the HWP and polariser, the polarised light is then incident onto a horn array which is laid out as in Figure 3.20. The horn array is rotated by 45 degrees with respect to the GRF so that the resulting pattern was also rotated by 45° (Figure 3.21) and the off-axis peaks of the PSF didn't fall on 2 mm gaps between the bolometer quadrants (as seen in Figure 3.16) which would be the case for the unrotated pattern in Figure 3.8.

The horn array is comprised of a collection of back-to-back feedhorns (sky and downward/instrument facing sides); each horn pair is identical and has the geometry seen in Figure 3.22. These horns were designed to have 12.9º Gaussian far-field beam at 150 GHz and since they are back to back, the sky-facing horns provide a 12.9° FOV for the instrument, and the downward facing horns transmit a 12.9° beam into the instrument. In between the horns is a switch that allows the horn to be open (transmits radiation) or closed (does not transmit radiation), essentially turning the horns on or off. This allows for specific horns and baselines to be investigated, which is vital for the self-calibration of the instrument. Cavaliere *et al.* (2020) provide a detailed description of the operation of the switches in the feed horns.

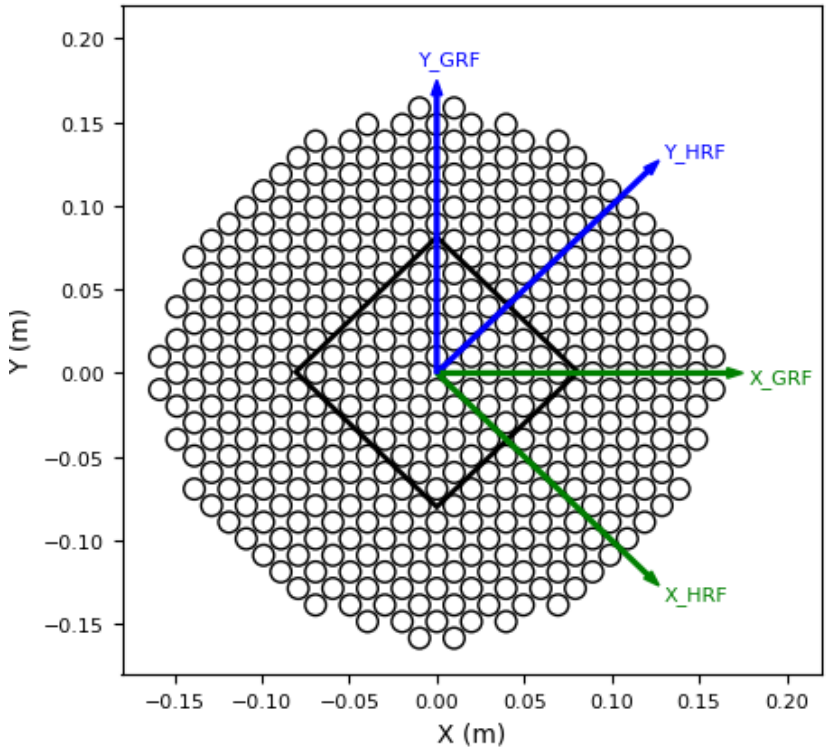

Figure 3.20: Schematic of the layout of the QUBIC feedhorn array for the FI (400 horns) looking down from the sky. The black square shows the position of the feedhorns used in the TD (64 horns) and the arrows indicate the orientation of the horn array relative to the GRF (i.e Secho_ARF in Table 3.3).

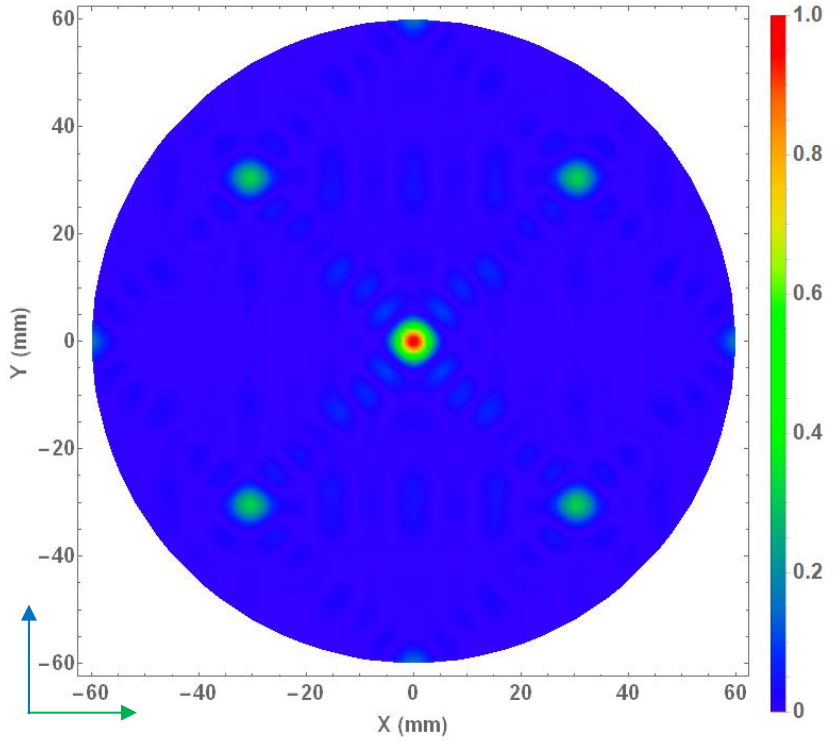

Figure 3.21: PSF of an ideal instrument on the on-axis focal plane when the horn array is rotated by 45°. The green and blue arrows show the orientation of the *x* and *y* axes of the ONAFP_RF reference frame.

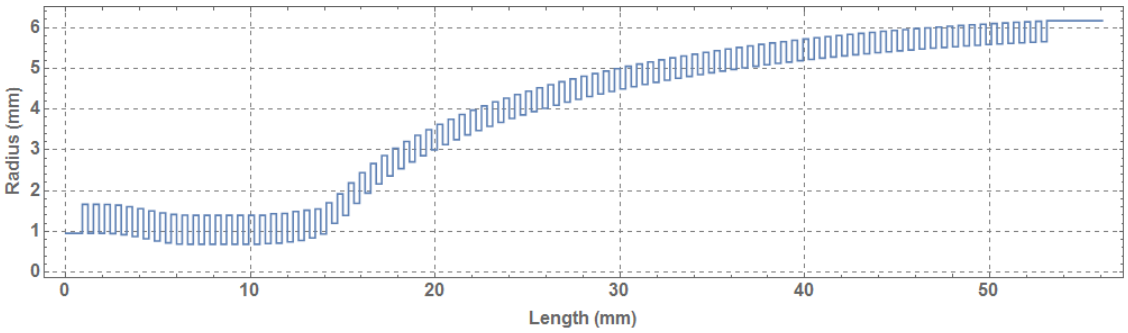

Figure 3.22: Geometry of one side of the corrugated horn in the QUBIC instrument.

Throughout this thesis there will be beam patterns shown from different horn positions and the horns will be labelled using an indexed identifier (*x#y#*) stemming from its location in the horn array in both the x and y direction of the horn reference frame (see Figure 3.23). These identifiers will be kept constant between the FI and the TD.

Truncation due to cryostat window

The truncation of the horn beams due to the cryostat window will be most evident on the edge horns. The centre of any edge horn (any horn in with an *x* or y position of 1 or 22 in Figure 3.23) is a lateral distance of 147 mm from the *x* or *y* axis of the local reference frame. The cryostat window is a distance of about $z = 367.8$ mm from the opening apertures of the back-to-back horn array, and as mentioned is 560 mm in diameter, meaning there is lateral separation between the centre of the edge horn and the cryostat window edge of 113 mm as seen in seen in Figure 3.24. The angle between these horns and the edge of the cryostat window can then be approximated as $\tan^{-1}\left(\frac{133}{367.8}\right) = 19.88°$ (seen in Figure 3.24). The FWHM of the horn

beam is 12.9° so this will not adversely affect the FOV of the instrument and comparing this angle with the horn beam pattern (Figure 2.17) it can be seen that this corresponds to a very low truncation level of about -30 dB.

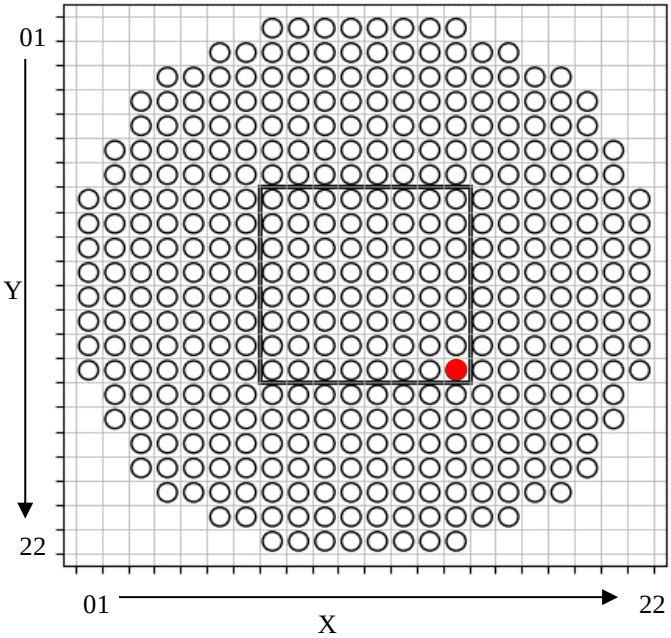

Figure 3.23: Schematic of the horn array (orientated in the Secho_ARF), looking down from the sky, showing the numbering used for the horn labelling. Note that the for the TD horns (black box) indexing is in the range 8 – 15 in both the x and y directions. As an example, the red filled horn is labelled $x15y15$.

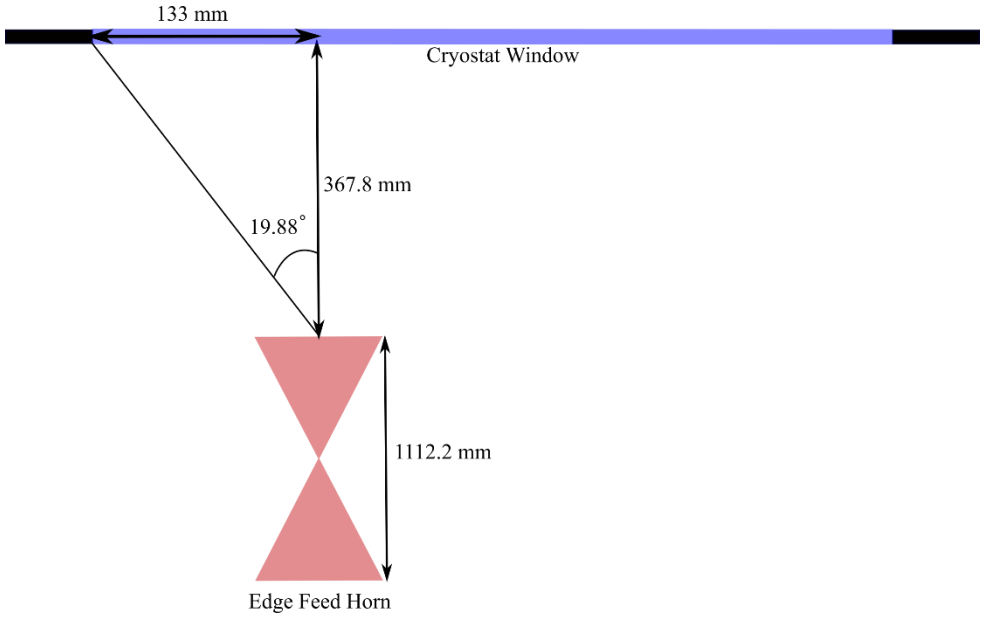

Figure 3.24: Schematic of truncation of an edge feed-horn due to the cryostat window. Note that this is not to scale.

3.3.3.5 Primary mirror

The surface of a mirror can be defined in MODAL with the quadratic equation [31] as described in Chapter 2. The QUBIC primary mirror (M1) surface (Figure 3.25) is a section of a parabola defined by this equation along with the coefficients in Table 3.5. To fully define the mirror in MODAL, a bounding volume

must be defined. For mirrors this is usually done by defining a "coring cylinder" and extracting the shape that is common to the cylinder and the parabola. In the case of the primary mirror for the full instrument this was performed coring elliptical cylinder with major axis of 600 mm and minor axis of 480 mm and was offset from the M1_RF origin by 190 mm in the *x*-direction as in Figure 3.25.

Table 3.5: Quadratic coefficients for the primary mirror.

Parameter	Value
A	-2.77e-3 m^{-2}
B	-2.77e-3 m^{-2}
C	-7.15e-5 m^{-2}
D	0
E	0
F	0
G	0
H	0
I	-1.84205e-3 m^{-1}
J	-1e-6

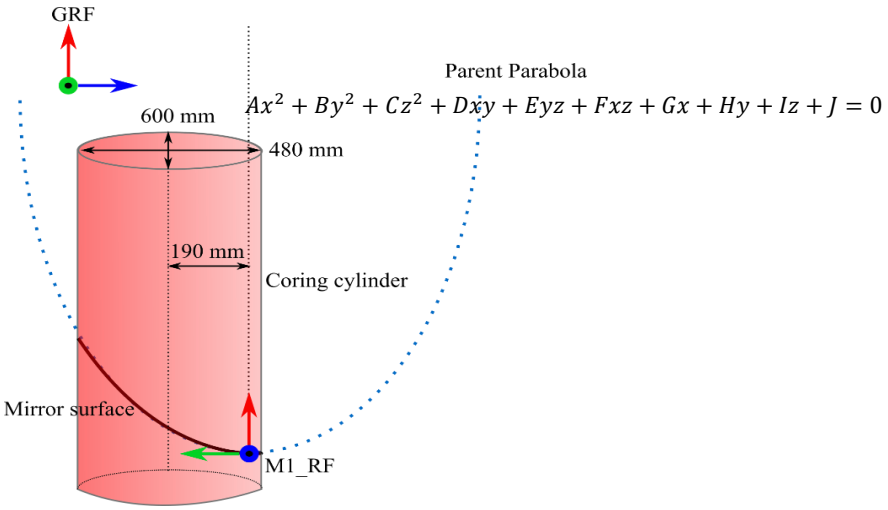

Figure 3.25: To model the primary mirror a section of the parent ellipse is selected by "coring" out a rim using a cylinder with certain dimensions. The green (*x*-axis), blue (*y*-axis) and red (*z*-axis) arrows are representative of the axes and location of M1_RF relative to the GRF (the GRF axes is only an indication of orientation not position). For detailed discussion see Scully (2015).

3.3.3.6 Cold stop

A cold stop is placed between the primary and secondary mirrors in the cryostat. This surface is coated in absorber material (along with other surfaces) and thus does not radiate and appears 'cold' to the bolometers, as well as limiting stray light striking the focal plane. The cold stop aperture is positioned and sized to allow for the maximum transmission of the beams while still limiting the stray light on the focal plane. This cold stop was redesigned from its original shape and this will be discussed in detail in Section 3.5.2.

3.3.3.7 Secondary Mirror

The secondary mirror (M2) is also defined by equation [31], with the coefficients in Table 3.6. The rim of the mirror is defined with a 600 mm diameter coring cylinder offset by 120 mm as in Figure 3.26.

Table 3.6: Quadratic coefficients for the secondary mirror.

Parameter	values
A	1 m^{-2}
B	1.12388 m^{-2}
C	1.1023 m^{-2}
D	0
E	0
F	0.103414 m^{-1}
G	0.25987 m^{-1}
H	0
I	-0.108468 m^{-1}
J	-0.136285

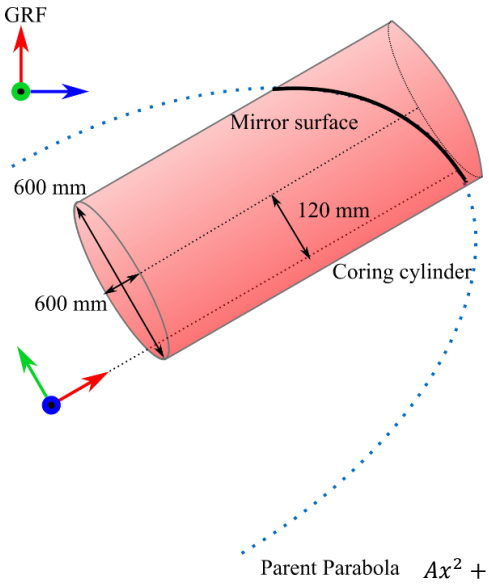

$$Ax^2 + By^2 + Cz^2 + Dxy + Eyz + Fxz + Gx + Hy + Iz + J = 0$$

Figure 3.26: Schematic showing the coring cylinder on the parent parabola for the secondary mirror. The green (*x*-axis), blue (*y*-axis) and red (*z*-axis) arrows are representative of the axes and location of M2_RF relative to the GRF (the GRF axes is only an indication of orientation not position). For detailed discussion see Scully (2015).

3.3.3.8 Dichroic and focal planes

For the instrument to operate in a dual band configuration, the two frequency bands need to be separated so that the instrument can observe both simultaneously. It is envisioned that a dichroic (design to be finalised but the current design can be seen in Figure 3.27) will be used to separate the two bands and propagate them onto two independent identical focal planes (both consist of TES bolometers as in Figure 3.16). This optical element and its design will be explored more in Chapter 6.

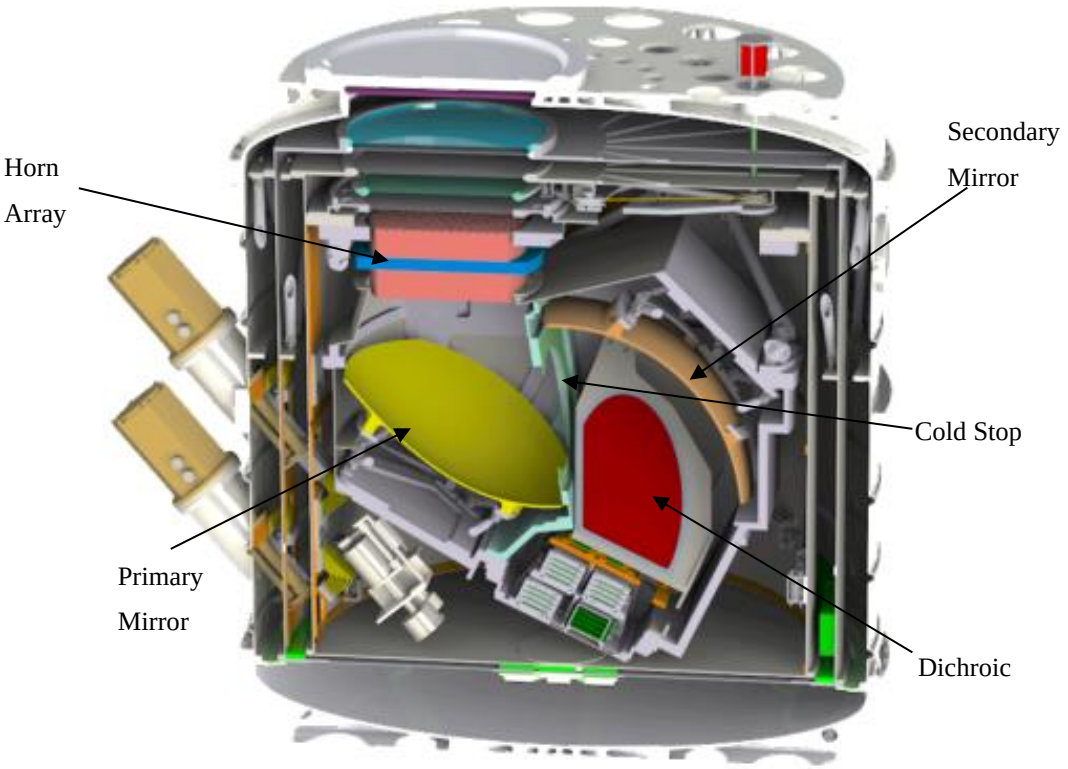

Figure 3.27: Sectional cut of the cryostat showing the subsystems of QUBIC with the dichroic highlighted in red. Image adapted from Hamilton *et al.* (2020).

3.3.4 PO modelling of the optical combiner

As mentioned in Chapter 2, MODAL can be run in batch mode on the computing cluster at Maynooth University such that the beam from each horn is propagated through the instrument independently. This allows for investigation of an individual beam profile or the generation of the full PSF (all horns) or any combination of baseline interference patterns using equation [35]. This was performed in MODAL by exciting the horn array with a 150 GHz plane wave to simulate the observation of a far-field point source with the following sequential propagation chain:

Sky (source)
↓
Horn
↓
Primary mirror
↓
Cold stop
↓
Secondary mirror
↓
Focal Plane

The aberrations introduced by the off-axis design of QUBIC are clearly apparent from the individual beam patterns on the focal plane (Figure 3.28). This shows that the beam profiles are asymmetric, unlike what is observed for an on-axis instrument. This is due to field curvature aberrations introduced by the short focal length and the off-axis design of the mirrors. It is also evident that different horn beams have different profiles. Looking at a simple GBM model of the optical combiner in MODAL as in Figure 3.29, it can be seen that different beams will strike different parts of the mirrors, meaning that the field curvature is not uniform across the horn array. This also means different horn beams will have slightly different focal lengths as they pass through the combiner. It is clear that these aberrations also cause asymmetry in the baseline interference pattern, clearly evident when compared to the idealised model (Figure 3.30). The combination of all the beams on the focal plane thus generate a PSF that has the asymmetry present in it, as in Figure 3.31. As mentioned these aberrations result in a sensitivity drop of the instrument by an acceptable 10 %.

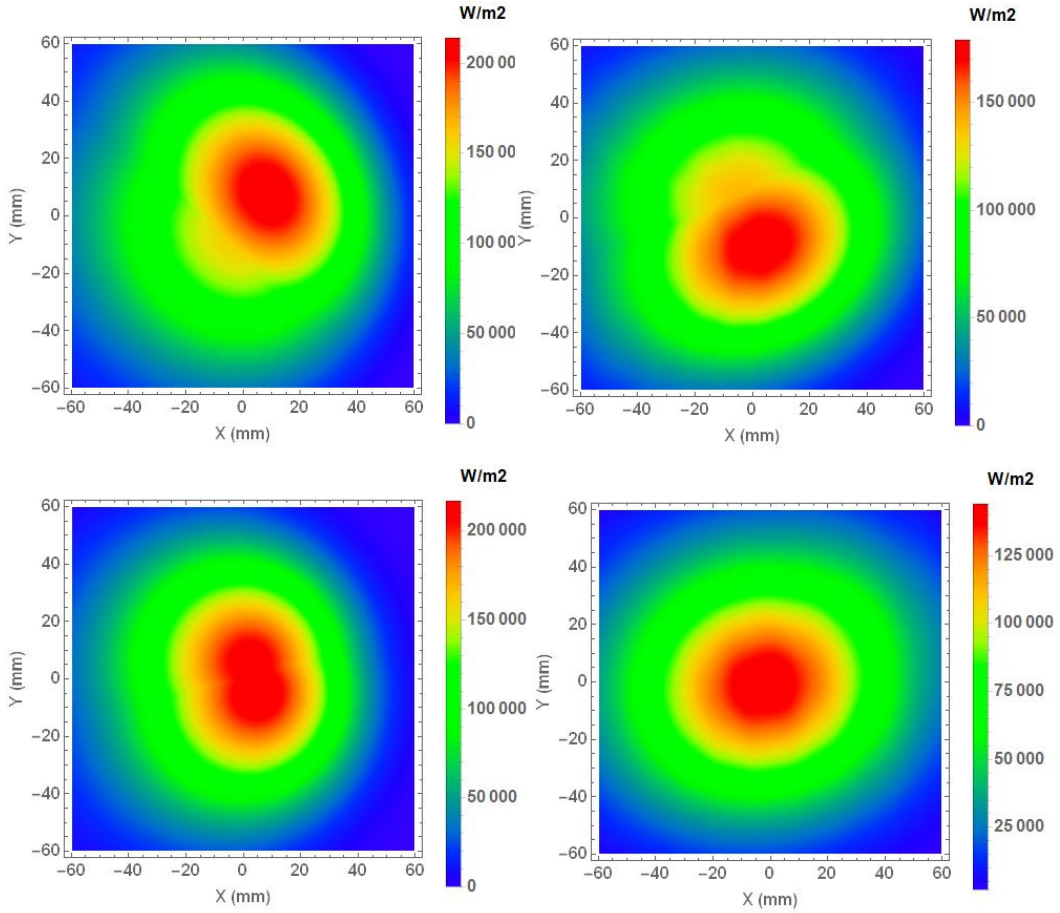

Figure 3.28: Focal plane beam patterns (in intensity) for horns *x*01*y*09 (top left), *x*08*y*22 (top right), *x*13*y*14 (bottom left) and *x*17*y*02 (bottom right).

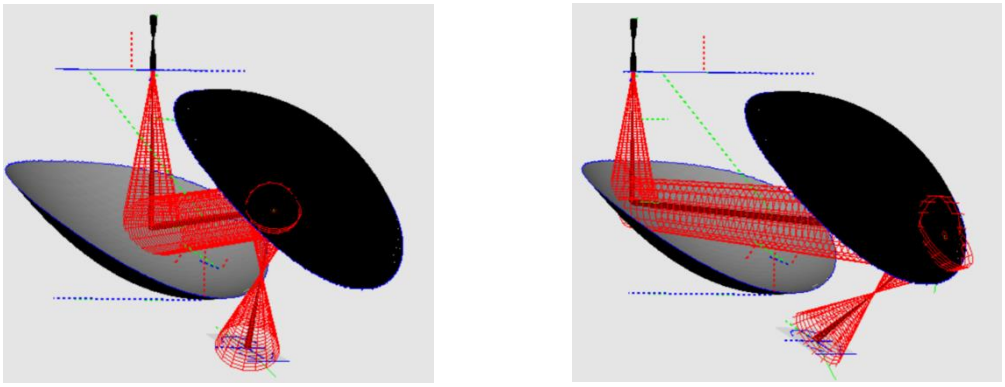

Figure 3.29: MODAL GBM model of beams from horn *x*01*y*09 (left) and *x*08*y*22 (right) passing through a simple optical combiner consisting of the horn, primary and secondary mirrors and the focal plane. The 1*w* radius of the beam is shown by the red mesh.

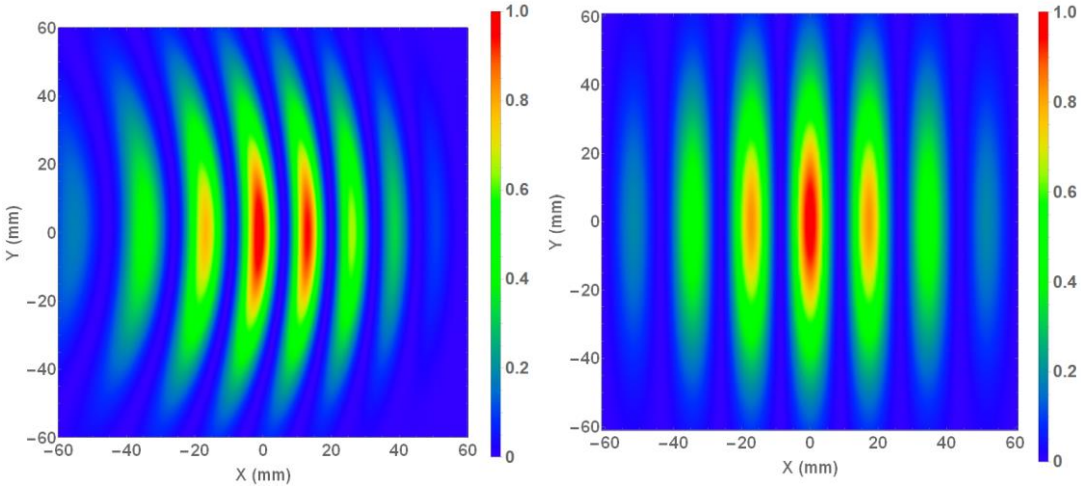

Figure 3.30: Interference pattern (normalised intensity) on the focal plane from the baseline with *x*08*y*10 and *x*10*y*08. Left shows the MODAL results (therefore including aberrations) and right shows the idealised model obtained with ABCD matrices (no aberrations).

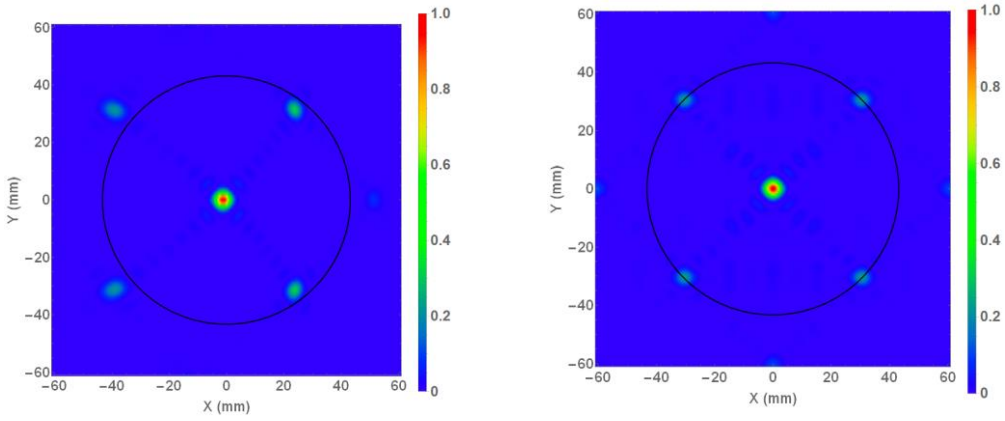

Figure 3.31: Left shows a PSF of the real QUBIC instrument, modelled in MODAL PO by exciting the horns with a 150 GHz plane wave. Right shows a PSF of the ideal instrument obtained with ABCD matrices. The black circle (radius of 43.2 mm which is equivalent to 8.2° on the focal plane) indicates where the peaks are expected for an ideal instrument.

3.3.4.1 Cross polarisation introduced by the combiner

As shown in Figure 2.17, the QUBIC horn has low cross-polarisation levels at the design frequency when compared with the co-polarisation (Figure 3.32). When modelled in MODAL, the total power of the cross polar beam can be simply obtained by summing up the intensity from each PO point in the captured field propagated from the horn. The ratio of this value to the total field (combined cross- and co-polar fields) power is 0.00059 (-32 dB) or 0.059%.

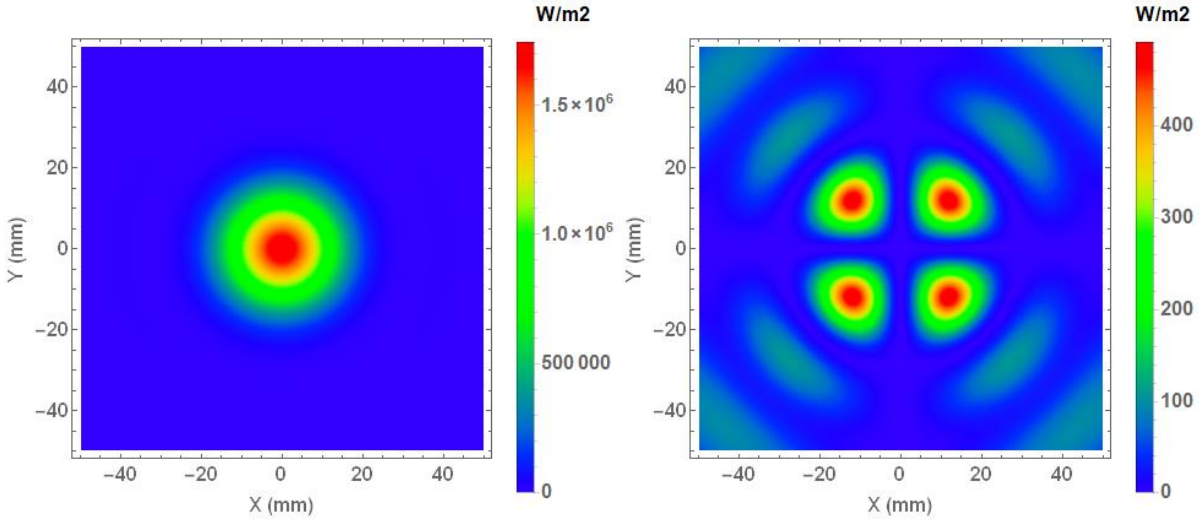

Figure 3.32: Co-polar beam (left) and cross-polar beam (right) on a 100×100 mm^2 screen 10 cm from the horn aperture in MODAL. The horn was excited with a 150 GHz on-axis plane wave.

Performing the same analysis on the beam pattern that is present on the focal plane for an arbitrary selection of horns (Table 3.7) shows that there is a difference in the cross polar component of the total electric field at the focal plane in comparison to the output directly after the horn. This is due to the offset design of the optical combiner. The asymmetry that is introduced into the beam from the combiner also causes an increase in the cross-polarisation levels of the beam. The increase is not uniform, with the levels of cross polarisation differing depending on where the beams strike the primary and secondary mirrors (as in Figure 3.29) with increases in the cross polar component from 0.5 % to 1.9% (which would also be the cross-polar component of the PSF). These levels are still low and it is important to remember that even though the cross-polarisation levels are essentially a measure of the purity of the beam, since QUBIC incorporates a HWP and polariser before the horn array, the radiation that reaches the horn array is already of the correct polarisation to extract the Q and U parameters. Also, since the TESs in the focal plane will couple to both polarisations any cross polarisation levels will not create systematic errors, they will simply affect the efficiency of the instrument (essentially the lower the cross polar power of the horn the better the coupling will be between the horn and the incident radiation with the polarisation matching that of the co-polar direction).

Table 3.7: Relative cross-polar component of the total (integrated) electric field at the focal plane from a selection of horns for the FI and for one horn that is in the TD horn array which will be discussed in more detail in the next section.

Horn ID	QUBIC model	Position	Cross polar component (ratio)
*x*13*y*22	FI only	Edge	0.0193 (-17.143 dB)
*x*14*y*01	FI only	Edge	0.0053 (-22.7946 dB)
*x*01*y*09	FI only	Edge	0.0186 (-17.3068 dB)
*x*13*y*12	FI and TD	Centre	0.0063 (-22.03 dB)

3.4 Technological Demonstrator

3.4.1 Justification for the TD

In 2015 it was decided that a TD instrument should be developed before the FI as a proof of technologies for QUBIC. Tests performed by the QUBIC pathfinding missions were promising, but these instruments were relatively small in comparison to QUBIC, with MBI only containing 4 feedhorns and without the complex mechanical systems of QUBIC. The idea of the TD is to have an instrument that utilises nearly all (there will be no dichroic in the TD) of the novel technologies of the QUBIC instrument described above. The TD is very similar in design to the FI so that when the tests have been finalised it is relatively easy to upgrade to the FI.

3.4.2 Differences with the FI

The TD was designed to be as similar as possible to the FI, and the same cryostat will be used for both instruments. This allows for a full test of the cryogenic systems, and allows for most of the mechanical housings to be present in the TD and thus the upgrade to the FI will be simplified. For modelling purposes this is also useful, as it means that the positions of the origins for the all of the element reference frames are the same, so it only required minor alterations to the existing FI model in MODAL.

There are three main mechanical differences between the TD and the full instrument: the horn array size, the size of the primary and secondary mirrors, and that there will only be a single quarter focal plane, meaning that the instrument will only operate over a single band (150 GHz) with no need for dichroic.

Horn array

The TD will have an array of 64 back-to-back feedhorns instead of the 400 in the FI, as seen in see Figure 3.20, while retaining the same horn design and inter-horn separation. The smaller number of baselines means that cosmologically significant results will likely not be obtained, however, there will be enough baselines to perform significant testing of the capabilities of bolometric interferometry and the novel self-calibration technique.

There will be a calibrator lamp placed on the side of the horn array that will be used for the intercalibration of the TESs on the focal plane of the instrument (it is predicted that the same source will be used for both the FI and the TD), and the differences in the array size will have an effect on the position of this source and on how it propagates through the optical combiner. This will be modelled and discussed further in Chapter 4 (for the TD) and in Chapter 6 (for the FI).

Focal Plane

As seen in Figure 3.16, each focal plane in the FI is made up of four individual quadrants, each consisting of 248 active bolometers. It is planned for the FI to have two focal planes, i.e. eight quadrants in total, while the TD has a single quadrant of a single focal plane (the bottom left quadrant of Figure 3.16). This is acceptable for the TD as it will only be operating at 150 GHz and there are enough bolometers for the testing required (both for the operation of the optical combiner and the novel techniques afforded by bolometric interferometry, i.e. the control of the systematic effects provided by self-calibration).

Mirrors

The mirrors for the full instrument were very large and had to be outsourced for manufacture. Since the TD had a smaller horn array and there was less radiation to capture, it was possible to reduce the size of the mirrors, so that they could be manufactured in-house by collaborators in Milan.

The description of the primary and secondary mirror surfaces (Table 3.5 and Table 3.6) are the same for the TD and the FI, the only change is the size and shape of the bounding rim.

3.5 Resizing optical components

Starting with the FI model, beam footprints (explained in detail in Scully (2015)) were used in resizing and redefining the smaller mirrors for the TD. To obtain the footprint of a beam on a surface, the beam file from MODAL was utilised along with equation [30] for the power contained within a radius r (note that this method is an idealisation, as it assumes a perfect Gaussian). The footprint then describes the size of the beam that contains a user-defined fraction of the total power. For example, the user can define the size of the footprint, r from equation [30], in terms of Gaussian width w. If this was set to $1w$ (capturing 86% of the power) then the footprint would appear as in Figure 3.33. Unlike the beam profile, which decreases in intensity (and thus changes the colour in the visualisation) as it moves from the centre, if any point is within $1w$ or any other user defined boundary of the centre of the beam, then it is plotted in the same colour. Multiple user defined boundaries can be set up, so that different power levels can be displayed.

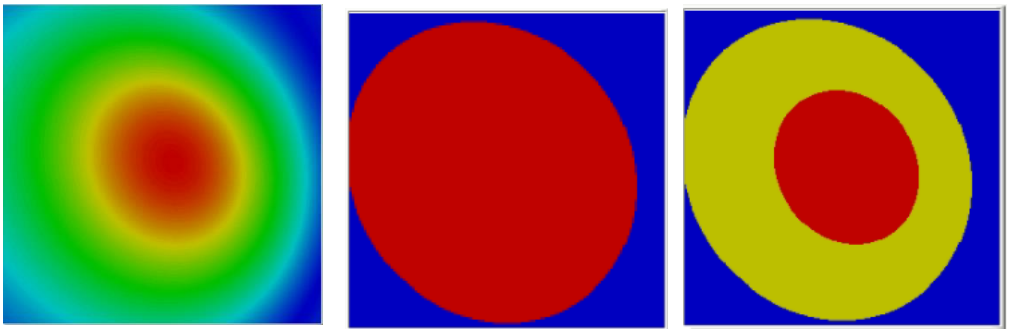

Figure 3.33: Left shows the horn x01y09 beam profile on focal plane of QUBIC. The middle shows the corresponding footprint to 1w – 86% of power. The right shows the footprint with 0.5w (red) – 39% of power – and 1w (yellow) of the beam on the focal plane of QUBIC.

When dealing with multiple beams, the footprint is simply the combination of the individual beam footprints. For example, take two beams on the focal plane as in Figure 3.34. The two individual footprints are obtained out to $1w$ and then the overall footprint is the result of combining these, such that if anywhere

on the focal plane is withing the $1w$ boundary of either beam, it is included in the total footprint. Any overlap between the beams does not affect the results, the area is still treated as being within $1w$.

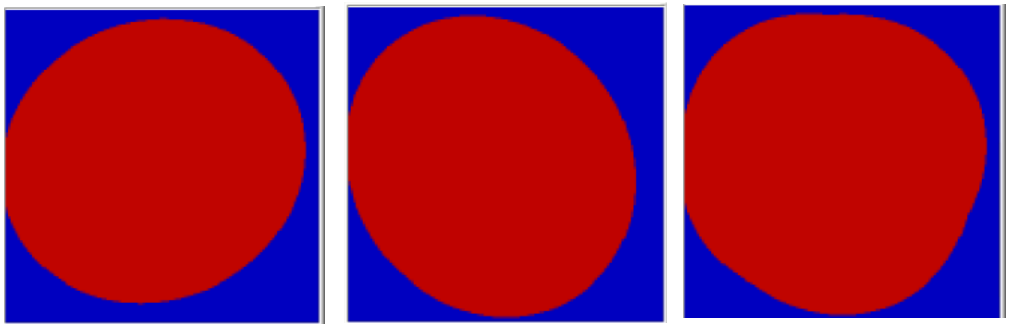

Figure 3.34: $1w$ footprinnts on the focal plane for horn $x01y09$ (left) and $x14y03$ (middle) are combined to provide an overall footprint (right).

This method not only allows for an approximation of the power incident onto the surfaces, but also the location in which the beams strike the surface. This provides information on the potential truncation of the beams by the optical elements, which is vital when the elements are being reduced in size.

3.5.1 Resizing the mirrors for the TD

When determining the new size for the mirrors, it was decided that it would be sufficient if the newly sized mirrors could capture at least 98.8% of the total power from each of the 64 TD feedhorns (equivalent to truncation at $r = 1.5w$ or greater). Figure 3.35 shows that if the rim was defined by a 400 mm coring cylinder then more than 98.8 % of the power of each beam is captured by both the primary and the secondary mirror. These mirrors are larger than the requirement, but they were still small enough to be constructed in house by collaborators in Milan (Figure 3.36).

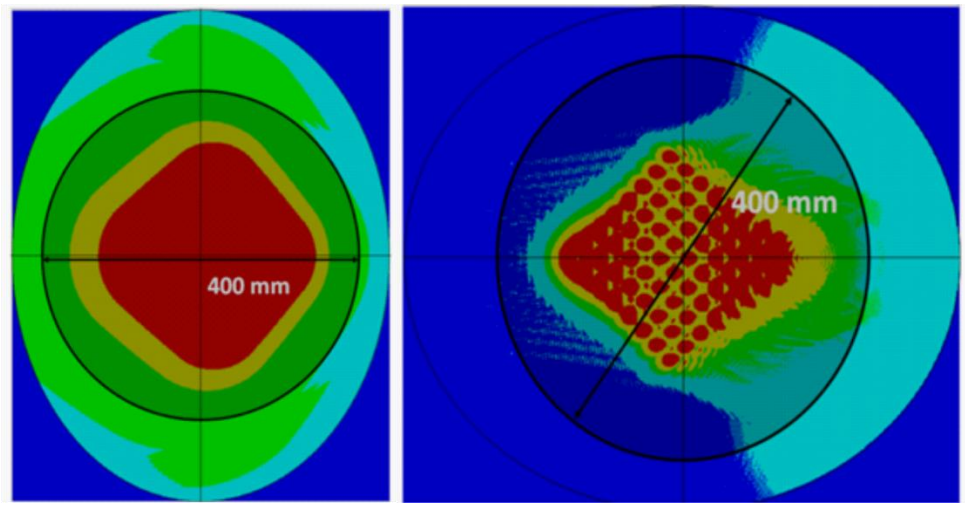

Figure 3.35: The 64-beam horn footprint on the primary mirror (left) and the secondary mirror (right). (Red = 86.4% power, yellow = 98.8 % power and green = 99.9 % power).

Figure 3.36: Manufactured primary (left) and secondary (right) mirrors for the TD instrument, made in-house by collaborators in Milan. Image provided by M. De Petris of the Sapienza University of Rome.

It can be seen in Figure 3.36 and in the CAD models of Figure 3.37 that the TD secondary mirror has a well-defined circular rim, but the TD primary mirror rim has an unusual elongated shape, one that could not be obtained with a simple coring cylinder as described for the FI. In reality making the mirror is not as straightforward as taking a cylinder and extracting the mirror surface from a perfect quadratic. In consultation with D. Gayer of Maynooth University (Gayer, 2020), it was decided that to model the real primary TD mirror more accurately in MODAL, it should be represented as a section of a mirror obtained with a coring shape rotated by 30° (as in Figure 3.38) on the same quadratic surface defined previously. The coring shape is a combination of three shapes which can be easily replicated in MODAL with its CSG functions (Figure 3.39). This is an example of why MODAL was chosen as the modelling software; the simplicity with which these complex shapes can be implemented is very useful and leads to accurate surface definitions. This change in the modelling generated a slightly longer primary mirror (Figure 3.40), while the secondary mirror was straightforward and could still be defined in terms of a simple 400 mm diameter coring cylinder as before.

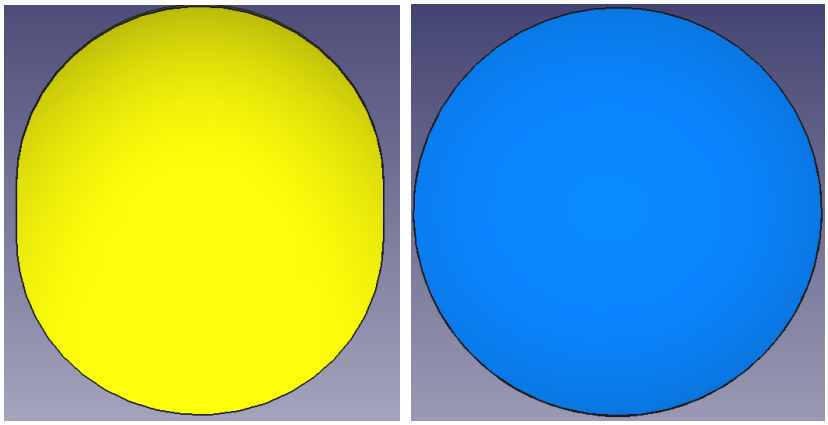

Figure 3.37: Top-down view of the CAD (FreeCAD) models for the primary (left) and secondary (right) TD mirrors.

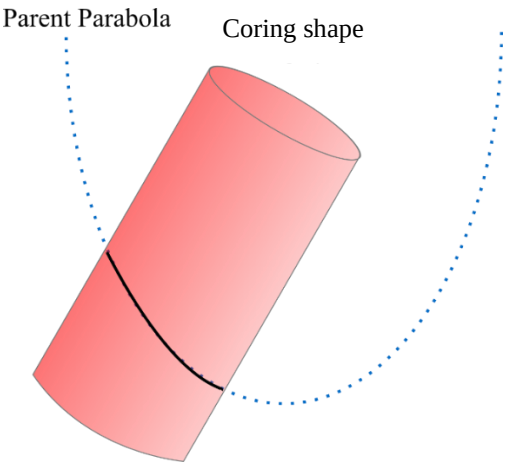

Figure 3.38: Coring cylinder at 30° to extract a mirror surface from a parent parabola.

.

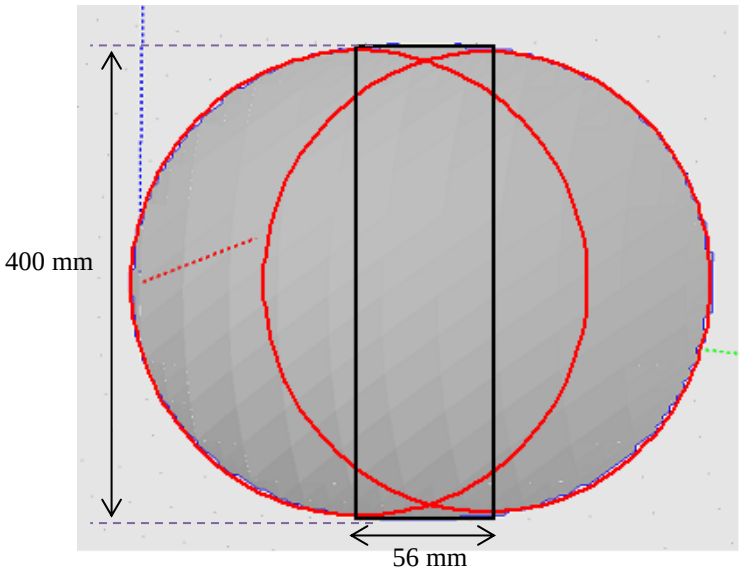

Figure 3.39: CSG union of three shapes in MODAL to obtain the accurate primary mirror rim for optical modelling.

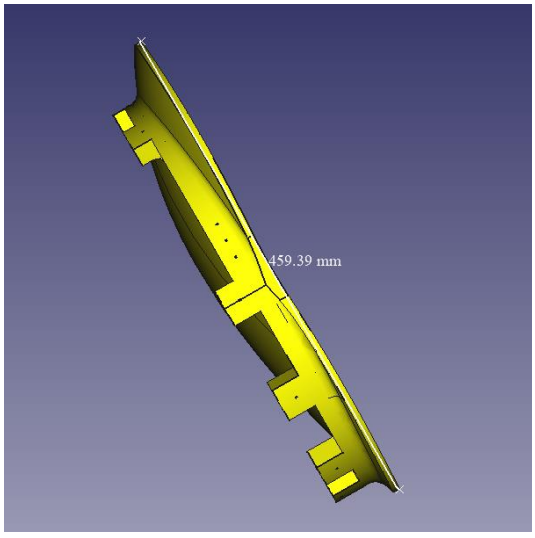

Figure 3.40: CAD model of the constructed primary mirror showing the full length of the mirror is 459.4 mm.

3.5.2 Resizing the cold stop for the TD and FI

There are multiple stages to the instrument testing and calibration, as detailed in the Technical Design Report (The QUBIC collaboration, 2016) during which the instrument will undergo cooling cycles before it gets down to the nominal operating temperatures. During calibration, a neutral density (ND) filter is placed in the cryostat, just behind the cold stop, to ensure that there is no saturation of the detectors. The original design of the cold stop aperture was a 300 mm×260 mm ellipse, however, the ND filter could only be manufactured as a disk of maximum diameter 200 mm (private communication, QUBIC collaboration), so the cold stop had to be resized. The footprint method was again used however, this time the FI was modelled (the 400 horns and the larger mirrors), since the cold stop is a part of the cryostat and will be the same in the TD and the FI. If it was acceptable for the FI then it would also work for the TD with its smaller horn array.

The ND filter was to be mounted onto the cold stop and thus it was decided to alter the cold stop size so that it was equal in area to the filter, maximising its size and ensuring as much power as possible could be transmitted. Figure 3.41 shows that the previous 1.5w requirement for the mirrors could not be achieved with the smaller cold stop. However shifting the cold stop by -27.6 mm in the x direction of its local reference frame allowed it to capture most of the required power. Since the size was restricted this was a compromise that was required.

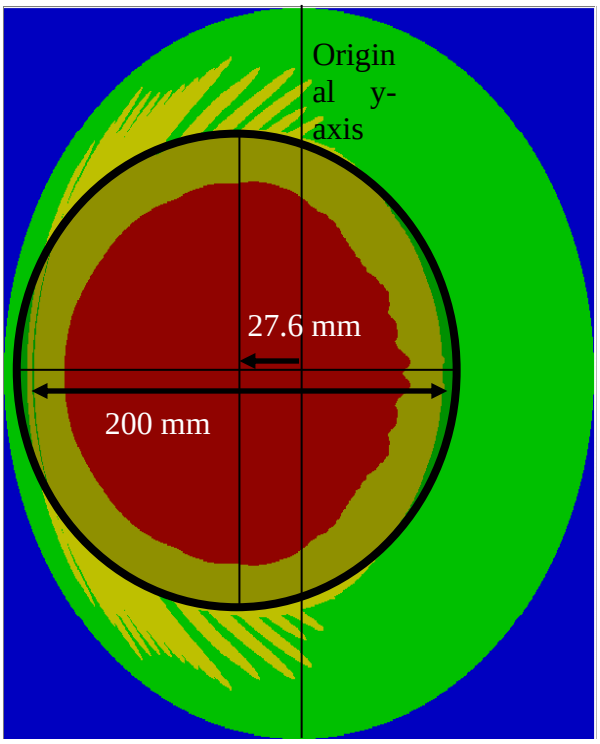

Figure 3.41: Footprint of all 400 beams from the FI on the cold stop with the original 300 mm×260 mm elliptical shape (red=1w, yellow=1.5w and green=2w). A shifted 200mm diameter disc allows the newly sized cryostat to capture nearly all the desired 1.5w footprint.

Since the maximum size of the new cold stop could not capture the required power, a further analysis was performed. An arbitrary selection of horns were chosen and their beams were propagated through the optical combiner and onto the focal plane where the total power was obtained and the beam patterns were analysed

to see if there was any noticeable diffraction resulting from truncation of the beams. This was performed at 130, 150 and 220 GHz. Figure 3.42 shows that there was no discernible diffraction observed in beam patterns on the focal plane due to the smaller cold stop for all the horns that were selected.

Table 3.8 shows that there was no loss of power due to the smaller cold stop when compared to the instrument without the cold stop in both operating bands. While the beam would be truncated by the cold stop, the focal plane does not capture the full transmitted beam and so the effects of this truncation are not seen.

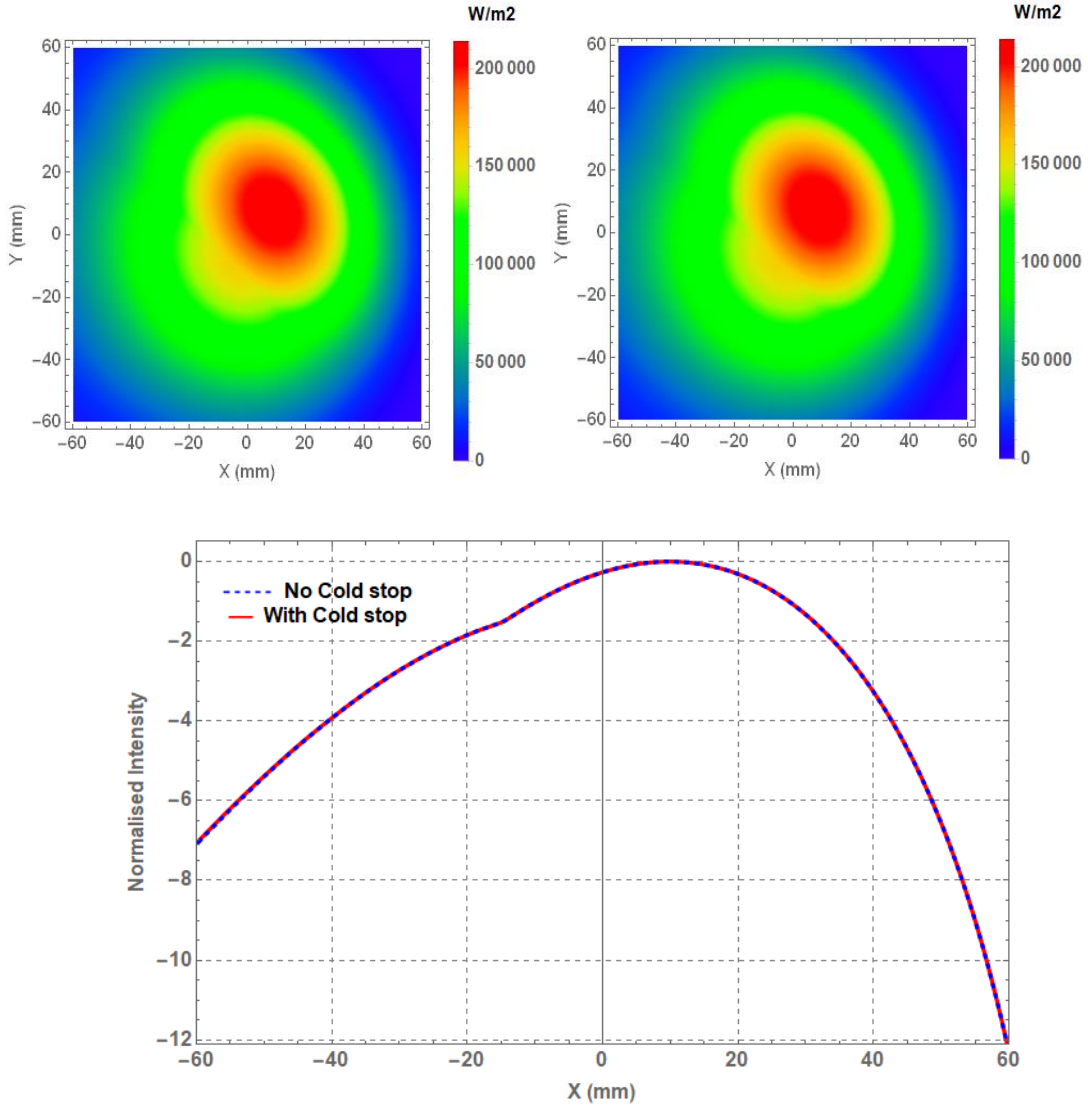

Figure 3.42: Beam patterns (intensity) of the horn *x*01*y*09 at 150 GHz without the cold stop (top-left) and for the newly resized cold stop (top-right) with the horizontal cuts (bottom) in dB, where both cuts are normalised to the same peak. Similar results were found for other horns tested.

Table 3.8: Power collected on the focal plane as a percentage of the total power emitted from the horn at frequencies of 130, 150 GHz and 220 GHz. 130 GHz has widest beam so would be the most affected by the smaller cold stop.

Horn	130 GHz		150 GHz		220 GHz	
	200 mm cold stop	No cold stop	200 mm cold stop	No cold stop	200 mm cold stop	No cold stop
x08y22	73.12 %	73.13 %	84.24 %	84.24 %	82.66 %	82.66 %
x13y14	79.92 %	79.92 %	88.96 %	88.96 %	88.11 %	88.11 %
x17y02	69.51 %	69.50 %	81.36 %	81.35 %	79.16 %	79.17 %
x17y18	76.74 %	76.74 %	86.58 %	86.58 %	85.31 %	85.31 %
x21y06	69.51 %	69.50 %	81.36 %	81.35 %	79.16 %	79.17 %
x01y09	74.53 %	74.53 %	84.95 %	84.95 %	83.41 %	83.41 %

The newly sized cold stop did not affect the focal plane beam patten or the power incident on the focal plane. However if the cold stop was to be reduced further in size there would be some loss in power, with noticeable effects occurring when a 150 mm diameter cold stop is utilised, seen clearly in the beam pattern on the focal plane (Figure 3.43).

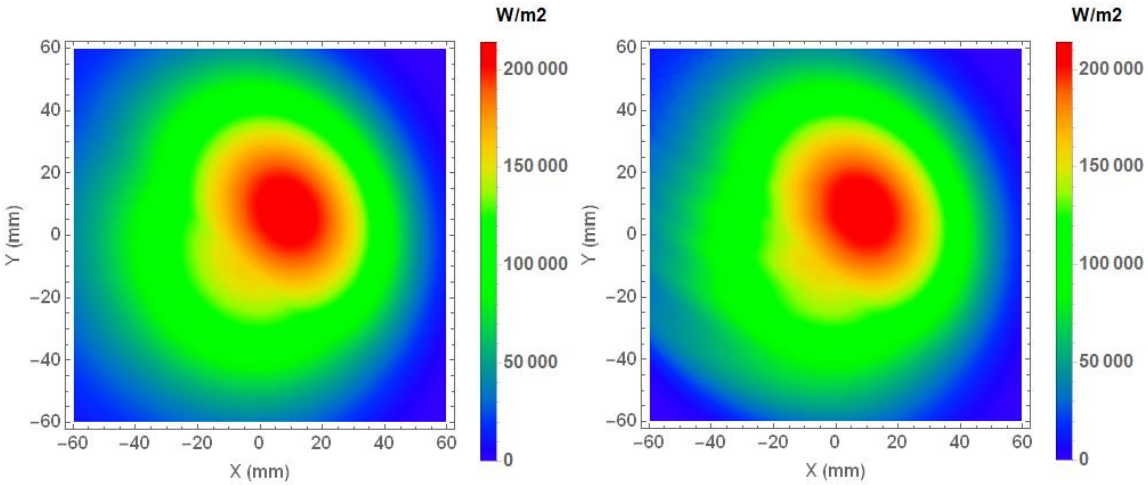

Figure 3.43: Beam patterns (intensity) of the x01y09 horn at 150 GHz for the 200 mm cold stop (left) and for a 150 mm diameter cold stop (right).

3.5.2.1 *Redefining the reference frame*

To ensure that this power could be transmitted through the new cold stop, its aperture was centred at a new offset position of -27.6 mm along the local x-axis. This was then chosen as the new origin for the cold stop reference frame (CS_RF). This new frame, as with all the other frames, had to be defined in terms of the GRF, hence this local translation had to be defined in the GRF and added onto the current CS_RF, by using the Euler rotations.

The individual $ZY'Z''$ rotations through angles (α, β, γ) respectively can be mathematically expressed as matrices as in equations [51], [52] and [53]. These matrices can then be combined by simple matrix multiplication $(Z'' \times Y' \times Z)$. Any point (x, y, z) in a coordinate system can then be transformed to another coordinate system by performing $(Z'' \times Y' \times Z)\times(x, y, z)$

$$Z = \begin{pmatrix} \cos(\alpha) & -\sin(\alpha) & 0 \\ \sin(\alpha) & \cos(\alpha) & 0 \\ 0 & 0 & 1 \end{pmatrix} \quad [51]$$

$$Y' = \begin{pmatrix} \cos(\beta) & 0 & \sin(\beta) \\ 0 & 1 & 0 \\ -\sin(\beta) & 0 & \cos(\beta) \end{pmatrix} \quad [52]$$

$$Z'' = \begin{pmatrix} \cos(\gamma) & -\sin(\gamma) & 0 \\ \sin(\gamma) & \cos(\gamma) & 0 \\ 0 & 0 & 1 \end{pmatrix}. \quad [53]$$

(α, β, γ) rotations for the CS_RF were already known (Table 3.3), hence the local translation can be obtained by performing the reverse operations and thus (-0.0276 m, 0 m, 0 m) in the local frame corresponds to (0 m, 0.00394 m, -0.02697 m) in the GRF which then, is added onto the CS_RF from Table 3.3, creating the new frame for the cold stop as in Table 3.9.

Table 3.9: Definition of the new reference frame for the resized cold stop

Frame	***dx* (m)**	***dy* (m)**	***dz* (m)**	***Alpha* (rad)**	***Beta* (rad)**	***Gamma* (rad)**
CS_RF_New	0	0.23504	-0.29261+ Δz	- π/2	-1.42768	0

3.6 Synthetic beam and PSF that result from optical modelling

3.6.1 Point Spread Function vs the synthetic beam for QUBIC

The PSF of the instrument has been shown previously in this chapter (Figure 3.31) and while it is important to analyse and can be used to investigate the effects of changes in the design of the optical combiner, the synthetic beam (response of a single pixel) is of most interest for the science. This synthetic beam is used to generate the image (equation [39]) and is what can be measured in the lab before intercalibration of the TESs, so for this reason it is important to be able to model this efficiently and understand it.

The synthetic beam and the PSF of QUBIC are two distinct yet similar properties. The PSF describes the response of the full focal plane to a single point source on the sky, while the synthetic beam describes the response of a single pixel on the focal plane to different positions across the sky. An ideal instrument would produce a PSF and synthetic beam that are identical (the combiner focal length can be used to relate linear distance on the focal plane to angular distance on the sky, $\theta = \tan^{-1}(d/f)$) for corresponding incident angles and TES positions (i.e. a 5° off axis PSF would resemble the synthetic beam for a TES that is 5° off-axis on the focal plane). However, it has been shown that the instrument is not ideal and the off-axis design of the combiner introduces asymmetry into the beams and thus the locations of the peaks in the PSF. This asymmetry is introduced into the PSF after the horn array, and is particularly pronounced because of the short focal length of the combiner. The synthetic beam will not suffer from this asymmetry in the peak location at the same level of beams from the horns are propagated to the sky as will be explained at the end of this section.

3.6.2 How to generate the synthetic beam of a TES bolometer in MODAL

Multiple methods of obtaining the synthetic beam (or an approximation to it) were tested, always conscious of the computational time required. The full back-to-back horn model was used in these simulations.

Method one: moving the source across the sky

This method used MODAL to directly model observations of point sources placed at an array of positions across the sky. In MODAL this was achieved by tilting an incoming plane wave source at an array of angles (i.e. imposing a phase slope). The angle of tilt is equivalent to the off-axis angle of a source on the sky. The response at a given angle for a TES was modelled by simulating the focal plane signal on that TES for a point source at a particular location on the sky. The full synthesised beam was built up by calculating the focal plane image for a point source at a grid of locations on the sky. Each point on the sky requires a full simulation. When modelling the full focal plane, all TES synthesised beams can be obtained by extracting the data from the relevant positions but it is very computationally intensive. As well as this, if there are alterations to the design of the optical combiner the full suite of computations must be repeated.

Method two: imposing a phase slope on the focal plane data

Using the standard model of QUBIC, a focal plane image was obtained for each horn for on-axis plane wave excitation. A phase slope was then added to it approximating the simulation had an off-axis source been used, as in method one. This method produces a similar suite of data sets to method one and the focal plane information for the TES in question could be obtained and a synthetic beam built up as in method one. This method is simpler and quicker than method one but it just an approximation as the phase slope is implemented on the focal plane data rather than on the incident beam which is propagated through the combiner and onto the focal plane. This method was used in the initial stages of QUBIC (and for early window function simulations).

Method three: back propagation from the focal plane to the sky

Instead of propagation from the sky to the focal plane, using reciprocity, a beam from a point source centred on a TES could be propagated from the focal plane to the sky. As mentioned in Chapter 2, point sources are not real but can be approximated with the illuminated aperture source in MODAL (if the aperture is very small). This source was placed onto the centre of a TES and then propagated through the instrument from the focal plane moving in the opposite direction to the propagation chain shown previously (without the cold stop aperture to save on computation time and since it has been shown that the beam patterns were not affected by including this). For this method an output plane was placed onto the sky and only one simulation needed to be performed for each TES. Figure 3.44 shows a synthetic beam produced by this method. To fully replicate the synthetic beam over the total TES area, several point sources could be placed over the TES area on the focal plane and their synthetic beam intensities summed. For this work a grid of nine points over the TES active area was chosen. This would simulate the integration over the TES area (this is shown for a selection of TES locations in Section 4.5.3). Figure 3.44 shows that the synthetic beam does indeed look more symmetric than the PSF. The longer propagation distance (here 12 m – in the far-field of the TD instrument rather than the 300 mm for the PSF) means that the phase aberrations tend to show up as small variations in the peak heights rather than in their positions. If the beam for every TES is not required then this method reduces the computation time compared with method one.

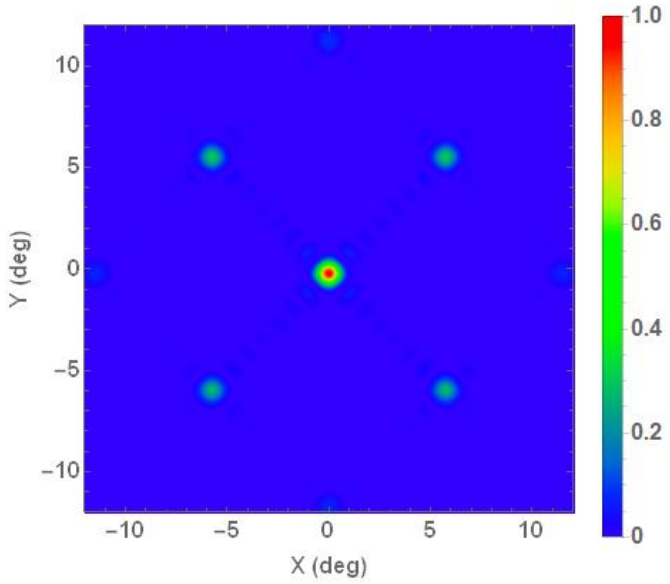

Figure 3.44: Synthetic beam (normalised intensity) on the sky (12 m in front of the origin of the GRF) when the horns are excited by a 150 GHz point source centred on the TES at (-2.5 mm, -2.5 mm) on the focal plane.

3.6.2.1 Comparisons between methods

Taking cuts along the diagonals of the synthetic beam (since the horn array is rotated by 45° wrt the GRF, this will provide cuts corresponding the *x* and *y* directions of the horn array) allows for easy comparison of the three methods (Figure 3.45). It can be seen that all methods give similar results. Initial QUBIC simulations used method two, now we typically require accurate simulation for particular TESs and so use method three.

Method one takes a long time to get a full sky image. Each position on the sky requires a full simulation making it too computationally expensive, thus it can be seen that the sampling on this method is a lot lower than with the others. Method two uses an assumption but does give results that match well with the other two methods. Method three is the easiest to set up and provides accurate results, with no further analysis of the data required after the simulation, which is very useful when the data is required by international collaborators. It easily allows specific TESs to be monitored and only one simulation is required to generate the synthetic beam for specific TESs. This method was chosen and is used predominantly throughout this thesis when generating synthetic beams.

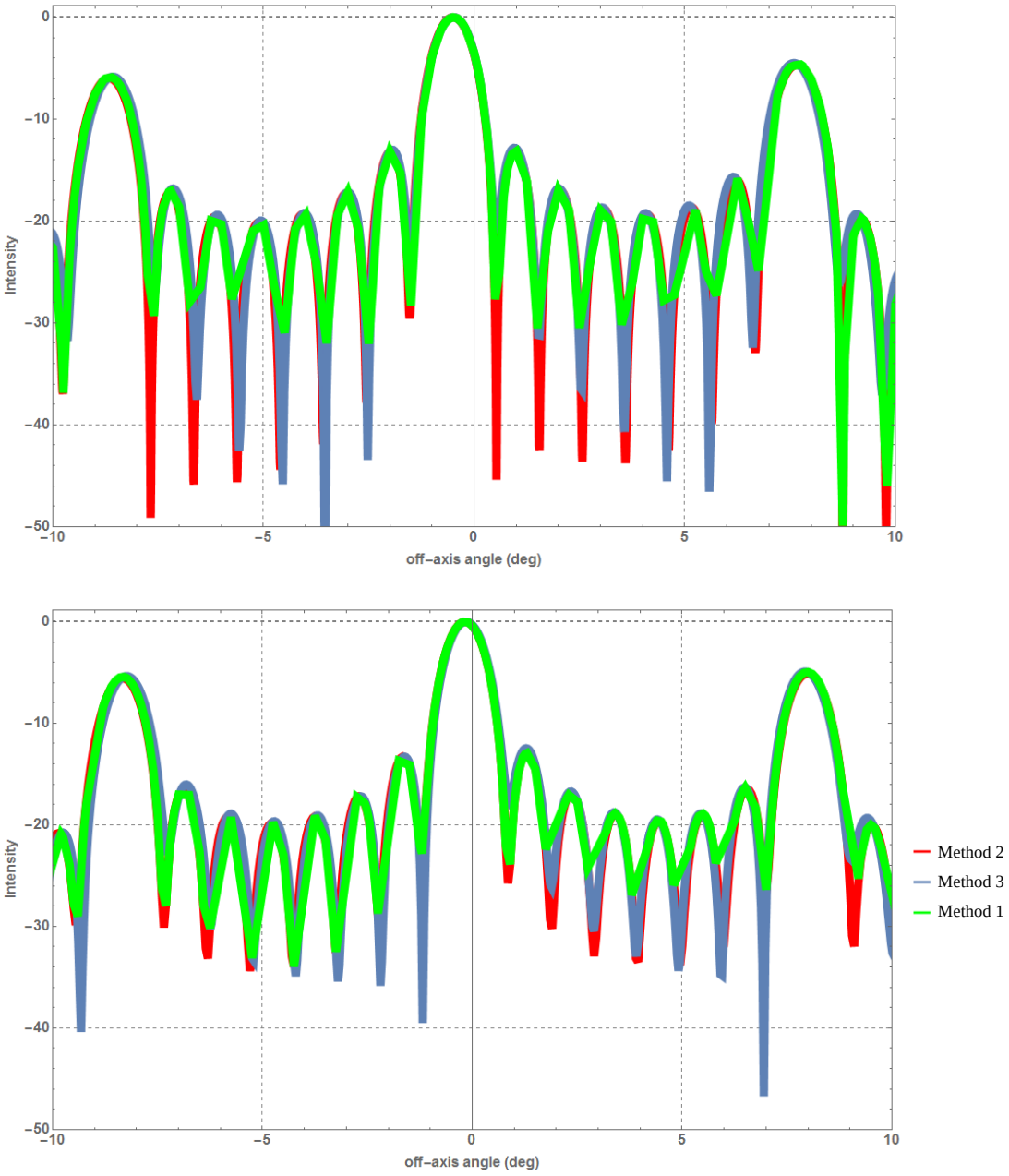

Figure 3.45: Cuts of a synthetic beam for a synthetic beam of the TES centred at (-2.5 mm, -2.5 mm) on ONAFP_RF for all three methods (normalised intensity in dB) in the *x* direction (top) and in the *y* direction (bottom).

3.7 Summary

In this chapter I introduced the QUBIC instrument which hopes to detect the very faint B-mode polarisation signal imprinted onto the CMB in the early universe. I discussed some of its precursors and the previous research that has been performed on the design of the instrument. To achieve the high levels of sensitivity required, the instrument will utilise the novel technique of bolometric interferometry which I have highlighted in this chapter. Some of the other integral sub-systems that will be used in QUBIC such as the cryogenics and readout electronics have been briefly detailed.

The main focus of this thesis is the optical combiner of the instrument and its operation; an overview of each optical element was given with a particular focus on elements that were important in this research. I

showed how the real instrument was modelled in MODAL. The window function which was used as a figure of merit for the instrument performance was described.

During this research it was decided by the collaboration to provide a proof of technologies known as the Technological Demonstrator. The differences between this instrument and the full QUBIC instrument were provided as well as the modelling that went into resizing the mirrors and the cold stop (whose new smaller size will be used in the FI as well).

Finally I have modelled and detailed the differences between the PSF of the instrument and the synthetic beam of TES pixels on the focal plane of the instrument which have both been used throughout this research to validate the design or in the testing phases of the instrument. I have described three methods used to simulate the synthetic beam and shown how their results are in excellent agreement.

The next chapter will focus on more rigorous modelling performed for the TD instrument.

4 Optical modelling of the Technological Demonstrator

4.1 Introduction

Calibration and testing of the QUBIC TD instrument began in 2018 in APC, Paris. In this chapter I will describe the detailed modelling of the test set up. As assembly of the instrument progressed, different parameters, such as the tolerance on the mirror positions had to be defined. MODAL models were used to both optimise the TD optical combiner configuration and to generate a baseline to which the real measurements could be compared. This chapter will present the results obtained from this modelling.

The following procedures and measurements were carried out during the calibration and testing in APC:

- optical components were aligned before measurements began
- two internal calibrator sources were used to help intercalibration of the TESs in the focal plane
- the PSF (and possibly fringe patterns) will be measured by observing a far-field calibrator source in the centre of the instruments FOV
- the synthetic beam of each TES was measured by scanning the far-field calibrator source across the FOV.

The simulations in this chapter contribute to all four of these as follows:

Window functions calculated from PO simulations were used to determine the accuracy to which the combiner mirrors had to be located (Section 4.2)

Simulations of the internal calibrator beams on the focal plane (Section 4.3) were provided as a benchmark to which the TESs can be calibrated. This calibration will done using the TES IV curves initially and then can be verified using these measurements (for a detailed description of this see Piat *et al.* (2020)).

Once the intercalibration is complete then the PSF can be measured using an external far-field calibrator source. Optical simulations of the calibrator beam (Section 4.4) were used to find the most suitable position for it in the laboratory. The PSFs were also simulated for later comparison with the measurements.

The synthetic beam for each of the TESs does not depend on the relative calibration between them and so this was the first set of measurements ready for analysis. Optical simulations (Section 4.5) were carried out for comparison and were extended to include the full frequency band and finite TES size. Some early measurements are shown.

4.2 Tolerance on the mirror position

Before any laboratory measurements could be carried out, the mirrors had to be aligned and I worked on finding a tolerance on the alignment of the mirrors. Donnacha Gayer of Maynooth University (Gayer, 2020) looked at the CAD files for the QUBIC mirrors and their mounts and determined a position and axis at the back of each mirror about which rotation misalignments were most likely to occur (Figure 4.1). Reference frames centred on these positions were defined using the same Euler rotation definitions as before (Table 4.1). A tolerance analysis of translations and rotations was carried out using these frames in MODAL. The window function was used as the merit function to test the tolerance of the mirrors to positional and orientation misalignments.

Table 4.1: Rotation axis and origin for rotation of the primary (M1) and secondary (M2) mirror relative to the GRF. Note that these positions are on the mirror surfaces.

Mirror	Reference frame name	dx (mm)	dy (mm)	dz (mm)	α (rad)	β (rad)	γ (rad)
M1	M1_Tol_RF	0	-20.6665	-392.947 +Δz	-π/2	5 π/6	π
M2	M2_Tol_RF	0	505.1470	-160.4282 +Δz	-π/2	2.3561916	π

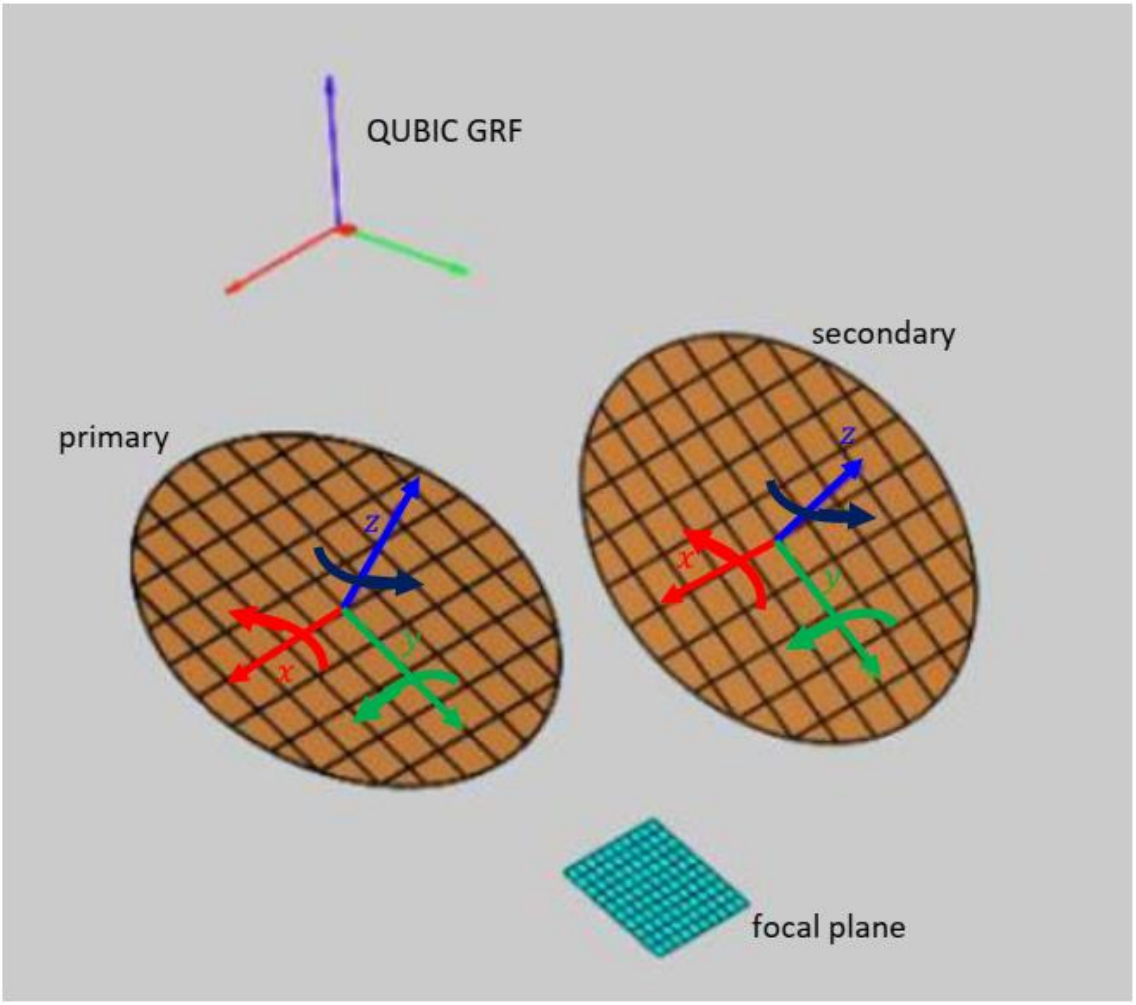

Figure 4.1: Planes defined with respect to the mounts of the primary and secondary mirrors (Image provided by D. Gayer of Maynooth University (Gayer, 2020)).

Software provided by J.C Hamilton of APC was used to obtain a synthetic beam for each set of MODAL data. This software takes the beam patterns that are incident on the focal plane from an observation of an on-axis point source and uses method 2 from Section 3.6.2 to generate the synthetic image of the sky that would be observed over the whole sky (this analysis was performed before the simulations with a source on the focal plane generating a synthetic beam (method 3) were available and tested. The work in Section 3.6.2 shows the success of this method). This image is then decomposed into spherical harmonics and the window function is calculated. This allows for a quantitative analysis of the instrument configuration.

The window function for the nominal instrument was used as a baseline, this is simply obtained from the simulation of the instrument with all the elements in their nominal positions (from Table 3.3). Minor adjustments were them made to the mirror positions by translation along their local axes or rotation about the pivot points (shown in Figure 4.1) and the new window function calculated. Note that the tolerance on each mirror was analysed independently (i.e. when the primary mirror was being analysed the secondary mirror was in its nominal position and vice versa).

4.2.1 Orientation and position analysis

Each mirror was rotated by ± 0.1º and ± 0.5º about its local reference frame axes and for each rotation a window function was generated (Figure 4.2 and Figure 4.3). It can be clearly seen in the plot of the relative window functions that the rotations about the *x*- and *y*-axes do cause non-negligible differences in the response of the instrument for both mirrors. The elements are nearly perfectly symmetric about the *z*-axis so the differences for rotations about the *z*-axis are very small as expected (though it is a good check). The secondary mirror is more sensitive to the rotations, which makes sense as this directs the radiation onto the focal plane itself.

At ± 0.1º the difference is minimal for both mirrors, though more prominent in the case of the secondary mirror. When rotated by ± 0.5º the difference becomes quite noticeable for some multipoles (reaching a 20% difference for the secondary mirror *x*-axis rotation). The tolerance on the error of the orientation was set at ± 0.1º, which was thought to be achievable as well as providing acceptable deviations from the ideal window function.

A similar analysis was performed for the translational errors of the mirrors and it was found that the deviations here were minimal for the translations of 1 mm tested (Figure 4.4 and Figure 4.5). ± 1 mm was determined to be an achievable tolerance on the mirror locations.

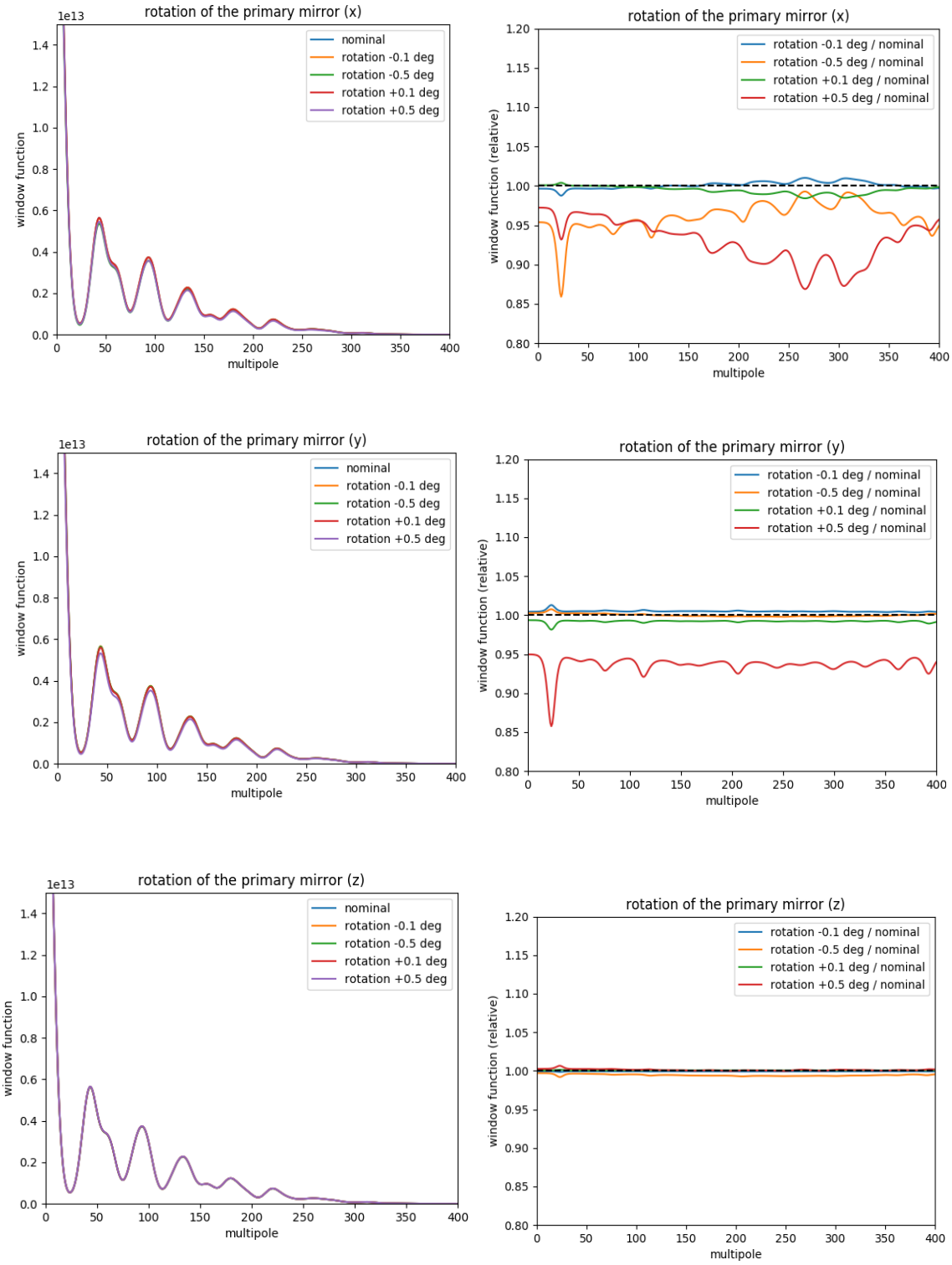

Figure 4.2: Window functions of different primary mirror rotations (left) and relative to the optimal position window functions (right). Note that the units are arbitrary.

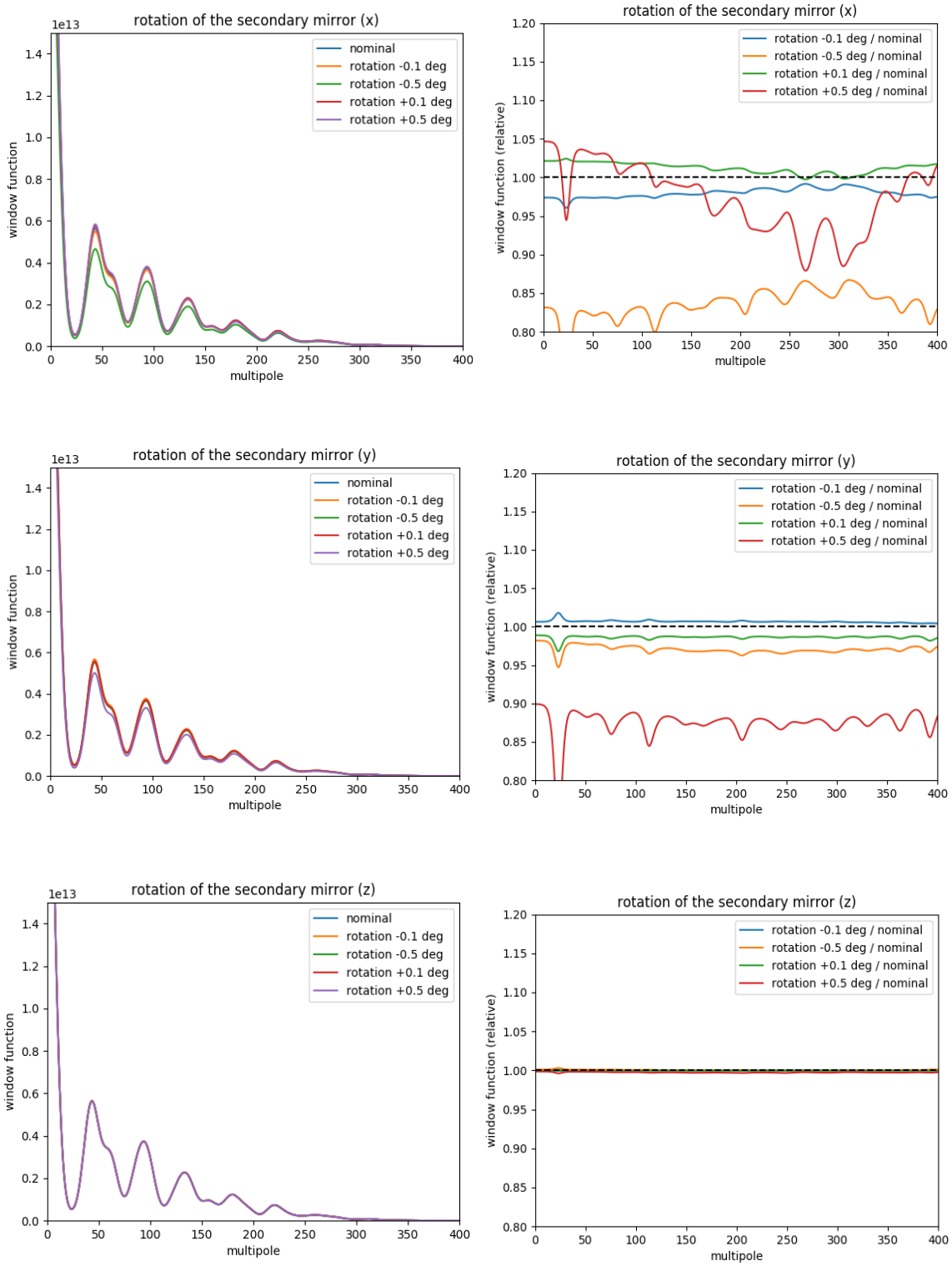

Figure 4.3: Window functions of different secondary mirror rotations (left) and relative to the optimal position window functions (right). Note that the units are arbitrary.

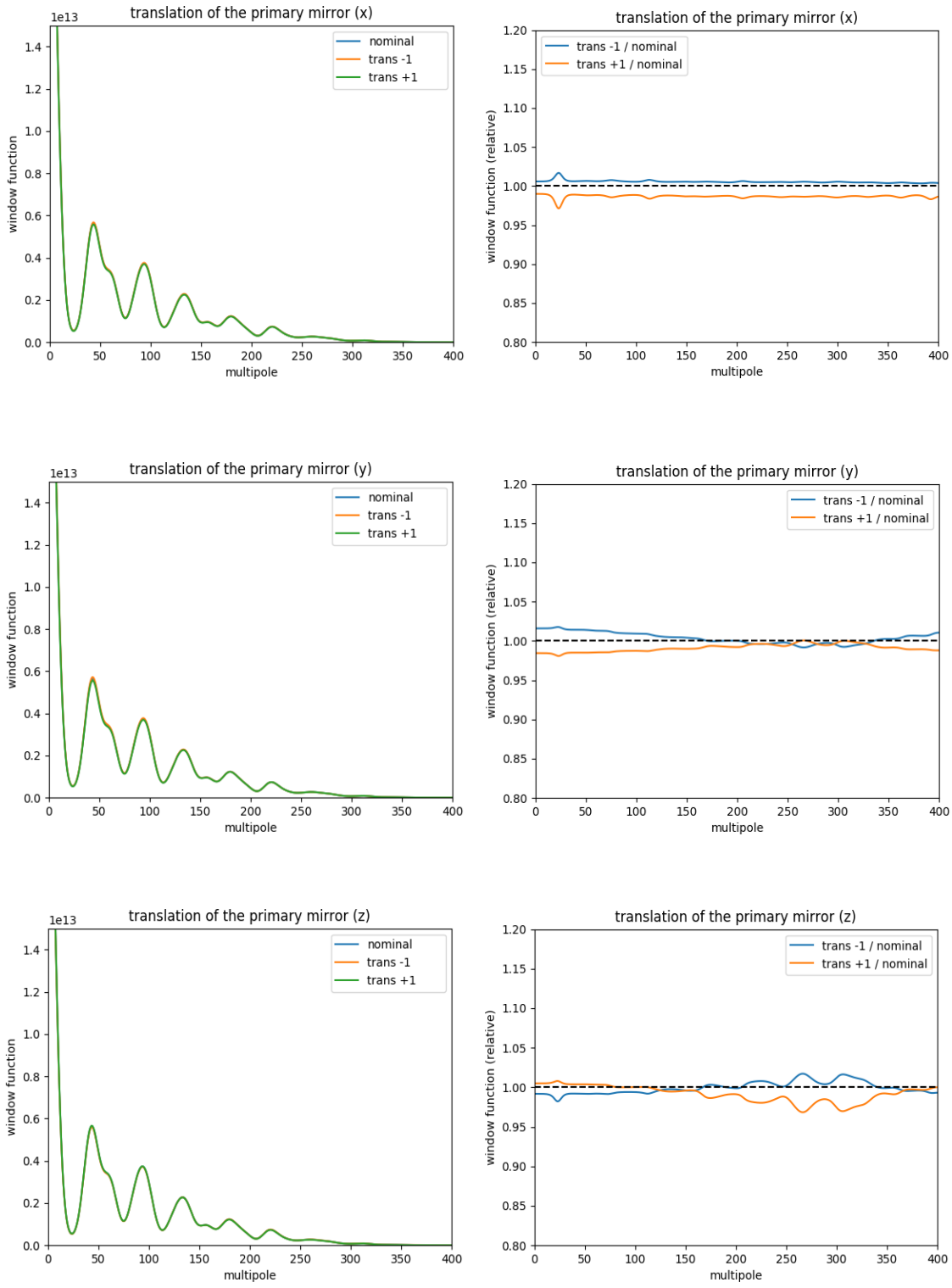

Figure 4.4: Window functions of different primary mirror translations (left) and relative to the optimal position window functions (right). Note that the units are arbitrary.

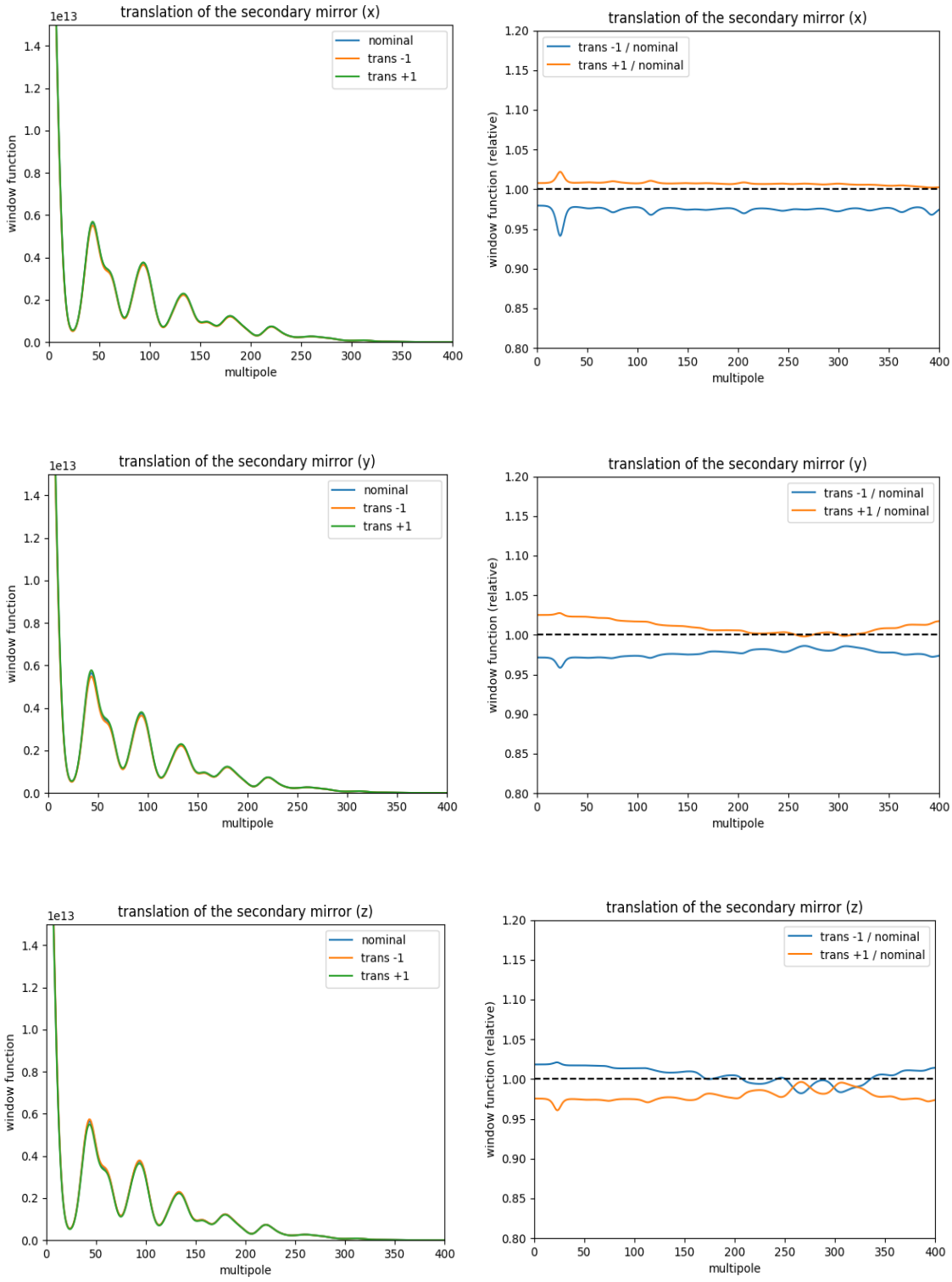

Figure 4.5: Window functions of different secondary mirror translations (left) and relative to the optimal position window functions (right). Note that the units are arbitrary.

4.3 Internal calibrator lamps in the cryostat

A calibrator lamp will be placed inside the cryostat at the side of the horn array and will be used for the intercalibration of the TES detectors. This lamp will consist of a carbon fibre source which will be used to excite a Winston cone (this was a left over from the Planck instrument and suited the needs of QUBIC). The radiation from this set up roughly resembles a 50° Gaussian beam (QUBIC collaboration, private communication). There are two Winston cones that will be placed on the horn array (Figure 4.6) at positions in the local reference frame given in Table 4.2. The aim of these sources is to aid in the inter calibration of the TES detectors by providing uniform illumination of the focal plane, if possible.

These horns were implemented into the MODAL model to investigate the beam pattern they produce on the focal plane. This setup was also modelled in GRASP by M. De Petris of the Sapienza University of Rome and is a good example of a validity test of MODAL.

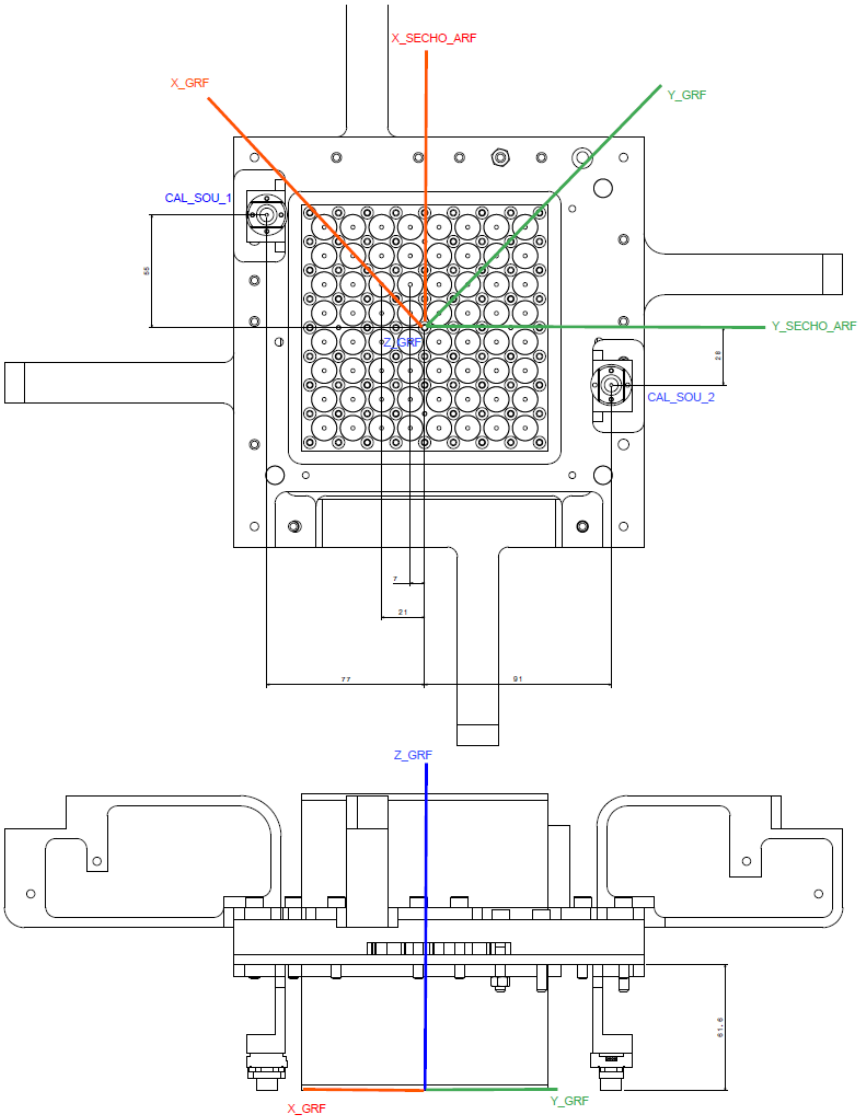

Figure 4.6: Winston cone calibrator sources on TD feed horn array. Image provided by M. De Petris of the Sapienza University of Rome.

Table 4.2: Positions of the Winston Cones in the horn array reference frames (SECHO_ARF in Table 3.3).

Calibrator	X (mm)	Y (mm)	Z (mm)
CAL_SOU_1	55	-77	0
CAL_SOU_2	-28	91	0

The illumination from the Winston cone sources when modelled by GRASP and MODAL at 150 GHz and only utilising the mirrors and the cold stop can be seen in Figure 4.7 and Figure 4.8. The differences in the structure of the patterns predicted by the two software packages is expected and is due to the differences between the definitions of the mirrors. The mirrors are defined in MODAL as described in Section 3.3.3. GRASP cannot define the primary mirror as the combination of shapes like MODAL, so they are simply defined with an ideal 400 mm diameter bounding rim (Figure 3.25). It is clear from these plots how important the correct definition of the elements is. Both models, however, contain comparable patterns and have the same intensity range. When modelled for the full instrument with identical mirror definitions in both software packages (see Figure 2.2 and this will be discussed further in Section 6.2) the focal plane patterns have the same structure.

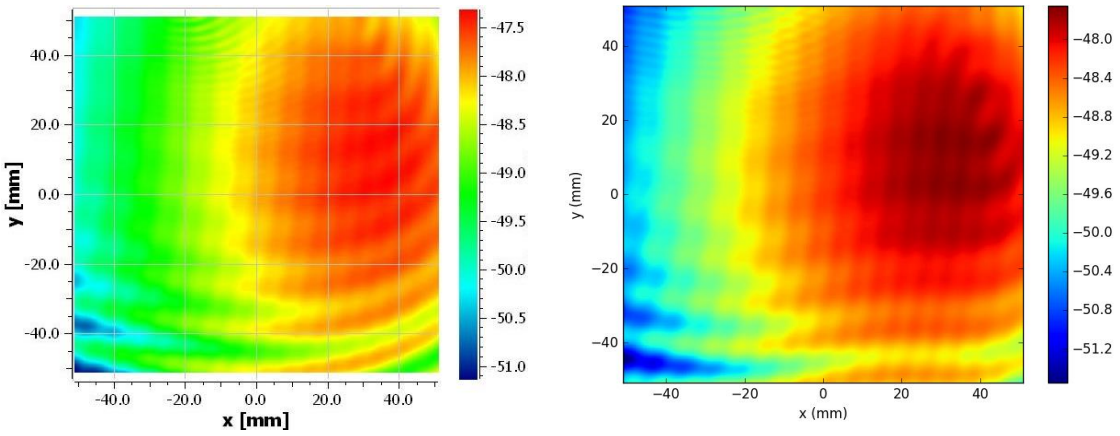

Figure 4.7: Cal_SOU_1 focal plane illumination from GRASP (left) and MODAL (right) normalised to the peak of the input radiation of the Winston cone. GRASP uses the ideal mirror rims while MODAL includes the real rims.

The focal plane illumination is not uniform and at very low levels. This is due to the fact that the optics are designed for a narrow beam but the beams from the Winston cone are so large in comparison to the optical elements and they suffer from substantial truncation as they pass through the combiner. This non-uniformity initially appears to be not ideal (having uniform illumination would mean all the TESs had the same incident power and would be a useful test of the intercalibration), however having a known structure on the focal plane – which will require accurate modelling that includes the full measured model of the mirrors (to be performed by J. Murphy (Murphy, 2021)) – could be used to provide a good test of the intercalibration of by other means (TES IV curves – see e.g. Piat *et al.*, 2020).

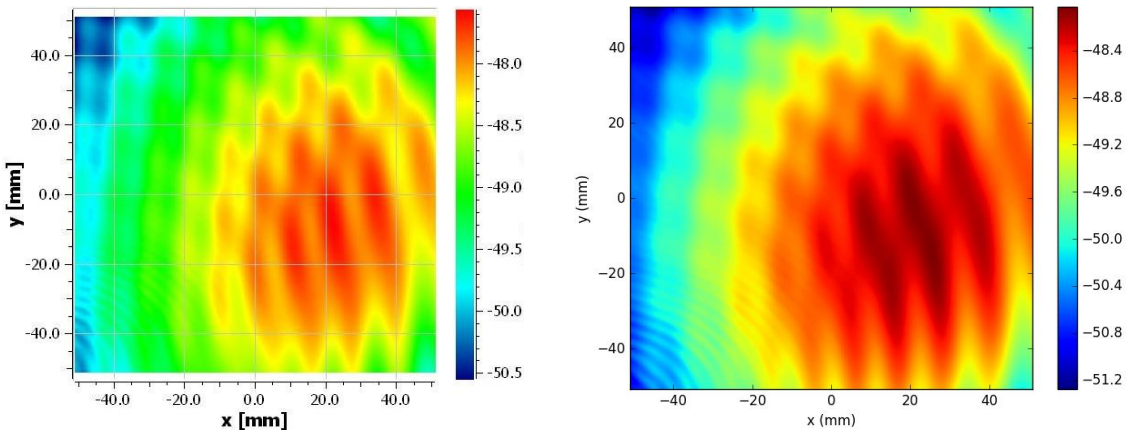

Figure 4.8: Cal_SOU_2 focal plane illumination from GRASP (left) and MODAL (right) normalised to the peak of the input radiation of the Winston cone. GRASP uses the ideal mirror rims while MODAL includes the real rims

4.4 Calibrator source

The optical performance of the instrument was measured in the lab by observing a well-defined Gaussian beam which was generated with an active calibrator source, capable of radiating a few mW of power (The QUBIC collaboration, 2016), coupled to an ultra-Gaussian (99.88%) corrugated horn developed by Thomas Keating ltd (Thomas Keating ltd., 2019). When excited, the horn then emits a 10º FWHM Gaussian beam (Figure 4.9).

While it is possible to use exact horn geometries in MODAL, the profile of this particular horn was not known by the collaboration (hence the beam profile from the horn shown in Figure 4.9 could not be calculated), but since it is a highly Gaussian beam it was decided to model it in MODAL by using the Gaussian-like source element described in Section 2.2.2. Using equation [20], a 10º FWHM Gaussian beam has a waist of 4.29 mm when operating at 150 GHz.

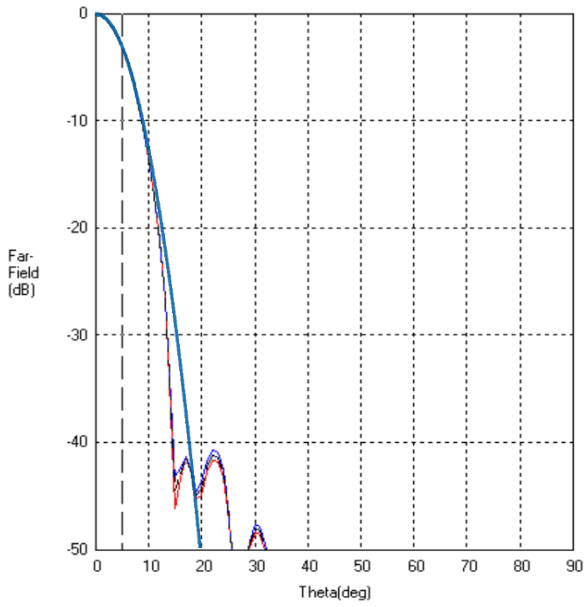

Figure 4.9: Far field pattern of the calibrator horn at 150 GHz (provided by Thomas Keating ltd.). The blue line shows an ideal Gaussian beam of 10°, showing very close agreement down to -20 dB. The horn beam also has very low sidelobe levels (occurring at levels less than -40 dB).

4.4.1 Distance from the instrument

For accurate analysis of the instrument it is important to place the observed source in the far-field. In MODAL a plane wave simulates the observation of a far-field point source, in that both the amplitude and phase are flat when incident on the QUBIC instrument. This ensures that each feedhorn couples with identical radiation.

As the radiation from a real source propagates through space it will expand spherically resulting in areas of locally constant amplitude and flat phase. A source that is on-axis and in the far-field of an instrument will produce electromagnetic radiation with these characteristics at the instrument aperture, similar to that of a point-like source. If it is not in the far-field, the radiation will be non-uniform.

The aim of the work in this section is to see if we can find a position in the lab where the calibrator source can be positioned so that it is in the far-field of the QUBIC instrument. Observation of its radiation then mimics the observation of a point-like source allowing for the generation of the PSF of the instrument (detailed in Section 3.6) on the focal plane.

From now on in this section the interference pattern on the focal plane from the combination of the radiation from all 64 horns in the TD instrument will be called the PSF regardless whether the source is in the far-field or not. A model of the 150 GHz source was positioned at an on-axis distance of 1 m, 5 m and 10 m from the TD aperture. We were initially told that a source distance of 5 m could be achieved within the lab, with 10 m a possibility; 1 m was investigated as an example of a near-field source. For each position to following was determined:

- the incident radiation over the horn array
- the horn output (at a distance of 60 cm) for two arbitrarily chosen horns: x08y08 and x11y11
- the resulting PSF on the focal plane formed from the radiation for all 64 horns in the TD array.

Incident radiation over the horn array

Both the amplitude and phase of the incident field from the on-axis calibrator source were investigated at the input of the horn array. It can be seen clearly in Figure 4.10 that the farther away the beam is from QUBIC the more uniform the amplitude is, and the flatter the phase becomes, as expected.

Horn output

Investigating the output of different horns in the array will provide another insight into the coupling to the incident source radiation. For this analysis, a screen was placed 60 cm from the horn (far enough to capture the far-field pattern while also being close enough that a large capture screen was not required, thus minimising the number of PO points required). Incident radiation couples with the horn and excites it, causing it to emit a beam (approximately a 12.9º Gaussian beam in the far-field in this case). For an on-axis source in the far-field of the instrument, the radiation over the array would be uniform and the coupling should be the same for all of the horns, meaning that all the horns will emit a Gaussian like beam of the same amplitude and the same phase (this is different for-off axis sources which will be dealt with in Section 4.5.1). If the incident radiation is not uniform over the array, as is the case for the source at 1 m, then it will not couple to the horns in the same way and the horn output will be different as seen in Figure 4.11. When the source moved farther away the coupling across the array became more uniform as expected. All of the

horn beams have the same profile, the difference in coupling can be seen as the difference in the peak intensity, it can be clearly seen that at 10 m away the beams from the two sample horns are very nearly the same.

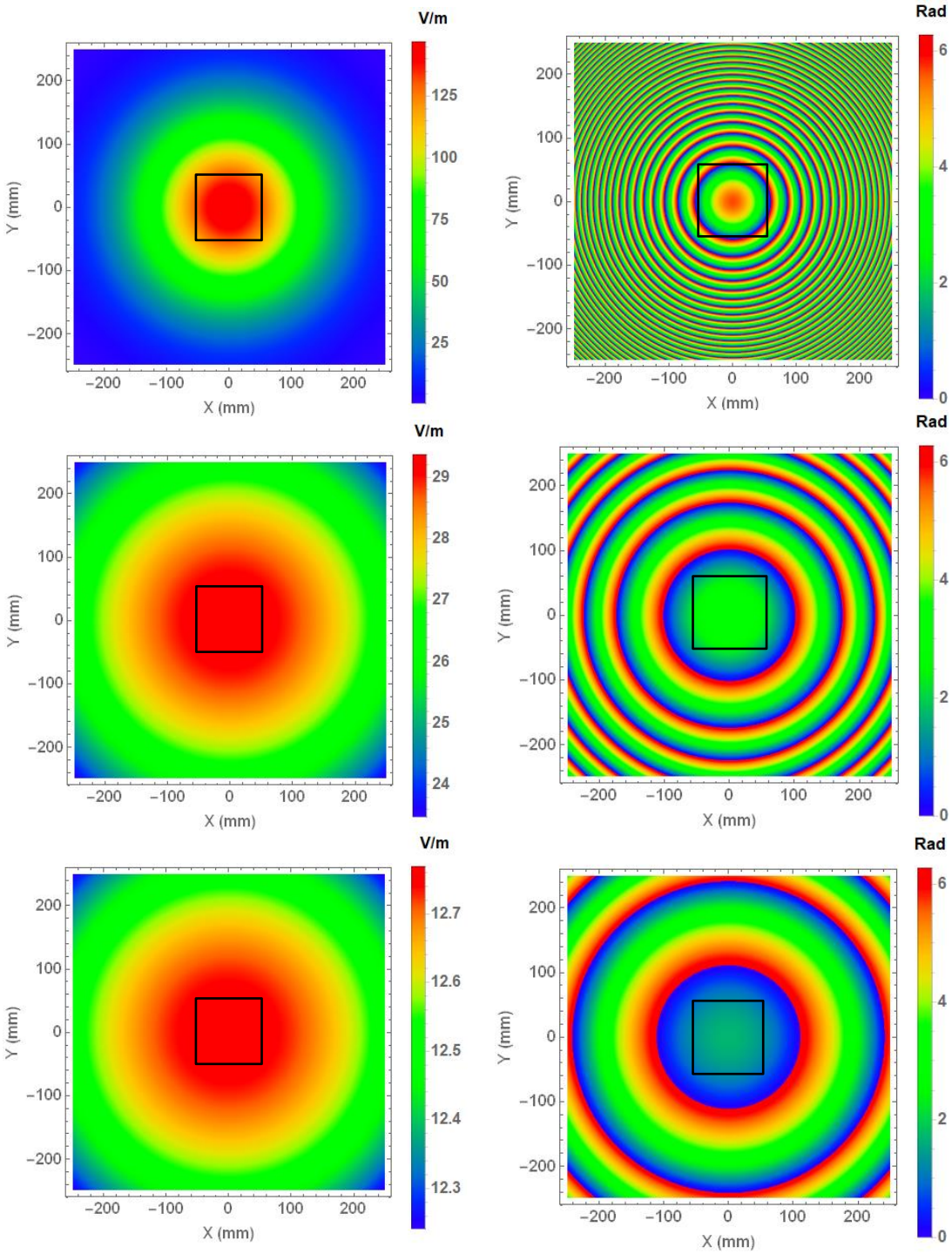

Figure 4.10: Beam pattern amplitude (left) and phase (right) from the 10 º source over the horn array of QUBIC when the calibrator source is placed at on-axis distances of 1 m (top), 5 m (middle) and 10 m (bottom) from the aperture, with the position and size of the horn array shown in black.

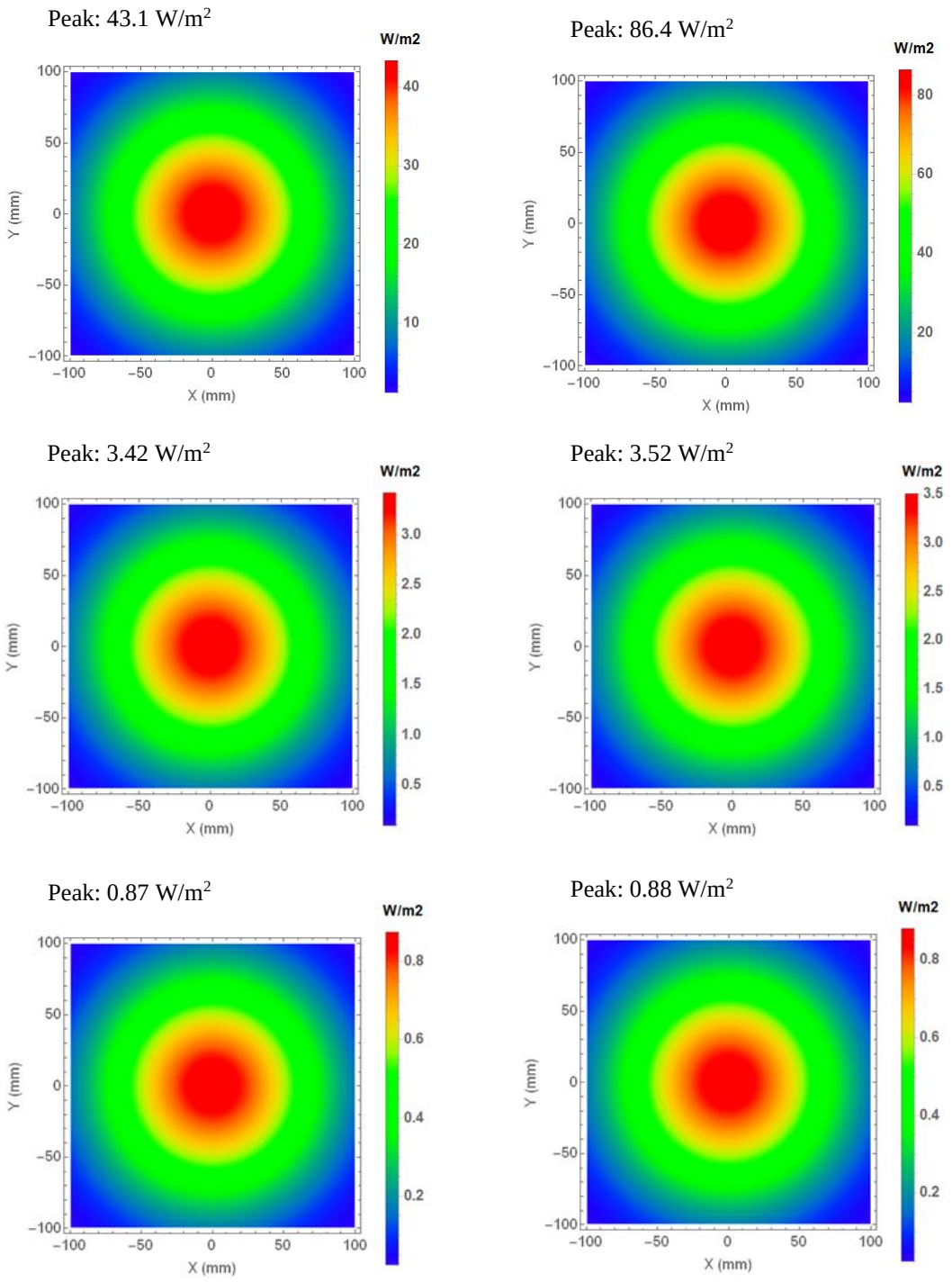

Figure 4.11: Beam profiles (intensity) for horns x08y08 (left) and x11y11 (right) when the source is 1 m away (top), 5 m away (middle) and 10 m away (bottom) recorded on a screen 60 cm from the horn aperture.

Interference pattern on QUBIC focal plane (PSF)

The PSF calculated for the three calibrator source distances investigated are shown in Figure 4.12. It was clear that when the source was placed 1 m from the array, the image on the focal plane did not resemble the PSF expected of the TD as seen in Chapter 3 (see Figure 3.31 for the real and ideal PSFs of the instrument). The source distances of 5 m and 10 m gave a pattern that does resemble the expected PSF. As expected, it is clear that the farther the source is from the horn array aperture, the more point like it appears to the instrument.

As a result of this this work I concluded that a source distance of 5 m is sufficiently far away for the calibrator to be used to measure the PSF of the TD, but placing it farther would clearly provide better results. In fact, as detailed in Section 4.4.3, an optical path of 11.5 m was achieved by placing the source on a lab wall using a mirror to reflect it into the QUBIC instrument. An on-axis example of this with a source distance of 11.5 m produces a PSF as in Figure 4.12.

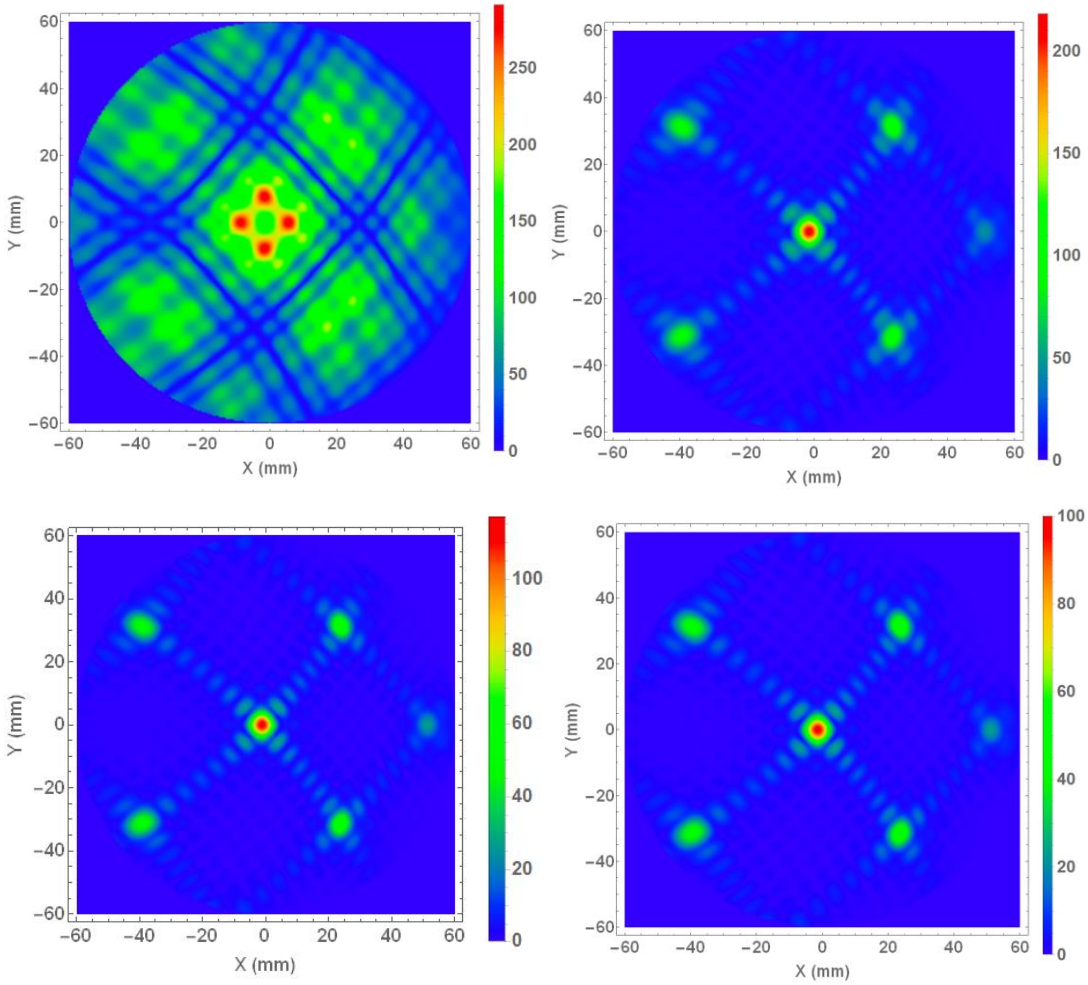

Figure 4.12: Amplitude of the interference pattern on the QUBIC focal plane when observing a 10 º source at a distance of 1 m (top left), 5 m (top right) 10 m (bottom left) and 11.5 m (bottom right) from the instrument aperture.

4.4.2 Effects of the cryostat window and filters

The previous simulations were performed using a simple QUBIC system, not including the cryostat window and filters (positions and sizes given in Table 3.3 and Table 3.4 respectively) in front of the horn array; these would be expected to cause some level of truncation of the beam. This truncation and its effects were investigated by assuming that each of these optical components was a perfect transmitter and thus could simply be approximated by using apertures in the MODAL model (Figure 4.13).

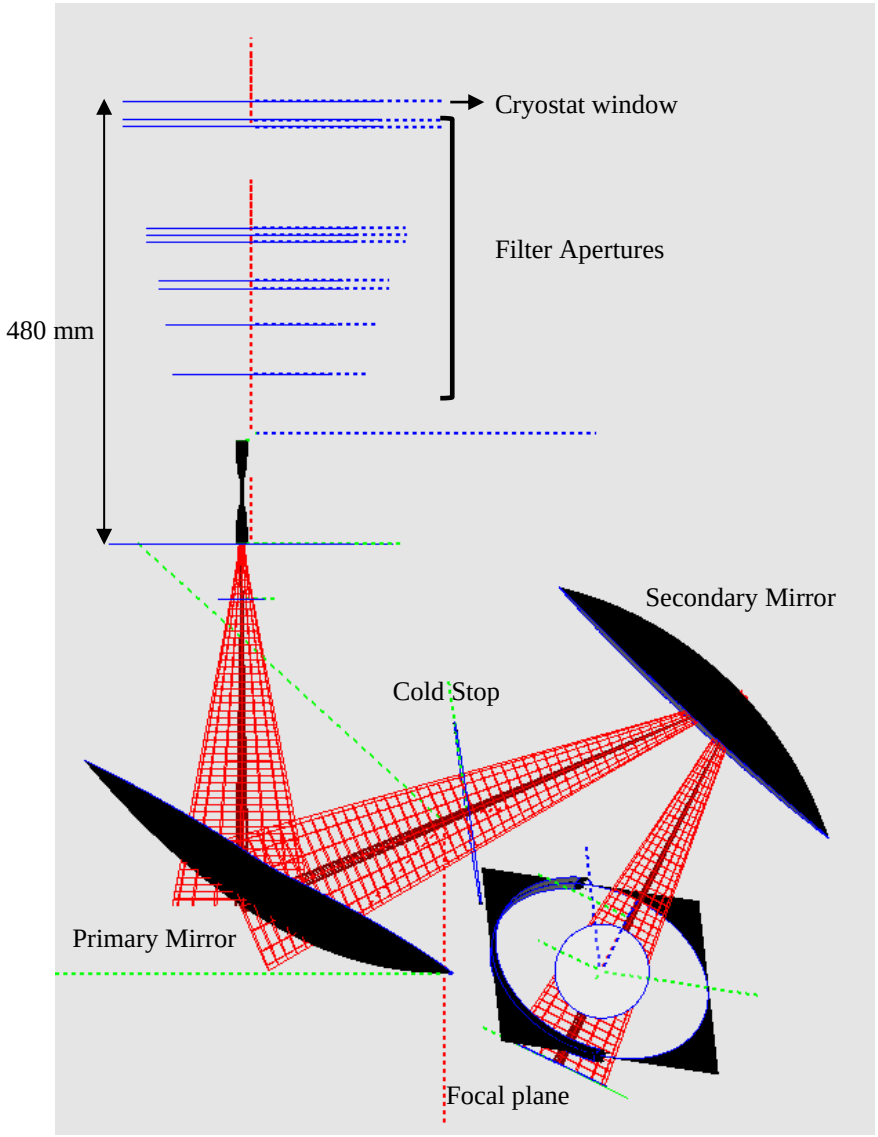

Figure 4.13: MODAL model of the QUBIC TD optical combiner with the filters modelled as apertures above the horn array.

4.4.2.1 *Truncation due to filters and the cryostat window*

Propagating the 10º calibrator source beam from a distance of 11.5 m from the horn array through the cryostat window and filters resulted in a non-uniform beam pattern in front of the horn array as indicated in Figure 4.14. The horns were then excited by this beam and produced an interference pattern on the focal plane of the optical combiner (Figure 4.15).

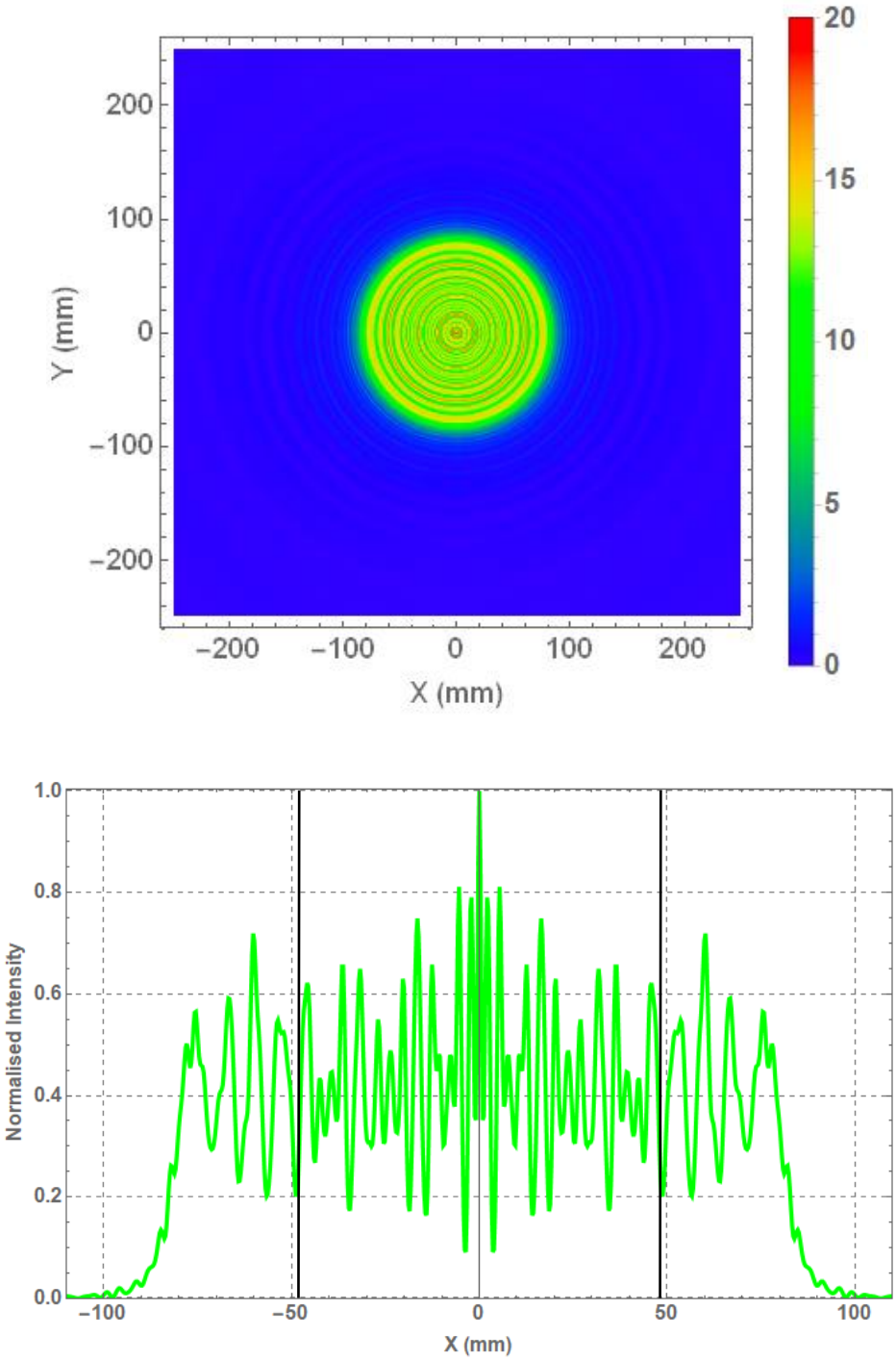

Figure 4.14: Beam pattern (top) and horizontal cut (bottom) of the beam in front of the horn array after truncation by the cryostat window and filters with the black lines indicating the size of the TD horn array. This was captured in the near-field of the aperture.

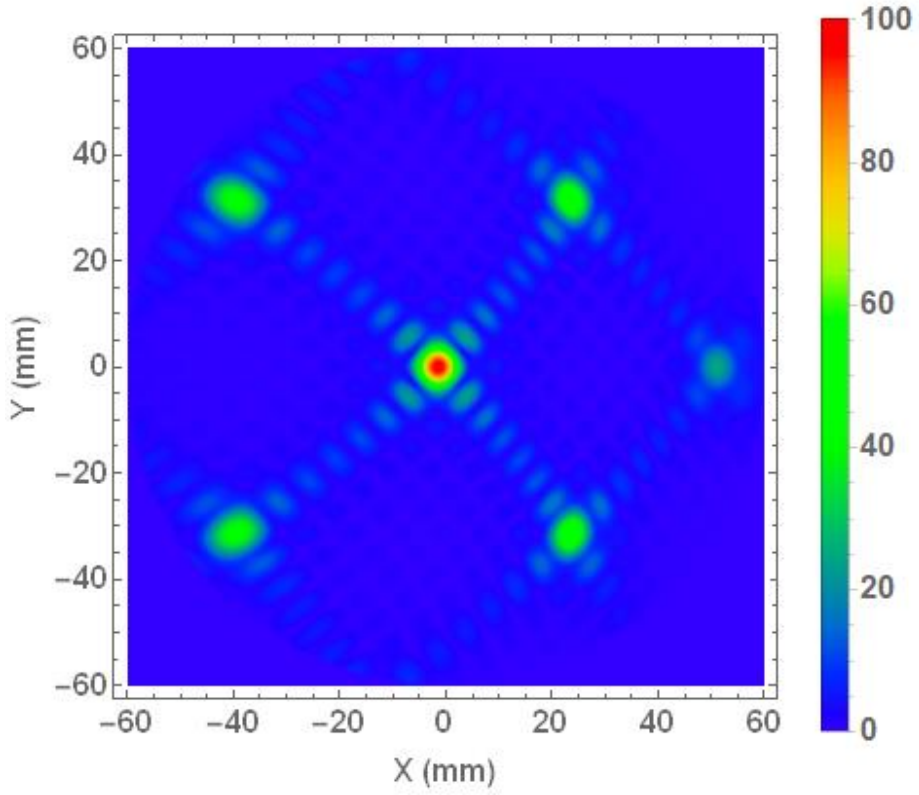

Figure 4.15: PSF (amplitude) on the focal plane when the horns are excited with a beam that passes through the cryostat window and filter apertures.

Figure 4.16 shows that the structure and the intensity of the predicted pattern was effectively the same regardless of whether the beam was truncated by the filters or not. While the apertures did affect the radiation incident onto the horn array this was not at a level that the coupling between the horns and the incident radiation was affected, meaning the output of the horns was very similar in amplitude to those in Figure 4.11 and visually identical PSFs were generated on the focal plane (Figure 4.16).

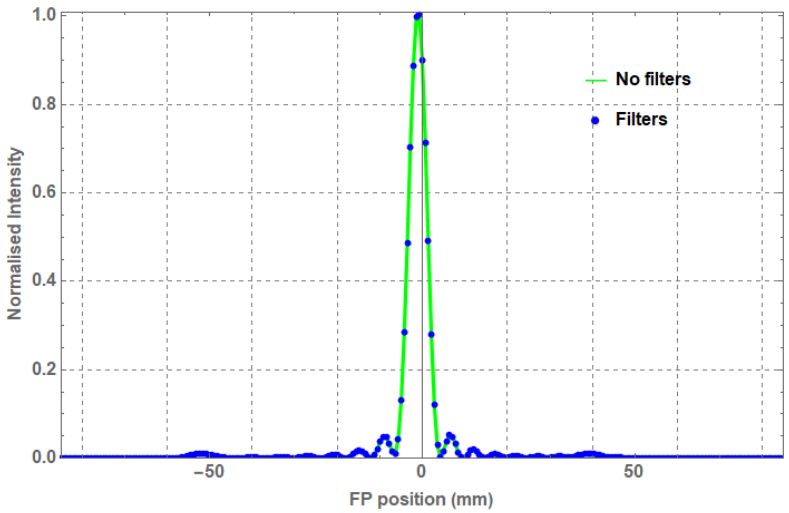

Figure 4.16: Horizontal cut of the PSF produced by a 10 º Gaussian beam 11.5 m away propagated directly onto the horn array and a beam that has been first truncated by the filter apertures. Both patterns have been normalised to the same peak (that of the non-truncated beam).

4.4.2.2 Cryostat window

When the instrument is cooled and in its vacuum state the cryostat window curves due to the pressure difference inside and outside the cryostat. Analysis performed by M. De Petris of the Sapienza University of Rome with the industry standard software Zemax OpticStudio showed that when the incident radiation passed through the curved cryostat window, it imprinted a phase curvature on the wavefront (Figure 4.17).

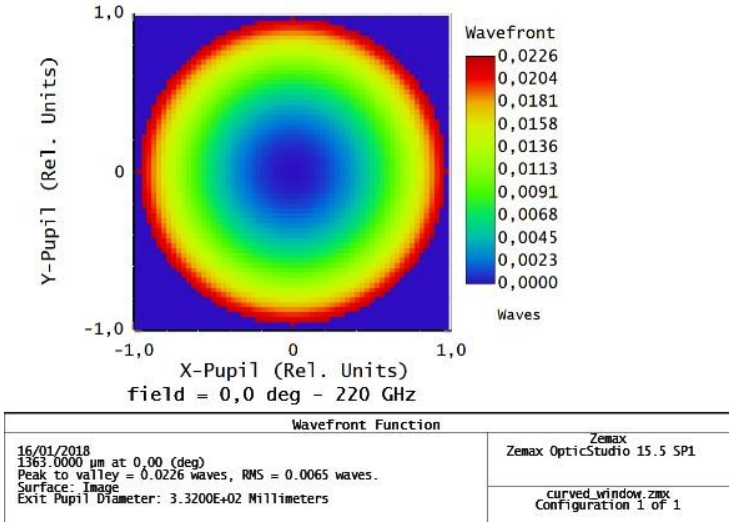

Figure 4.17: Phase front in Optical Path Difference (OPD) of the incident radiation over the FI horn array (332 mm diameter) after passing through a model of the cryostat window. Image provided by M. De Petris.

To discover the potential effects of this curvature, the situation was modelled in MODAL with some notable changes. When this analysis was performed, MODAL could not fully implement curved transmitting surfaces of different refractive index to imprint a phase curvature on the incident radiation. However, a Gaussian source (the same as the calibrator source above) was placed at varying on-axis distances from the horn array, in order to replicate the phase curvature in Figure 4.17 (equivalent to a phase range of 0.142 rad). This analysis showed that this curvature was the equivalent of observing the calibrator source at a distance of roughly 420 m from the horn aperture (Figure 4.18), which also gave uniform amplitude over the horn array. This distance is two orders of magnitude greater than the acceptable far-field distance of 5 m shown in Section 4.4.1, meaning that effects of this window curvature would be negligible.

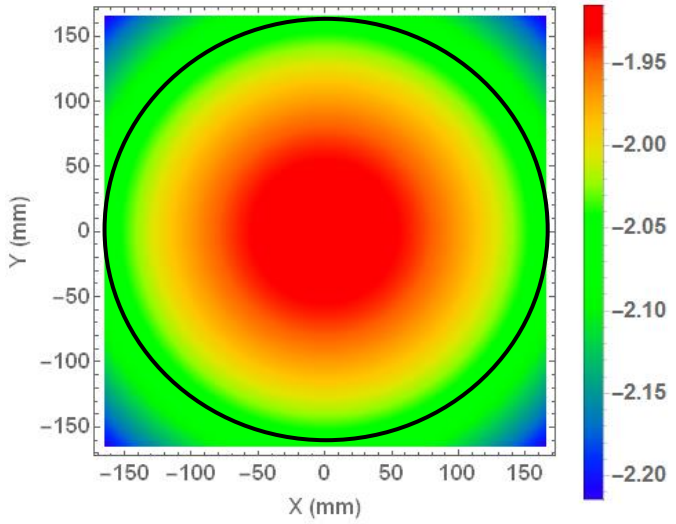

Figure 4.18: Phase front over the horn array of a 10° Gaussian beam propagated from an on-axis source at a distance of 420 m. The black circle corresponds to the cryostat window aperture size of diameter 332 mm shown in Figure 4.17. Within the black circle there is a phase curvature range (about 0.15 rad) roughly corresponding to the OPD range (0.0226) in Figure 4.17.

4.4.3 Laboratory calibrator setup

It was difficult in practice to set up the on-axis system that has been modelled above. Using a plane mirror mounted at an angle in the lab (Figure 4.19), the source – which is a Gunn oscillator running at 10 GHz using two multipliers to reach the frequencies of the lower band required (Torchinsky *et al.*, 2020) – could be placed off-axis with the beam reflected towards QUBIC, providing a much larger optical path (Figure 4.20), than was originally envisioned for the lab.

Initially there were three possible configurations considered for the system with the calibrator source at the same horizontal distance from QUBIC but at different heights. Each position of the source required the mirror to be rotated at a slightly different angle to bring the calibrator beam back on-axis providing slightly different optical paths as seen in Table 4.3.

Table 4.3: Path length of beam corresponding to height of the source

Source Height (m)	Path Length (m)
1	11.78
2	11.57
4	11.43

It would be most desirable to choose the position that has the longest optical path. However, since QUBIC is operating at wavelengths that are within an order of magnitude or so of the size of the optical elements, it is not that straight forward due to diffraction effects caused by blockage by the instrument itself (see Figure 4.21). A GBM analysis was performed to see if there would be substantial truncation.

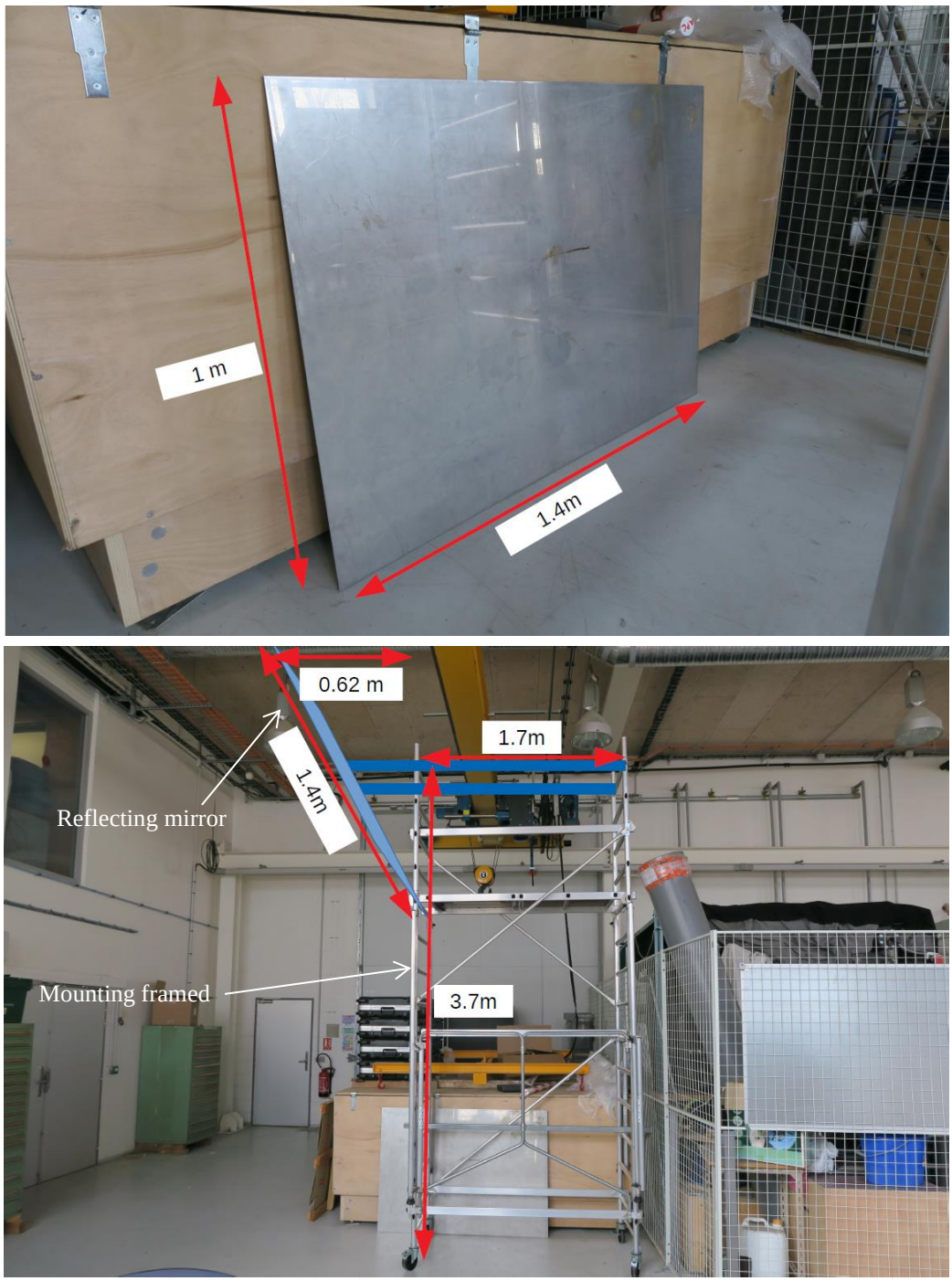

Figure 4.19: Plane mirror that will be used to redirect the calibrator beam (top) and reflecting mirror mount (bottom) in the QUBIC test lab (image provided by collaborators in APC Paris).

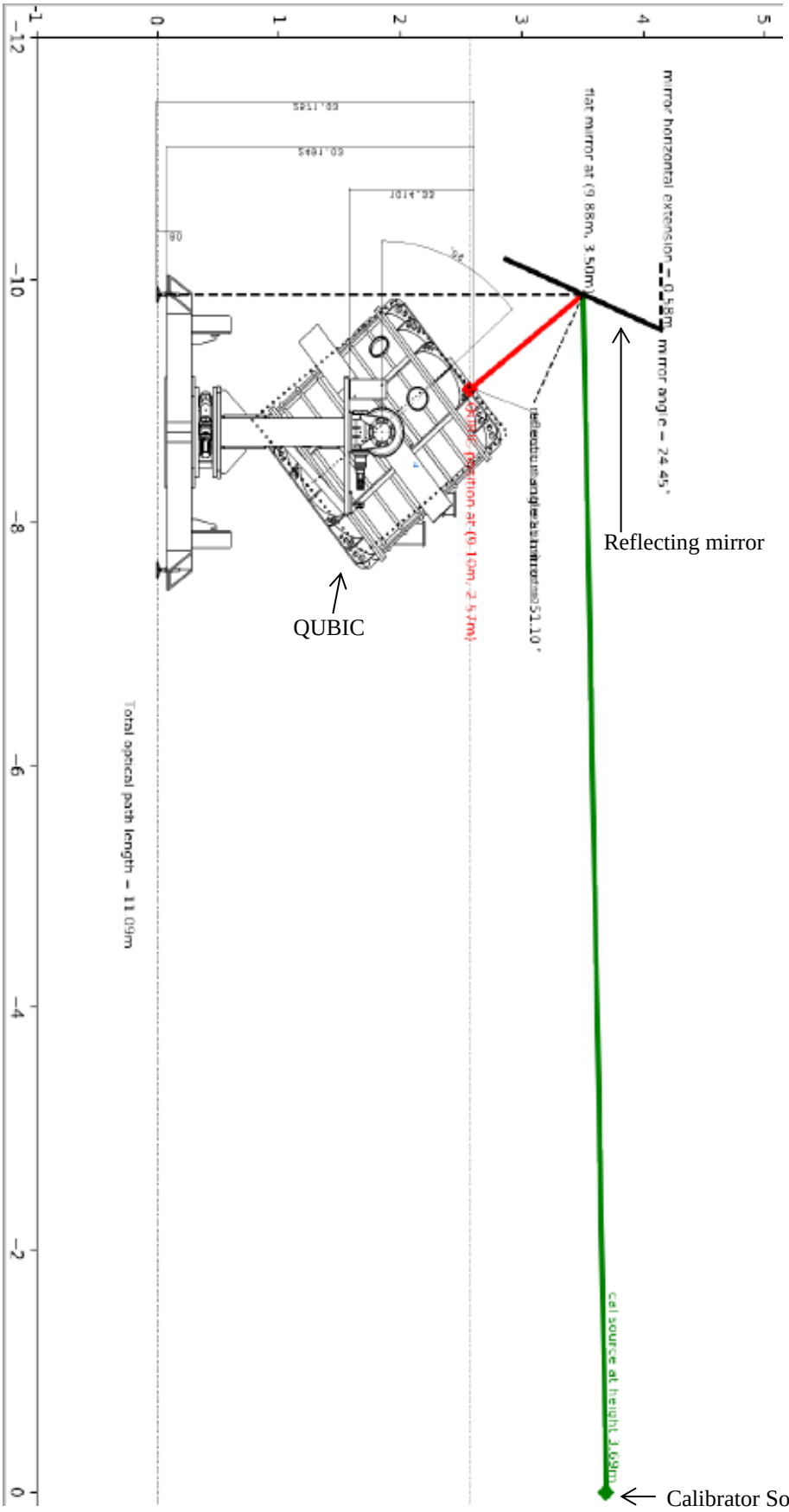

Figure 4.20: Calibration test setup of QUBIC including the plane mirror (image provided by S. Torchinsky of APC Paris).

4.4.3.1 Gaussian beam mode analysis

To investigate the blockage of the calibrator source beam, a model of the system was set up in MODAL as in Figure 4.21. The cryostat itself has a relatively complex design, which is difficult to implement in MODAL. However, we do not need to implement the cryostat exactly, to investigate the truncation. As an approximation a rectangular surface was implemented with the same height as the cryostat and the width equal to the diameter of the cryostat.

It is desirable for the calibrator beam to have as little cross sectional intersection with the cryostat as possible. Observing the models with the source at 2 m and 4 m it can be clearly seen from the simple GBM example in Figure 4.22 that there is substantial intersection with the Gaussian beam and the cryostat in both situations, but it is worse for the 2 m source height as expected. Because of this there are no major advantages in choosing the shorter source height, the increase in optical path is very small, and it has already been shown that a 5 m source distance is sufficient and does not outweigh the disadvantages of the beam truncation with the cryostat.

Due to physical limitations it was not possible to mount the calibrator at a height of exactly 4 m and so it was positioned at a height of 3.69 m above the ground, providing the optical path of 11.5 m outlined above. This was the setup that was tested with a PO analysis to generate predictions to compare with measurements.

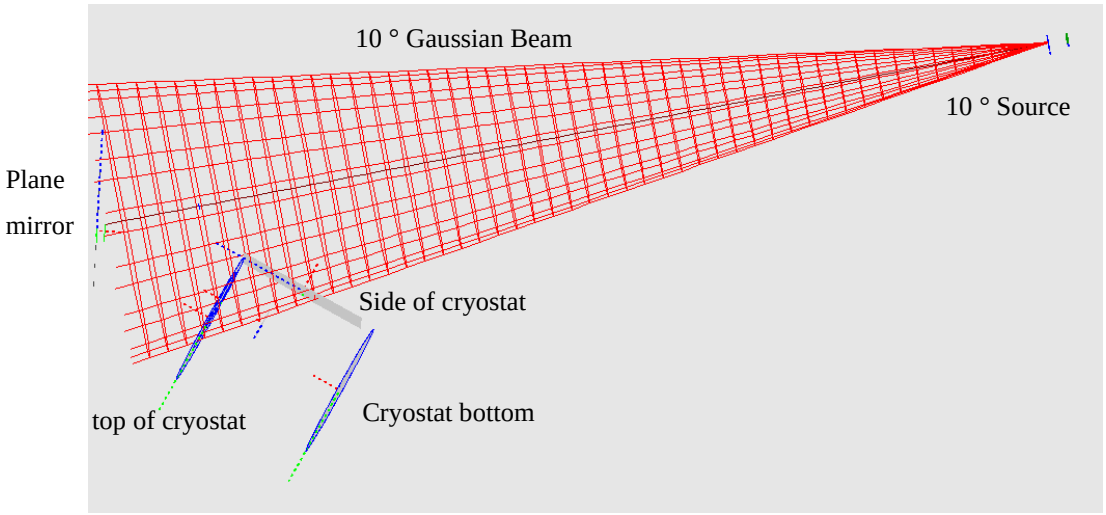

Figure 4.21: Labelled MODAL model of the system for analysis, the source is located at a height of 2 m and the red beam indicates the beam at a radius of 1w (capturing 86 % of the total power with equation [30]).

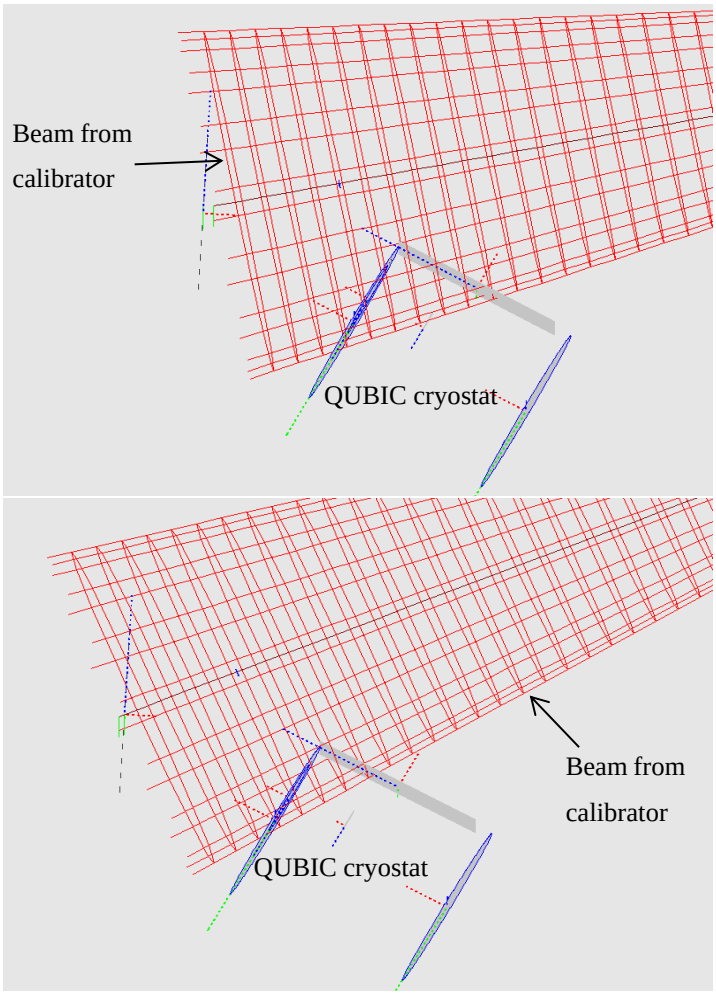

Figure 4.22: GBM analysis with the source at 2 m (top) and at 4 m (bottom). See Figure 4.21 for full setup.

4.4.3.2 PO analysis of the off-axis source

A full PO analysis showed that the cryostat does truncate the calibrator beam when the source is placed at a height of 3.69 m as seen in Figure 4.23, causing a faint diffraction pattern to occur in the beam. However, this does not alter the shape of the beam severely and there is no significant power loss due to the beam truncation with both this and the ideal setup capturing about 30 % of the total power from the calibrator source.

Filter and window truncation

The effect of the cryostat truncation on the radiation incident over the horn array was analysed for the off-axis beam using the same filter and window setup as before. The beam reflected from the mirror was propagated through the apertures and the pattern over the horn array was observed. It can be seen clearly from Figure 4.24 that performing the same process while accounting for the truncation due to the cryostat produces nearly identical results. This indicates that the truncation from the cryostat is negligible in comparison to the truncation from the apertures in front of the horn array. Hence for modelling this situation further the truncation of the cryostat was ignored saving valuable computational time.

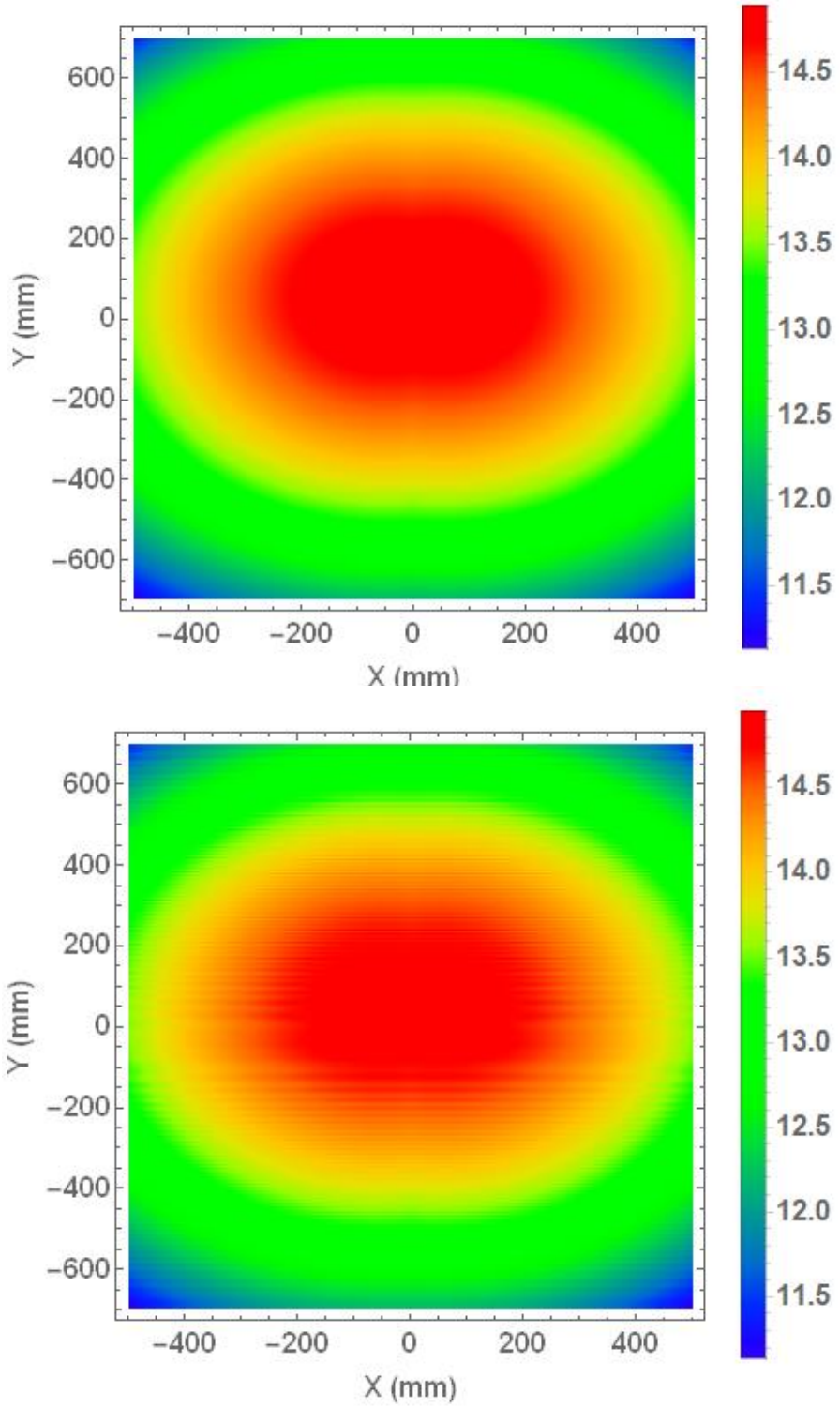

Figure 4.23:The top shows the amplitude of the beam pattern on the plane mirror without accounting for cryostat truncation while the bottom shows the beam when this truncation is included. The calibrator source is placed at a height of 3.69 m for both models.

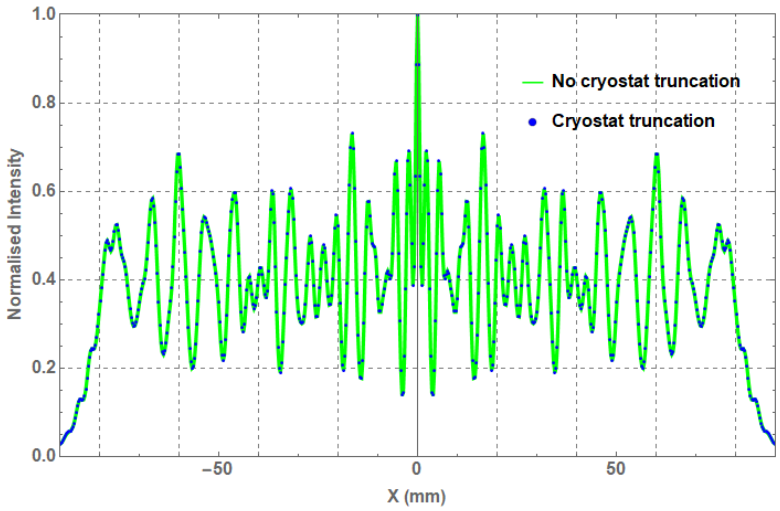

Figure 4.24: Horizontal cut of the normalised beam pattern (both plots are normalised to the same peak) of the radiation incident on the horn array with and without blockage by the cryostat.

Figure 4.25 shows that the field at the horn array was very similar for both the direct (on-axis) and the reflected (off-axis) calibrator source positions, hence the coupling to the horns is similar for both models and the resulting PSF is nearly identical (Figure 4.26). This shows that for modelling these observations, the on-axis source is sufficient and the full off-axis reflected system with the plane mirror does not need to be modelled, again saving computation time.

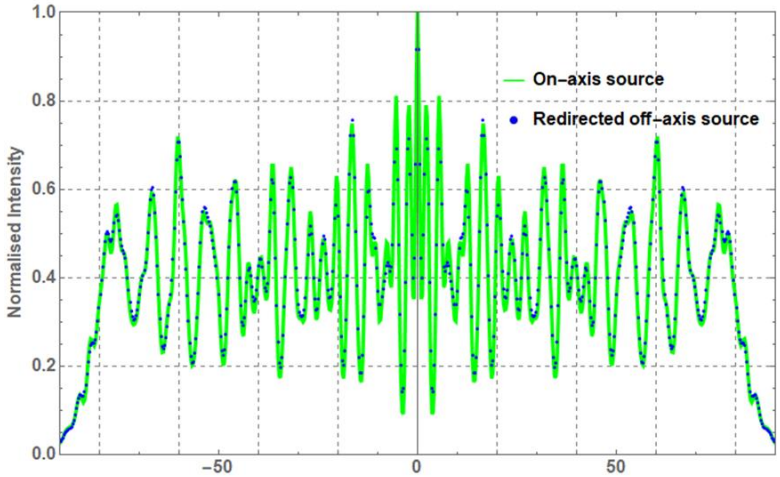

Figure 4.25: Horizontal cut comparison of the field at the horn array for the reflected source and the on-axis direct source from Figure 4.14. Note that both models have an optical path length of 11.5 m and are normalised with respect to the same peak.

This work gave a theoretical prediction that could be used to compare with lab measurements and showed that they are extremely close to what would be measured from an on-axis far field point source.

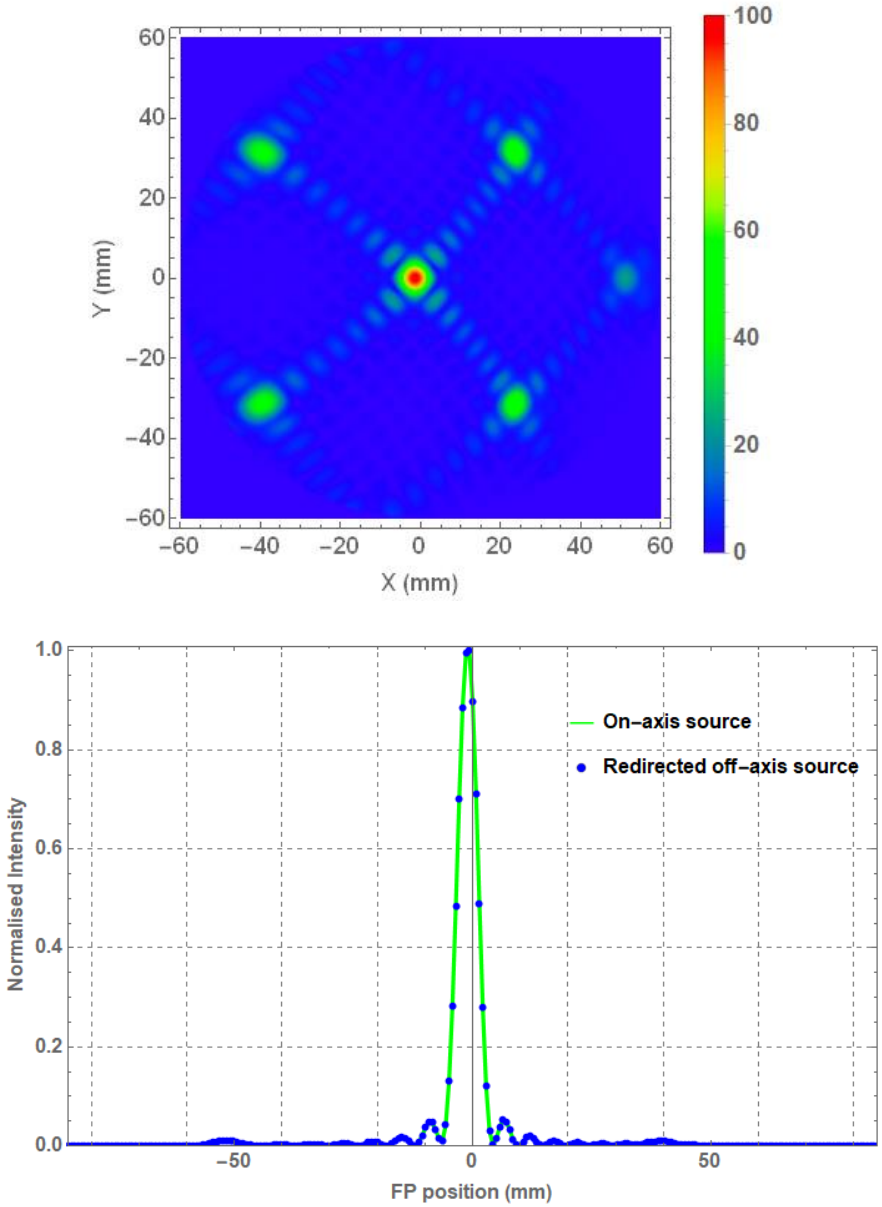

Figure 4.26: PSF produced on the focal plane from excitation with the 150 GHz redirected calibrator source with aperture filters included (top) and diagonal cut comparison of the PSF shown in Figure 4.15 (bottom). Both patterns are normalised to the same peak.

4.5 The synthetic beam

The synthetic beam shown up to this point has been generated for a limited set of situations. This section will explore the synthetic beam from different positions on the focal plane, at frequencies other than 150 GHz and when accounting for the full surface area of the TES pixel. In this section method 3 from Section 3.6.2 will be used by observing the pattern on a 4 m×4 m observation screen in the far-field (12 m from horn aperture) of the instrument.

4.5.1 The synthetic beam for off-axis TESs

As part of the testing phase of the QUBIC instrument the synthetic beam is obtained for multiple detectors in the quarter focal plane used on the TD. This section will show the differences between the beam patterns of a hypothetical on-axis detector located at (0 mm, 0 mm) in the ONAFP_RF and off-axis detectors (some

radial distance away from the centre). This will be done by modelling the instrument in MODAL and obtaining synthetic beams at 150 GHz with the point source method (method 3).

The QUBIC feedhorn array is made up of back-to-back identical horns, meaning that they have a FOV of 12.9º and emit a 12.9º beam when excited with EM radiation (Figure 4.27). Thus, the far-field pattern of the QUBIC horn is identical for the receiving and transmitting sides of the feedhorn. This pattern acts as the envelope for the synthetic beam as described in Chapter 3 and shown in Figure 4.28 (the main peak is slightly off-axis, due to combiner design). It can be clearly seen in the cut of the synthetic beam that the off-axis peaks drop in intensity, according the profile of a Gaussian beam described by equation [54].

$$\left(\exp\left(-\frac{\theta^2}{\left(\frac{\mathrm{FWHM}}{\sqrt{2\ln(2)}}\right)^2}\right)\right)^2 \qquad [54]$$

where FWHM is 12.9º for the QUBIC horns, and θ is the off-axis angle.

For an on-axis pixel modelled in MODAL the radiation emitted from the point source aligns with the peak of the instrument facing envelope, meaning that the coupling will be maximised in terms of intensity. Since the radiation from a point source on the focal plane is close to a plane wave, for off axis TESs it can be considered as a plane wave tilted by angle ($\Delta\theta$) corresponding to the angular distance from the centre of the focal plane (given by equation [55]). This causes a reduction in the coupling between the horns and the field from the off-axis detector, attenuating the far-field pattern by a factor that can be calculated by substituting $\Delta\theta$ for θ in equation [54]. This produces a far-field pattern envelope of the same shape (12.9° Gaussian) but lower intensity (Figure 4.29) than for the on-axis TES.

$$\Delta\theta = \tan^{-1}\left(\frac{\text{radial distance of detector}}{\text{instrument equivalent focal length}}\right) \qquad [55]$$

where the equivalent focal length of QUBIC is 300 mm.

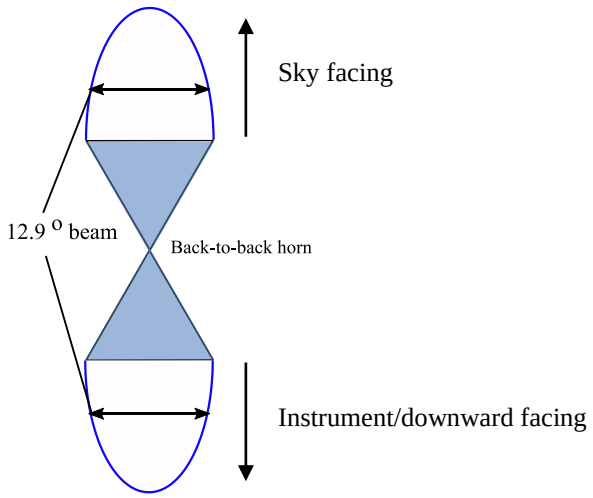

Figure 4.27: Back-to-back QUBIC feedhorn.

When a synthetic beam is generated for an off-axis detector, the positions of the peaks move across the sky (under the beam envelope) by an angular distance corresponding to the off-axis distance, $\Delta\theta$, of the detector (Figure 4.30 and Figure 4.31).

Figure 4.31 shows that the heights peaks of the synthetic beam for the off-axis pixel are described by the attenuated envelope (note that this envelope is not shifted off-axis, simply lower in intensity), however it can be clearly seen that they do not follow this profile as well as the beam for the on-axis pixel. This is due to aberrations that are introduced by the off-axis design of the instrument that affect the coupling of the radiation to the horns. This will be discussed in more detail with respect to the full instrument in Chapter 6.

So there are two attenuations to consider corresponding to both sides of the back-to-back horns. One horn pattern results in the secondary peak heights being lower than the on-axis peak, the other reduces the amplitude of the full pattern with respect to that of an on-axis pixel.

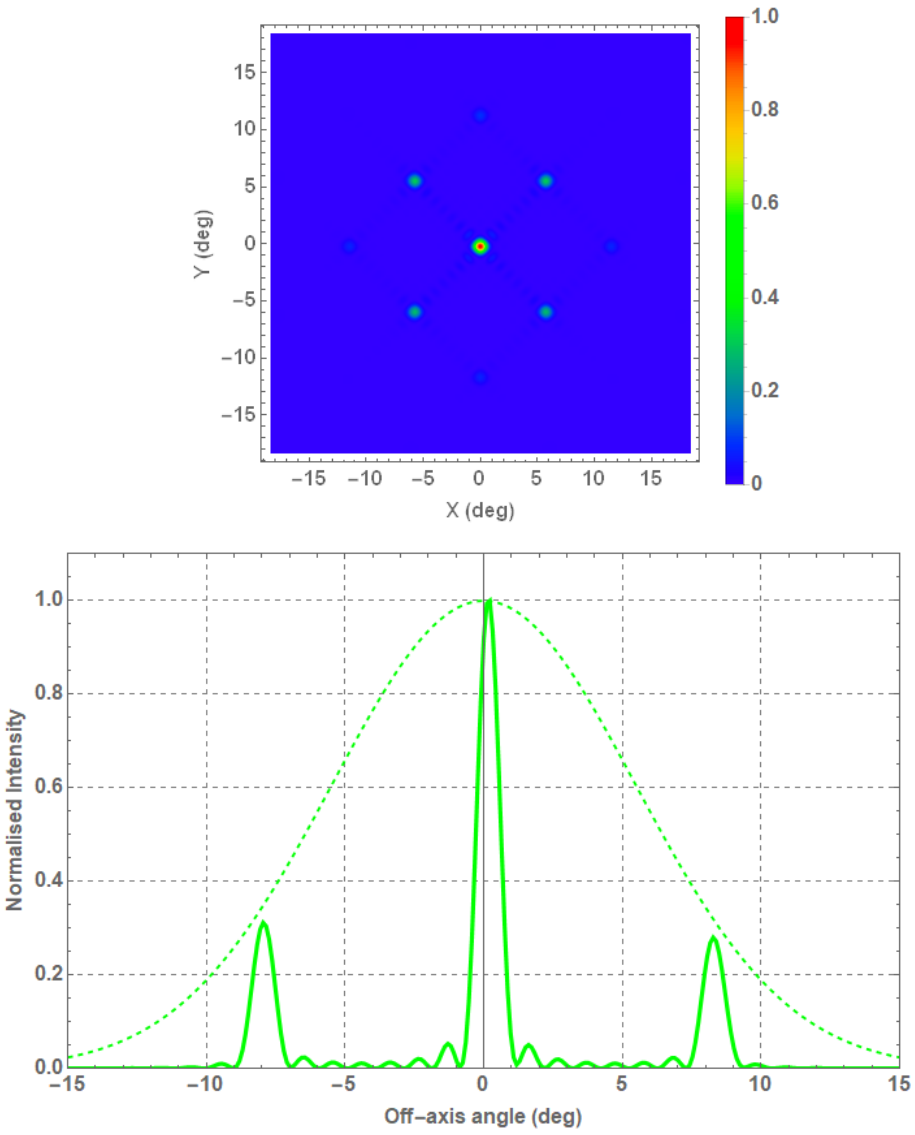

Figure 4.28: synthetic beam for an on-axis TES detector (top – normalised intensity) and a diagonal cut (top left to bottom right) of this synthetic beam (bottom) with the far-field envelope indicated by the dashed line.

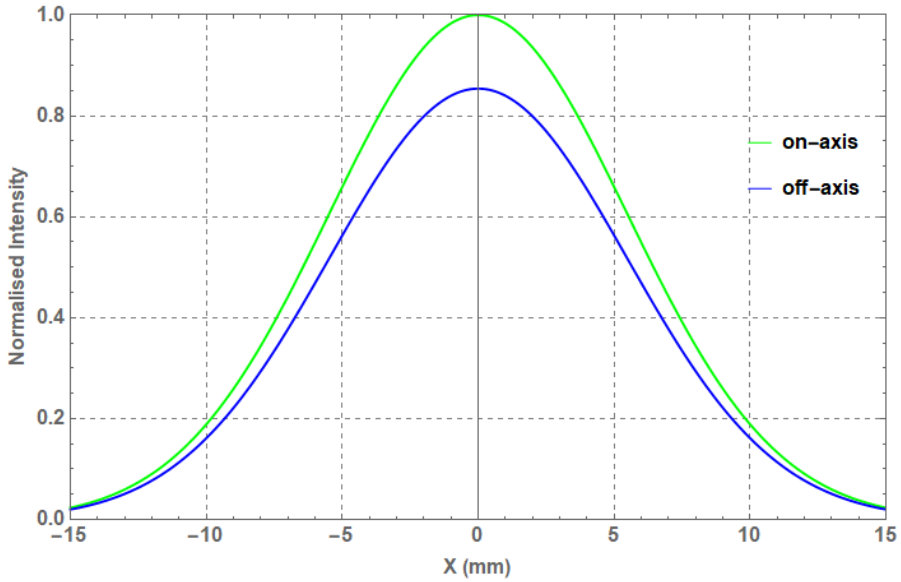

Figure 4.29: 12.9° Gaussian beam envelope profiles for an on-axis pixel and a theoretical 3.07° off-axis pixel (corresponding to a position of (−11.4 mm, −11.4 mm) in the ONAFP_RF, that will be modelled later). Both are normalised with respect to the peak of the on-axis beam.

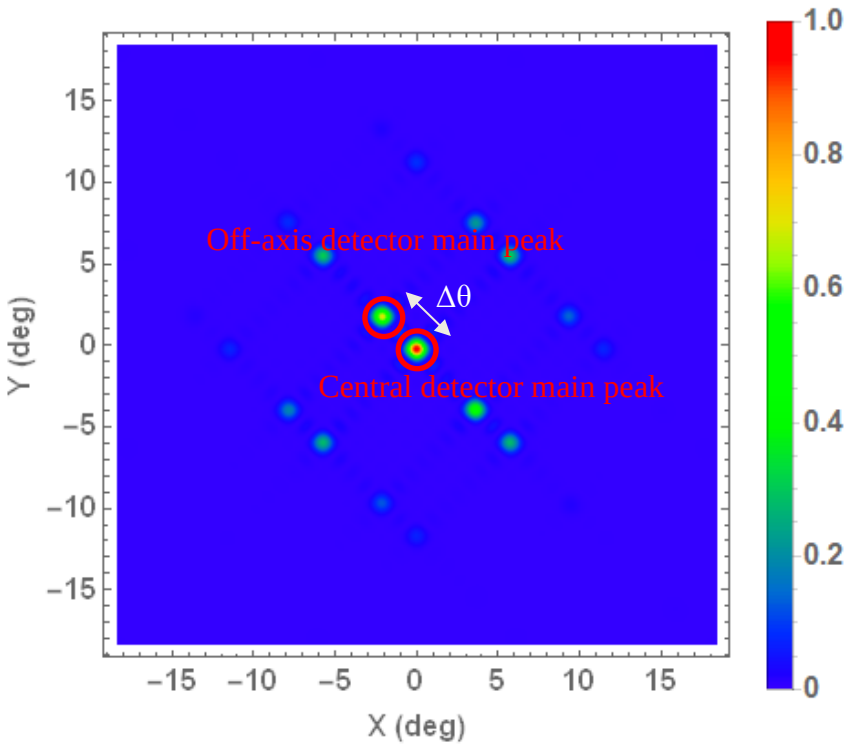

Figure 4.30: Normalised synthetic beams observed for point-like detectors located at (0 mm, 0 mm) and at (−11.4 mm, −11.4 mm) in the ONAFP_RF. The most prominent peaks of each beam are highlighted and they are separated by an angle of 3.07° corresponding to the linear separation of the pixels on the ONAFP_RF ($\tan^{-1}\left(\frac{\sqrt{2(11.4)^2}}{300}\right) = 3.07°$).

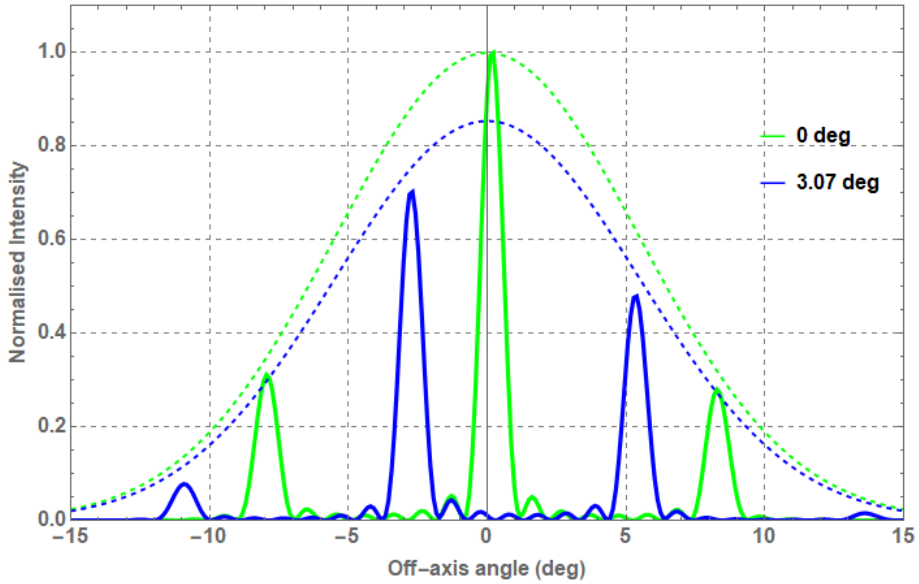

Figure 4.31: Synthetic beam cuts and envelopes (from Figure 4.29) for a (hypothetical) central detector and a 3.07° off-axis detector at (−11.4 mm, −11.4 mm) in the ONAF_RF.

4.5.2 Frequency variation of the synthetic beam

The lower band of QUBIC has a 25% bandwidth (130-170 GHz). The beam pattern from the horns has been described as a 12.9° Gaussian beam, however this is at the design frequency of 150 GHz; the beam pattern will vary with frequency as can be seen in Figure 4.32 (note that the variation of the beam pattern with frequency will be explored in more detail in Chapter 5). These patterns were generated by exciting a back-to-back horn pair with a plane wave. The difference in peak height observed in the beam profiles is expected as the peak intensity of the beam is proportional to the frequency. Table 4.4 shows how some of the beam parameters change with the frequency, note that even though the power over the entrance aperture of the horn is the same, the relative output power is not the same showing that the coupling between the horn and the incident radiation is not the same for all frequencies (this will be explored more in Chapter 5).

Table 4.4: Power in the full 2D beams at different frequencies from MODAL when excited with an incident field 1W in power (measured over the entrance aperture of the horn).

Frequency (GHz)	Peak Power relative to 150 GHz	Total power at output of horn (relative to the total power at 150 GHz)
130	0.673	0.939
150	1.000	1.000
170	1.238	0.985

Since the beam patterns vary with frequency, the envelopes of the synthetic beam (and the PSF) also vary, meaning that the peaks of the beam are attenuated accordingly (Figure 4.33). Table 4.5 shows that the power in the synthetic beam (from the simulations that resulted in the beams seen in Figure 4.33) varies in the same way as the individual beams from the horns. When the TD horn array was excited with a direct on-axis plane wave (the radiation was not passed through the optical combiner) the resulting beam patterns

on the sky (Figure 4.34) are very similar to those of Figure 4.33. Table 4.6 shows that there is virtually no difference in the power from direct excitation or from radiation passed through the combiner. This means that, in terms of power, there are no ill effects from the off-axis design of the combiner.

Table 4.5: Relative power in the synthetic beam resulting from excitation for a 1 W point-like source centred at (0 mm, 0 mm) in the ONAFP_RF.

Frequency (GHz)	Peak Power relative to 150 GHz	Power captured over full 2D synthetic beam relative to 150 GHz
130	0.679	0.939
150	1.000	1.000
170	1.226	0.983

Table 4.6: Relative power in the synthetic beam resulting from the direct excitation with a plane wave.

Frequency (GHz)	Peak Power relative to 150 GHz	Power captured over full 2D synthetic beam relative to 150 GHz
130	0.678	0.939
150	1.000	1.000
170	1.228	0.983

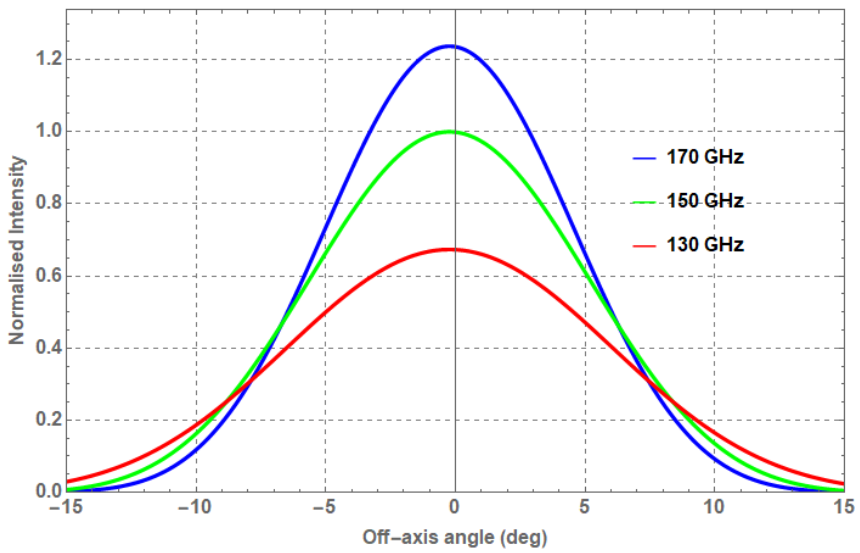

Figure 4.32: Beam patterns from the horns in MODAL, generated by propagating the beam from the horn onto a far-field observation screen. All patterns are normalised to the peak of the 150 GHz pattern.

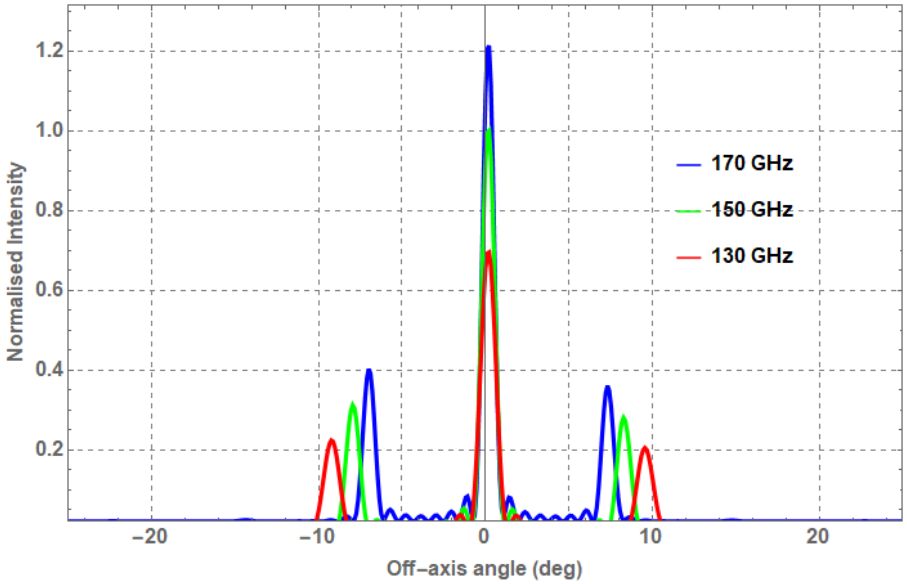

Figure 4.33: Synthetic beam pattern for the TD at 150, 130 and 170 GHz, normalised to the peak value of the 150 GHz beam. These were calculated for a 1 W point-like source centred at (0 mm, 0 mm) in the ONAFP_RF.

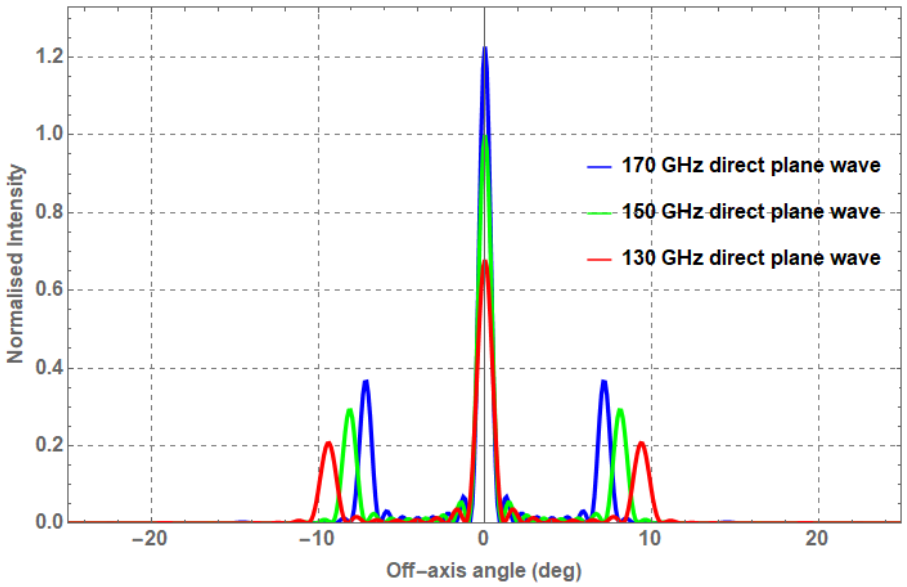

Figure 4.34: Synthetic beam pattern for the TD at 150, 130 and 170 GHz, normalised to the peak value of the 150 GHz when the horn array is excited with a direct on-axis plane wave.

4.5.2.1 Structural changes in synthetic beam

It can be clearly seen in Figure 4.33 that the separation between the peaks in the synthetic beam changes with frequency as expected from equation [37]. Table 4.7. shows good agreement between the theoretical ideal model and the simulated results obtained from a point source positioned on the centre of the focal plane in the MODAL model.

Table 4.8 investigates the relationship between the frequency and the FWHM of the peaks (which corresponds to the angular resolution of the instrument) in the synthetic beam. The theoretical FWHM was obtained from the ideal interference pattern resulting from equation [33], and it can be seen that there is good agreement between the two models. In Chapter 2, the relationship between the number of sources and

the width of the beam peaks was observed, and the results in Table 4.8 show the width of the beam peaks is also dependent on the wavelength such that the relation in equation [56] holds.

$$\mathrm{FWHM}_{\mathrm{peak}} \propto \frac{\lambda}{\text{width of horn array}}. \qquad [56]$$

Table 4.7: Theoretical predictions of the angular separation between peaks in the synthetic beam at frequencies across the lower QUBIC band with a horn separation of 14 mm. Two values for the simulated peak separation was obtained by measuring the distance between the first peak either side of the central peak, the separations are different for the MODAL model because of optical aberrations in the combiner.

Frequency (GHz)	Wavelength (mm)	Theoretical Peak separation (º)	Simulated peak separation (º)
130	2.31	9.49	9.31, 9.51
140	2.14	8.88	8.65, 8.73
150	2.00	8.21	8.11, 8.18
160	1.88	7.70	7.61, 7.63
170	1.76	7.24	7.14, 7.16

Table 4.8: Theoretical prediction of the angular width of the central peak in the synthetic beam at frequencies across the lower QUBIC band. This was performed for the TD instrument, which has an 8×8 horn array, with an inter-horn separation of 14 mm, giving an array size of 112 mm. The simulated FWHM was taken from the central peak of the synthetic beam.

Frequency (GHz)	Wavelength (mm)	Theoretical FWHM (º) – ideal instrument	Simulated FWHM (º) – including aberrations
130	2.31	1.052	1.148
140	2.14	0.976	1.030
150	2.00	0.913	0.910
160	1.88	0.855	0.883
170	1.76	0.805	0.835

4.5.2.2 Synthetic beam across the band

When performing sky observations, the instrument will use the full bandwidth (defined by the filters and horn cut on). From the tables above it can be seen that the off-axis peak separation differs by about 2.4º between the lowest and highest operating frequency and all have beams widths of nearly half this. This indicates that the synthetic beam across the band will have smeared off-axis peaks. This was investigated by sampling the full band at five and three frequencies. A comparison between the results will give us an indication of what frequency sampling is required for such simulations.

Five sample cases across the band

The synthetic beams for 130, 140, 150, 160 and 170 GHz were incoherently combined and then averaged over the band (Figure 4.35). This shows that the on-axis peak of the full band beam has a similar intensity as the central frequency beam. The off-axis peaks are also clearly smeared and there is a drop by about 50 % in intensity compared to the central frequency off-axis peaks.

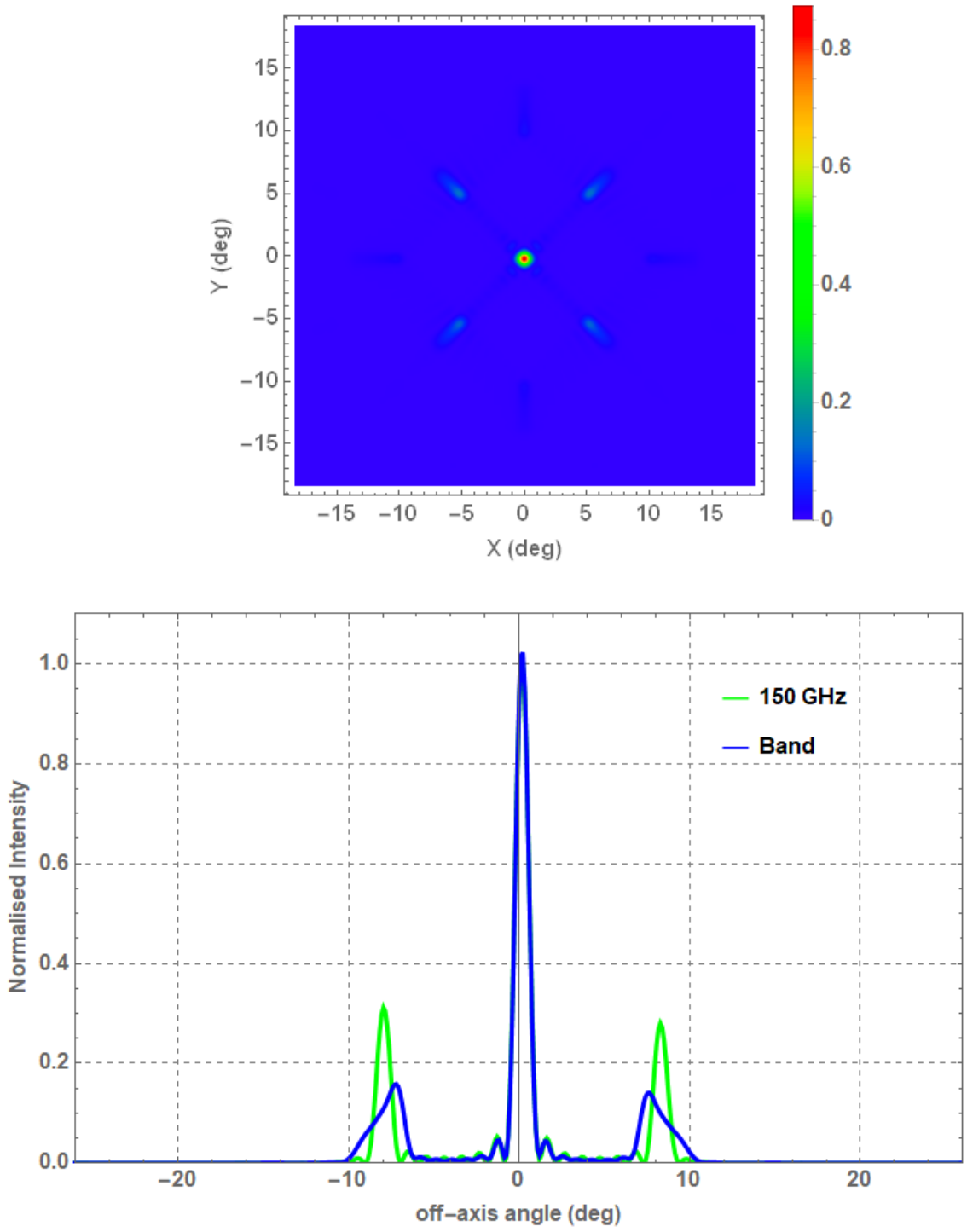

Figure 4.35: Synthetic beam resulting from the incoherent combination of the synthetic beams for a point source at the centre of the focal plane at 130, 140, 150, 160 and 170 GHz (top). Diagonal cut of the synthetic beam compared with the 150 GHz synthetic beam, where both cuts are normalised to the peak of the 150 GHZ cut (bottom).

Three samples across the band

For this simulation, only the 130, 150 and 170 GHz synthetic beams were incoherently combined and averaged. Figure 4.36 shows that the on axis peak intensity remains the same as before. The off-axis peaks are still smeared and they also drop in intensity by about a half, but they have more structure to them. Thus, it was determined that a 10 GHz step across the band would be sufficient for modelling the full band response.

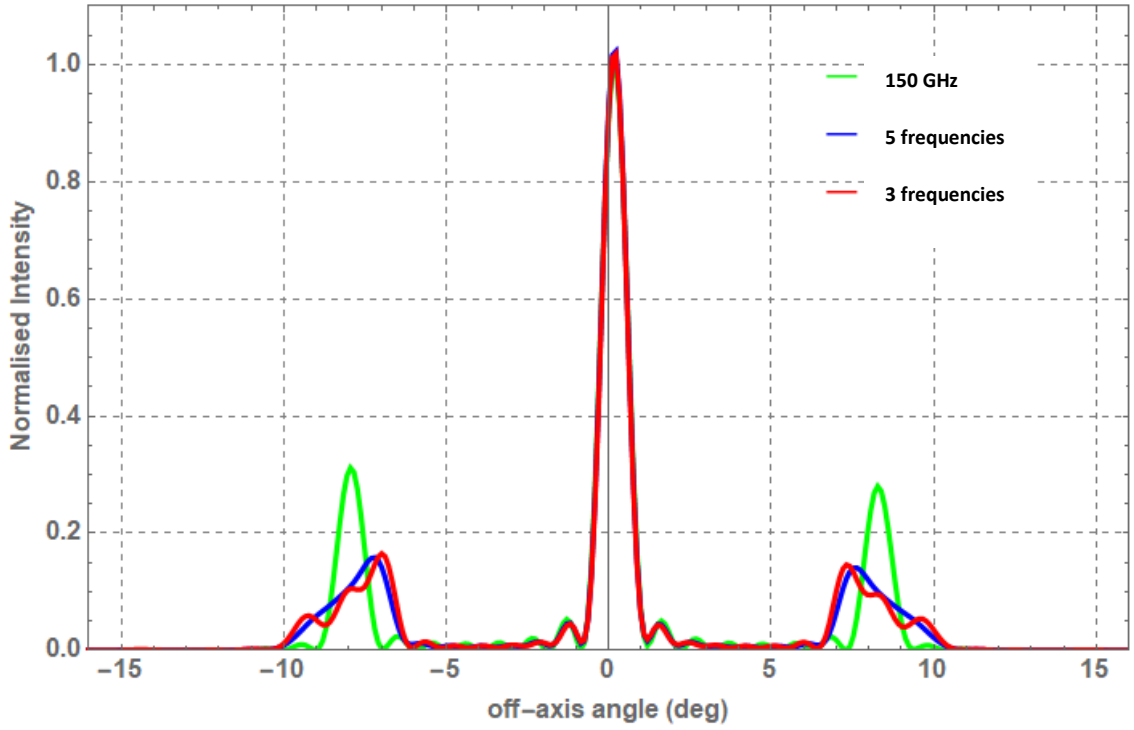

Figure 4.36: Diagonal cut of the synthetic beam resulting from the incoherent combination of the synthetic beams for a point source at the centre of the focal plane for five samples across the band (10 GHz steps) and three samples across the band (20 GHz steps) compared with the 150 GHz synthetic beam. All are normalised to the peak of the 150 GHz beam.

4.5.3 Response integrated over TES area

The synthetic beams shown so far in this thesis have been generated in MODAL by propagating a single point-like source from the focal plane back through the optical combiner and out onto the sky. However, as seen in Figure 3.16 and Figure 4.37, the TES pixels are not point like, they have a square surface area that is sensitive to incident radiation. To simulate the response over this area, point-like sources were placed at nine locations in a 3 × 3 grid across the pixel. A synthetic beam is generated for each of these positions. The averaged incoherent combination of the nine synthetic beam patterns is then obtained to simulate the total synthetic beam of the TES. This was done for two real pixel locations; one near to ‘on axis’ (arbitrarily selected) centred at (-11.4 mm, -2.4 mm) on the ONAFP_RF and one ‘off-axis’ (arbitrarily selected) centred at (-35.4 mm, -23.4 mm) on the ONAFP_RF (Figure 4.37).

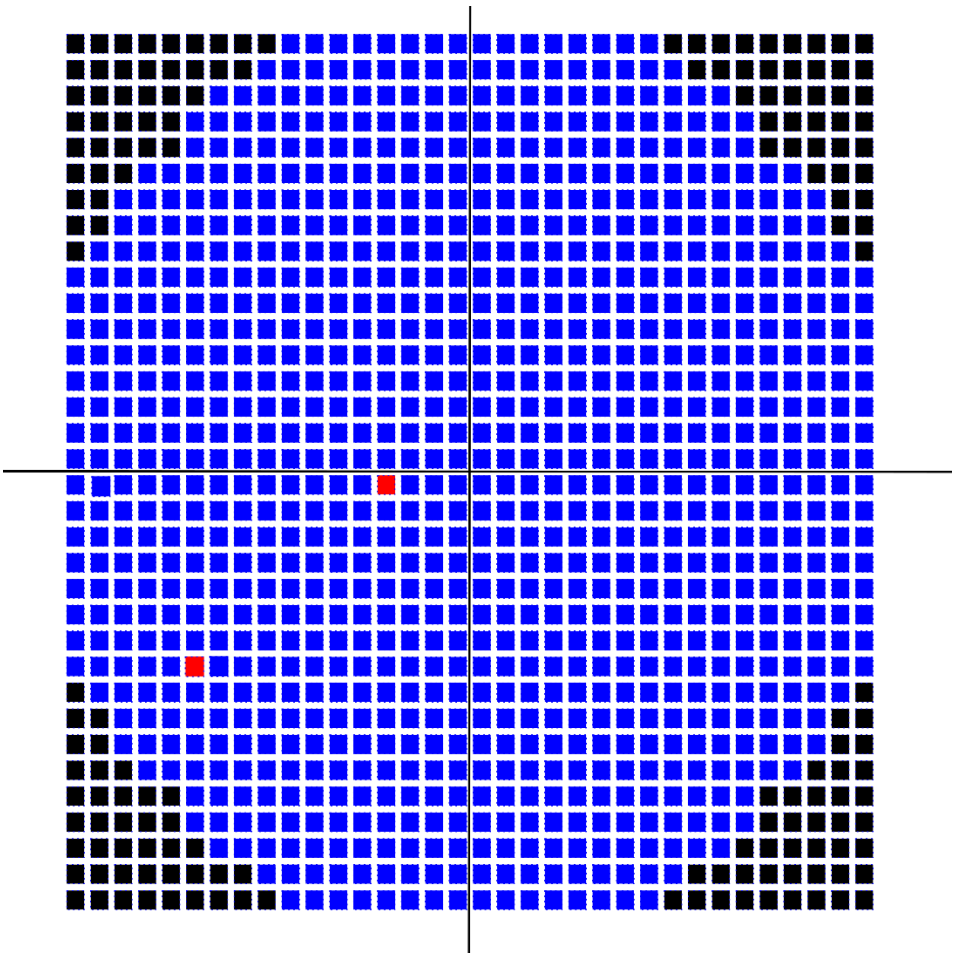

Figure 4.37: TES focal plane array with the location of the (-11.4 mm, -2.4 mm) and (-35.4 mm, -23.4 mm) TESs highlighted in red.

Two synthetic beams will be compared:

1. The synthetic beam from a single point source located at the centre of the TES in question.

2. The integrated synthetic beam which resulted from the incoherent addition of the individual synthetic beam patterns from the nine sources over the surface area of the TES, and then a subsequent division by 9 to get the average over the TES. This will be called the integrated synthetic beam from now on.

4.5.3.1 Integrated vs single point source synthetic beam for TES (-11.4 mm, -2.4 mm)

From Figure 4.38 it can be seen that the peak value for the integrated beam pattern was less than that for the single point source. This was expected since a central point source would have the greatest response of the entire surface area of the TES. Figure 4.39 shows that the main peak of the integrated synthetic beam had about 80 % of the response of the single source beam.

A widening of the peaks can be seen in the cuts (Figure 4.39). It was found that the main peak of the integrated synthetic beam had a had a FWHM of 1.02° compared to 0.91° for the single source (point-like) synthetic beam.

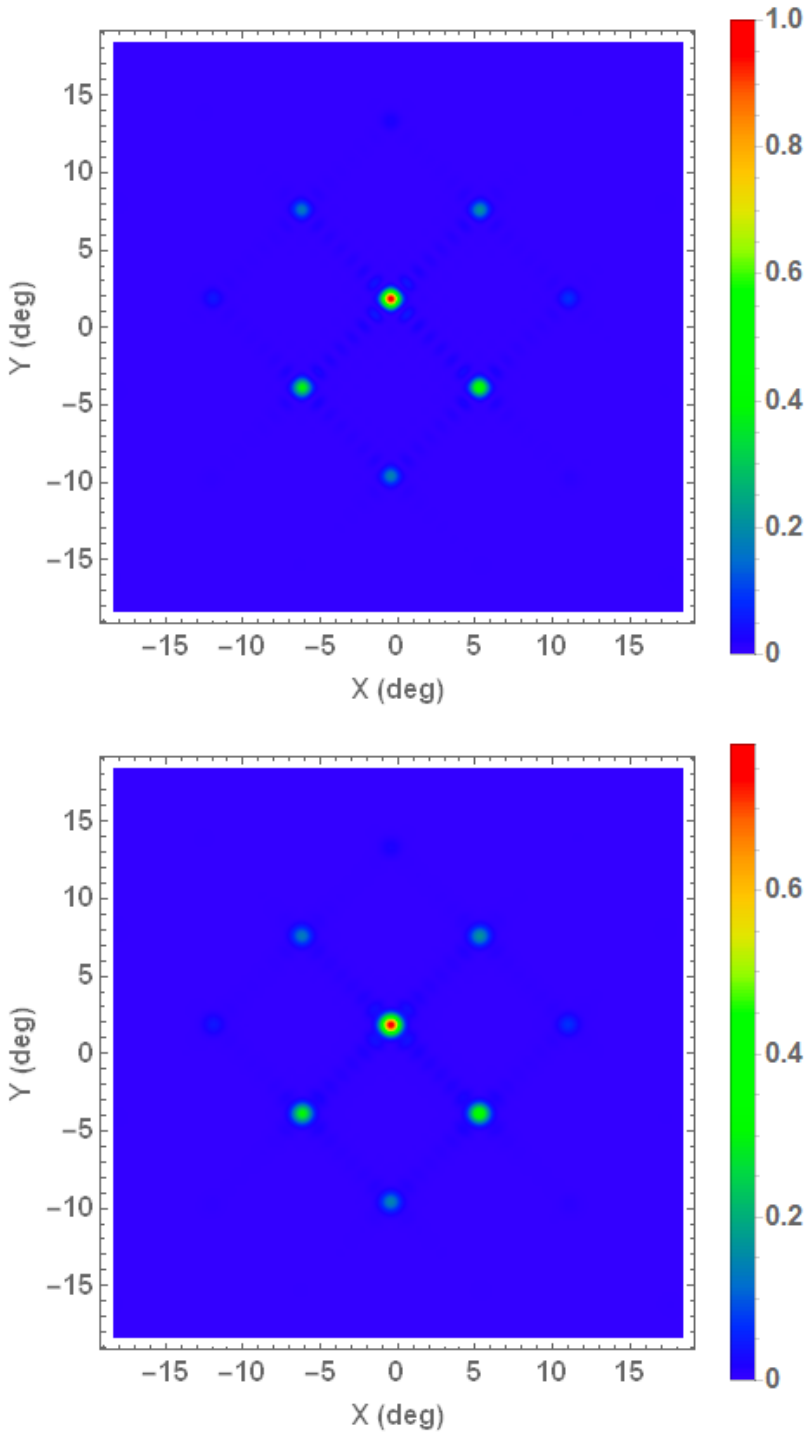

Figure 4.38: Synthetic beam intensity plots for a single point like source (top) and the integrated synthetic beam (bottom). Each beam is normalised to the peak of the point-like beam (top image).

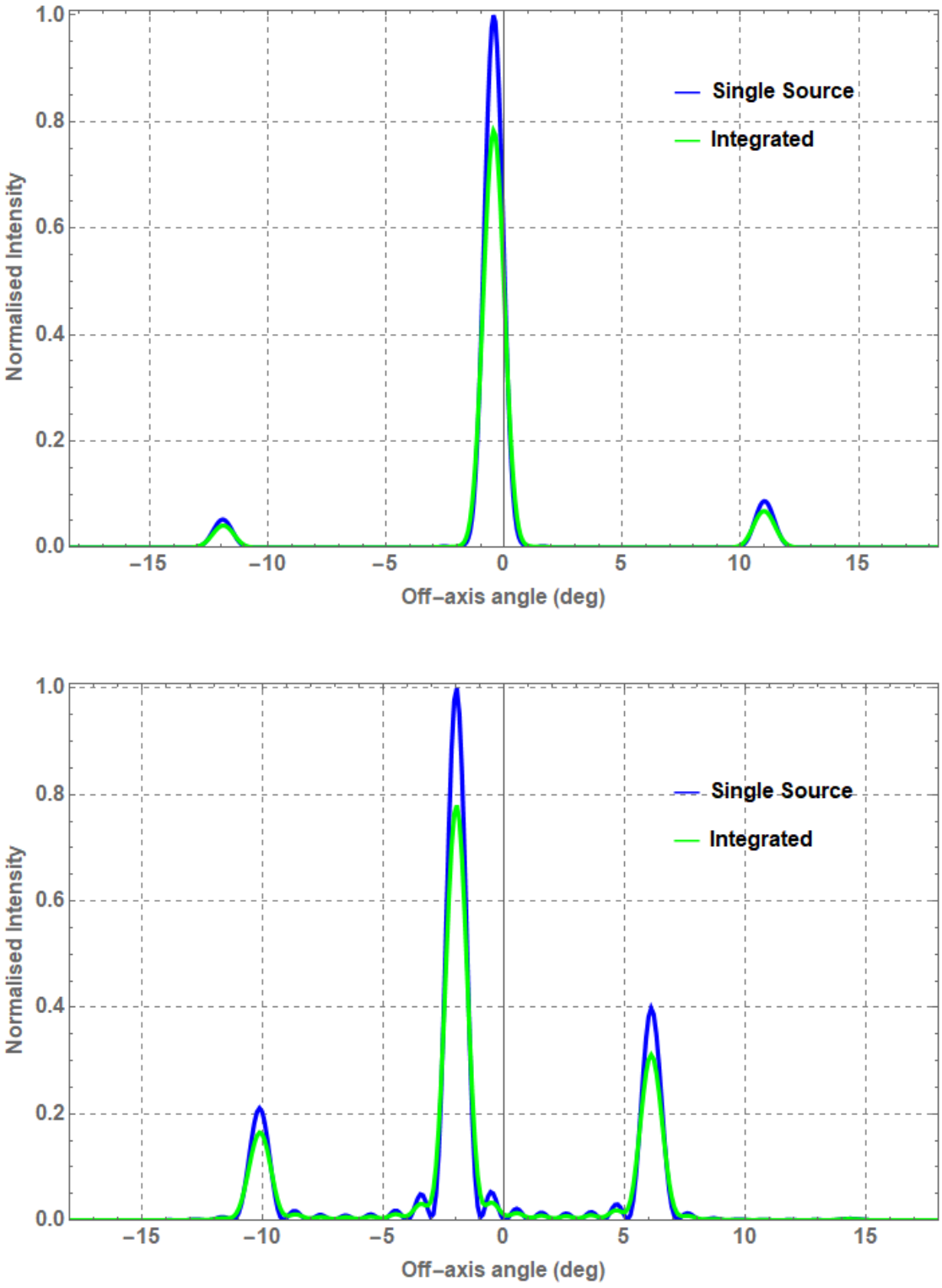

Figure 4.39: The top plot shows a horizontal cut along the main peak of the synthetic beams from Figure 4.38. The bottom plot shows a diagonal cut (top left to bottom right) through the main peak of the synthetic beams from Figure 4.38. Note that the cuts normalised to the peak intensity of the synthetic beam for a single central point source.

4.5.3.2 Integrated vs single point source synthetic beam for off axis pixel (-35.4 mm, -23.4 mm)

Figure 4.40 shows that the peaks of the synthetic beam will change position relative to those of the on-axis pixel as expected. The effects of the integrating over the pixel are similar for the off-axis pixel as for the

on-axis case. There is widening due to the finite TES area occurring here as well as seen for the (−11.4 mm, −2.4 mm) TES, which results in a FWHM of the integrated source of 1.09° compared to 0.98° which is a very similar increase to the case for the 'on-axis' TES.

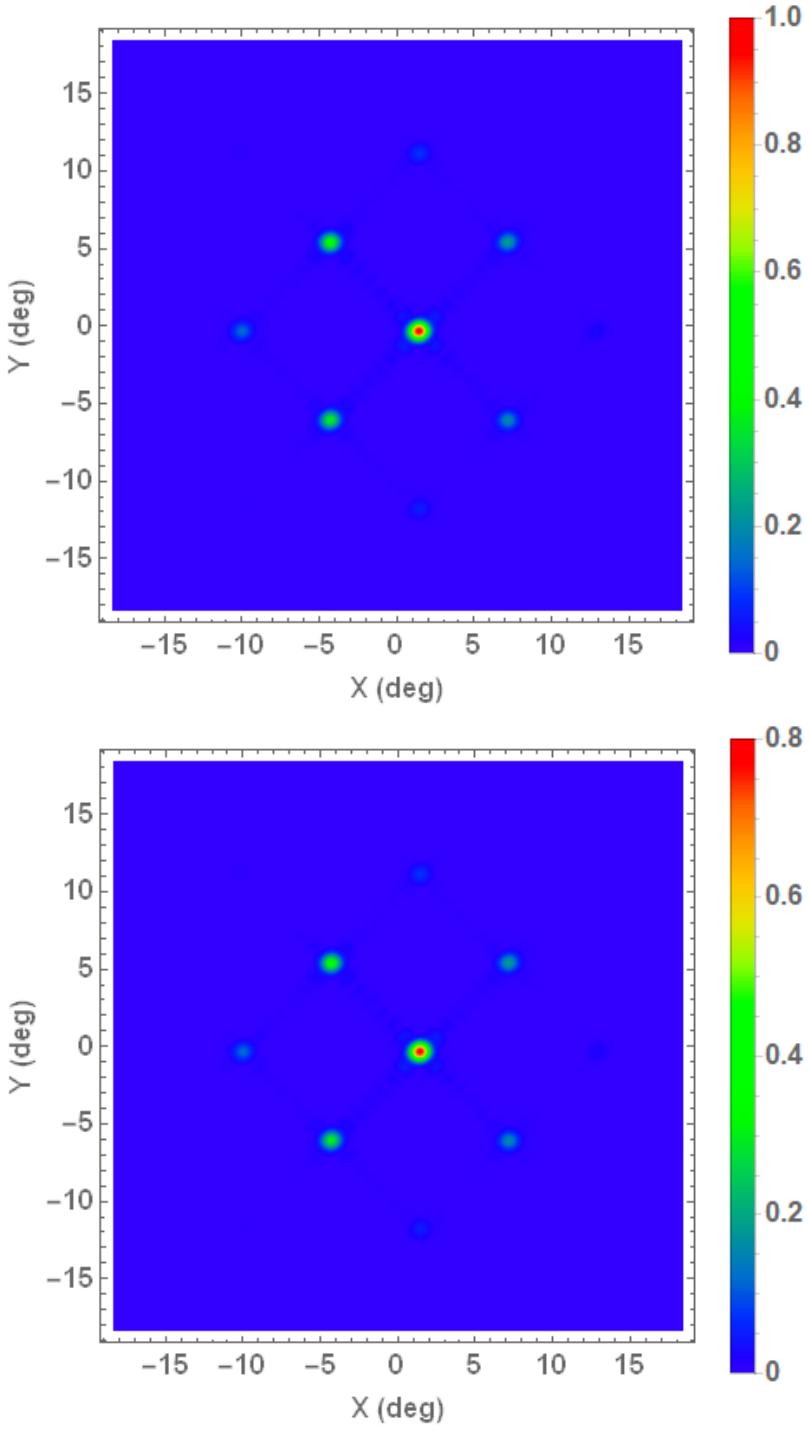

Figure 4.40: Synthetic beam intensity plots for a single point like source (top) and the integrated synthetic beam (bottom). Each beam is normalised to the peak of the point-like beam (top image).

Figure 4.41 shows that off-axis TES have similar drops in response for the integrated synthetic beams again with a roughly 20 % drop observed.

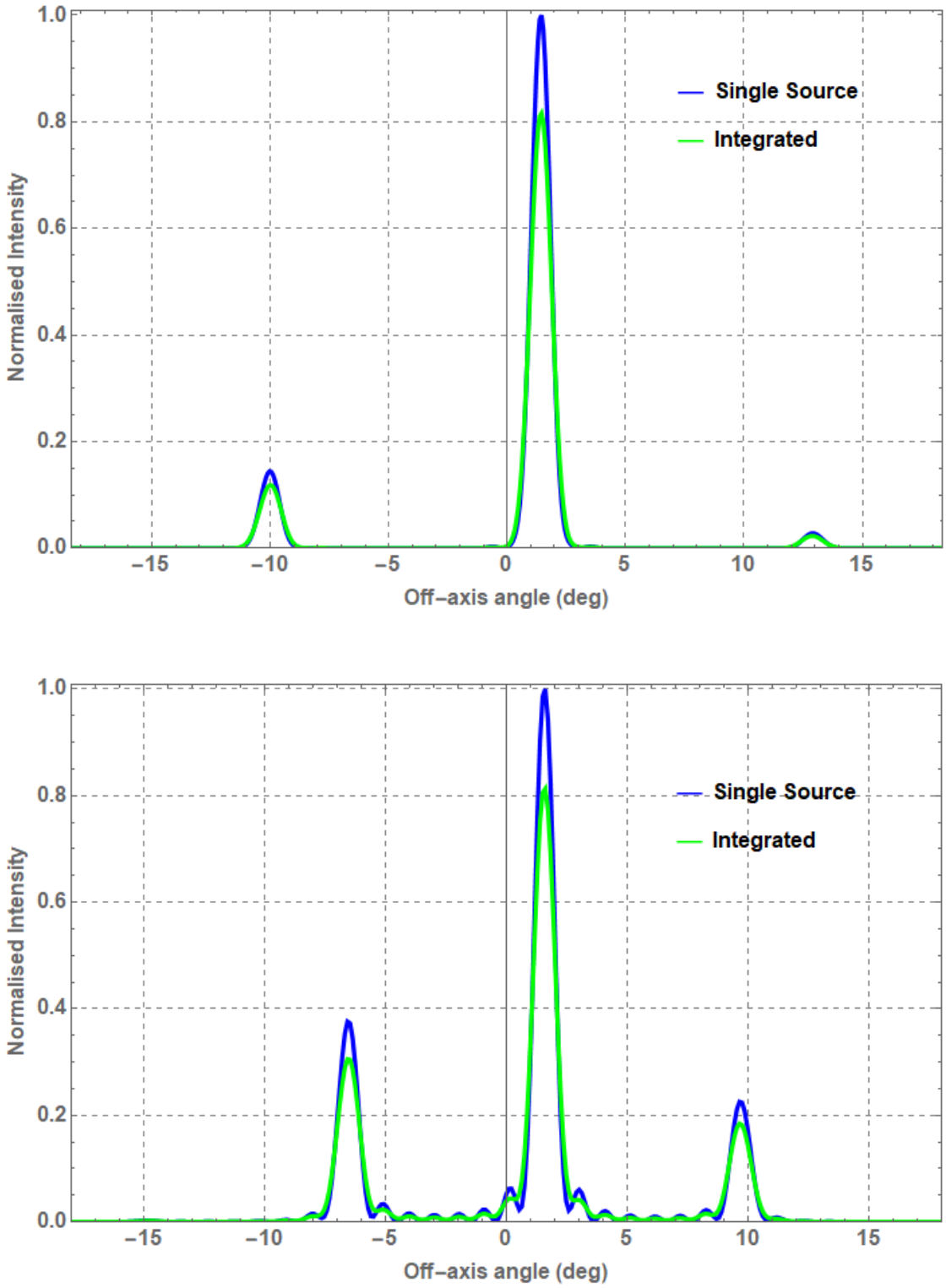

Figure 4.41: The top plot shows a horizontal cut along the main peak of the synthetic beams from Figure 4.40. The bottom plot shows a diagonal cut (top left to bottom right) through the main peak of the synthetic beams from Figure 4.40. Note that the cuts normalised to the peak intensity of the synthetic beam for a single central point source.

This integration method should be used to more accurately simulate the synthesised beam. Comparisons between the integrated and single source method show that there is a difference in the observed response of the full TES and in the structure of the synthetic beam it produces.

4.5.4 Measured and simulated synthetic beam comparison

The synthetic beam for the real instrument has been measured for a few select TESs in the focal plane at varying frequencies across the band during the initial tests performed in 2019 (e.g. Figure 4.42); these initial results show a beam pattern that is quite consistent with the pattern shown for the simulations to date.

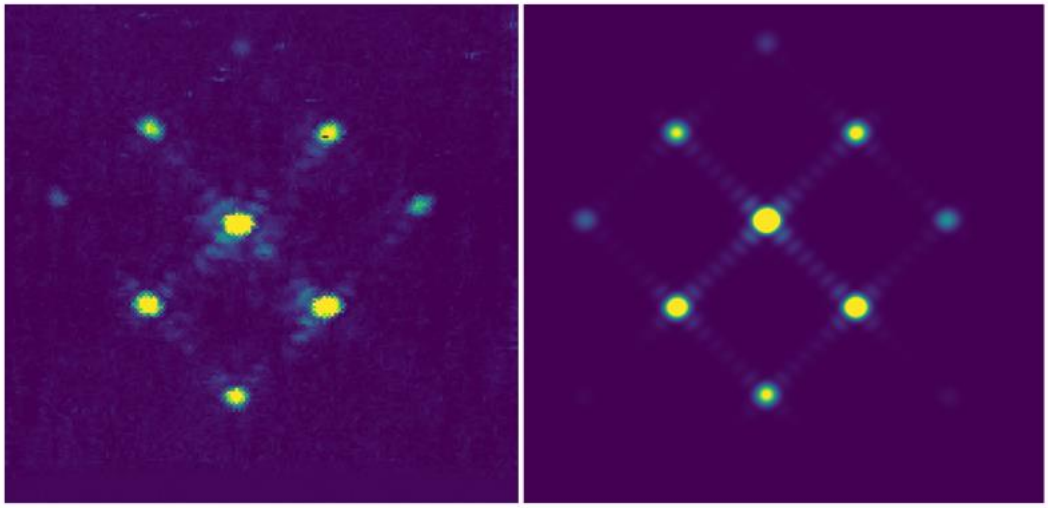

Figure 4.42: Example of a measured synthetic beam (left) compared with the simulated pattern (right)at 150 GHz for a TES (-2.4 mm,-2.4 mm) close to the centre of the focal plane. These plots show relative intensity on a logarithmic scale (the TES signal for these measurements was saturated and so the colour range for the simulated pattern has been clipped for comparison) and cover and area of 33° × 33°. Image obtained from (C O'Sullivan *et al.*, 2020).

Figure 4.43 shows that the peak separation of the measured and simulated peaks for a selection of TESs (seen in Figure 4.44) are reasonably consistent. There were some deviations observed, but this is likely to improve as the calibration setup is better understood and refined. Realignments and changes to elements within the combiner have taken place since, as well as achieving better operating temperatures with the cryogenic systems.

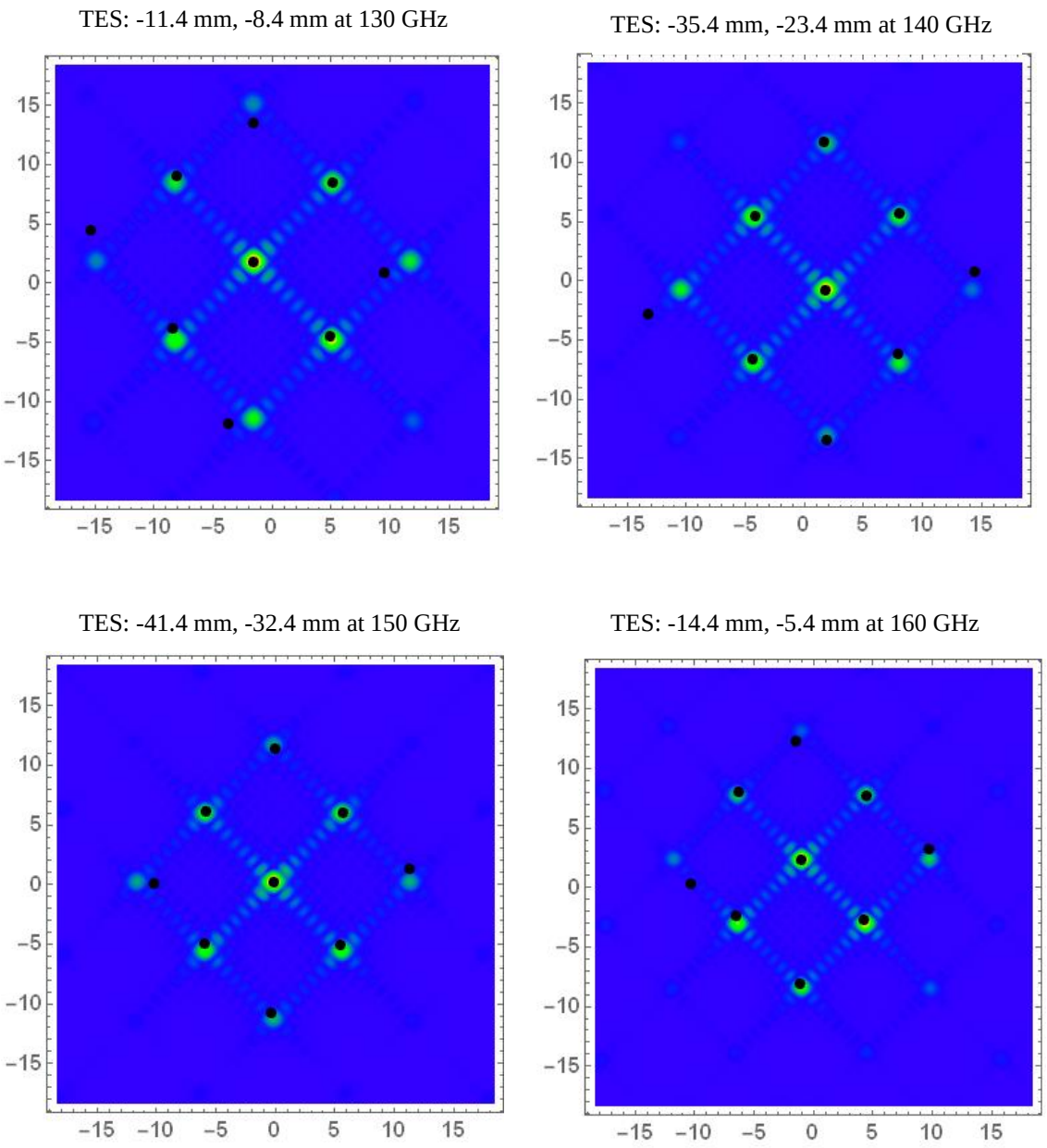

Figure 4.43: Simulated synthetic beams for the TD instrument for a selection of TES at different frequencies across the lower operating band. The overlayed black circles correspond to the location of the peaks in the real measured peaks whose locations (in azimuth and elevation) was provided by L. Mousset of APC (the measured pattern was shifted so that the central peaks aligned).

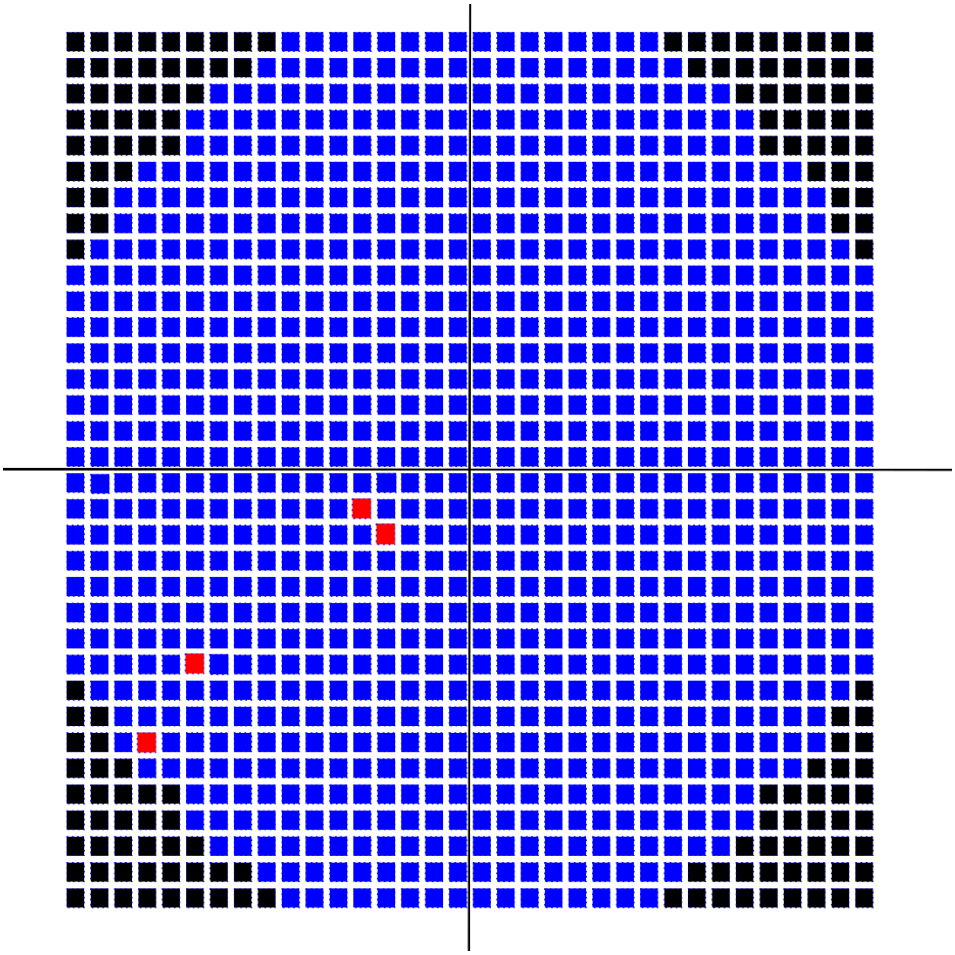

Figure 4.44: TES focal plane array with the location of the (−11.4 mm, −8.4 mm), (−14.4 mm, −5.4 mm) (−41.4 mm, −32.4 mm) and (−35.4 mm, −23.4 mm) TESs highlighted in red.

4.6 Summary

In this chapter I presented rigorous PO simulations of the QUBIC TD to be used during the calibration campaign. These included simulations to determine the accuracy required for mirror alignment, and focal plane patterns to compare with measurements from internal and far-field calibrator sources.

The window function of the instrument was obtained using a PO analysis performed in MODAL and was used as the merit function for a tolerance analysis. The tolerance on the orientation of the mirrors was found to be $\pm$ 0.1° and $\pm$ 1 mm.

Internal calibrator lamps are being used to illuminate the focal plane during laboratory testing. The beam produced by these lamps is very large (roughly resembling a 50° Gaussian beam). This means that the beam is susceptible to truncation from the optical elements in the combiner and results in a non-uniform illumination on the focal plane. The pattern they produce on the focal plane was simulated and can be used as a check of the intercalibration of the TES pixels.

Further testing of the instrument is performed in the laboratory by observing a calibrator source placed in the far-field. In this chapter, a suitable far-field distance of this source was determined from a PO analysis. It was found that a distance of 5 m or more from the horn array was reasonable. Collaborators in APC found that an optical path length of 11.5 m could be obtained by placing the calibrator source off-axis and using a plane mirror to redirect its beam into the instrument. Different truncations (from the plane mirror,

blockages from the cryostat and from the filters before the horn array of the instrument) were modelled, and it was found that these had negligible effects on the pattern produced on the focal plane.

The synthetic beam for various on- and off-axis TESs were simulated in MODAL and were found to agree with the measured beams in terms of the peak locations. Further refinements to the laboratory set-up, scanning mechanism etc. should improve this still further. At the time of writing calibration tests of the TD were ongoing in APC, Paris.

Finally the simulations were then extended to include the integration over the full active area of the TES and the full frequency bandwidth.

The next chapter will use mode matching techniques to analyse the EM properties of the QUBIC feedhorns.

5 QUBIC feed horn mode matching analysis

5.1 Introduction

The QUBIC horns were designed to operate across two wavebands. It has been shown that the horns emit a beam that is close to a 12.9° Gaussian at 150 GHz. It is important to understand how the horns operate at all frequencies in the bands, and that is what this chapter will focus on.

This chapter will introduce the idea of EM modes and how they can be used to describe the radiation inside a waveguide. It will show how mode matching techniques and the in-house SCATTER software (Colgan, 2001; Gleeson, 2004) can be used to model the EM performance of corrugated cylindrical horns. This will then be applied to the nominal QUBIC horns across both operating bands to investigate their performance, note that in this chapter only one side of the horn (Figure 5.3) is analysed, not the full back-to-back horn. The idea of single- and multi-moded operation will be explored, with the horn supporting more modes at the higher band, causing it to have noticeably differing characteristics than the lower band.

Analysing the nominal geometry provides a good overview of how the horn will operate, but it is important to understand how the actual manufactured horns will behave in practice. In the manufacturing of the horns there were defects created on the corrugations of the horns that are intrinsic to the method of manufacture. These defects are called cusps within the collaboration and these will be added to the nominal horn geometry and modelled with the SCATTER software to investigate their impact on the performance of the horn, and how it deviates from the nominal operation.

The full geometry profile for the horns in the TD were measured and provided by collaborators in Milan. Mode matching techniques were used to analyse these horns in a similar way as for the nominal and cusp geometry. A selection of these horns were also analysed in a laboratory setting in Milan, the comparison between the simulated and real results will be shown. In the lab it was only possible to excite the horn with linearly polarised radiation, which was replicated in the simulations, if unpolarised light was used all the modes would be excited.

5.2 Modes in horns

The QUBIC horns are corrugated in design, this means they can be thought of as a collection of cylindrical waveguides of alternating increasing and decreasing radius to create the corrugated effect that is seen in Figure 5.1. The actual profile of the QUBIC horn and how it was generated will be discussed later in the chapter, for now the focus will be on the method of modelling the output of these corrugated horns (a good overview of corrugated horns is provided by Clarricoats and Olver (1984)).

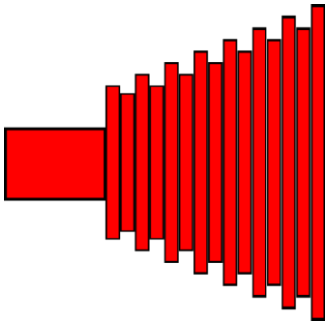

Figure 5.1: Simple profile of a corrugated horn consisting of cylindrical waveguides.

Each of the corrugations in the QUBIC horn can be treated as a uniform smooth walled cylindrical waveguide with a cross section lying in the *x*-*y* plane as in Figure 5.2. When excited with radiation propagating in the *z*-direction the EM radiation in a waveguide can be described with TE (Transverse Electric, E_z=0) and TM (Transverse Magnetic, H_z=0) modes. The radius of the waveguide determines the modes that are present in the waveguide.

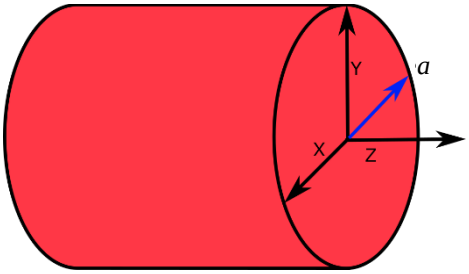

Figure 5.2: Example of a uniform cylindrical waveguide of radius '*a*'.

5.2.1 Mathematical Description of modes

To find mathematical expressions for the modes (this derivation follows Ramo, Whinnery and Van Duzer (1994)) first consider a waveguide arranged as in Figure 5.2 with the radiation propagating in the *z* direction. Each component of a monochromatic wave (equations [57] and [58]) satisfies the wave equation:

$$\nabla^2 E + k^2 E = 0 \qquad [57]$$

$$\nabla^2 H + k^2 H = 0 \qquad [58]$$

where k is the wavenumber of the material filling the waveguide (for this thesis it will assumed to be free space, so $\mu = \mu_0$ and $\varepsilon = \varepsilon_0$, k can be related to the cut-off frequency with:

$$k^2 = k_c^2 - \gamma^2. \qquad [59]$$

where $k_c$is the cutoff wavenumber and γ is the propagation constant that describes wave properties (e.g. attenuation and phase) such that $\gamma = j\beta$, where β is the waveguide wavenumber.

Since the radiation is propagating along the *z*-axis, the EM fields have a dependency in this direction of $e^{-\gamma z}$. Using Maxwell's equations the transverse field components can be expressed in terms of the axial field components. For a dielectric system, assumed to be linearly homogenous and isotropic, and expanded in cylindrical coordinates, these are (Ramo, *et. al*, 1994):

$$E_r = -\frac{j}{k_c^2}\left(\beta \frac{\partial E_z}{\partial r} + \frac{\omega\mu}{r}\frac{\partial H_z}{\partial \varphi}\right) \qquad [60]$$

$$E_\varphi = \frac{j}{k_c^2}\left(-\frac{\beta}{r}\frac{\partial E_z}{\partial \varphi} + \omega\mu \frac{\partial H_z}{\partial r}\right) \qquad [61]$$

$$H_r = \frac{j}{k_c^2}\left(\frac{\omega\varepsilon}{r}\frac{\partial E_z}{\partial \varphi} - \beta\frac{\partial H_z}{\partial r}\right) \quad [62]$$

$$H_\varphi = -\frac{j}{k_c^2}\left(\omega\varepsilon\frac{\partial E_z}{\partial r} + \frac{\beta}{r}\frac{\partial H_z}{\partial \varphi}\right). \quad [63]$$

The solutions for the transverse magnetic and electric modes can be considered separately and will provide expressions for the modes present inside a waveguide.

Transverse Magnetic modes

The separation of variables technique shown by Ramo, *et. al* (1994) is used to provide a solution for E_z:

$$E_z = A_{nl}J_n(k_c r)\begin{pmatrix}\cos n\varphi \\ \sin n\varphi\end{pmatrix} e^{j(\omega t - \beta z)} \quad [64]$$

where n is the azimuthal order, l is the radial order, $J_n$is a Bessel function of the first kind of order n and A_{nl} is a constant that satisfies the boundary conditions of the electric field. The cos and sin terms represent orthogonal mode solutions.

For every azimuthal order *n* there are modes corresponding to a radial order l that propagate inside a waveguide. These propagating modes are determined by the size of the waveguide itself. A boundary condition that must be satisfied by solutions is that along the surface of a perfect conductor the electric field must be equal to zero (i.e. $E_z = E_\varphi = 0$). In Figure 5.2 the radius of the waveguide is *a* and to satisfy the boundary condition the argument for the Bessel function at $r = a$ must be one of the roots such that

$$J_n(k_c a) = 0$$

where $k_c a = p_{nl}$ and p_{nl} is the l^{th} root of the Bessel function $J_n(k_c a)$.

For every azimuthal order n, there is an infinite number of radial orders l that satisfy this boundary condition, these radial orders can be considered as the TM modes that are propagating in the waveguide. There is a frequency below which propagation of these modes will not occur, known as the cutoff frequency and this can be obtained from $k_c = p_{nl}/a$, showing that the radius of the waveguide as well as the frequency of the radiation has an effect on the modes present in a waveguide. Using equations [60]-[63] the transverse components of the electric and magnetic fields of the TM modes can be expressed in Cartesian coordinates as seen in equations [65]-[68] (see e.g. Gleeson (2004)). It is useful to express the modes in cartesian coordinates as it allows for the separation of the co- and cross- polar components (*x* and *y* respectively if incident radiation is polarised in the *x*-direction) which is important in the analysis of the performance of a waveguide.

$${e_{nl}^{TM}}_x = \sqrt{\frac{(2-\delta_{n0})}{4\pi a^2 J_{n+1}^2(p_{nl})}}\left(J_{n-1}\left(p_{nl}\frac{r}{a}\right)\begin{bmatrix}\cos(n-1)\,\varphi \\ -\sin(n-1)\,\varphi\end{bmatrix} - J_{n+1}\left(p_{nl}\frac{r}{a}\right)\begin{bmatrix}\cos(n+1)\,\varphi \\ -\sin(n+1)\,\varphi\end{bmatrix}\right) \quad [65]$$

$$e_{nl}^{TM}{}_{y} = -\sqrt{\frac{(2-\delta_{n0})}{4\pi a^2 J_{n+1}^2(p_{nl})}}\left(J_{n-1}\left(p_{nl}\frac{r}{a}\right)\begin{bmatrix}\sin(n-1)\,\varphi\\ \cos(n-1)\,\varphi\end{bmatrix} + J_{n+1}\left(p_{nl}\frac{r}{a}\right)\begin{bmatrix}\sin(n+1)\,\varphi\\ \cos(n+1)\,\varphi\end{bmatrix}\right) \quad [66]$$

$$h_{nl}^{TM}{}_{x} = \sqrt{\frac{(2-\delta_{n0})}{4Z_{TM_{nl}}^2 \pi a^2 J_{n+1}^2(p_{nl})}}\left(J_{n-1}\left(p_{nl}\frac{r}{a}\right)\begin{bmatrix}\sin(n-1)\,\varphi\\ \cos(n-1)\,\varphi\end{bmatrix} + J_{n+1}\left(p_{nl}\frac{r}{a}\right)\begin{bmatrix}\sin(n+1)\,\varphi\\ \cos(n+1)\,\varphi\end{bmatrix}\right) \quad [67]$$

$$h_{nl}^{TM}{}_{y} = \sqrt{\frac{(2-\delta_{n0})}{4Z_{TM_{nl}}^2 \pi a^2 J_{n+1}^2(p_{nl})}}\left(J_{n-1}\left(p_{nl}\frac{r}{a}\right)\begin{bmatrix}\cos(n-1)\,\varphi\\ -\sin(n-1)\,\varphi\end{bmatrix} - J_{n+1}\left(p_{nl}\frac{r}{a}\right)\begin{bmatrix}\cos(n+1)\,\varphi\\ -\sin(n+1)\,\varphi\end{bmatrix}\right) \quad [68]$$

Transverse Electric modes

A very similar method is used to obtain the expressions for the TE modes. The solution for H_z is obtained with the separation of variables method (Ramo, *et, al*, 1994)

$$H_z = B_{nl} J_n(k_c r)\begin{pmatrix}\cos n\varphi\\ \sin\ n\varphi\end{pmatrix} e^{j(\omega t-\beta z)} \quad [69]$$

where n is the azimuthal order, l is the radial order, J_n is a Bessel function of the first kind of order n, and B_{nl} is a constant that satisfies the boundary conditions of the magnetic field.

Again, the boundary condition that the electric field at the surface ($r = a$) is zero must be satisfied. This is satisfied for H_z when

$$\frac{dJ_n}{dz}(k_c a) = 0$$

where $k_c a = p'_{nl} = q_{nl}$, and q_{nl} is the l^{th} root of the derivative of the Bessel function $J_n(k_c a)$

similar to before using equations [60]-[63] the transverse components of the electric and magnetic fields of the TE modes can be expressed in Cartesian coordinates (see example Gleeson (2004)):

$$e_{nl}^{TE}{}_{x} = \sqrt{\frac{(2-\delta_{n0})}{4\pi a^2(1-(n/q_{nl})^2)J_n^2(q_{nl})}}\left(J_{n-1}\left(q_{nl}\frac{r}{a}\right)\begin{bmatrix}\cos(n-1)\,\varphi\\ -\sin(n-1)\,\varphi\end{bmatrix} + J_{n+1}\left(q_{nl}\frac{r}{a}\right)\begin{bmatrix}\cos(n+1)\,\varphi\\ -\sin(n+1)\,\varphi\end{bmatrix}\right) \quad [70]$$

$$e_{nl}^{TE}{}_{y} = -\sqrt{\frac{(2-\delta_{n0})}{4\pi a^2(1-(n/q_{nl})^2)J_n^2(q_{nl})}}\left(J_{n-1}\left(q_{nl}\frac{r}{a}\right)\begin{bmatrix}\sin(n-1)\,\varphi\\ \cos(n-1)\,\varphi\end{bmatrix} - J_{n+1}\left(q_{nl}\frac{r}{a}\right)\begin{bmatrix}\sin(n+1)\,\varphi\\ \cos(n+1)\,\varphi\end{bmatrix}\right) \quad [71]$$

$$h_{nl}^{TE}{}_{x} = \sqrt{\frac{(2-\delta_{n0})}{4Z_{TE_{nl}}^{2}\pi a^{2}(1-(n/q_{nl})^{2})J_{n}^{2}(q_{nl})}}\left(J_{n-1}\left(q_{nl}\frac{r}{a}\right)\begin{bmatrix}\sin(n-1)\,\varphi\\ \cos(n-1)\,\varphi\end{bmatrix} - J_{n+1}\left(q_{nl}\frac{r}{a}\right)\begin{bmatrix}\sin(n+1)\,\varphi\\ \cos(n+1)\,\varphi\end{bmatrix}\right) \quad [72]$$

$$h_{nl}^{TE}{}_{y} = \sqrt{\frac{(2-\delta_{n0})}{4Z_{TE_{nl}}^{2}\pi a^{2}(1-(n/q_{nl})^{2})J_{n}^{2}(q_{nl})}}\left(J_{n-1}\left(q_{nl}\frac{r}{a}\right)\begin{bmatrix}\cos(n-1)\,\varphi\\ -\sin(n-1)\,\varphi\end{bmatrix} + J_{n+1}\left(q_{nl}\frac{r}{a}\right)\begin{bmatrix}\cos(n+1)\,\varphi\\ -\sin(n+1)\,\varphi\end{bmatrix}\right) \quad [73]$$

5.2.2 Mode matching software

The mode matching software, SCATTER, used for this work has been developed in the department of Experimental Physics at Maynooth University over many years (examples can be seen in Colgan (2001); Gleeson (2004); Kalinauskaite (2018)). This software produces a scattering matrix, which describes the modes transmitted and reflected in a waveguide (this research assumes the waveguide is made from PEC – perfect electrical conductor – material). This section will give an overview of how the scattering matrix is calculated and how it is used to analyse the QUBIC horns, a detailed mathematical derivation of the scattering matrix is provided by Kalinauskaite (2018) for example.

5.2.2.1 Scattering matrix

We refer to the input and output of the horn as Port 1 and Port 2 respectively (Figure 5.3) and the column vectors [A], [B], [C] and [D] contain the mode coefficients of the incident field at port 1 and port 2 ([A] and [C] respectively) and output fields at port 1 and port 2 ([B] and [D] respectively). These column matrices are related to each other by the scattering matrix as given in equations [74] – [76] (Olver *et al.*, 1994). The scattering matrix is calculated for each corrugation (or waveguide) in the horn and then cascaded onto the scattering matrix for all proceeding corrugations (note that this method will only analyse geometries with stepped discontinuities, i.e. a sudden jump in the profile). This continues along the entire horn for each corrugation generating the four scattering matrices seen in Figure 5.4 describing the scattering for the entire horn as it would for a waveguide.

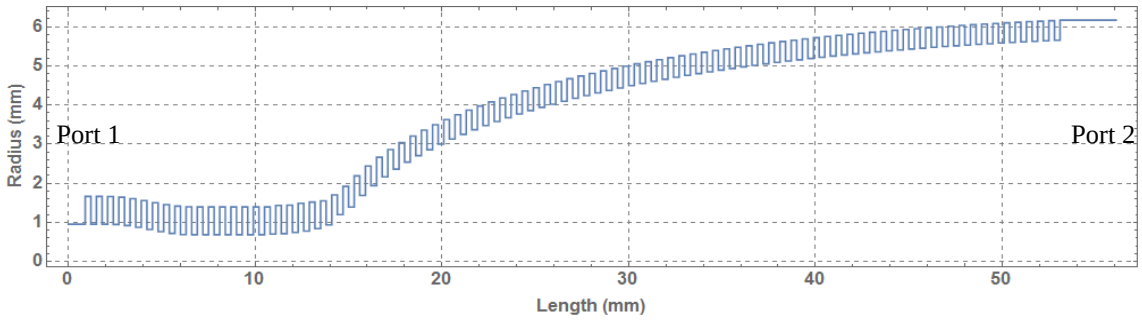

Figure 5.3: QUBIC horn profile, where the radiation is incident on Port 1 (normally called the throat) and Port 2 (normally called the aperture) is the output.

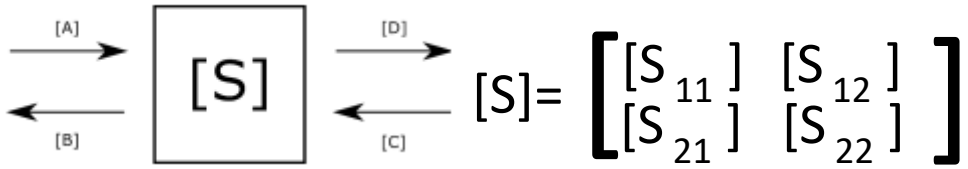

Figure 5.4: The scattering matrix can be subdivided into matrices that describe the modes incident and reflected from port 1 [$\mathbf{S_{11}}$], incident from Port 1 and transmitted to Port 2 [$\mathbf{S_{21}}$], etc.

[A], [B], [C] and [D] are column vectors describing the modal coefficients of the input and output fields:

$$\begin{bmatrix}[B]\\[D]\end{bmatrix} = [S]\begin{bmatrix}[A]\\[C]\end{bmatrix} \quad [74]$$

or

$$[B] = S_{11}[A] + S_{12}[C] \quad [75]$$

$$[D] = S_{21}[A] + S_{22}[C]. \quad [76]$$

Using the mode matching software

The user must define the number of azimuthal orders n to be investigated and the software will output the four scattering matrices per azimuthal order which will be structured as in Figure 5.5. The user also defines the number of TE and TM radial order modes l that are analysed, resulting in an $L\times L$ matrix (where $L = 2l$). Each column describes the amount of scattering from one mode to all other modes (note that these are complex values), e.g. the first column describes the scattering from the TE_{11} mode to all the other TE and TM modes (the first 1 to l rows are to all TE modes and the next $l + 1$ to L rows are to all TM modes). Each row describes the amount of scattering from all other modes to a single mode, e.g. first row is the proportion of all modes defined that are scattered into the TE_{11} mode (again this is split evenly into the TE and TM modes). It is important to note that there is no scattering between azimuthal orders for a symmetric waveguide, and so their scattering matrices can be considered separately. As mentioned previously there are an infinite number of TE and TM modes that satisfy the boundary conditions for each azimuthal order. It is not computationally possible to perform an analysis on an infinite number of modes, however not all

of the satisfying modes will carry equal power and some will eventually become negligible, so it is not necessary to analyse all of these modes but there must be a sufficient number of TE and TM modes investigated to give an accurate description of the radiation. For this thesis 30 TE and 30 TM modes per azimuthal order were sufficient to describe the scattering inside the QUBIC horn. This gave rise to 60 total waveguide modes.

Essentially the scattering matrix is used to describe what happens to an input field described by [A] inside a waveguide. [A] is of length L, where each element is an input mode coefficient. Rows 1 to l describe the input TE modes and rows $l+1$ to L describe the TM modes. For simplicity, if a mode is in the input field then it will have a value of '1', and if not it will have a value of '0', essentially the modes at the input will be 'on' or 'off'. The scattering matrix can then be utilised (equations [75] and [76]) to get the output field at either port. E.g. if a horn is excited with the TE_{11} mode only (the first element in [A] is set to 1 and the rest are set to 0) then the first column of the scattering matrix is used solely to determine what happens to this mode inside the waveguide and to get the output. The coefficients are normalised to unity so that the total power of the reflected and transmitted fields will be one. The scattering matrices, therefore, allow for the generation of the transmitted and reflected power (also known as return loss), as well as the generation of the far field pattern.

$$[S_{BA}] = \begin{bmatrix} TE_{11,B} \leftarrow TE_{11,A} & TE_{11,B} \leftarrow TE_{12,A} & \cdots & TE_{11,B} \leftarrow TM_{11,A} & TE_{11,B} \leftarrow TM_{12,A} & \cdots \\ TE_{12,B} \leftarrow TE_{11,A} & TE_{12,B} \leftarrow TE_{12,A} & \cdots & TE_{12,B} \leftarrow TM_{11,A} & TE_{12,B} \leftarrow TM_{12,A} & \cdots \\ TE_{13,B} \leftarrow TE_{11,A} & TE_{13,B} \leftarrow TE_{12,A} & \cdots & TE_{13,B} \leftarrow TM_{11,A} & TE_{13,B} \leftarrow TM_{12,A} & \cdots \\ \vdots & \vdots & \cdots & \vdots & \vdots & \cdots \\ \vdots & \vdots & \cdots & \vdots & \vdots & \cdots \\ TM_{11,B} \leftarrow TE_{11,A} & TM_{11,B} \leftarrow TE_{12,A} & \cdots & TM_{11,B} \leftarrow TM_{11,A} & TM_{11,B} \leftarrow TM_{12,A} & \cdots \\ TM_{12,B} \leftarrow TE_{11,A} & TM_{12,B} \leftarrow TE_{12,A} & \cdots & TM_{12,B} \leftarrow TM_{11,A} & TM_{12,B} \leftarrow TM_{12,A} & \cdots \\ TM_{13,B} \leftarrow TE_{11,A} & TM_{13,B} \leftarrow TE_{12,A} & \cdots & TM_{13,B} \leftarrow TM_{11,A} & TM_{13,B} \leftarrow TM_{12,A} & \cdots \\ \vdots & \vdots & \cdots & \vdots & \vdots & \cdots \\ \vdots & \vdots & \cdots & \vdots & \vdots & \cdots \end{bmatrix}$$

Figure 5.5: structure of a scattering matrix for the first azimuthal order, which describes the scattering from Port A to Port B. Image obtained from Cahill (2015).

5.2.3 Single moded operation

5.2.3.1 Reflected and transmitted power

The S_{21} and S_{11} matrix can be used to analyse the transmitted and reflected power respectively. I will describe two methods for doing this. The first is mathematically straight forward and simply requires equations [75] and [76]. The other involves a singular value decomposition (SVD) of the matrix. Both of these methods will be examined in this section (they will be called the scattering matrix and SVD method respectively) using the scattering matrices generated for the QUBIC nominal horn design at 150 GHz, 30 TE and 30 TM are used, resulting in 60×60 scattering matrices. At this frequency, the horn is said to be single moded. This 'single mode' corresponds to one hybrid mode, where the hybrid modes are the natural eigenmodes of corrugated horns (in the same way the TE and TM modes are the natural modes of the individual sections/waveguides). A single mode in the output field of such a corrugated horn is a combination of TE and TM modes, that maintain a fixed phase relationship. For example when a horn is

designed to be single moded and excited by the TE_{11} mode then power from this modes scatters to the TM_{11} mode resulting in a single moded output field which is a combination of both the TE_{11} and TM_{11} modes, this is the hybrid mode called HE_{11} which (when balanced) can be approximated as a combination of 85 % of the TE_{11} and 15 % of the TM_{11} mode (Figure 5.6). This will be reflected in the scattering matrix, which will be shown later in this chapter.

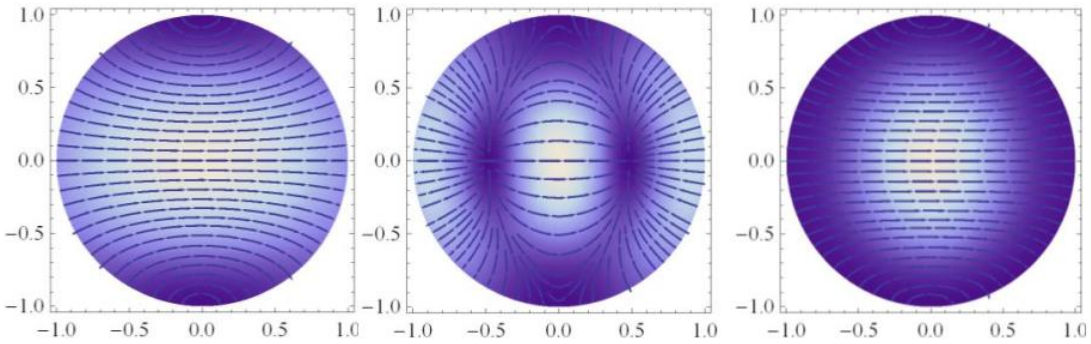

Figure 5.6 TE_{11} mode (left) and TM_{11} mode (middle) are combined with the ratio ($0.85TE_{11}$ +0.15 TM_{11}) to generate the HE_{11} mode (right). The magnitude is indicated by the brightness of the plot and polarisation by the lines/arrows. Image adapted from Scully (2015).

Scattering matrix method

In this method the [C] column vector can be set to 0 as it is assumed that the incident radiation is only present at Port 1, hence the output fields are entirely dependent on the scattering matrix and the input field [A] as in equations [77] and [78].

$$[B] = S_{11}[A] \qquad [77]$$

$$[D] = S_{21}[A] \qquad [78]$$

Firstly, the S_{21} matrix will be investigated. As mentioned previously the S matrices are normalised so that the total power of the combined reflected and transmitted modes/fields will be one. The elements of the S matrices are also complex, so the power in the scattering of each transmitted mode can be obtained by multiplying the S_{21} matrix by its complex conjugate. The total power can be obtained by simply summing up the power of all the elements (modes) as in Table 5.1. It can be seen that there is quite high transmission at this band and this was one of the reasons that this horn design was chosen for QUBIC. At these frequencies it is clear that only scattering from one mode is supported within the horn, since over 99% of the total power is contained within the 1st column (which describes scattering from the TE_{11} mode). Hence across this band the scattering in the horn is accurately described by an input column matrix [A] consisting of 60 elements but only the first entry is 'on':

$$[A] = \begin{bmatrix} 1 \\ 0 \\ 0 \\ \vdots \end{bmatrix}$$

Table 5.1: Summed values of the powers of all modes in the S21 matrix and for the 1st and 31st column. Note that these correspond to the [D] output vector field.

Frequency (GHz)	Total S21	1st Column (TE11)	31st column (TM11)
130	0.8869	0.8867	0.0002
150	0.9949	0.9947	0.0002
170	0.9968	0.9965	0.0003

The same can be done for the S_{11} matrix (Table 5.2) and it was found that the total power was very low, note that the S_{11} presented in this thesis was obtained by analysing only one side of the back to back horn (Figure 5.3) meaning that for the full horn the S_{11} would be at least twice as large. Again it is seen that nearly all of the power is contained within the 1st column, which corresponds with the results for the S21 matrix. Also note that the combining the power in Table 5.1 and Table 5.2 provides a value of unity, thus any power that is not transmitted can be assumed to be reflected (valid for a PEC material where there is no loss).

Table 5.2: Summed values of the powers of all modes in the S_{11} matrix and for the 1st and 31st column. Note that these correspond to the [B] output vector field.

Frequency (GHz)	Total S11	1st Column (TE11)	31st column (TM11)
130	0.1142	0.1138	0.0005
150	0.0057	0.0055	0.0002
170	0.0041	0.0037	0.0004

The reflected and transmitted power from each mode was summed across the lower band (130 – 170 GHz) in 1 GHz steps, which resulted in the graph seen in Figure 5.7. Note that since the total power is normalised to unity the power for the reflected pattern at each frequency can be obtained by simply subtracting the transmitted power from one or by using the scattering matrix method.

It can be seen from Table 5.3 (which corresponds to the output vector field [D]) that the HE_{11} mode is propagating. At all the frequencies investigated roughly 98% of the total power is contained within the TE_{11} and TM_{11} modes, with a ratio close to that of the 85/15 balanced ratio of the HE_{11} mode made above. At these frequencies, the QUBIC horns only support scattering from the TE_{11} mode (if other modes are present in the input field they will not contribute any meaningful power at the output).

Table 5.3: Values of the 1st and 31st elements in the 1st column of the S_{21} matrix. Note that the total power in these two elements alone contain nearly the total power from Table 5.1.

Frequency (GHz)	1st row(TE11)	31st row (TM11)	Total
130	0.6834	0.1875	0.8709
150	0.7954	0.1791	0.9745
170	0.7847	0.1892	0.9739

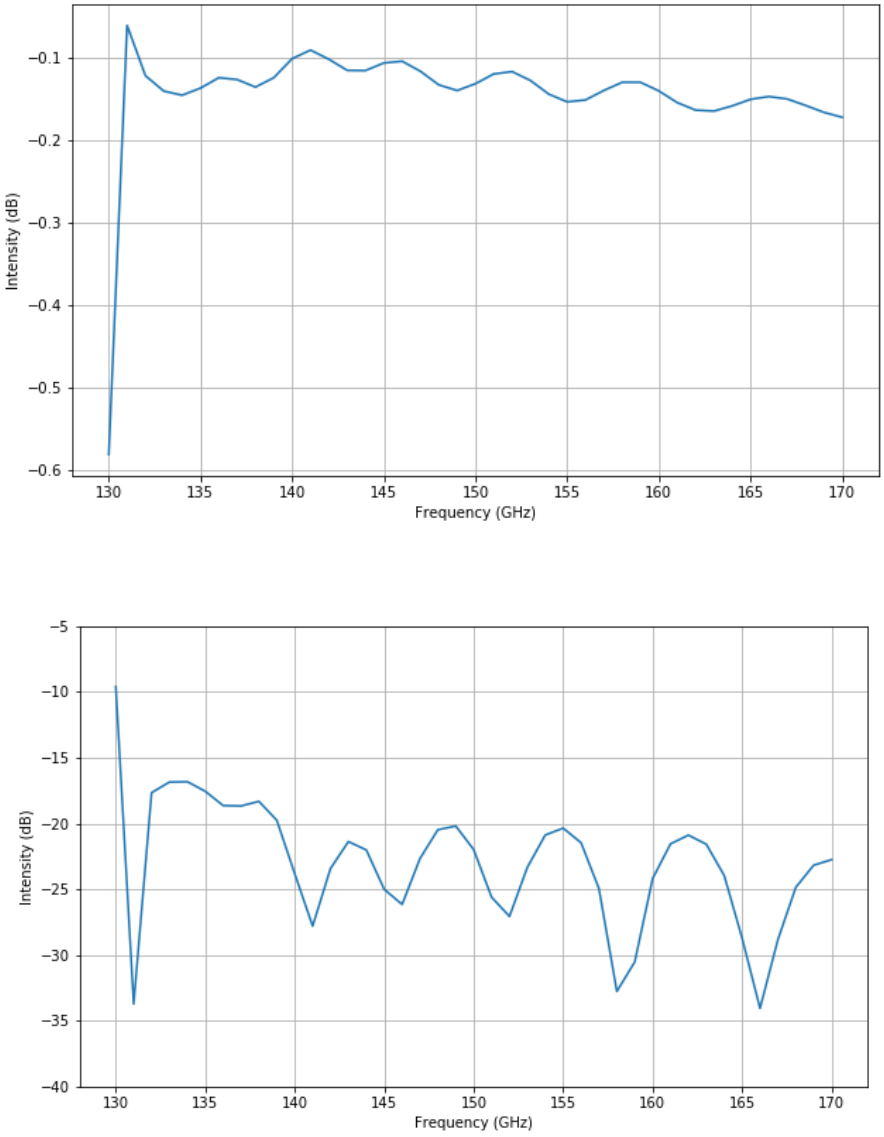

Figure 5.7: Transmitted power (top) and reflected power (bottom) from the QUBIC horn using the scattering matrix method on one side of the horn.

SVD method

A SVD can be performed on the scattering matrix so that it can be expressed as the product of three matrices $[U]$, $[\Sigma]$ and $[V^*]$ (Wilson (2014) and McCarthy (2014) give a detailed discussion of this method) as shown in equation [79]. $[U]$ and $[V^*]$ are $L \times L$ matrices which contain the input and the complex transpose of the output waveguide modes respectively (hence none of the complex information about the modes is lost) and $[\Sigma]$ is an $L \times L$ diagonal matrix in which the elements along the main diagonal are real numbers that describe the singular values of the scattering matrix. These singular values are the relative weights of the modes in the waveguide arranged in order of decreasing value.

$$[S_{ab}] = [U][\Sigma][V^*]. \quad [79]$$

These three matrices can be used to generate the output field [D]:

$$[D] = [\Sigma][A] \quad [80]$$

An important result of the SVD analysis was that the singular values represent power contained by independent (i.e. the hybrid) modes in the waveguide. Essentially any non-negligible (i.e. > 0.001) value in the main diagonal of $[\Sigma]$ corresponds to a hybrid mode in the waveguide (this method makes clear the hybrid nature of the modes in the QUBIC horn). These modes have no phase relation to each other and thus are mutually incoherent and represent independent power channels inside waveguide. If there are multiple values along the main diagonal, then the horn is considered to be multi-moded (the horn is also multi-moded if there is power in more than one azimuthal order, this will be discussed more in Section 5.2.4) and knowing this will be very useful when analysing the horn at the higher operating frequencies. Squaring these singular values provides the power present in each mode. Table 5.4 is convincing evidence that the QUBIC horn is single moded across the lower band. Note, as expected, the singular value at 150 GHz is the same as the total power shown in the S_{21} matrix above.

Table 5.4: Square of the first two singular values (Σ_{11} and Σ_{22}) of the S_{21} matrix generated at 150 GHz for the n=1 azimuthal order.

Frequency (GHz)	Σ_{11}^2	Σ_{22}^2
130	0.88695	0
132	0.98697	0
134	0.98291	0
136	0.98892	0
138	0.98751	0
140	0.99649	0
142	0.99744	0
144	0.99538	0
146	0.99904	0
148	0.99354	0
150	0.99491	0
152	0.99931	0
154	0.99411	0
156	0.99358	0
158	0.99955	0
160	0.99825	0
162	0.99405	0
164	0.99635	0
166	1.00013	0
168	0.99888	0
170	0.99686	0

Obtaining the reflected and transmitted power using this method results in the plots seen in Figure 5.8. Both methods give the same transmitted power across the band. The reflected power does show some differences between the methods, but since it is at such low power levels and there would be some numerical round-off errors as expected, they are acceptable.

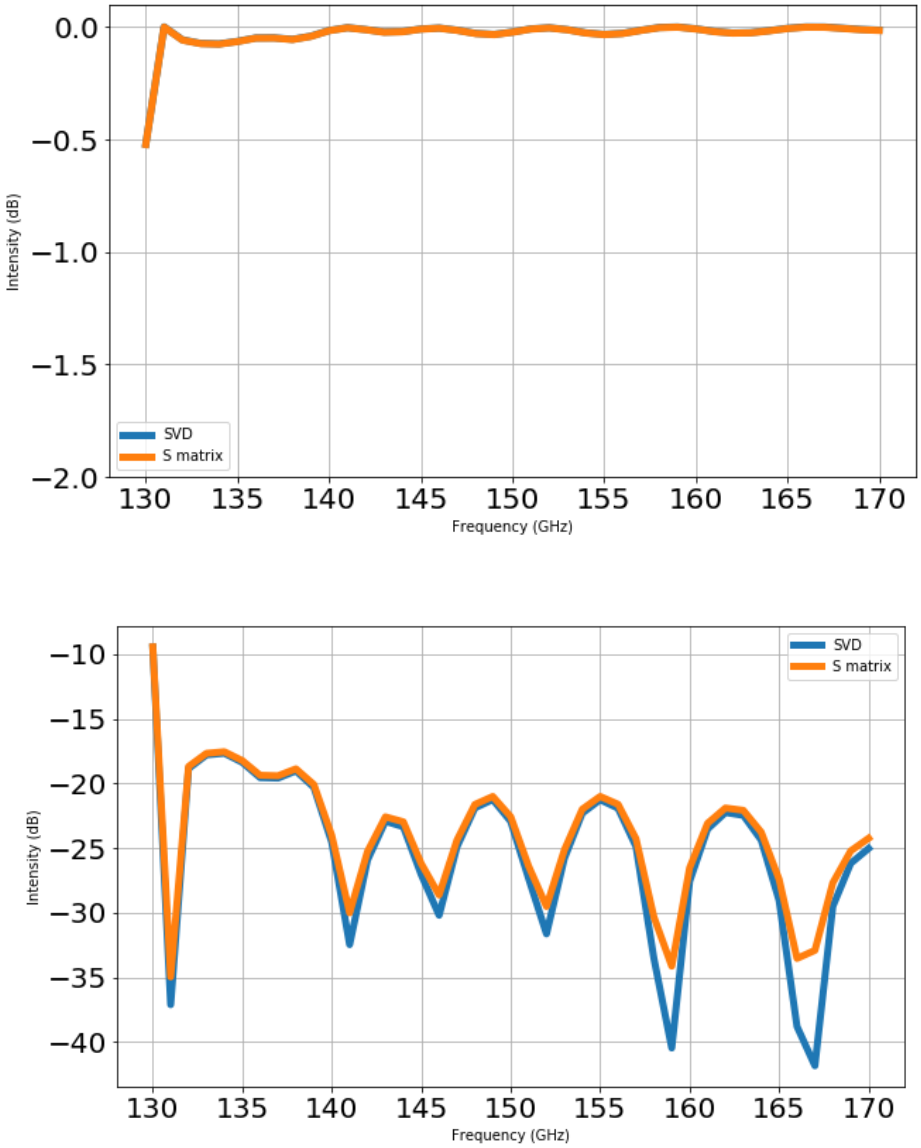

Figure 5.8: comparison between the transmitted power (top) and reflected power (bottom) for both methods used on one side of the horn.

5.2.3.2 Far-field generation

As described by Gleeson (2004), the far-field pattern of an electromagnetic wave may be projected onto an *x*-*y* plane (as in Figure 5.9) and can be expressed in polar coordinates, as in equation [81], with the modal field components coming from equations [65]-[68] and [70] [70]-[73]. Each TE and TM mode must be treated separately and then can be recombined later.

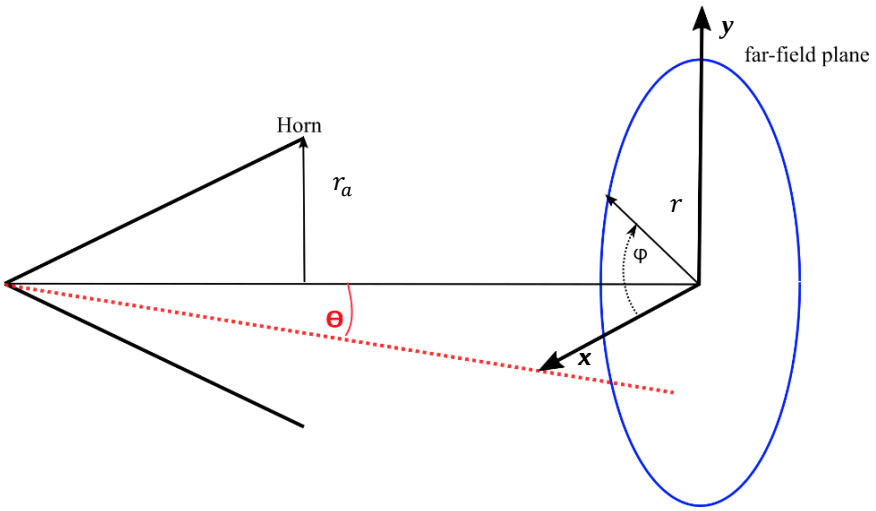

Figure 5.9: Schematic of coordinates used for a horn beam propagating onto a far-field plane.

$$E^{FF}(\theta,\varphi) \propto (1+cos\,\theta)\left(f_x(\theta,\varphi)\hat{\imath} + f_y(\theta,\varphi)\hat{\jmath}\right) \quad [81]$$

Where θ is the elevation angle in the far-field, φ is the azimuthal angle in the far-field, $f_x(\theta,\varphi)$ is the Fourier transform of the *x*-component of the TE or TM modal electric field, $f_y(\theta,\varphi)$ is the Fourier transform of the *y*-component of the TE or TM modal electric field.

The Fourier transformed components shown below can be obtained from the mathematical descriptions of the TM and TE modes – equations [65]-[66] and [70]-[71] respectively – as shown in Gleeson, (2004).

$$[e_{nl}^{TMx}(\theta,\varphi)]^{FF} \propto (1+\cos\theta)\sqrt{\frac{(2-\delta_{n0})}{4\pi a^2 J_{n+1}^2(p_{nl})}} \times\left(\mathfrak{I}_{n-1}^{FF}(\theta;p_{nl})\begin{bmatrix}\cos(n-1)\,\varphi\\ -\sin(n-1)\,\varphi\end{bmatrix}\frac{2\pi}{i^{-(n-1)}} - \mathfrak{I}_{n+1}^{FF}(\theta;p_{nl})\begin{bmatrix}\cos(n+1)\,\varphi\\ -\sin(n+1)\,\varphi\end{bmatrix}\frac{2\pi}{i^{-(n+1)}}\right) \quad [82]$$

$$\left[e_{nl}^{TMy}(\theta,\varphi)\right]^{FF} \propto -(1+\cos\theta)\sqrt{\frac{(2-\delta_{n0})}{4\pi a^2 J_{n+1}^2(p_{nl})}} \times\left(\mathfrak{I}_{n-1}^{FF}(\theta;p_{nl})\begin{bmatrix}\sin(n-1)\,\varphi\\ \cos(n-1)\,\varphi_o\end{bmatrix}\frac{2\pi}{i^{-(n-1)}} + \mathfrak{I}_{n+1}^{FF}(\theta;p_{nl})\begin{bmatrix}\sin(n+1)\,\varphi\\ \cos(n+1)\,\varphi\end{bmatrix}\frac{2\pi}{i^{-(n+1)}}\right) \quad [83]$$

$$[e_{nl}^{TEx}(\theta,\varphi)]^{FF} \propto (1+\cos\theta)\sqrt{\frac{(2-\delta_{n0})}{4\pi a^2(1-(n/q_{nl})^2)J_n^2(q_{nl})}} \times\left(\mathfrak{I}_{n-1}^{FF}(\theta;q_{nl})\begin{bmatrix}\cos(n-1)\,\varphi\\ -\sin(n-1)\,\varphi\end{bmatrix}\frac{2\pi}{i^{-(n-1)}} + \mathfrak{I}_{n+1}^{FF}(\theta;q_{nl})\begin{bmatrix}\cos(n+1)\,\varphi\\ -\sin(n+1)\,\varphi\end{bmatrix}\frac{2\pi}{i^{-(n+1)}}\right) \quad [84]$$

$$\left[e_{nl}^{TEy}(\theta,\varphi)\right]^{FF} \propto -(1+\cos\theta)\sqrt{\frac{(2-\delta_{n0})}{4\pi a^2(1-(n/q_{nl})^2)J_n^2(q_{nl})}} \times \left(\Im_{n-1}^{FF}(\theta;q_{nl})\begin{bmatrix}\sin(n-1)\,\varphi\\ \cos(n-1)\,\varphi\end{bmatrix}\frac{2\pi}{i^{-(n-1)}} - \Im_{n+1}^{FF}(\theta;q_{nl})\begin{bmatrix}\sin(n+1)\,\varphi\\ \cos(n+1)\,\varphi\end{bmatrix}\frac{2\pi}{i^{-(n+1)}}\right). \quad [85]$$

where

$$\Im_{n\pm1}^{FF}(\theta;\chi_{nl}) = \int_{r_a=0}^{r_a=a} J_{n\pm1}(\chi_{nl}r_a/a)J_{n\pm1}(kr_a\sin\theta)r_a dr_a\ \Im_{n\pm1}^{FF}(\theta;\chi_{nl}) = \int_{r_a=0}^{r_a=a} J_{n\pm1}(\chi_{nl}r_a/a)J_{n\pm1}(kr_a\sin\theta)r_a dr_a \quad [86]$$

and

$$\chi_{nl} = p_{nl} \text{ or } q_{nl}.$$

The elements of the S_{21} matrix (i.e. the individual TE and TM modes) can be used with the expressions above to give a description of the far-field. Since the modes in the output field are incoherent, the full far-field is the summation of each mode at each (θ,φ) point being investigated:

$$E^{FF} = \sum_j \sum_i S_{ij} * {e_i}^{FF} \quad [87]$$

where ${e_i}^{FF}$ is the far-field of each waveguide mode, i, at the horn aperture.

Generating the far-field pattern using the individual TE and TM modes is accurate but computationally inefficient. Since the SVD method redescribes the horn output as a much smaller combination of hybrid modes this can be used to generate the far-field pattern much more efficiently. As shown by McCarthy (2014), the SVD approach can be used to calculate the far-field pattern as well (equation [88]). For single moded operating frequencies the SVD and the scattering matrix method provide identical results (as seen in Figure 5.10 below). As well as reducing the computation time for the far-field analysis, another advantage of the SVD method is that we are dealing with a smaller number of modes if they have to be propagated through an optical system. Due to the efficiency of the SVD method, it will be used to generate the far-field patterns in this research.

$$E^{FF} = \sum_j \Sigma_{jj} \sum_i U_{ij} * {e_i}^{FF} \quad [88]$$

where U_{ij} are all the elements in a column U_j, and Σ_{jj} are the singular values (main diagonal) of the S_{21} matrix.

One thing that also needs to be accounted for is the polarisation of the incident radiation. When a waveguide is excited by unpolarised EM radiations, for every mode that is present in a waveguide that is of azimuthal order $n > 0$ there is another orthogonal mode present. This can be accounted for mathematically in equations [82]-[85] by shifting φ through $\frac{\pi}{2}$, each orthogonal mode pair (corresponding to the sin/cos parts of solutions) is independent of each other and can be summed in quadrature when generating the far-field

pattern or the reflected power. In the QUBIC instrument the incident EM radiation will first pass through a polariser, making it linearly polarised in the single mode (HE_{11}) case.

QUBIC horn far-field patterns

When generating the far-field patterns for the QUBIC horns, to save time computationally, cuts of the far field pattern were obtained, rather than full 2-dimensional plots. These cuts are obtained by setting φ to a fixed value and moving θ through the desired elevation angles (-40° to 40° in this case). The cuts obtained here are the co-polar E-plane ($\varphi = 0°$), the H-plane ($\varphi = 90°$) and the cross-polarisation ($\varphi = 45°$) as seen in Figure 5.11. The E- and H-planes are slightly asymmetric with respect to each other, but the amount of asymmetry present is very low. The pattern is highly Gaussian and has low levels of cross-polarisation, which itself is a desirable feature of the horns and is a result of their corrugated design (also as seen in Figure 2.17, the QUBIC focal plane is not wide enough to capture the radiation from the sidelobes).

Figure 5.12 shows that the far-field patterns do not alter much in shape across the band, and there is an expected scaling of the beam width wavelength. This is due to the single-moded nature of horn at these frequencies, so a similar system response can be expected when operating across the entire band. The low levels of cross polarisation also persist across the band (Figure 5.13), again showing that the horn operates optimally over this frequency range.

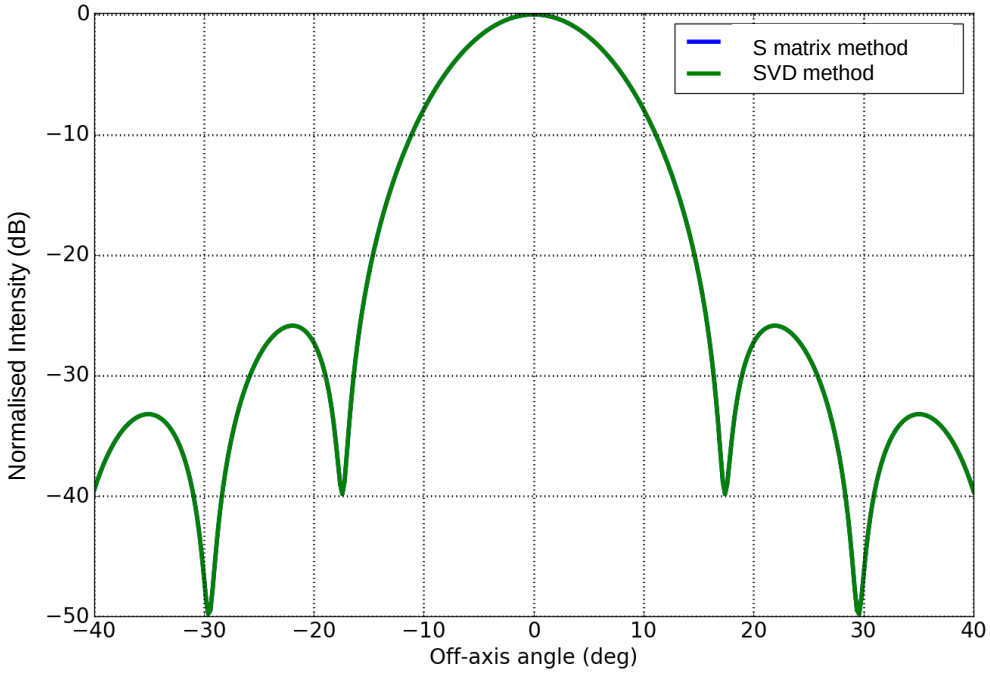

Figure 5.10: E-plane cut of the far-field generated using the scattering matrix and SVD method.

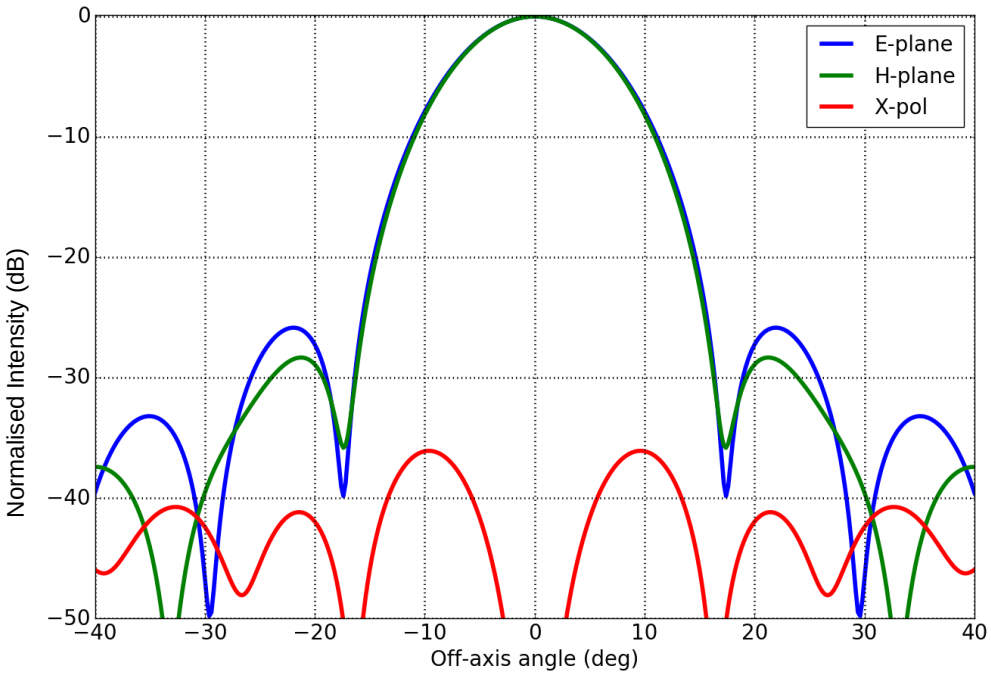

Figure 5.11: Cuts of the far-field pattern of the QUBIC horn at 150 GHz.

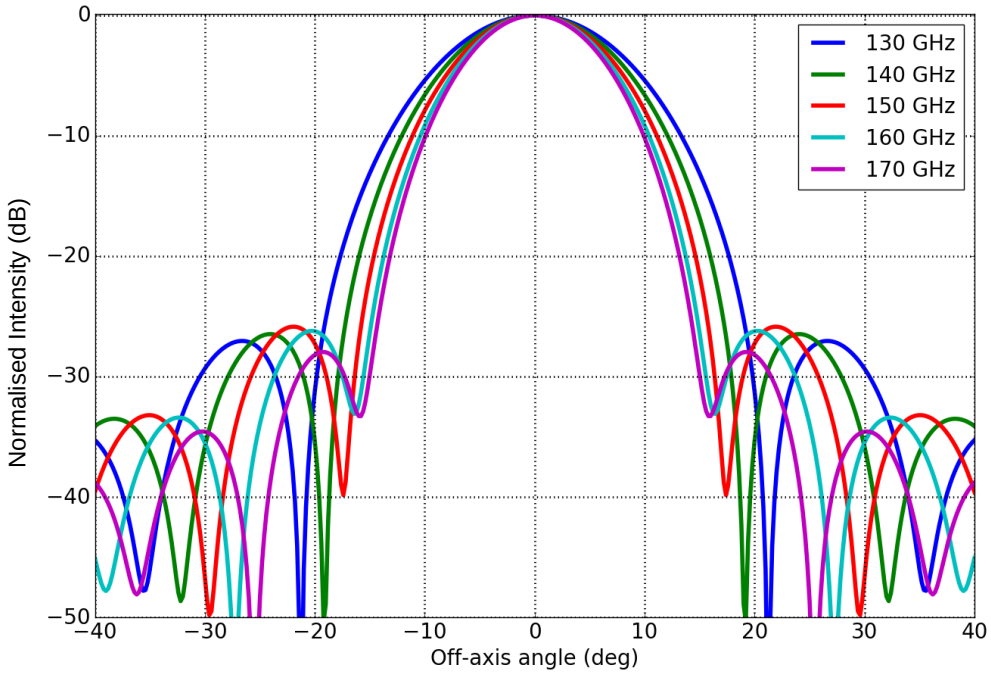

Figure 5.12: E-plane co-polar cuts of the QUBIC horn across the lower band.

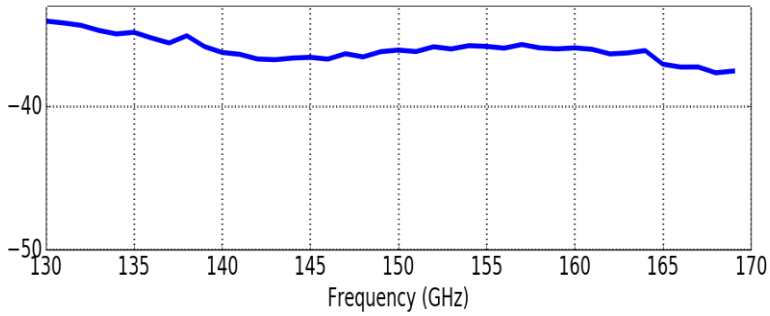

Figure 5.13: Peak cross-polarisation power across the lower operating band.

Verification of the mode-matching techniques

The far-field patterns were also generated at some spot frequencies by collaborators in Milan (data provided by A. Mennella of Università degli Studi di Milano Statale) using an industry standard software SRSR that is no longer available. This uses the very accurate (and computationally expensive) method-of-moments to calculate the far-field patterns, but is limited as it cannot analyse multi-moded operations. Comparing the plots generated using the mode-matching software (Figure 5.14) it can be seen that they agree well. The biggest difference is present in the cross polarisation pattern, however this is at low power levels. The structure is consistent across both software packages though, which is important. Also the mode matching software assumes that the far-field is a plane so some projection issues could cause the differences as the plots move off-axis.

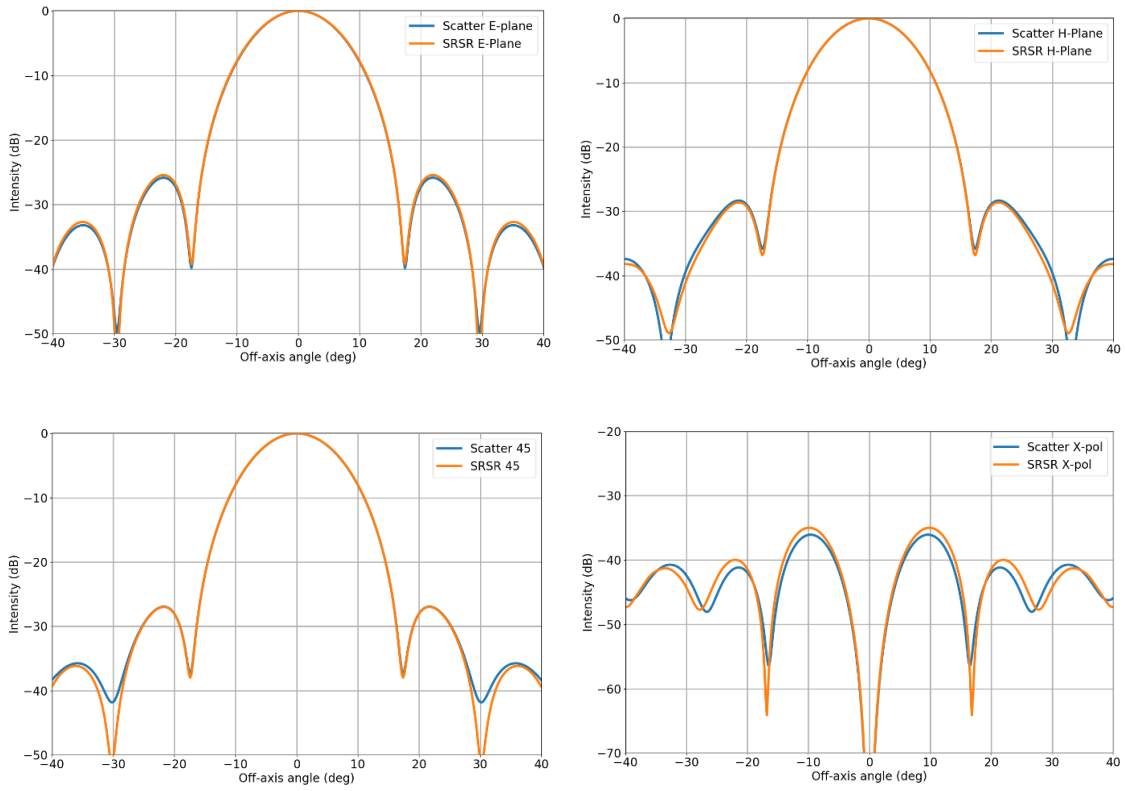

Figure 5.14: Far-field pattern software comparison at 150 GHz for the E-plane (top left), H-plane (top right) 45º cut (bottom left) and cross-polarisation (bottom right). SCATTER uses the mode matching techniques and SRSR uses method-of-moments.

5.2.4 Multi-moded operation

As mentioned, in order to correct for the polarised foreground, observations will be performed at 220 GHz. To limit the cost of producing another instrument, the QUBIC horns are designed so that they operate in two frequency bands. The upper band was initially set to have the same bandwidth as the lower one (25%), however as a result of this research it was decided that this was not ideal, for various reasons which will be discussed in this section.

The QUBIC horns are multi-moded across the upper operating band. This can be seen by performing an SVD analysis on the scattering matrix produced at the centre of this operating band (220 GHz), as shown in Table 5.5. Each azimuthal order is incoherent and can be treated as an independent mode of power transmission within the waveguide (as a consequence of this, multi-moded operating frequencies can have higher power throughput). When performing this analysis it was decided that unless there was a power of 0.05 or less within a mode in scattering matrix, then it was not considered to be propagating fully, and thus was not counted in the reflected or transmitted power or in the far-field patterns. For this reason the $n = 2$ azimuthal is not counted until after 205 GHz, even though there is power present at 200 GHz. This makes normalisation with respect to the number of modes more straightforward. Results were checked for threshold values down to 0.01 and no significant difference in results was found. It can be seen from the table that a fourth mode (within the $n = 1$ order) cuts on at the higher end of the band.

Table 5.5: SVD entries for the S_{21} matrix for the three azimuthal orders across the higher band.

Frequency	**Azimuthal Order**			
	0	**1**		**2**
	Σ_{11}^2	Σ_{11}^2	Σ_{22}^2	Σ_{11}^2
190	0.99278	1.00091	0	0
195	0.98944	0.99858	0	0
200	0.9866	0.99932	0	0.0003
205	0.98646	0.9994	0	0.12296
210	0.99386	0.99981	0	0.94384
215	0.98	0.99991	0	0.99126
220	0.97928	0.99954	0	0.9868
225	0.99121	0.9994	0	0.9966
230	0.96689	0.99337	0	0.99889
235	0.92326	0.96868	0	0.98525
240	0.87738	0.99836	0	0.98595
245	0.247	0.78889	0.00006	0.98677
250	0.00174	0.19935	0.56072	0.94234

Reflected power

Since all the azimuthal orders are independent, they can be treated separately and recombined at a later stage. There is only a single mode present in nearly all the azimuthal orders (except for $n = 1$ at frequencies greater than 245 GHz), for this reason below 245 GHz each azimuthal order can be treated like the single moded operation above. The output field [D] was obtained using the SVD method on the S_{21} matrix. The power in this field was obtained as before and the reflected power in the mode is then just this transmitted power subtracted from unity (based on the fact that the combined power from Table 5.1 and Table 5.2 sum to unity).

This calculation was performed for $n = 1$ and $n = 2$ across the entire band and for $n = 3$ when the mode propagates fully. A simple yet effective representation for the total power across all active modes can be obtained by averaging the power of the individual modes present in the waveguide, the averaging also renormalizes the total reflected and transmitted power to unity. This gives a reflected power across the band as in Figure 5.15. The reflections peak when the $n = 3$ azimuthal order mode begins to propagate at low non-negligible power levels, around 205 GHz, as expected from the above table. This is because the transmitted power is normalised assuming all modes that can propagate do so with initial power of unity. The reflected power also increases as the frequency increases, becoming quite prominent at 240 GHz. This is one of the reasons why it was decided to change the bandwidth of the upper frequency from 25% to 18% (i.e. to cut on at 200 GHz cut it off at 240 GHz). There are still some peaks with these restrictions and overall the reflectivity is clearly not as optimal as for the lower band but that is to be expected with multi-moded horns, and for most of the revised band it stays lower than -10 dB intensity level.

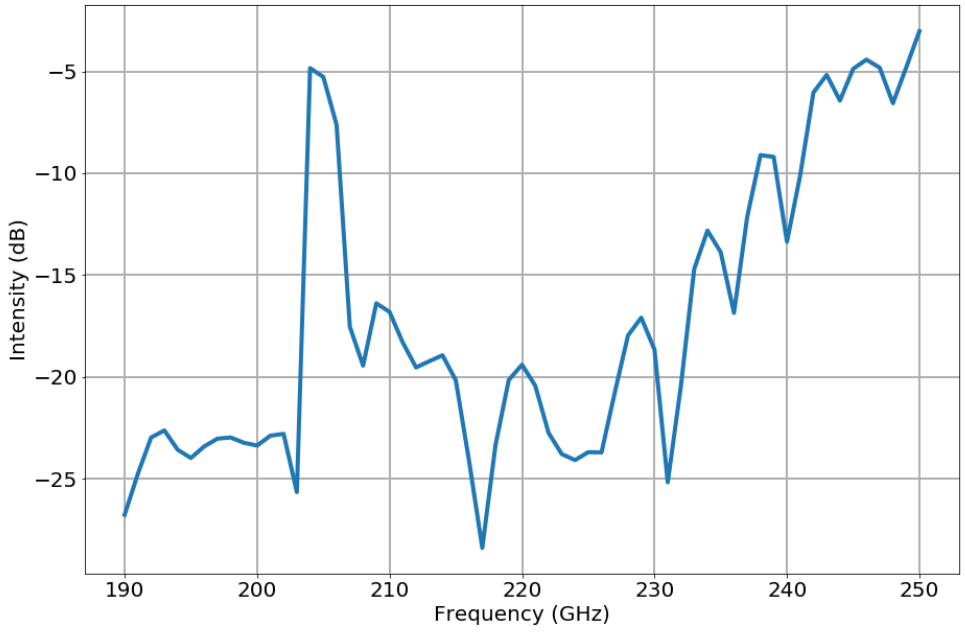

Figure 5.15: Reflected power across the higher operating band of the QUBIC horn when modelled.

Far-field patterns

If a waveguide is multi-moded, each of the modes present at its aperture has their own far-field pattern as shown in Figure 5.16. Since each of these modes are incoherent; to get the total far-field pattern the intensity of each of these modes are summed to get the total pattern, as in Figure 5.17. Since it is a combination of

modes the pattern loses the directivity that was present in the lower band, however high angular resolution and thus high directivity is not required for QUBIC and the increased sensitivity of the wider beam is an advantage. There is also a slight increase in the asymmetry of the beam, and the cross polarisation levels are a lot larger due to the multiple modes (modes other than HE_{11} are not linearly polarised), and this persists across the band (Figure 5.18). These are typical characteristics for multi-moded horns, and cross-polarisation introduced after the HWP (including by the horns) is not an issue for QUBIC as the TES bolometers respond to all polarisations. Another reason for the reduction in width of this band can be seen in Figure 5.19. the patterns are quite similar up to 240 GHz though, unlike for the lower band, there is a noticeable change in structure of the sidelobes. The width of the beam remains very similar across the band unlike the single-mode case where the width scales with wavelength. What is an issue is the pattern at 250 GHz, this pattern is noticeably different to the others with an on-axis dip and very noticeable peaks close to the centre. This is due to a drop in power of the primary mode and the relative increase in power of the higher order modes as seen in Table 5.5, and while directionality is not important, these peaks could cause very complex synthetic beams that are not desired. For this reason as well as because of the reflected power just discussed, it was decided to limit the higher operating band.

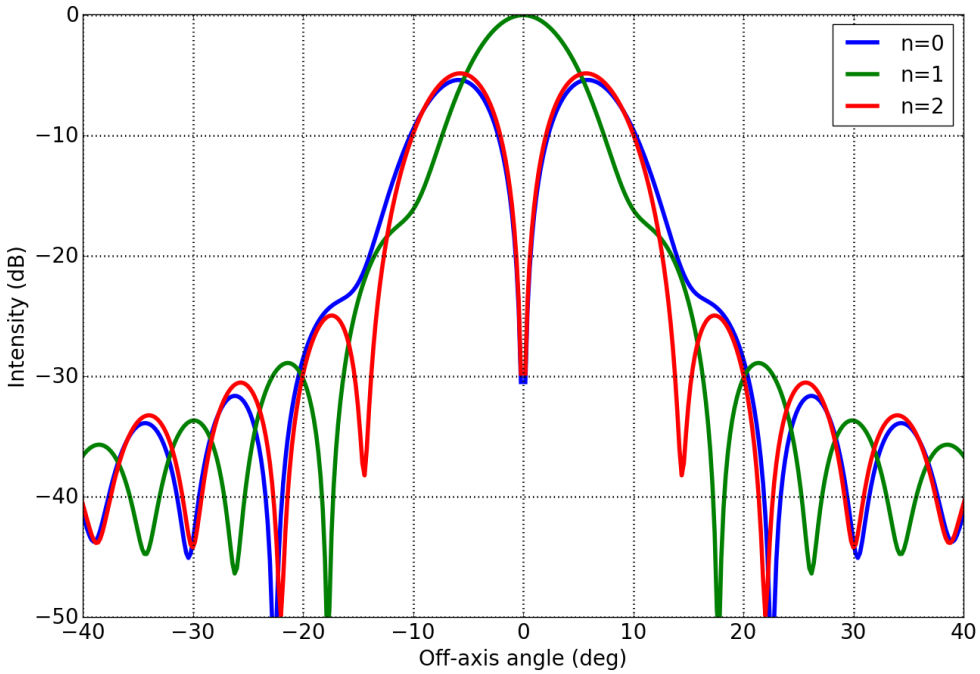

Figure 5.16: E-plane of the far-field of the hybrid modes in the QUBIC horn at 220 GHz.

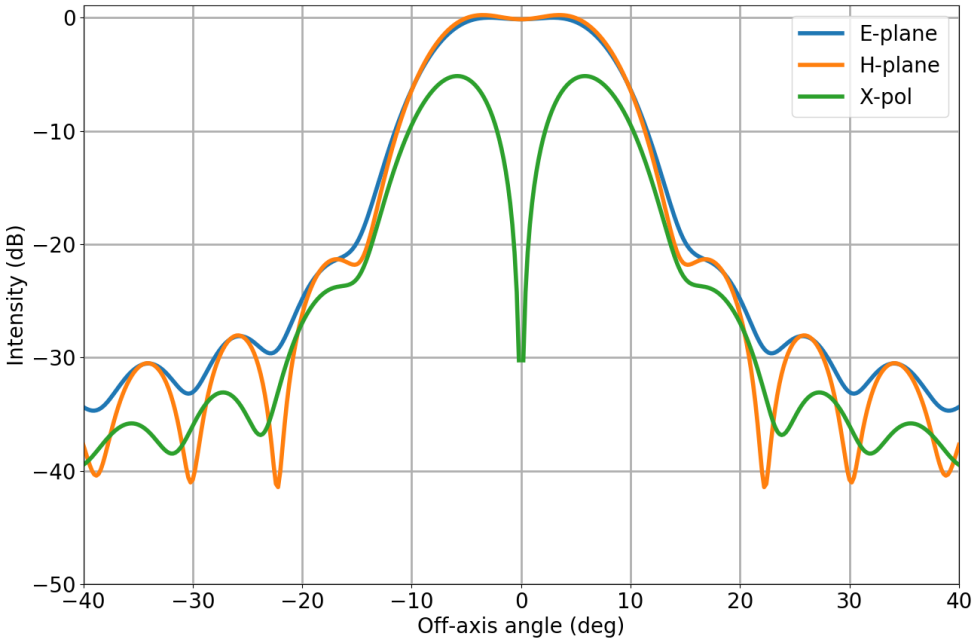

Figure 5.17: E- and H-plane co-polarisation cuts and cross-polarisation cut at 45° of the total far-field pattern at 220 GHz.

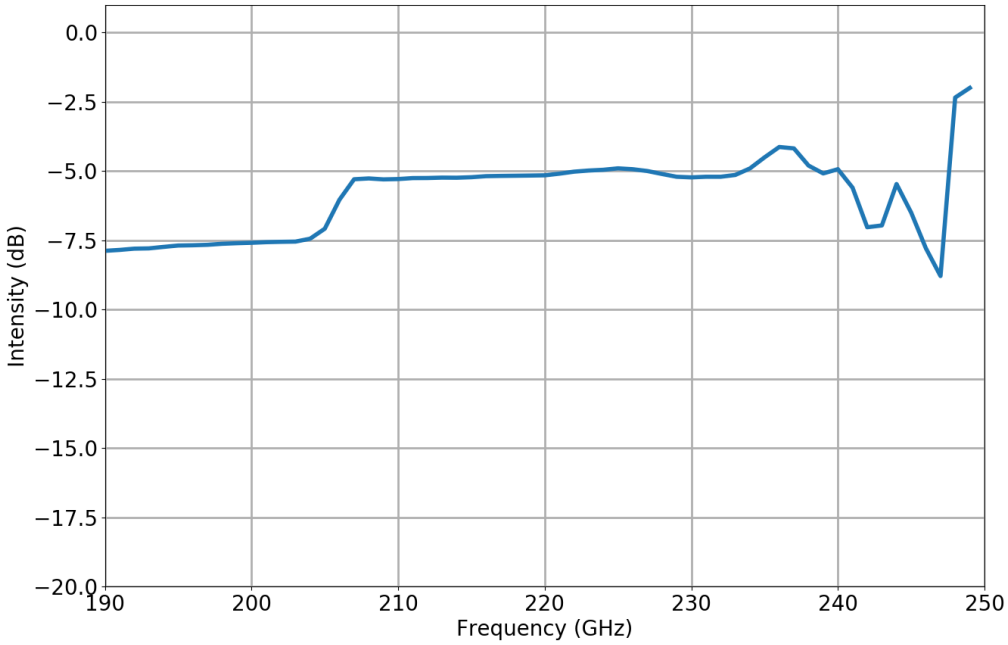

Figure 5.18: Peak cross-polarisation of the QUBIC horn across the higher operating band.

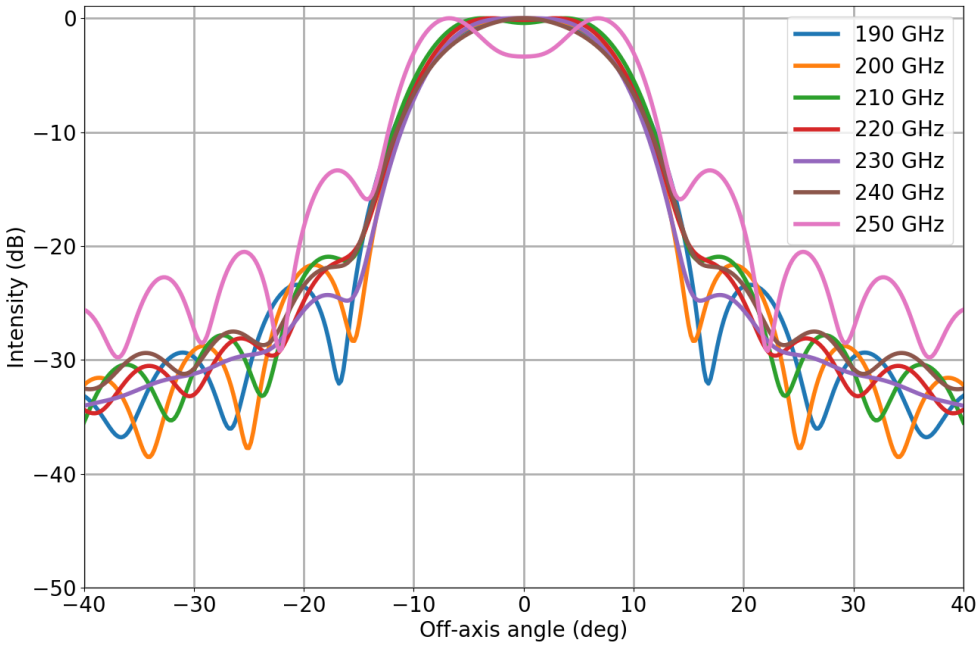

Figure 5.19: Far-field patterns for frequencies across the higher QUBIC operating band.

5.2.5 Manufactured horns

The QUBIC horn array is made using the "platelet" technique where holes (corrugations), at the position of each horn in the array, are etched onto thin sheets of metal (platelets) which are then stacked on top of each other and usually diffusion bonded together to make a single structure as described by Haas *et al.* (1993). This is an economically viable method for producing arrays of corrugated horns with good performance. For QUBIC the corrugations in the platelets were generated using photochemical etching, (with a tolerance of 0.05 mm) and milling (with a tolerance of 0.03 mm) of silver plated material and they were mechanically tightened with screws (Cavaliere *et al.*, 2020). There are 176 platelets all of thickness 0.3 mm (except for the throat and the aperture which are 0.9 and 3 mm thick respectively) which, when stacked together and create the horn profile as seen in Figure 5.20.

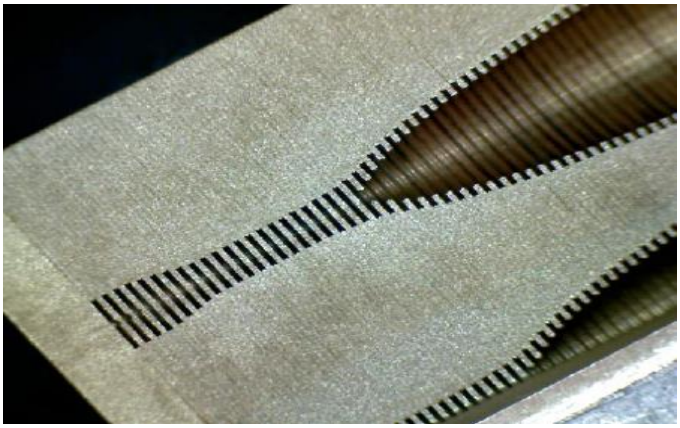

Figure 5.20: Cut through a stack of platelets showing the profile of a horn in the QUBIC array.

The full back-to-back feedhorn array is made by placing identical arrays of horns back-to-back. For the TD each side of this array will consist of a single block of 8×8 horns that are screwed together (Figure 5.21), note that the outer flanges (the thicker sections at Port 1 and Port 2 in Figure 5.3) were mechanically milled due to their increased thickness compared to the narrower platelets in between (which were chemically etched). For the FI, each side of the array will be split into four sections where each one is comprised of 100 horns (for a total of 400 back-to-back feedhorns) as seen in Figure 5.22.

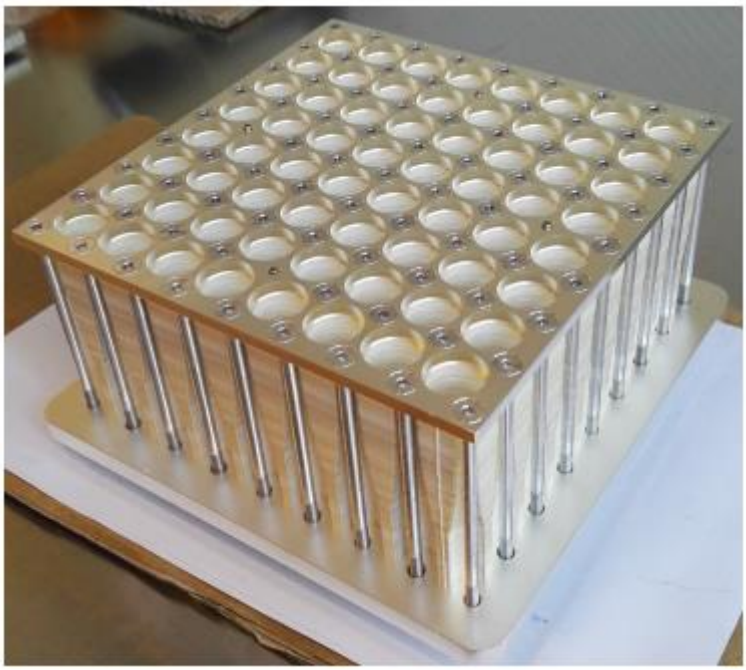

Figure 5.21: QUBIC 8×8 horn array for the technical demonstrator. Half of each back-to-back pair is shown (image provided by A. Mennella of Università degli Studi di Milano Statale).

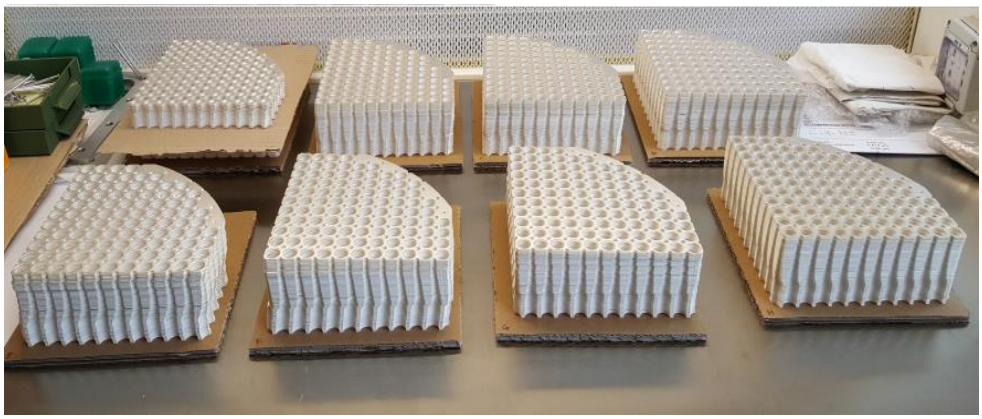

Figure 5.22: Collection of the eight partially assembled QUBIC feedhorn sections (image provided by A. Mennella of Università degli Studi di Milano Statale).

The required tolerance on radii of the corrugations was determined using a Monte-Carlo analysis (detailed in O'Sullivan, Burke *et al.* (2020)) with GRASP's CHAMP package (TICRA, 2005) and the in house SCATTER software described in this chapter. Horns with manufacturing tolerances of $\pm$ 25 μm, $\pm$ 50 μm and $\pm$ 75 μm rms were simulated and the resulting return loss and far-field patterns were obtained (Figure 5.23). It was found that 50 μm was a reasonable manufacturing tolerance which results in acceptable beam

pattern variation. It was also found that, due to the smaller size of the corrugations, the geometry at the throat of the horn caused more variations than the larger corrugations at the aperture. Figure 5.24 shows the return loss for the nominal model compared with two other models: one where the radius of the third corrugation from the throat of the horn was reduced by 25 μm, and the other where three of the final 10 corrugations of the horn (near the aperture) were arbitrarily selected and reduced by 50 μm. It can be seen that the change at the aperture of the horn had no effect on the return loss, while the single smaller change at the aperture has a minor yet noticeable effect.

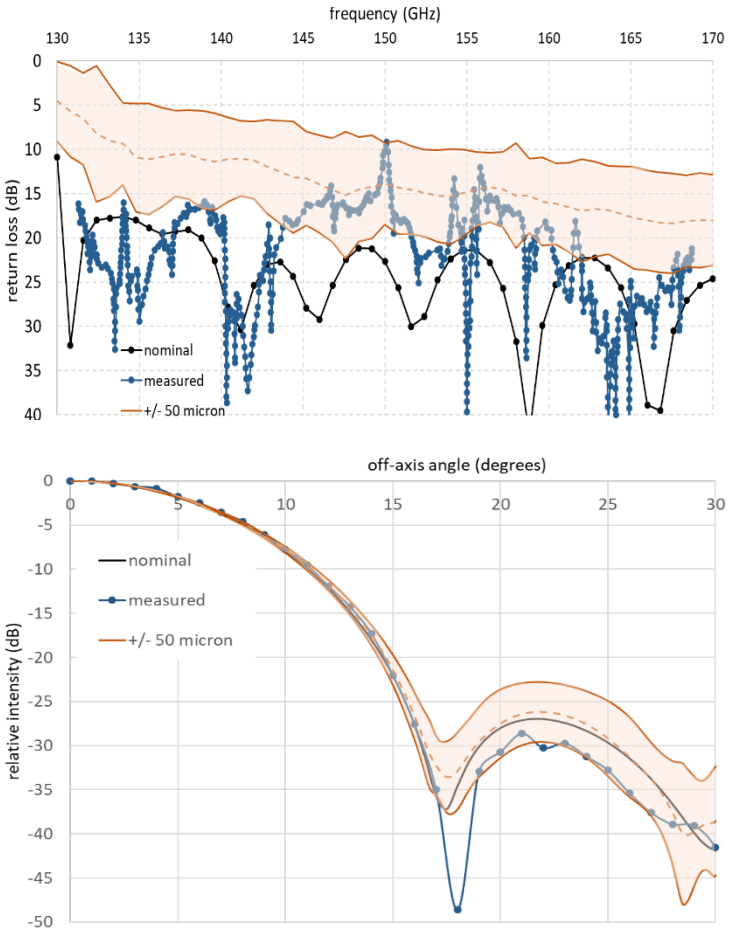

Figure 5.23: Measured and predicted return loss (top) and far-field pattern (bottom) for a tolerance of 50 μm or less in the platelet hole radius. The shaded area indicates the average and the average ± standard deviation simulations (image adapted from O'Sullivan, Burke *et al.* (2020)).

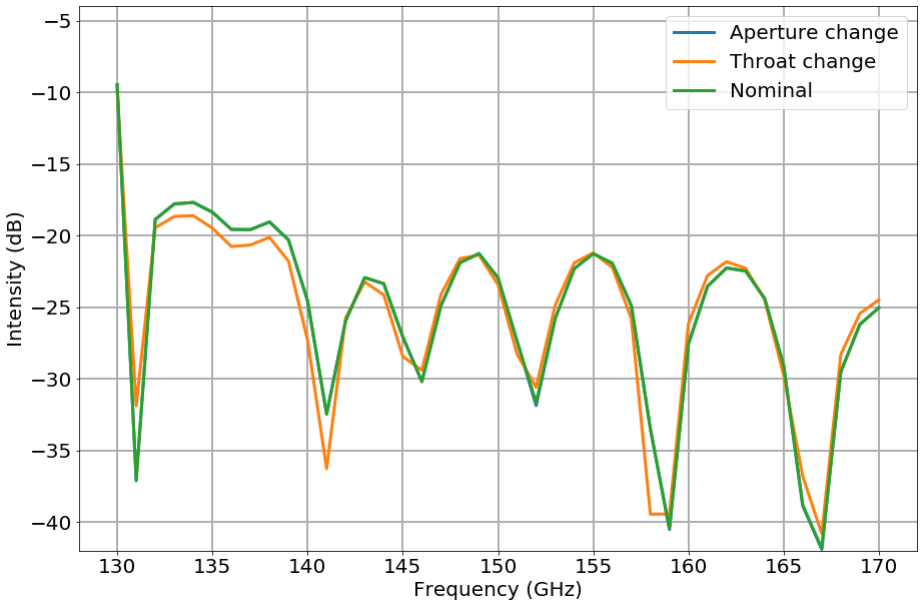

Figure 5.24: Return loss for the nominal geometry compared with two different horn geometries, one where the radius for a single corrugation near the throat was reduced by 25 μm, and one where three corrugations near the aperture were reduced by 50 μm.

5.2.6 Defects due to the platelet method

A notable deviation from the nominal geometry of the horn is the 'cusps' that are present on the corrugations due to the non-uniform erosion of the metal during the etching process (Cavaliere *et al.*, 2020) can be seen in Figure 5.25. An analysis using SCATTER mode matching was performed to investigate the effects of these cusps on the far-field pattern and return loss of the horns. To do this, the geometry of the horn was altered to account for them as follows. The cusps are 60 microns in height, and angled to a point however, since the software only accounts for discontinuities, they were first modelled as a step that was 60 microns in height and it was assumed that they were 0.1 mm wide and located at the centre of each platelet (Figure 5.26). Conveniently this is also likely to be the 'worst-case' scenario (a large sudden jump) where any differences from the nominal would be a maximum.

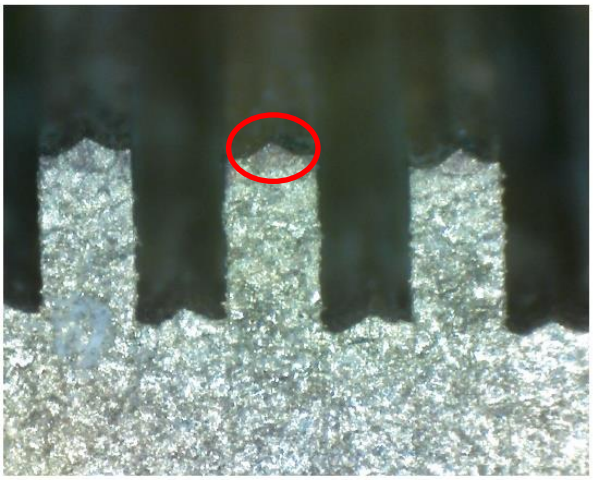

Figure 5.25: Example of the cusps (circled in red) present on the QUBIC horns (image provided by A. Mennella of Università degli Studi di Milano Statale).

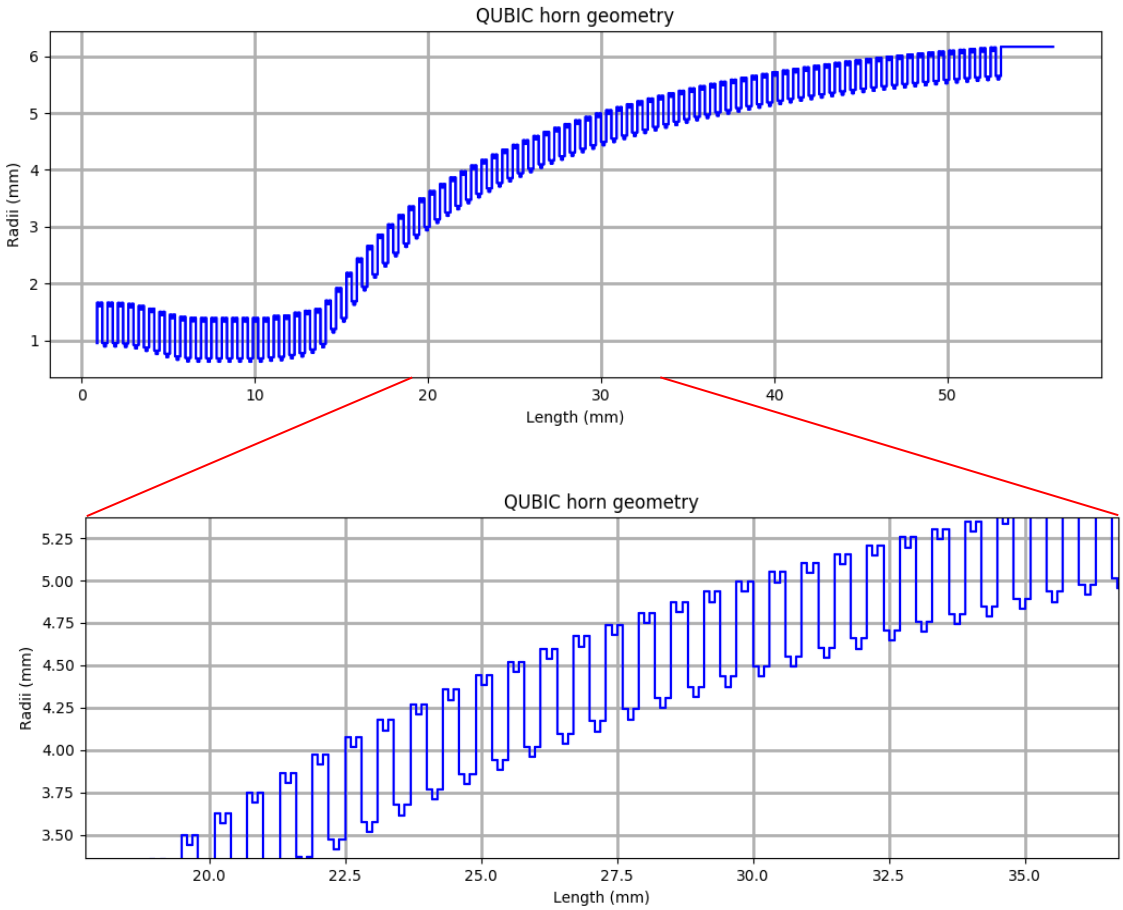

Figure 5.26: Geometry of the horn with the cusps implemented as a step. The lower plot shows a magnified section of the horn geometry with the cusps.

5.2.6.1 Lower band analysis

Reflected power

The reflected power for the geometry with cusps was analysed across the lower band in 1 GHz steps and the far-field pattern was obtained at 130, 150 and 170 GHz. These results were then compared with the corresponding nominal geometry results.

Figure 5.27 shows that there is a difference predicted in the reflected power from a horn with the cusp and one with the nominal geometry. This is the case particularly at the lower end of the band where there is noticeable differences in power. There was a frequency shift in the pattern of the reflected power across the entire band. This behaviour is not a big concern since it is at very low power levels and the changes in the reflected power is within acceptable limits. The frequency shift is an interesting result that was investigated further.

To make sure that this reflected power shift was likely in practice two other models were investigated, one where the cusp was generated using three steps per cusp instead of just one (this gave a more accurate description of the cusp but was computationally more intensive) and the other where the entire corrugation was increased in length by 60 microns (called the 'increased corrugation' model), making the horn narrower. This gave a total of four models that were modelled (Figure 5.28).

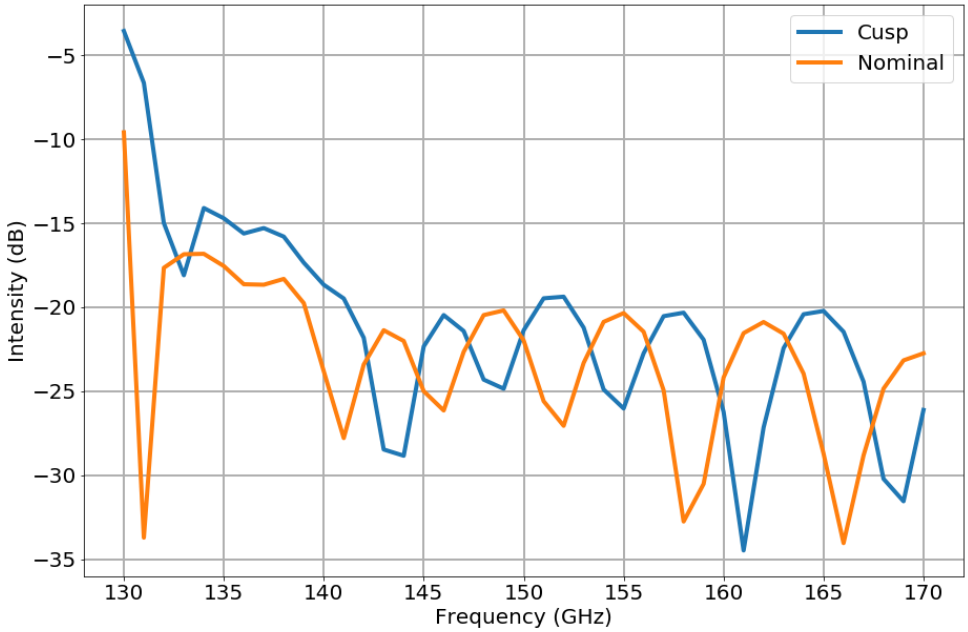

Figure 5.27:Reflected power from a horn with nominal horn and one with cusps.

The agreement between the return loss for both cusp models at such low power levels is shown in Figure 5.29 indicated that the single step is a good estimate for the model and that the previous results are realistic. Figure 5.30 shows that there are many similarities between the cusp and increased corrugation models, such as the noticeable deviation in power about 135 GHz (though much higher for the increased corrugation model) and the frequency shift in the position of the peaks as it moves across the band. The most interesting aspect to note is that the cusp model appears to provide a return loss pattern in between the nominal model and the increased corrugation model, which is a reasonable result.

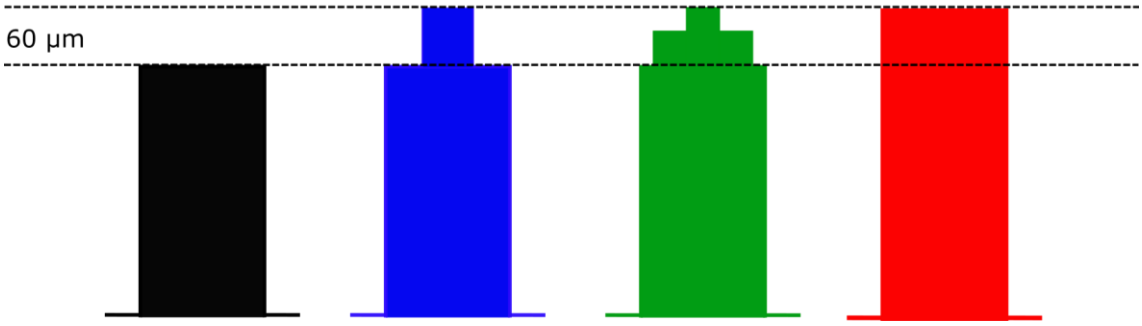

Figure 5.28: Simple description of corrugation types modelled: nominal corrugation (black), single step cusp (blue), staggered step cusp (green), increased corrugation (red).

Lower height cusps were also modelled as a single step at the centre of each corrugation with the same thickness as before. Figure 5.31 shows that the resulting frequency shifts were found to be proportional to the cusp height. These tests led us to believe that we do not expect any unusual features from the pointed cusp shape and that our approximate models are reliable.

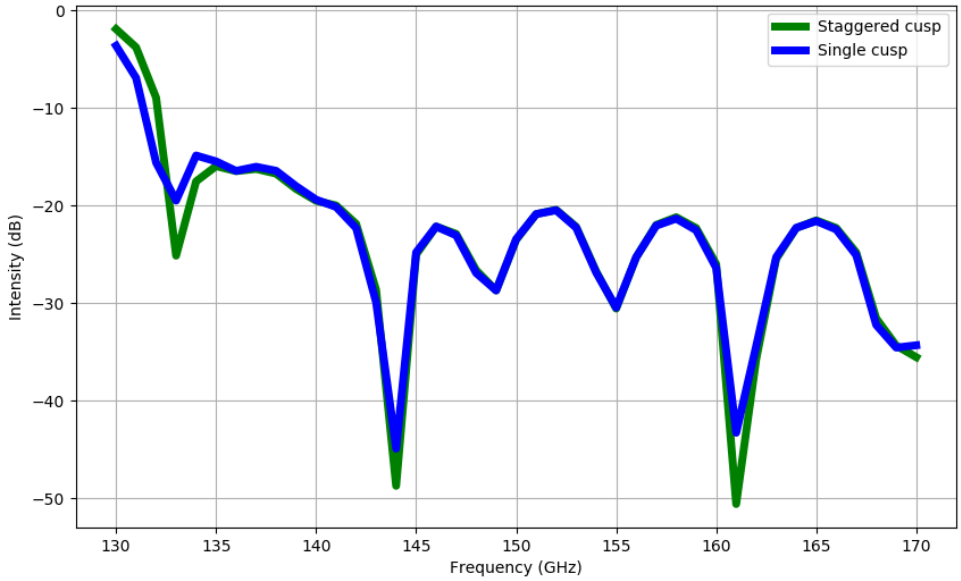

Figure 5.29: Return loss comparison of the single step and staggered step cusp models.

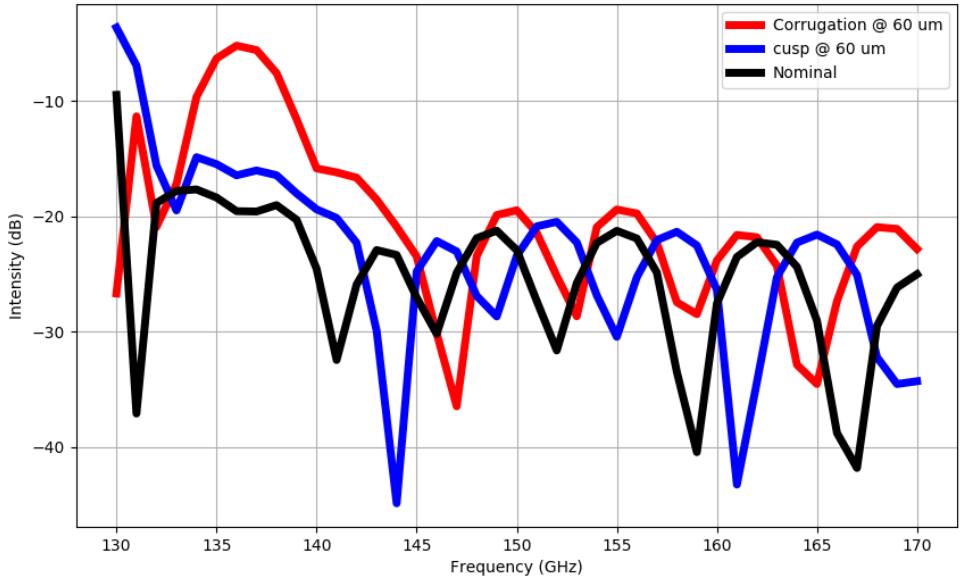

Figure 5.30: Return loss comparison of the nominal model, single step cusp model and the increased corrugation model.

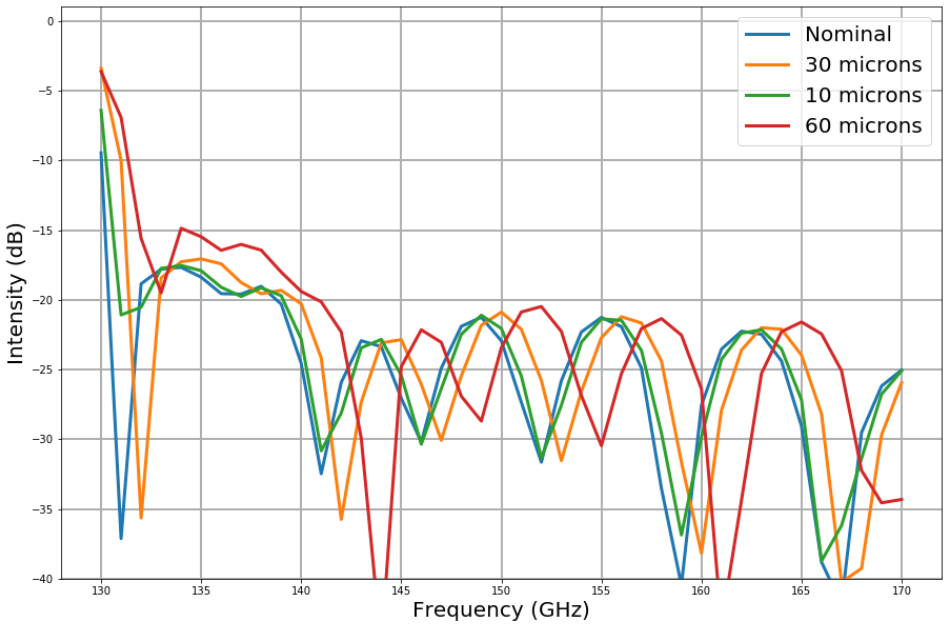

Figure 5.31: Return loss comparison between the nominal horn design, and for horns with a single step cusp with heights of 10, 30 and 60 microns.

Co- and cross-polarisation far-field patterns

The far-field patterns for horn geometries with and without the cusps (the blue and black models in Figure 5.28 respectively) were investigated next (Figure 5.32). There is a noticeable drop in the peak power between the models at 130 GHz and drop in the total transmitted power for the cusp model, which is consistent with the return loss results observed at this frequency. While this drop in transmitted power is not desirable, the return loss patterns of the models rapidly converge to similar low values, so it is not a feature across the entire frequency band. This is also evident from the near identical far-field agreement at 150 and 170 GHz.

In terms of the cross-polarisation behaviour, Figure 5.33 shows that, similar to above, there is a drop in power at 130 GHz, however at such low levels (- 40 dB) these changes are not going to be noticeable. This low power level is consistent across the band with the only change in the structure of the cross polarisation occurring as minor deviations at 170 GHz; again this was not a concern since the power levels are so low. Interestingly the difference in the return loss at 170 GHz, manifested itself more so in the cross polar pattern as opposed to the co-polar differences observed at 130 GHz. This result in general shows that the presence of the cusps should not affect the performance of the QUBIC horns in the lower band in any significant way.

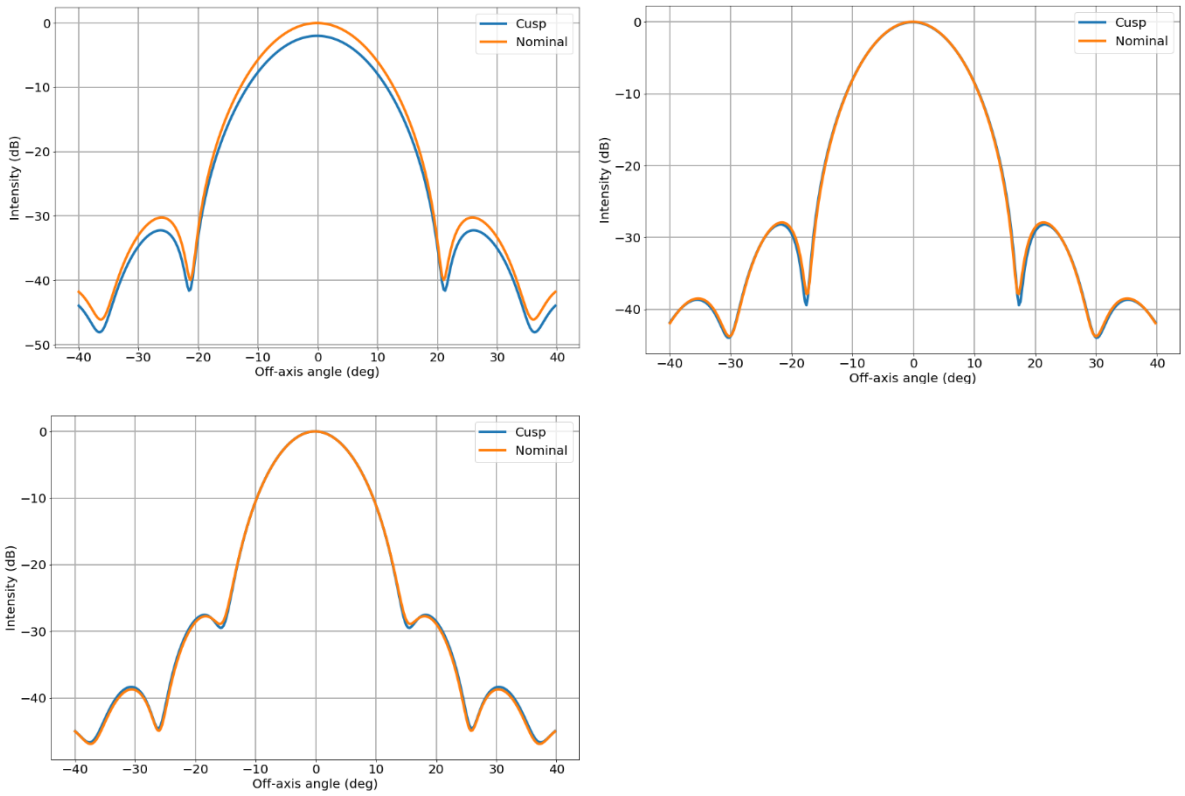

Figure 5.32: Co-polar far-field pattern comparison between nominal and cusp geometry at 130 GHz (top-left), 150 GHz (top-right) and 170 GHz (bottom), where each pattern is normalised to the nominal pattern peak.

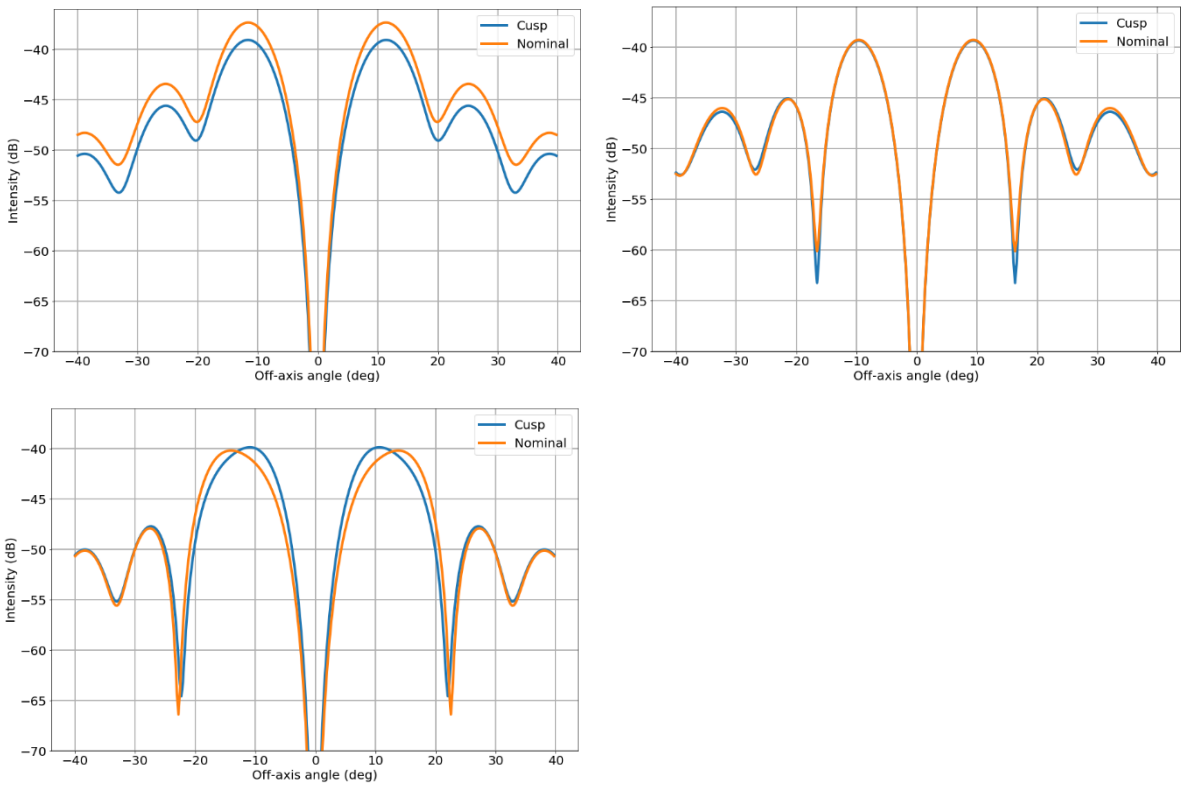

Figure 5.33: Cross polar far-field pattern comparison between nominal and cusp geometry at 130 GHz (top-left), 150 GHz (top-right) and 170 GHz (bottom), where each pattern is normalised to the nominal pattern peak.

5.2.6.2 Higher band analysis

As mentioned in Section 5.2.4, the QUBIC higher band was changed from 190-250 GHz to 200-240 GHz. However, for a direct comparison to previous patterns obtained, the reflected power was analysed across the old band (190-250 GHz) in 1 GHz steps. The far-field and cross polarisation pattern was obtained at 200, 210, 220 and 240 GHz. The cusp model used throughout this section is the blue model in Figure 5.28.

Reflected power

It can be seen from Figure 5.34 that, just as in the lower band, the structure of the reflected power pattern of the model including cusps looked similar to that of the nominal geometry pattern but with a frequency shift, particularly noticeable with the prominent peak at about 205 GHz in the nominal model shifting to 215 GHz in the cusp model. As shown in Table 5.6 this peak corresponds to a cut on of the $n = 3$ higher order mode. Comparing this to the results in Table 5.5 it is clear that the change in geometry causes this mode to cut on at a higher frequency. The frequency shift is not as uniform across the entire band as with the lower band; when the higher order mode cuts on the patterns begin to converge. The multi-moded nature of the horns at this band means that the cusps in the horn geometry do not alter the behaviour of the reflected power as predictably as for the lower band. The reflected pattern at the higher end of the band still shows very high reflectivity, the reason the band was limited to a maximum of 240 GHz.

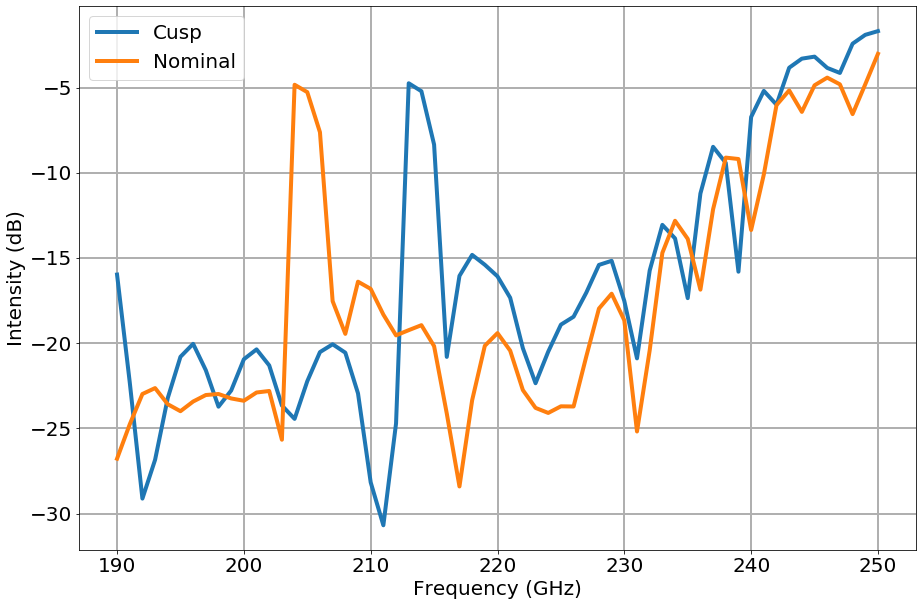

Figure 5.34: Reflected power of the nominal horn geometry and the cusp horn geometry.

Table 5.6: SVD entries for S_{21} matrix for the 3 azimuthal orders across the higher band for the single-step cusp model.

Frequency	Azimuthal Order			
	0	1		2
	Σ_{11}^2	Σ_{11}^2	Σ_{22}^2	Σ_{11}^2
190	0.92288	1.00132	0	0
195	0.97705	0.99799	0	0
200	0.97654	0.99930	0	0
205	0.98326	0.99879	0	0
210	0.99512	0.99958	0	0.00072
215	0.96286	0.99954	0	0.59869
220	0.95246	0.99920	0	0.97433
225	0.96925	0.99908	0	0.99313
230	0.96896	0.98785	0	0.99014
235	0.99350	0.96005	0	0.99131
240	0.41110	0.99733	0	0.95472
245	0.01881	0.58831	0	0.95344
250	0.00001	0.042077	0.00040	0.92560

Far-field and cross polarisation patterns

The far-field patterns (Figure 5.35) at 200 and 220 GHz were very similar between the nominal and cusp models, however at 210 and 240 GHz there were noticeable differences; while not easily predictable, they were expected due to the multi-moded nature of the band. At 210 GHz the $n = 3$ mode is not fully propagating in the cusp model, hence the far-field pattern is a combination of the $n = 1$ and $n = 2$ modes, unlike for the nominal model which is a combination of all 3 azimuthal orders, causing the noticeable difference in the patterns. Comparing the nominal model SVD values (Table 5.5) and cusp model SVD values (Table 5.6) shows that while all the modes do change across the band due to the geometry difference, this change is not uniform across all modes. A good example is at 240 GHz even though all three modes are propagating, there is a noticeable power difference in the $n = 0$ mode between the models, while the power in the other two modes are very similar between the models. This presents as an overall drop in the transmitted power and thus and increase in the reflected power at this frequency, which causes the changes

in the peak power of the far-field patterns at this frequency, this is still within acceptable levels (roughly 1 dB drop).

Even though there are changes in the beam pattern, they are not going to affect the results too much, since all the patterns still have a prominent main beam, low sidelobe levels, and directionality is not a big concern for the QUBIC instrument. The most important thing to note from this analysis is the variation that the multi-moded operation of the horns causes, this will be discussed and explored further in the section of this chapter when horn geometries from the measured horns are investigated.

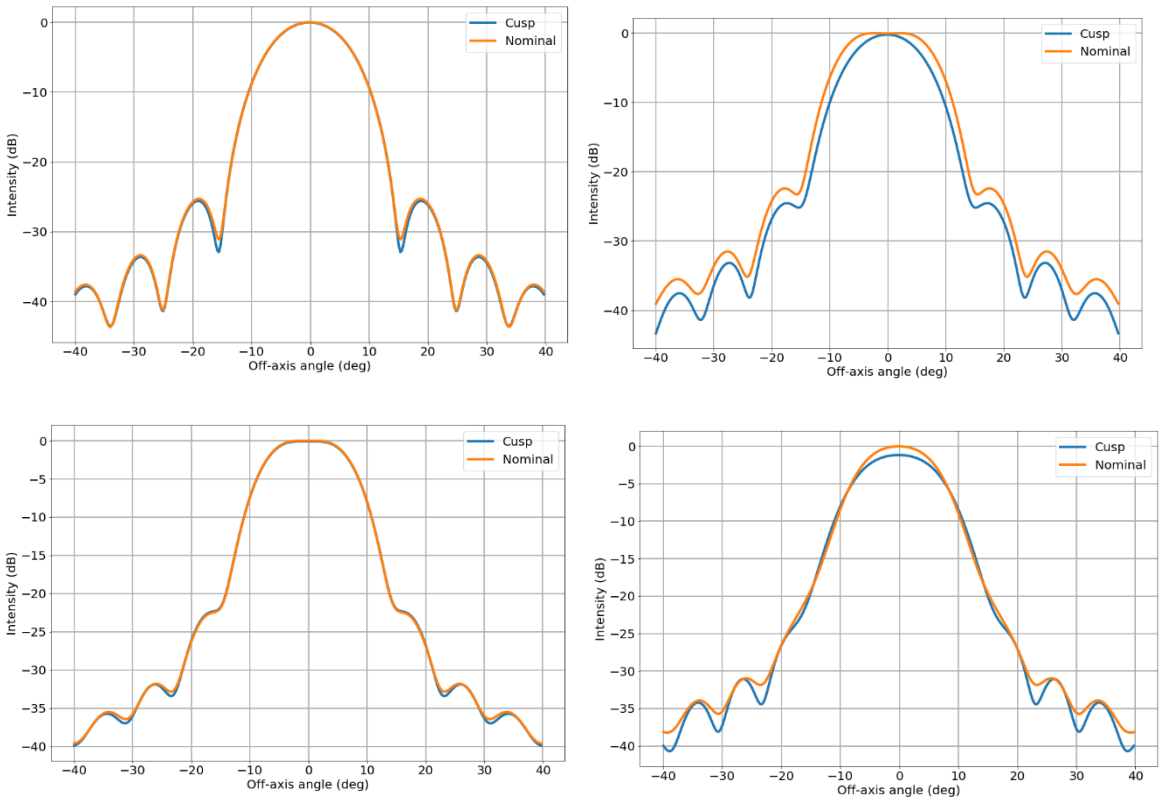

Figure 5.35: Co-polar far-field pattern comparison between nominal and cusp geometry at 200 GHz (top left), 210 GHz (top right) 220 GHz (bottom left) and 240 GHz (bottom right).

There was similar satisfactory agreement between the cross-polar patterns across this band (Figure 5.36) as was observed at the lower band, the higher peak power of these patterns was due to the multi-moded nature of the horns. Like the co-polar patterns, the cross-polar patterns differs mostly at 210 and 240 GHz, for the same reasons as discussed for the co-polar patterns.

Overall the cusps resulting from the manufacture of the horns did not present detrimental changes to the results in comparison to the nominal geometry. The most notable changes occurred at the multi-moded higher band, which was expected as each mode that is active in the horn is an independent carrier of power, meaning that there are more sources for deviations, unlike the single moded operation in the lower band.

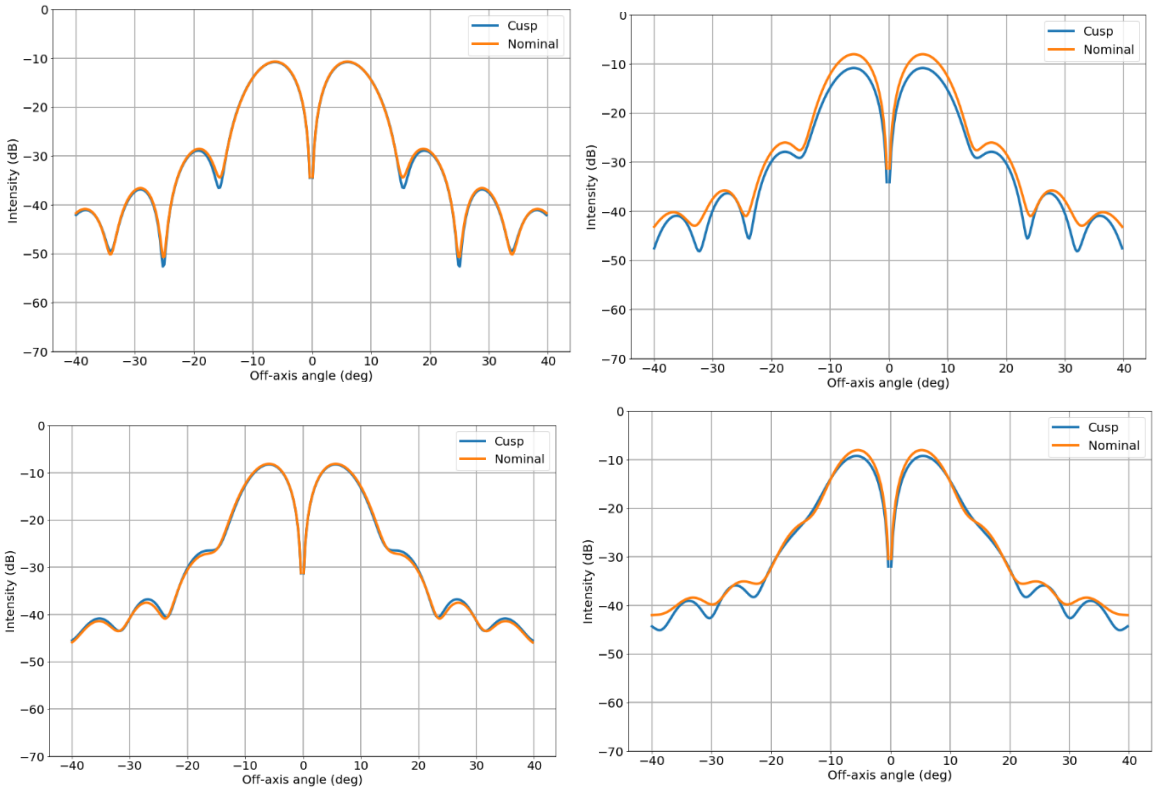

Figure 5.36: Cross-polar far-field pattern comparison between nominal and cusp geometry at 200 GHz (top left), 210 GHz (top right) 220 GHz (bottom left) and 240 GHz (bottom right).

5.3 Measured horn geometry: Simulations and comparison with measurements

The geometry profile of each horn (as manufactured) in both sides of the back-to-back TD horn array (for a total of 128 geometry files) was provided by collaborators from the University of Milan. As the horn arrays were being assembled the size of the corrugations for each horn were measured using the setup in Figure 5.37. As discussed by Cavaliere *et al.* (2020), due to issues with the chemical etching stage of manufacturing process it was found that the corrugations on some of the platelets for the TD array were outside the tolerances, this issue has been rectified for the FI horn array however.

Mode matching analysis was performed on all these horns (note that no cusps were included but as shown earlier, this would simply result in a frequency shift in the return loss so the analysis wasn't repeated here). The return loss was obtained across both operating bands and the far-field patterns obtained at 145, 150 and 155 GHz in the lower band as well as 190, 210, 220, 230, 240 and 250 GHz in the higher band. These frequencies were chosen as these are the frequencies at which a selection of the manufactured horns were measured with a VNA (Vector Network Analyser) using the setup shown in Figure 5.38, these measurements were performed by M. Zannoni of Università degli Studi di Milano-Bicocca.

Due to the nature of the setup only the H-plane of the co-polar far-field patterns could be obtained. Because of the nature of the VNA and attachments, it is difficult to set up the horns to propagate more than one mode. Only a single mode was measured (as expected) in the lab at nearly all frequencies in the higher operating band, there are some exceptions at the highest of frequencies which will be discussed later.

One thing to note is that this section uses the Milan University internal labelling system for the measured horns which names the horns 'Feed_*x*_*y*', where *x* and *y* do not relate to the labelling used in the GRF. Also, there are two arrays (array 1 and 2) these are simple arbitrary labels and do not indicate sky or instrument facing directions (since they are identical back to back horns the direction of either array does not matter).

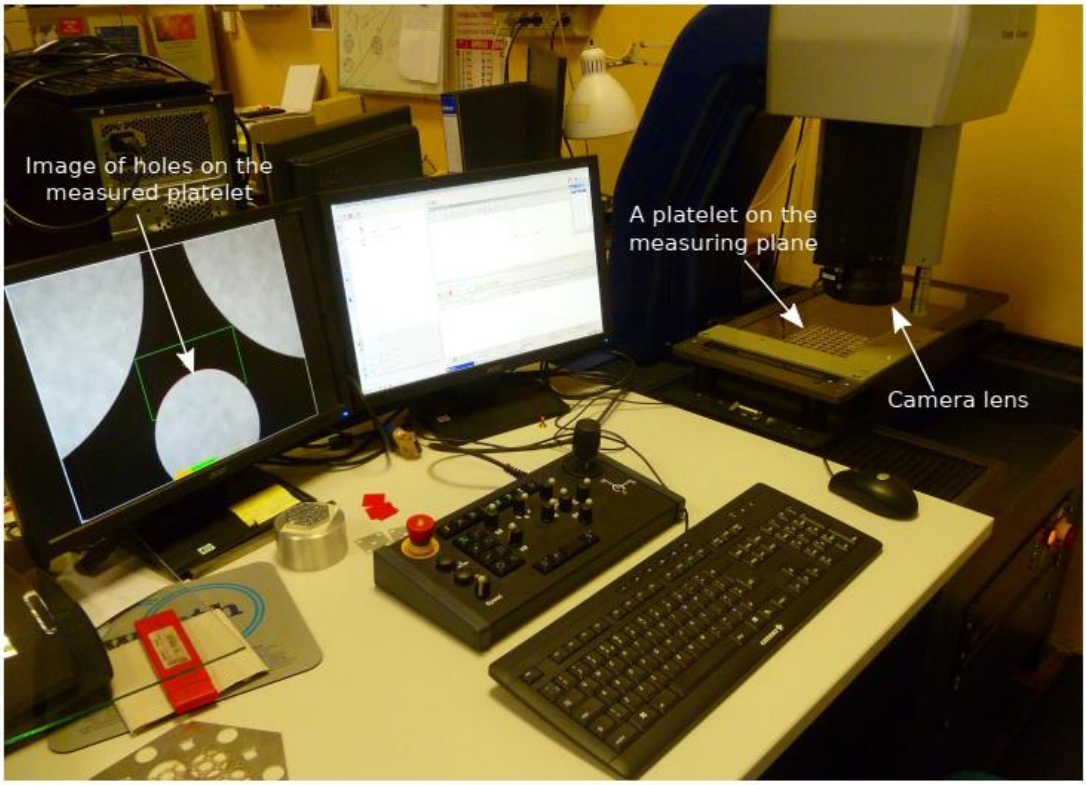

Figure 5.37: Measurement of the horn corrugations with a Werth ScopeCheck 200 metrology machine. Image obtained from Cavaliere *et al.* (2020).

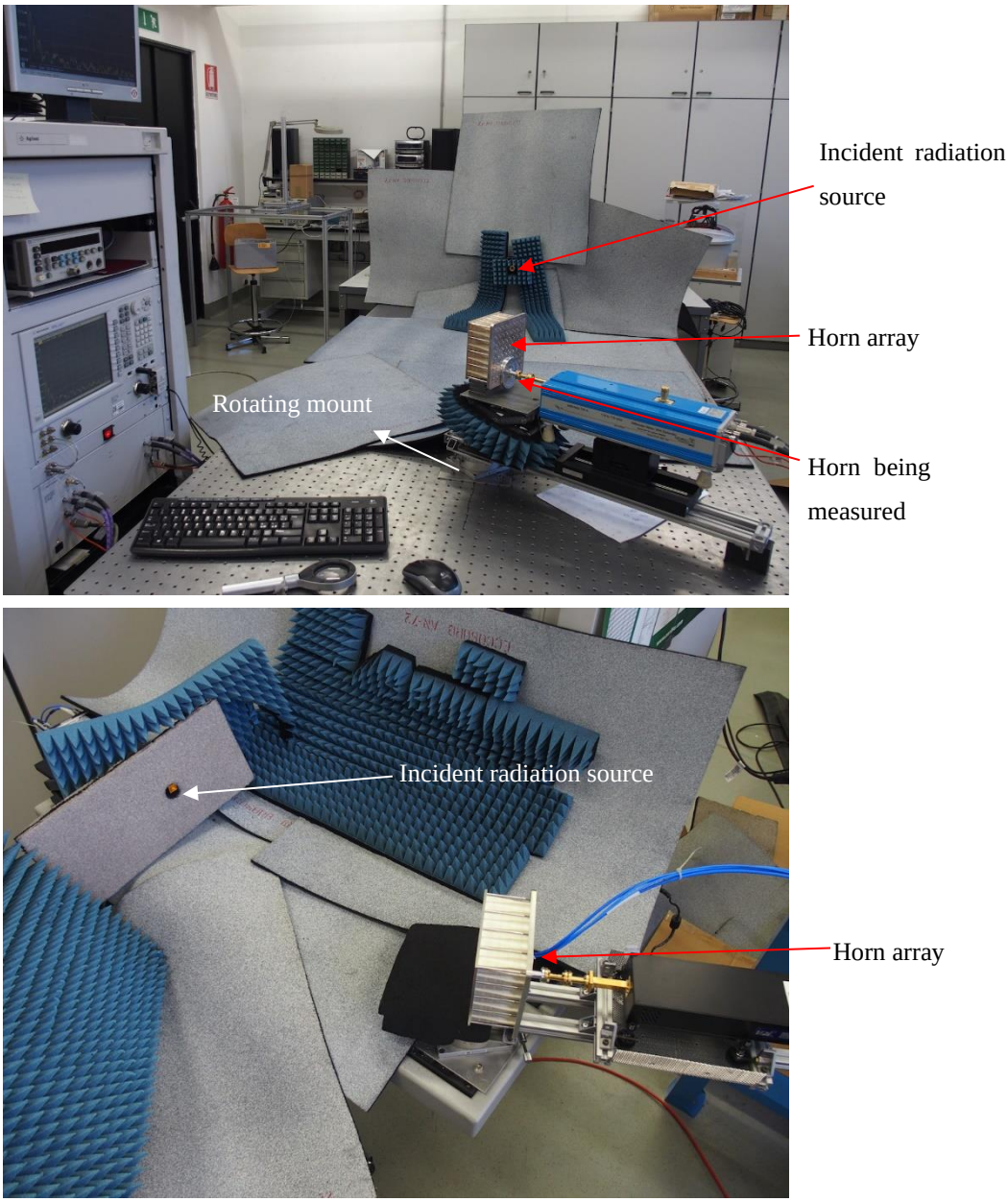

Figure 5.38: VNA setup for measuremetn of the beam pattern in *Università di Milano Bicocca* (Cavaliere *et al.*, 2020). The top setup is for the lower band measurements and the bottom setup is for the higher band measurements.

5.3.1 Lower band measurements

Return loss

Figure 5.39 shows the comparison of the nominal geometry with that of an arbitrarily chosen manufactured horn (all 128 of the measured horns compared similarly with the nominal geometry). Note that the geometry of the measured horn is off from the nominal case due to the chemical etching issues mentioned above. An SVD analysis shows that the horn remained single moded across the band (Table 5.7). Comparing the return loss for the measured, nominal and cusp geometries (Figure 5.40) showed that while the return loss of the measured horns varied quite a bit with the geometry, it averaged out to reasonable levels that are similar to those of the nominal and cusp geometries, with better results on average at the lower end of the band.

Table 5.7: Singular values of S21 matrix at lower band frequencies for feed_8_5.

Frequency (GHz)	Σ_{11}^2	Σ_{22}^2
130	0.96972	0
135	0.98411	0
140	0.96799	0
145	0.99426	0
150	0.98756	0
155	0.99529	0
160	0.98616	0
165	0.99706	0
170	0.99378	0

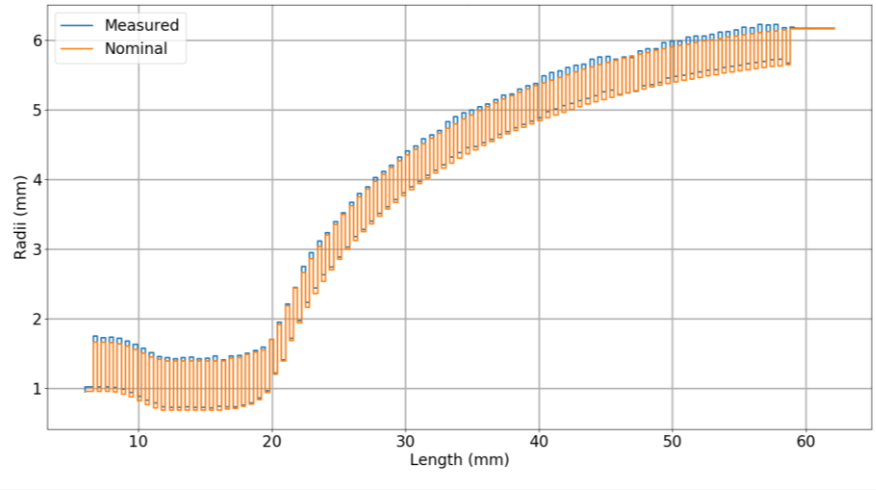

Figure 5.39: comparison of the geometry between the measured Feed_8_5 of array 1 and the nominal horn design.

In the simulations it is assumed that the platelet material is a PEC or perfect electric conductor and that there is no free space between the discontinuities. High conductivity material (silver plated) is used in the manufacturing process making it as close as possible to the idealised PEC. However, with the platelet method it is not always guaranteed that there is clear contact between the platelets and hence there could be some free space between the conductive corrugations of the horn, which can cause very undesirable effects in the transmitted and reflected parameters of horns. All this being said, it can be seen from Figure 5.41 that there is very good agreement between the simulated and measured data, providing evidence that the horns are manufactured and assembled correctly.

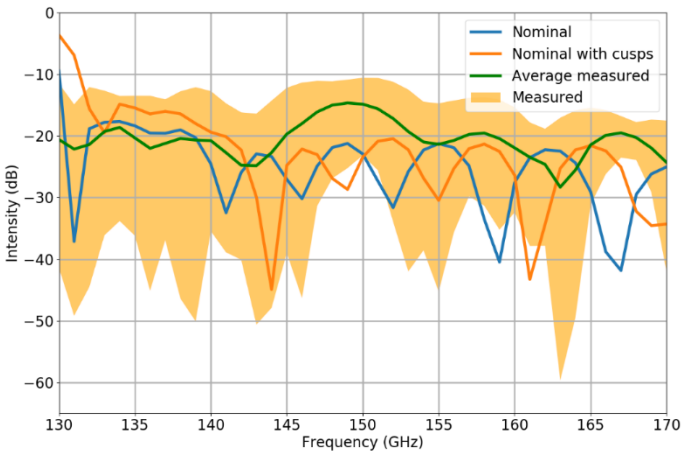

Figure 5.40: Predicted return loss comparison between the nominal geometry, cusp geometry and the measured geometries (the range was obtained from the maximum and minimum values at each frequency from the return loss analysis performed for all 128 measured horn geometries).

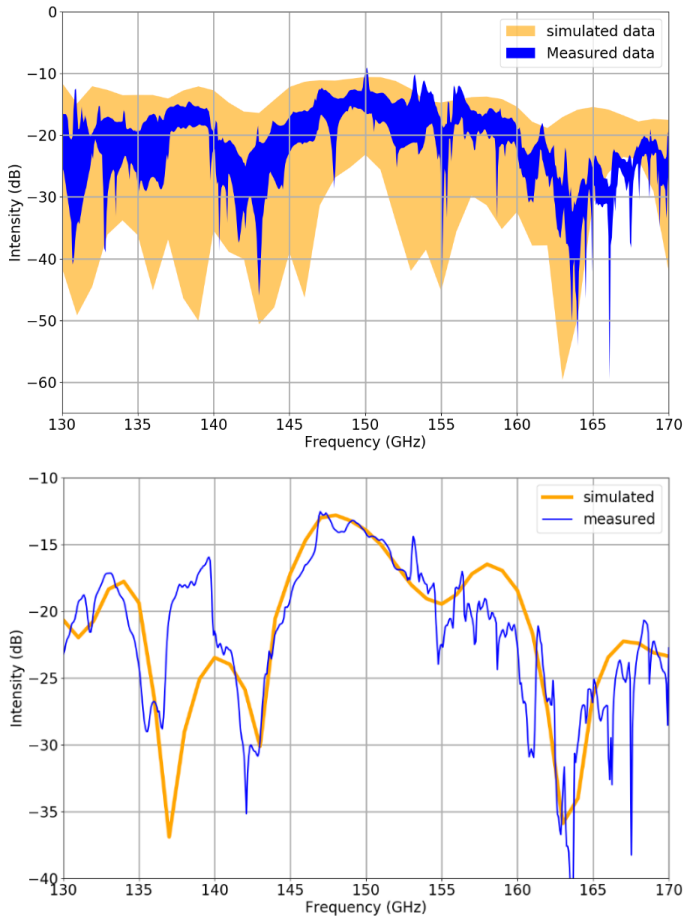

Figure 5.41: Top shows the return loss comparison between simulated and measured data (the measured data for the return loss were only obtained for 5 horns across the band, and these data sets represent the maximum and minimum values at each frequency for those 5 sets of data). The bottom shows a direct comparison between the measured and simulated data for feed 3_8.

Far-field pattern

It was found that the far-field pattern appeared as expected across the band for the different as manufactured horn geometries as well as being consistent across the different geometries (examples given in Figure 5.42), with the main differences appearing at off-axis angles that would not be captured by the focal plane.

Figure 5.43 shows that the measured and simulated main beam of the H-plane of the far-field match very closely and there is good agreement down to the first sidelobe at about -25 dB. There is some deviation in the structure of the patterns at lower power levels, but this is expected.

Overall, the agreement between measurements and simulations was very good over the lower band, providing more evidence that the horns are well manufactured and assembled, and showing that the platelet method of feed-horn array generation is viable for the QUBIC instrument, in that the array can be generated relatively easily and cheaply, and that the horns provide good performance in the design frequency band.

There are some interesting effects to notes with the simulated results: The E-plane around 150 GHz has a very wide range of values at high off-axis angles, unlike the results at 145 and 155 which have a very tight constraint on the power across the sky. Investigating the E-plane around this frequency (Figure 5.44) shows that there were similar wide range results observed at 149.9 and 150.1 GHz but not at 149 or 151 GHz, indicating that the horn is very susceptible to geometry changes around the design frequency. This being said it only affected the side lobes at large off axis angles, and since the focal plane itself only has a FOV of $\pm$ 11.5º it will not be an issue.

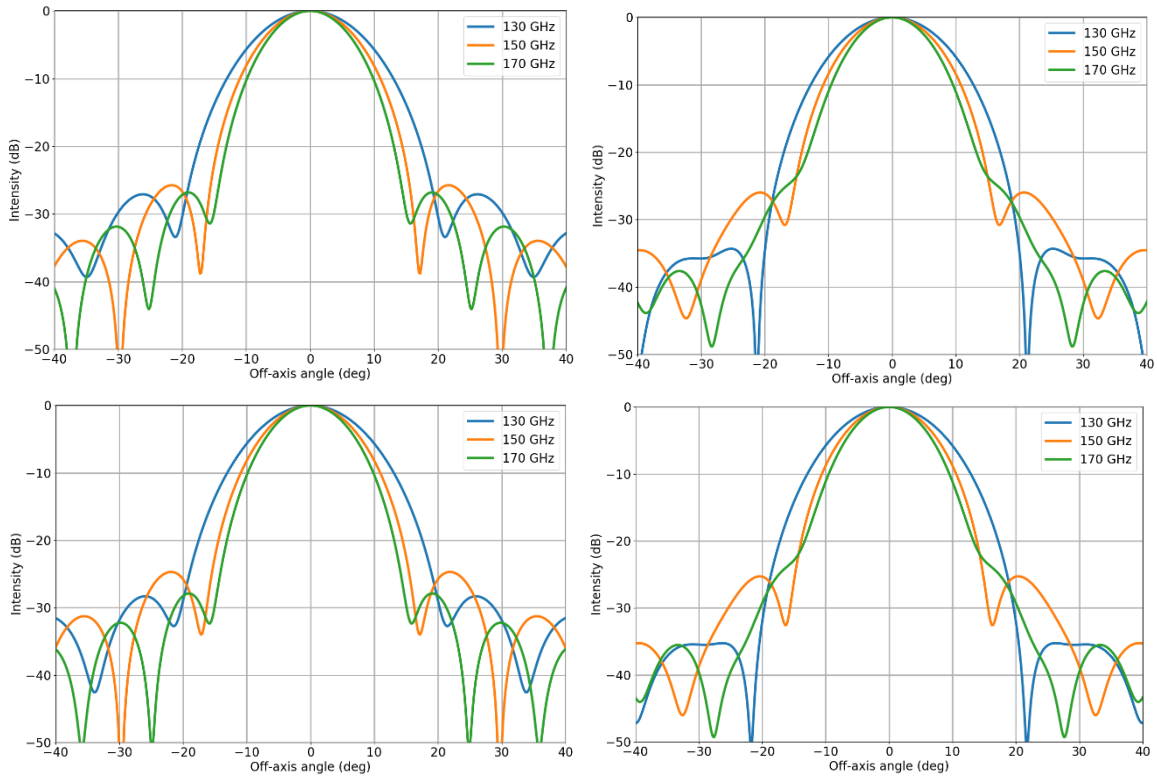

Figure 5.42: Simulated E-plane (left) and H-plane (right) of two arbitrarily chosen measured horn geometries feed_8_5 (top) and feed_1_2 (bottom).

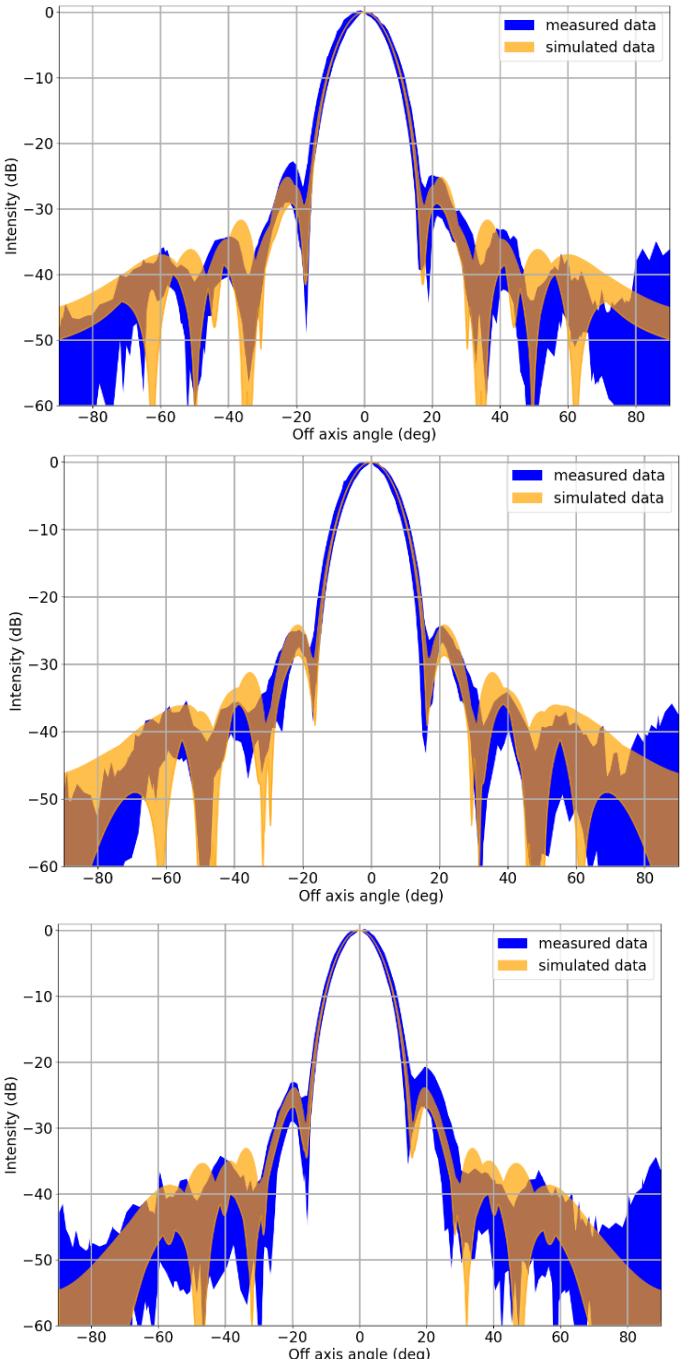

Figure 5.43: Comparison of the H-plane of the Far-field patterns between the max and min ranges for the simulated data (from all 128 horn geometries) and measured data at 145 (top), 150 (middle) and 155 (bottom) GHz.

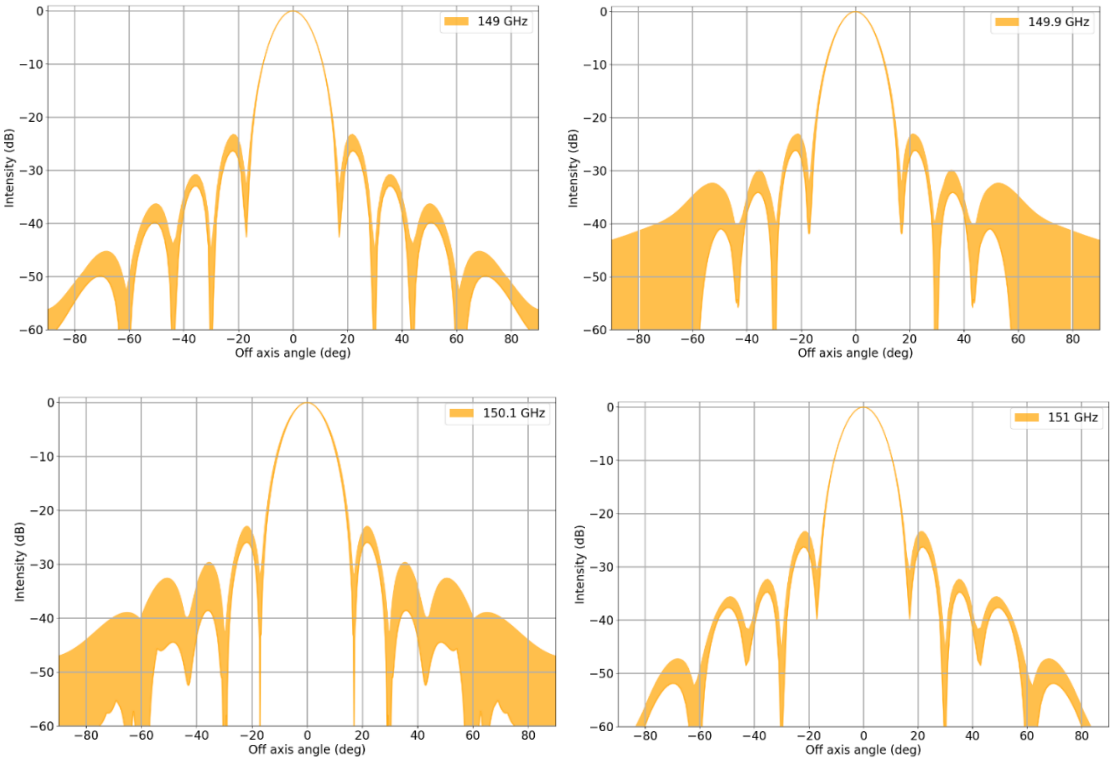

Figure 5.44: Range of values in the simulated E-plane of the far-field pattern at 149, 149.9, 150.1 and 151 GHz. E-plane measurements were not made.

5.3.2 Upper band measurements

As mentioned, at the higher operating band, only single moded measurements of the horns could be performed with the VNA. In terms of the simulations, this corresponded to exciting the horn with the $n = 1$ azimuthal order that has been discussed previously. So far the horn has only been considered from a multi-moded perspective, but Figure 5.45 shows these single moded simulations across the upper band. The most obvious difference with the lower band is the dissimilarity between the E- and H-plane patterns of the beam at the higher operating frequencies, particularly at 250 GHz. The E-plane simulations follow the predictable wavelength scaling where the main beam narrows with the decreasing wavelength. At 240 GHz, however, substantial power began to appear in the sidelobes and this increased even further at 250 GHz, with the sidelobe power being just a few dB less than the peak power. In the H-plane however, the wavelength scaling is followed until 240 GHz, where the beam widens, and at 250 GHz, the beam is wider than at 190 GHz. Even though the horn was only being excited with a single mode, as the frequency moved farther from the design frequency, the behaviour of the horn became more unpredictable.

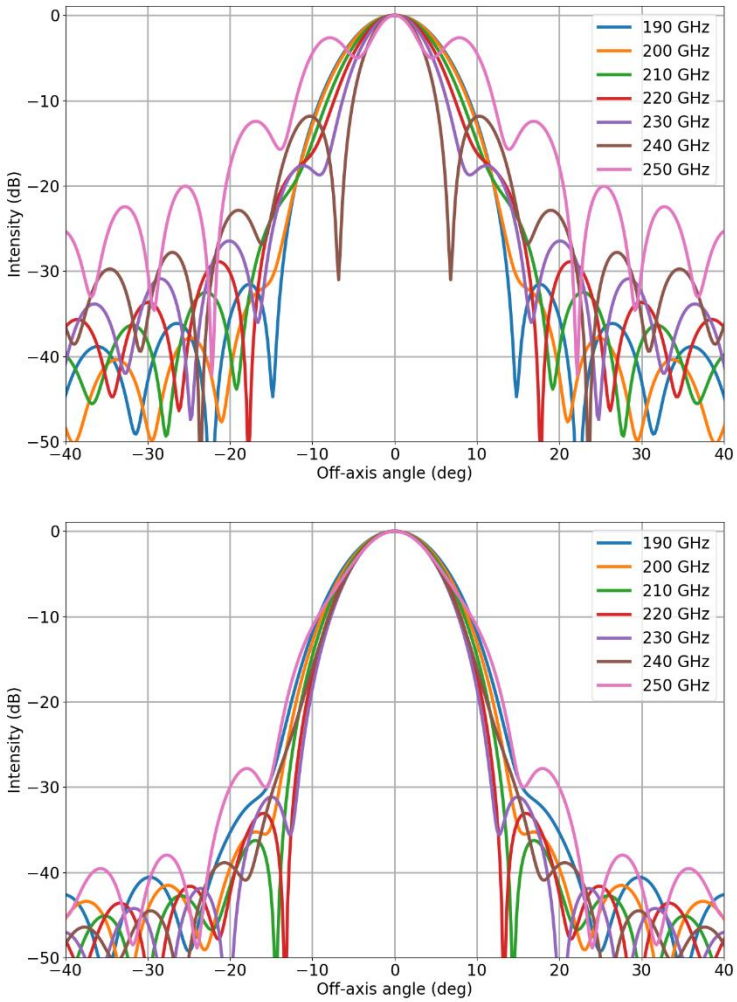

Figure 5.45: E-plane (top) and H-plane (bottom) of the single moded (n = 1) simulated far-field beam pattern across the higher operating band for the nominal QUBIC horn geometry.

When simulating beam patterns for two arbitrarily selected measured horn geometries (Figure 5.46 – the same horn geometries used to generate the fields in Figure 5.42) it was seen that there was much more variation in the beam patterns than there was at the lower band, and that as the frequency is increased, the corresponding patterns for the two horns deviate further, this is most likely due to variations in the throat of the horn geometries, as it was shown previously that the variations in the throat cause larger deviations when compared to variations in other parts of the horn (see Figure 5.24). These unpredictable effects on the beam pattern at the higher operating frequencies were expected, and is another example of why the operating frequency of this band was limited to a maximum of 240 GHz.

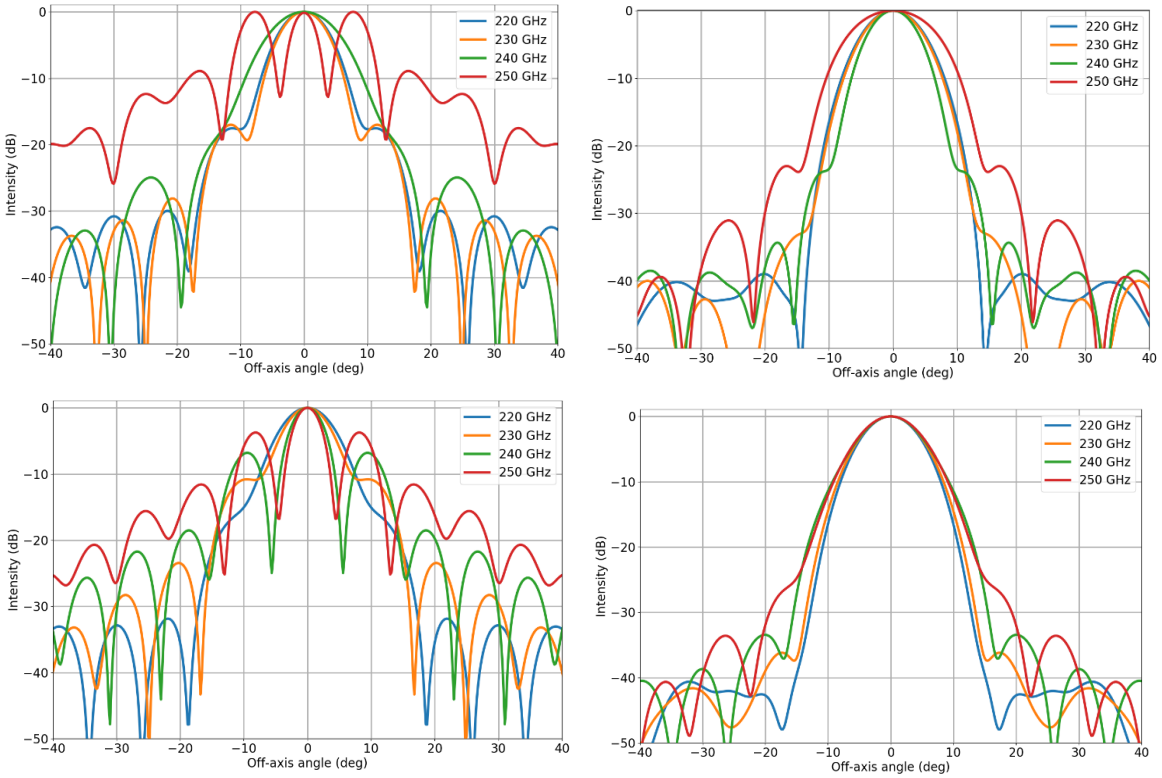

Figure 5.46: Simulated E-plane (left) and H-plane (right) of two arbitrarily chosen measured horn geometries feed_8_5 (top) and feed_1_2 (bottom). Only patterns at the higher end of the operating band are shown as they are the frequencies at which the beams are the most unpredictable and sensitive to variations in horn geometry.

5.3.2.1 Comparison with measured lab data (190-230 GHz)

Since the variation in the beam patterns at the higher end of the band was prominent, the comparison at 240 and 250 GHz will be explored separately in the next subsection. As already stated, only the H-plane of the far-field pattern was measured with the VNA and comparing this with the simulated H-plane patterns as in Figure 5.47 showed that there was very good agreement between the patterns at 190 and 200 GHz down to -40 dB, and as the frequency increased, the patterns began to deviate, however this was mainly restricted to low power levels (about -20 dB) which was deemed to be acceptable. The agreement between the return losses (Figure 5.48) over these frequency ranges was also observed to be very good. It should be noted that the measured return loss was only obtained for a single horn, and there was no record of which horn profile measurement this corresponded to, hence a direct comparison could not be made.

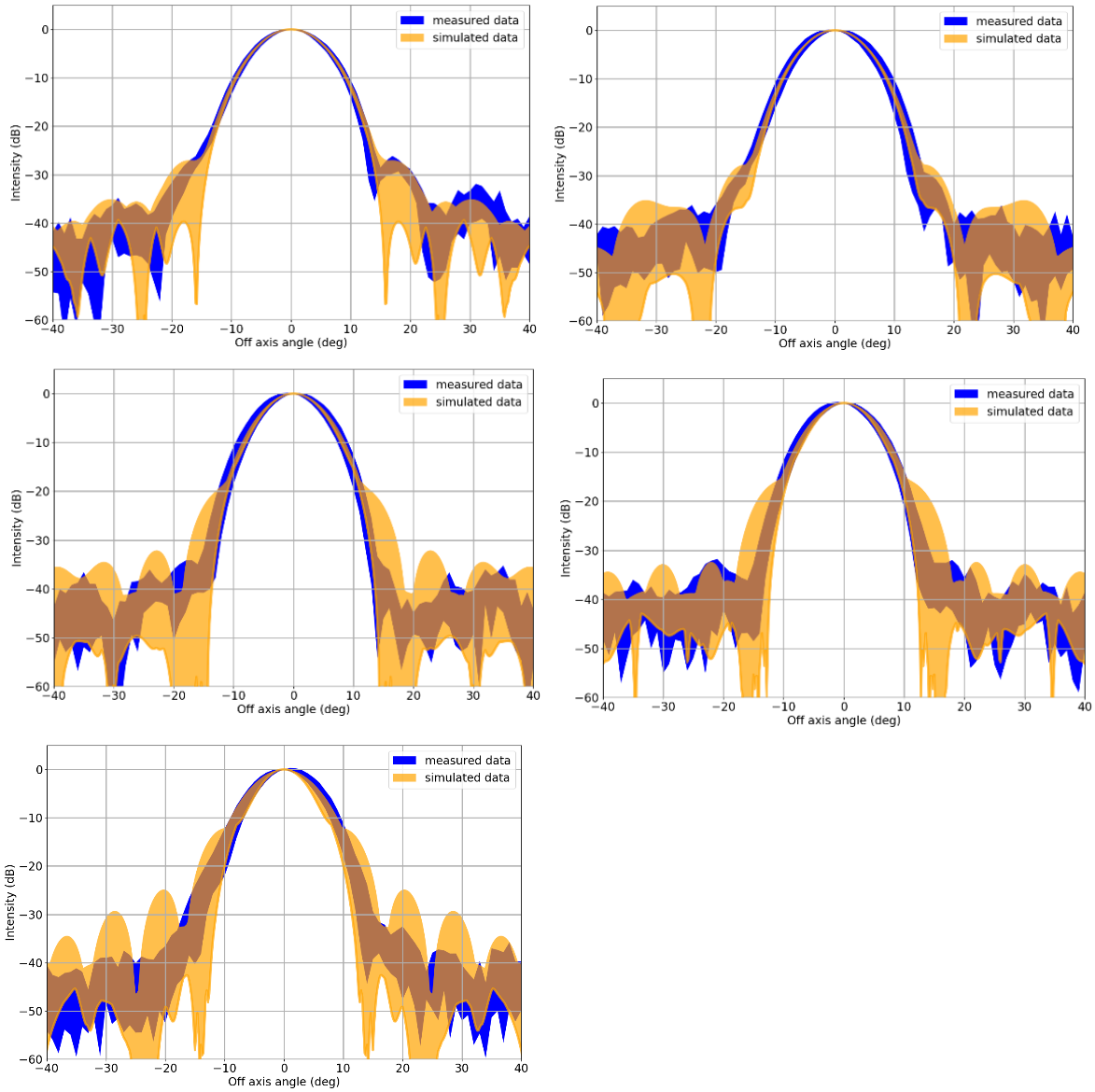

Figure 5.47: Comparison between the ranges for the simulated (from all 128 horn geometries) and measured (for 8 horns) co-polar H-plane far-field patterns at (from left to right) 190, 200, 210, 220 and 230 GHz.

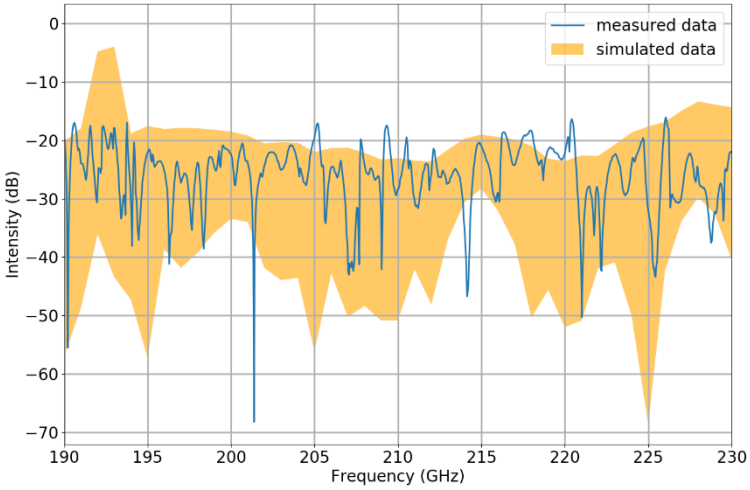

Figure 5.48: Return loss comparison from 190-230 GHz (128 simulations).

5.3.2.2 Comparison with measured far-field patterns (240-250 GHz) and investigation into the multi-moded behaviour of the measured horn geometries

Figure 5.49 shows that at the higher end of the band, the far-field patterns did not match as well as they do at the lower frequencies. The agreement shown between the measured and simulated data at all the other frequencies (both at the 150 GHz band and at the lower end of this band) implies that at these frequencies the discrepancies were not likely to be due to the manufacturing and assembly of the horns and thus this section will explore and propose a reason for these deviations.

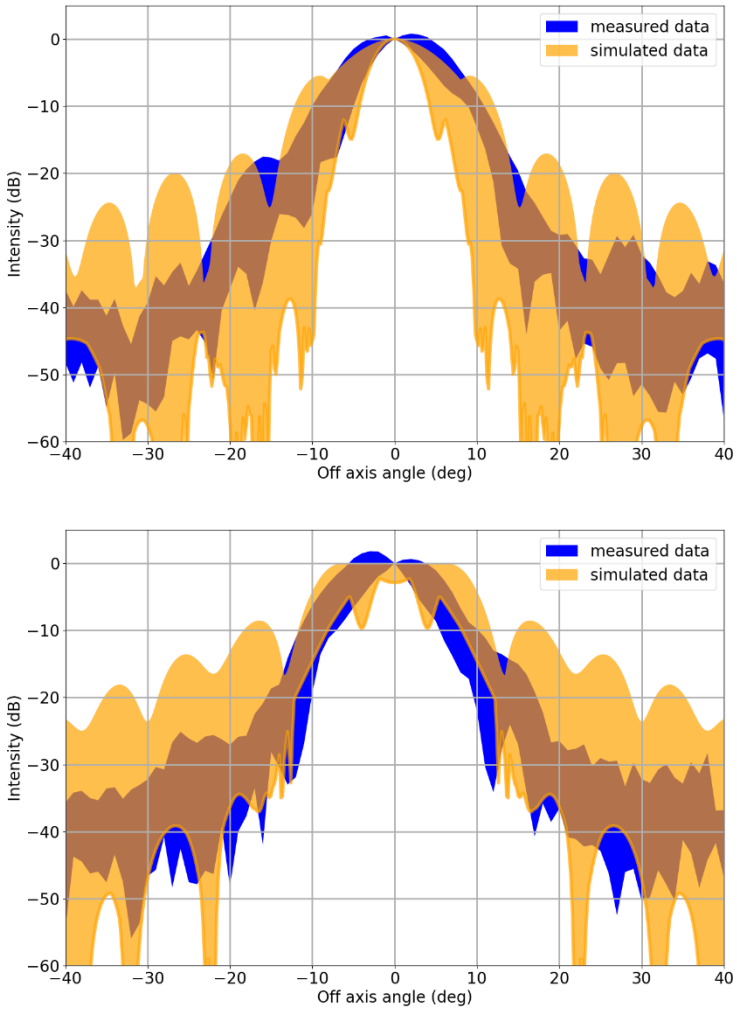

Figure 5.49: Comparison between the ranges for the simulated (from all 128 horn geometries) and measured (for 8 horns) co-polar H-plane far-field patterns at 240 GHZ (top) and 250 GHz (bottom).

Looking at the comparison for a single measured horn geometry (Figure 5.50) it was clear that there was significant asymmetry in the H-plane of the measured main beam, as well as it being noticeably wider than the simulated beam. This is very typical behaviour of a pattern that is the result of multi-moded excitation. Table 5.5 showed that within the $n = 1$ azimuthal order (this was the only azimuthal order investigated as this should have been the only order excited based on the previous results seen in the lower end of this band), there was a higher order hybrid mode present at relatively low power levels at the higher end of the band (seen at 245 and 250 GHz) for the nominal geometry. Performing a similar SVD analysis of the measured horn geometry (Table 5.8) showed that this same hybrid mode was also present in the measured horn geometry, but it cuts on earlier becoming prominent at 240 GHz (due to the geometry differences from

the nominal case). Taking this mode and adding it (in quadrature) onto the simulated far-field pattern (Figure 5.51) provided better agreement between the simulated and measured beam patterns. As will discussed in Chapter 6 and shown in VNA measurements by Kalinauskaite (2018), a coherent source can couple to higher order modes in a waveguide if it is incident from an off-axis angle for example. In the VNA setup it is possible that there was some misalignment in the testing setup which could cause this higher order mode excitation. The asymmetry in the beam could come from this higher order mode. If this mode is excited from the coherent source, then the resulting beam pattern is a coherent addition of the modes, thus the phase of the excited modes matter (and will be explored further in Chapter 6). Normally a multi-moded beam is the result of an incoherent summation of modes (which was performed for the simulated pattern in Figure 5.51), which assumes that there is no phase relation between the modes and provides a symmetric pattern. There is an issue with modelling this multi-moded behaviour accurately, as there is no way of determining the coupling between the source and the modes in the VNA setup, the full instrument will not suffer from this when measuring the CMB as it is a blackbody source, but it is important to keep these results in mind when testing begins at the higher band if a coherent source is used.

Table 5.8: Square of singular values in the S21 matrix of feed_8_5 in array 1. This can be compared with the values for the nominal horn geometry in Table 5.5.

Frequency	**Azimuthal Order**	
	1	
	Σ_{11}^2	Σ_{22}^2
190	0.9967	0
195	0.9998	0
200	0.9952	0
205	0.9985	0
210	0.9999	0
215	0.9980	0
220	0.9994	0
225	0.9945	0
230	0.9958	0
235	0.9704	2E-5
240	0.9024	0.7413
245	0.9752	0.5141
250	0.6635	0.0583

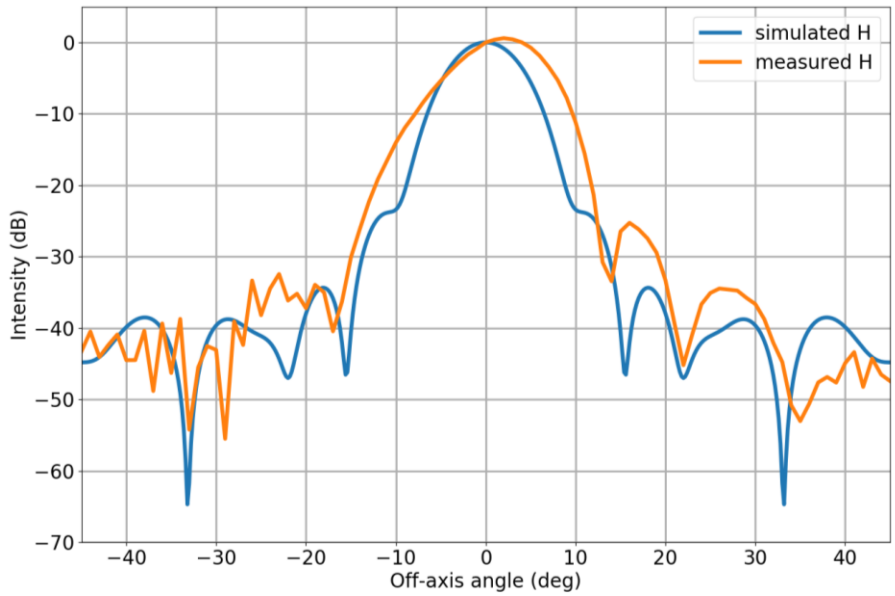

Figure 5.50: Comparison of the simulated and measured data for feed_8_5 at 240 GHz.

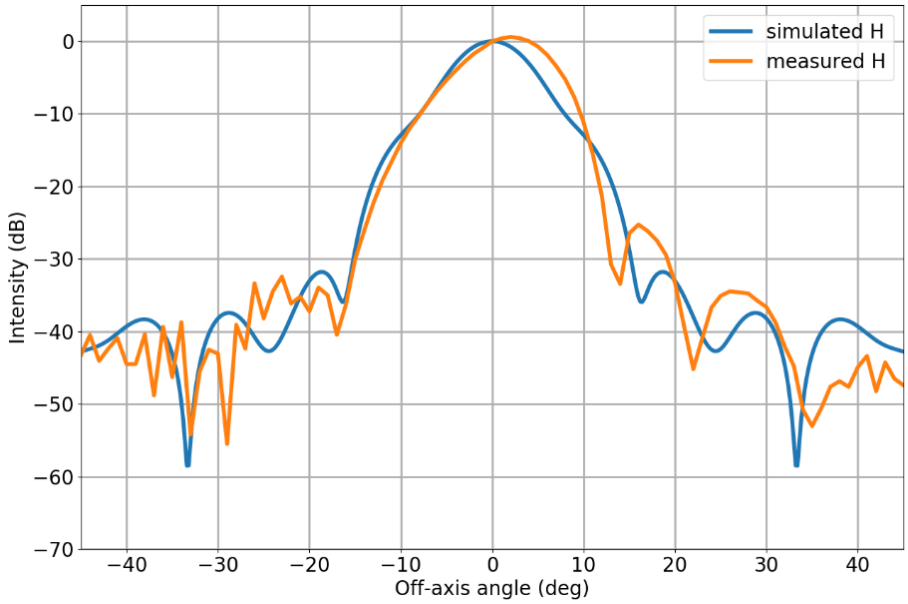

Figure 5.51: Comparison of the simulated data (with the higher order mode included) and measured data for feed_8_5 at 240 GHz.

Performing an SVD analysis of a different horn geometry provided the results in Table 5.9. Comparing this with Table 5.8 shows that there is similar power in the single mode that is propagating in the $n = 1$ azimuthal order at the lower end of the band, but when the higher order mode cuts on there is noticeable variance in the power of this mode (further evidence of unpredictability at the higher end of the higher operating band). It should be noted that while this higher order mode does have significant power at 240 GHz it is still less than the primary mode that is propagating, which Table 5.10 and Table 5.11 show is a result of scattering from the TE_{11} mode, which indicates that the primary mode is the HE_{11} mode, as expected.

Table 5.9: Square of singular values in the S21 matrix of feed_1_8 in array 1.

Frequency	Azimuthal Order	
	1	
	Σ_{11}^2	Σ_{22}^2
190	0.9993	0
195	0.9993	0
200	0.9991	0
205	0.9951	0
210	0.9981	0
215	0.9956	0
220	0.9981	0
225	0.9895	0
230	0.9939	0
235	0.9435	6E-6
240	0.9753	0.7738
245	0.9686	0.1750
250	0.3399	0.0965

Table 5.10: Summed values of the powers of modes from the S21 matrix and for the 1st and 31st column for feed 8_5 in array 1.

Frequency (GHz)	Total S21	1st Column (TE11)	31st column (TM11)
190	0.9967	0.9967	2E-5
220	0.9994	0.9971	0.0023
240	1.6438	0.8750	0.7688
245	1.4893	0.7998	0.6895
250	0.7219	0.1190	0.6029

Table 5.11: Summed values of the powers of modes from the S21 matrix and for the 1st and 31st column for feed 1_8 in array 1.

Frequency (GHz)	Total S21	1st Column (TE11)	31st column (TM11)
190	0.9993	0.9992	5E-5
220	0.9981	0.9863	0.0118
240	1.7490	0.9050	0.8440
245	1.1436	0.8863	0.2573
250	0.4364	0.1525	0.2838

Figure 5.52 shows the predicted (incoherent) multi-moded beam pattern across the upper QUBIC band. It can be seen that the beam is well-behaved up to the new upper cut-off of 240 GHz, and as with the nominal geometry, above this frequency it behaves unpredictably.

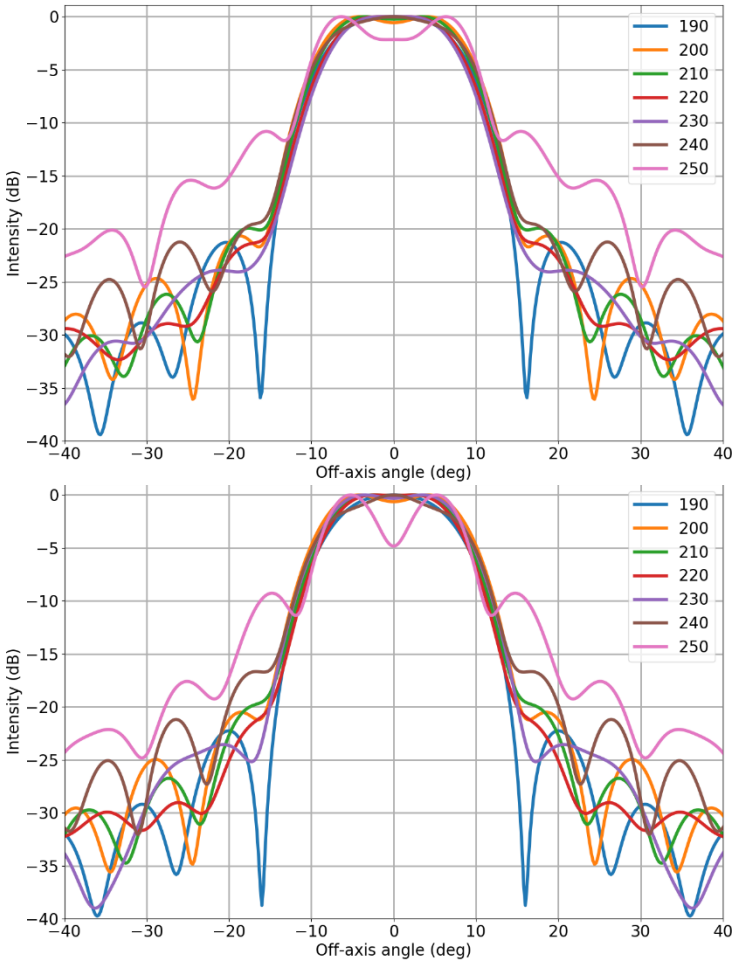

Figure 5.52: Predicted E plane of the co-polar far-field beam across the higher band for feed_8_5 (top) and feed_1_8 (bottom).

The measured return loss across the full band (Figure 5.53) also appeared to deviate from the simulated results at higher frequencies, roughly when the higher order mode cut on. However, this is not likely to be the cause of the discrepancy as even when a full multi-moded analysis was performed, the return loss (Figure 5.15) showed a similar pattern to that of this single moded operation analysis, with an increase at the higher end of the band. PEC materials are a good approximation for a system but they are not realistic and it is possible that the material from which some components are made is lossy at these higher frequencies. This means that some of the radiation incident upon them is lost (due to scattering or ohmic loss) that does not end up being transmitted through or reflected back out of the horn. As well as this, when testing the horns in the VNA a separate home-made waveguide setup, that will not be used in the QUBIC instrument, was utilised to connect the horn to the VNA probe itself. This waveguide could also be lossy and introduce the issues that we are having. An investigation into lossy waveguides was performed by Doherty (2012) with CST microwave studio (a commercially available software that provides exact solutions to Maxwell's equations with finite integration techniques), which found that lossy materials can absorb radiation which causes a decrease in the reflected power but no corresponding increase in the transmitted power as has been the case for the PEC assumptions made in this chapter.

The discrepancies between the simulations and the measured data caused the collaborator in Milan to enhance their measurement setup. They were able to set up a system in which only the reflection from the flanges of the horns were measured, and any reflections from the improvised waveguide setup. This generated the results seen in Figure 5.54 which agree much better at the higher frequencies.

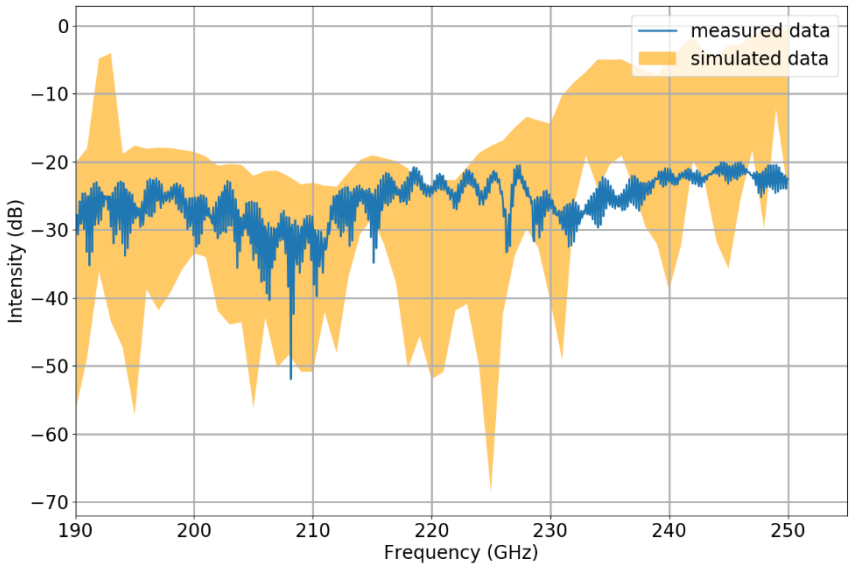

Figure 5.53: Return loss comparison across the entire operating band (128 simulations).

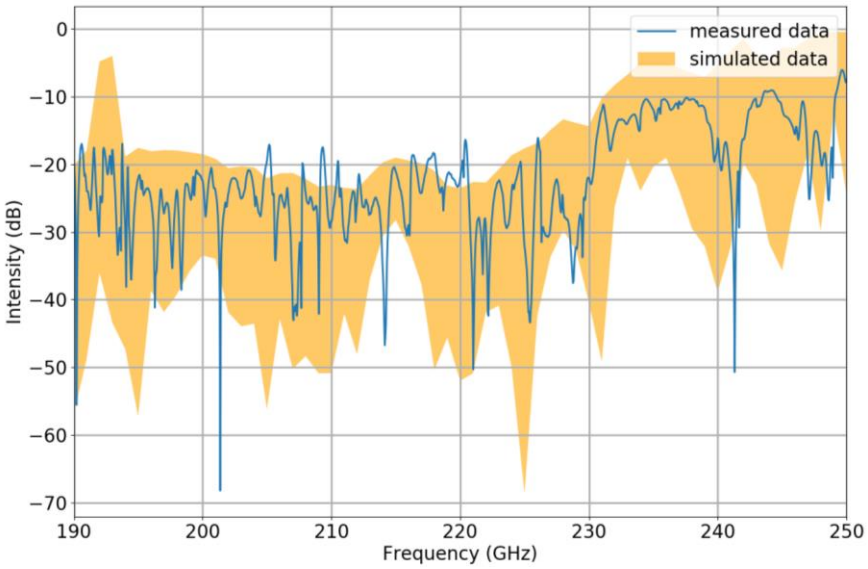

Figure 5.54: Return loss comparison across the band with the refined VNA setup (128 simulations).

5.4 Summary

QUBIC will operate over two bands, the lower band centred on 150 GHz and the upper band centred on 220 GHz. This chapter modelled the electromagnetic performance of the QUBIC horn in both bands using mode matching techniques. The idea of TE and TM modes being used to describe the radiation inside a waveguide was shown. Mode matching techniques can be used to generate four scattering matrices (S_{11}, S_{12}, S_{22} and S_{21}) that fully describe the modes transmitted and reflected by a waveguide. Since a corrugated horn can be considered as a collection of successive waveguides, the electromagnetic performance of the horn can then also be obtained by using mode-matching techniques. It was also detailed how corrugated horns can be described with hybrid modes (some combination of TE and TM modes) which are the natural modes of a corrugated horn in the same way that the TE and TM modes are the natural modes of smooth walled waveguides. An SVD analysis of the S_{21} matrix will give the number of hybrid modes present at the output of the horn, which then determines whether the horn is single-moded (only one hybrid mode supported) or multi-moded (more than one hybrid mode supported). A mode matching and subsequent SVD analysis was performed for the QUBIC horns. It was shown that the QUBIC horns are single-moded at the lower band and multi-moded at the upper band. The far-field patterns and return loss across both bands were also obtained, the lower band behaved as expected. The upper band however behaved unpredictably and undesirably at the higher end of the band and thus the bandwidth was reduced slightly.

Mode matching techniques were then used on horn geometries that were representative of the manufactured horns. First the effect of cusps that are present on the corrugations due to the method used to manufacture the horns was investigated and it was found that these would have no meaningful negative effects on the performance of the horns. A full mode matching analysis was then performed on 128 different horn geometries that were provided by collaborators from Milan, these results were then compared with the lab measured results obtained with a VNA (only single moded performance at all frequencies could be analysed in the lab) for a selection of these horns. It was found that at the lower band and for most of the upper band the simulations and the measured results agreed well. At the higher end of the upper band there were some discrepancies, however these could be explained by the multi-moded nature of the horns. There were some discrepancies with the reflected power, but after the lab measurements were refined it was shown that the

simulations and the measured data agreed. This analysis showed that the horns behaved as expected, indicating that they were well manufactured and assembled. It also highlighted the importance of careful measurements with a VNA, in particular at frequencies where multiple modes are supported within a waveguide.

The next chapter will explore more rigorous modelling in preparation for the future phases of the QUBIC instrument.

6 Modelling for future instrument

6.1 Introduction

It is planned that the QUBIC project will have three further phases once testing of the current TD in Paris has been completed.

Phase 1: Deployment of the TD in Argentina with testing being performed by collaborators in the laboratory at Salta and full operations planned to begin in January 2022.

Phase 2: Upgrade to the FI. It is estimated that this will be done after 1 year of operation of the TD and will take six months. This is when the instrument will reach its nominal sensitivity and should provide scientifically significant results after 3 years of observation.

Phase 3: Upgrade to QUBIC+, an improved version of the FI. It is envisioned that there will be an improvement in the cryogenics so that the focal plane and optical combiner temperatures can be reduced further and thus there will be lower detector and background noise. There will be hexagonal packing of the horn array instead of the current square packing, with the horn profile changed so that they operate with multi-moded optics at the lower band. This would generate a higher throughput and an increase in sensitivity.

Some modelling has already been shown for the FI but this chapter will focus on more detailed modelling that was performed for the FI, its calibration and potential future instrument upgrades. The multi-moded operation of the instrument will be explored using physical optics, with a particular focus on the observation of a coherent source, as occurs in the laboratory and calibration. The power gain from the multi-moded operation of the horns will be explored. Finally this chapter will describe the technique of spectro-imaging which has been proposed as a potential replacement for dual band observations using the dichroic. It is still the plan to have two focal planes (one for each operating band) in the FI, however, the manufacturing of the dichroic is proving to be difficult and an alternative method for operating the instrument at multiple frequencies may be required.

6.2 Calibrator lamps for the full instrument

The Winston cones that were mentioned in Section 4.3 will also be used in the FI (phase 2) for inter-calibration of the focal plane pixels (currently the only purpose of the Winston cone is for calibration of the pixels, and could be used for this purpose in phase 3 or any potential future phases of the instrument). As is the case with the TD, they will be mounted onto the side of the horn array (Figure 6.1) and their beams propagated through the optical combiner. The pattern produced on the focal plane by these lamps is non-uniform (shown before in Figure 2.2 and reproduced here in Figure 6.2). The variance in the pattern ranges over 15 dB as opposed to 2-3 dB for the TD. This can be explained by the position of the calibrator sources, which are as far from the origin of the array as possible. As a result, they will suffer from increased truncation by the optical elements in the combiner. However, as long as this is well understood and can be corrected for, there is no reason why these Winston cones cannot be used for the intercalibration of the focal plane pixel arrays. It may even prove useful to have a recognisable pattern on the focal plane.

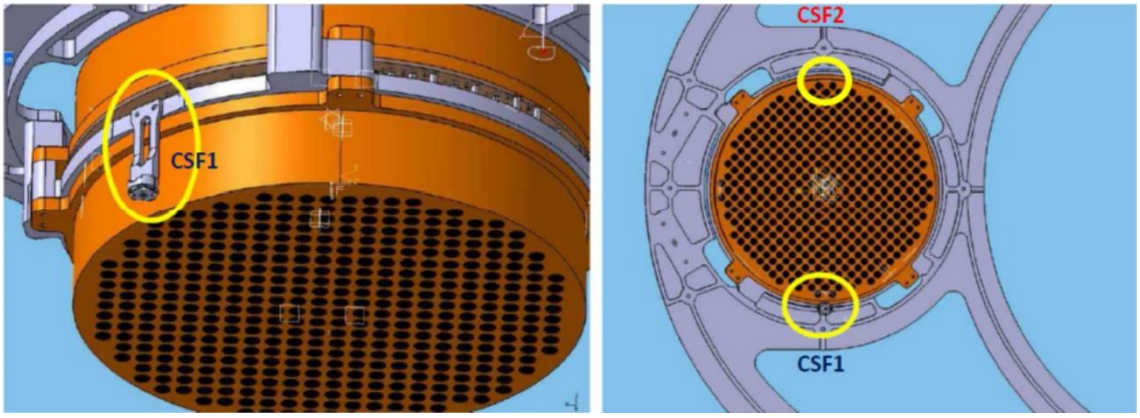

Figure 6.1: CAD model of the calibrator lamps on the full instrument horn array (CSF1 is positioned at (0 mm,181.11 mm,0 mm) and CSF2 at (0 mm,-181.11 mm,0 mm) on the GRF. Image and locations provided by M de Petris and D. Buzi of the Sapienza University of Rome.

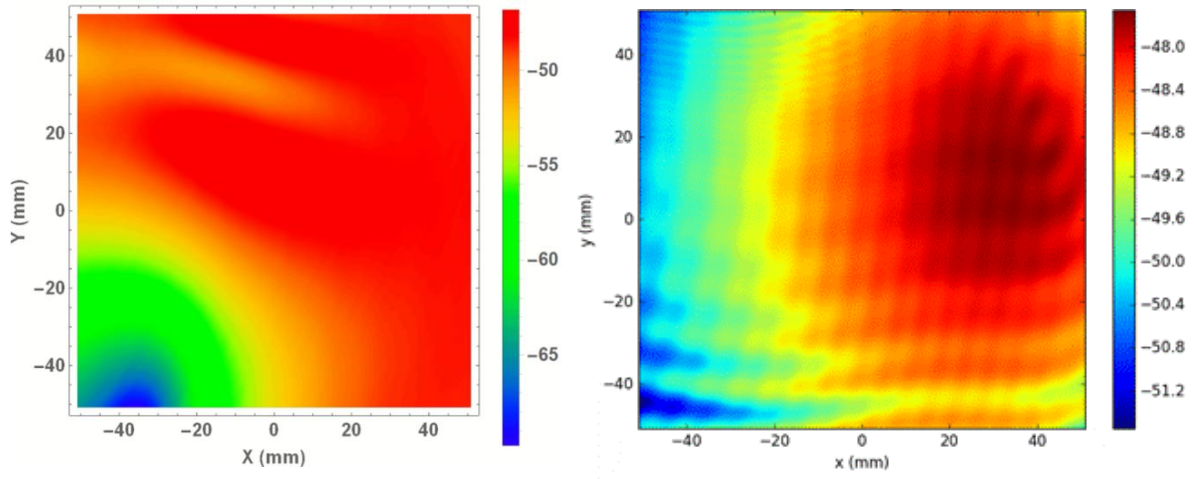

Figure 6.2: Beam pattern on the focal plane from of the QUBIC instrument from CSF1 on the FI (left) and Cal_SOU_1 on the TD (right) normalised to the peak of the input radiation of their respective Winston cone.. Shown previously in Figure 2.2 and Figure 4.7 respectively.

6.3 Synthetic beam

The synthetic beam for the FI at the lower operating band was obtained in this section using method 3 that was described in Section 3.6.2. Since the FI has a much larger horn array, the position of the far-field screen that captures the beams had to be placed farther from the aperture of the instrument than for the TD. As a result of this, the size of the screen had to be increased, which in turn required an increase in the number of PO points. On top of this, there are roughly six times more horns in the FI than the TD, meaning that there was a near ten-fold increase in the computation time for the FI over the TD.

As an example, the on-axis synthetic beam was obtained using a 150 GHz point source centred at (0 mm ,0 mm) on the ONAFP_RF (from Table 3.3), the beam from which was passed through an optical combiner containing only the primary and secondary mirrors (for speed, it has been shown that the cold stop will not affect the beams of the FI as they pass through the combiner and including the filters would cause the simulation to be too time consuming), and exciting the feedhorns whose outputs were propagated onto a screen positioned 30 m from the sky-facing horn aperture. The resulting synthetic beam is shown in Figure 6.3.

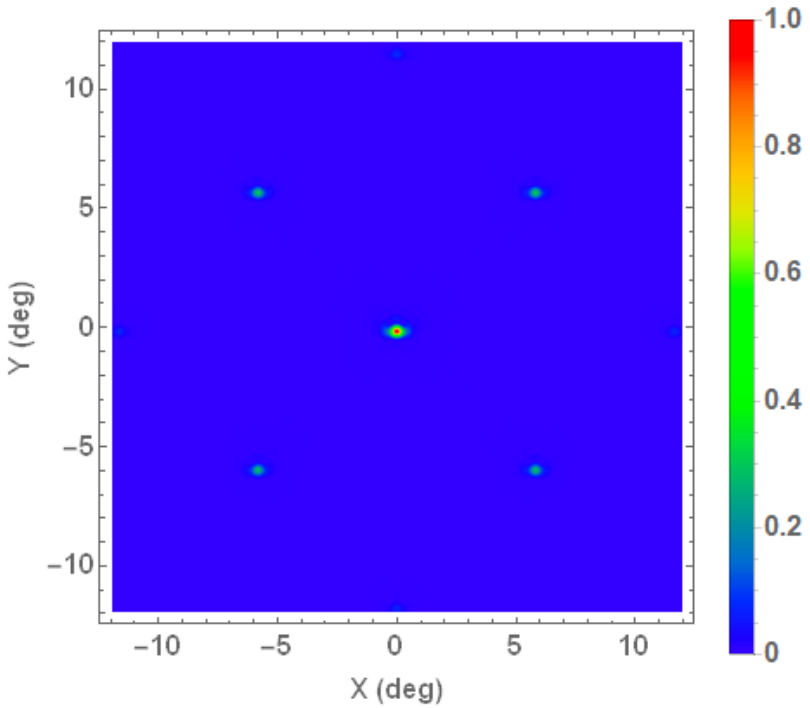

Figure 6.3: Synthetic beam of the full instrument recorded on a 7×7 m^2 screen placed 30 m away from the horn aperture, normalised to the on-axis peak.

It was shown in Chapters 2 and 4, how the width of the synthetic beam peaks are dependent on the size of the feedhorn array (equation [56]). Since the FI has and array that is about 2.5 times the size of the TD array, the width of the synthetic beam peaks for the FI (main peak width of 0.382º) are correspondingly narrower than those of the TD (main peak width of 0.910°) as seen in Figure 6.4. The fact that the peaks are narrow for the FI, means that it has a finer angular resolution and this is vital for the spectro-imaging technique which will be discussed later in this chapter.

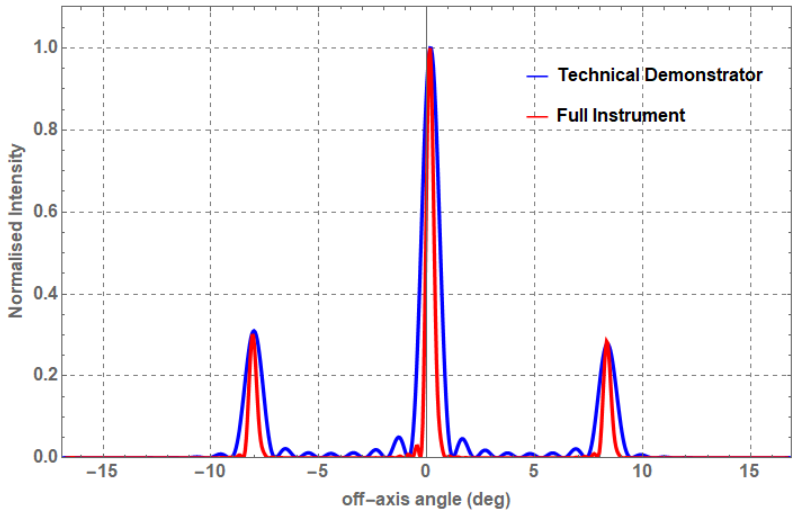

Figure 6.4: Cut of the synthetic beam of the FI and TD from a 150 GHz point-like source at (0 mm ,0 mm) on the ONAFP_RF showing the difference in the width of the peaks, as expected.

6.3.1 Asymmetry in the beam pattern

It was mentioned in Chapter 3, that the synthetic beam should not suffer from the same levels of asymmetry as the PSF, and this is still the case here. When looking at a 1-dimensional cut of the synthetic beam for the FI (Figure 6.5) however, it can be seen that there is some asymmetry in the beam. The main peak of the beam is slightly off axis – as was the case with the TD – and there is also a subsidiary peak that appears on the left of each of the expected peaks (most prominent on the main peak). Figure 6.6 shows the beam expected from an ideal (non-aberrating) combiner which has these small peaks symmetrically on either side of the peaks. Hence there is some asymmetry, albeit small, being introduced into the beam that was not present (or not as obvious) in the TD.

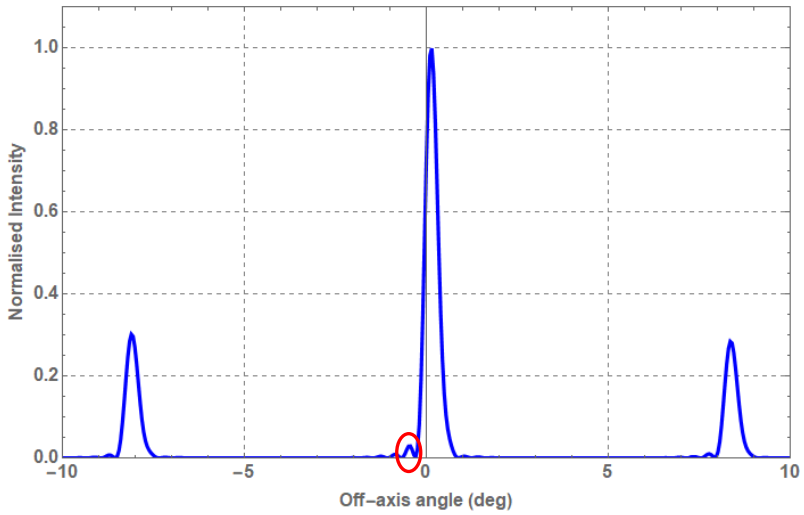

Figure 6.5: Diagonal cut of the synthetic beam from the top left to the bottom of right of Figure 6.3 with the asymmetric off-axis peak outlined in red at a relative intensity of 0.035 the main off-axis peaks are located at −8.094º and +8.375 º from the man central peak, close to the ideal case of 8.2 º, as expected.

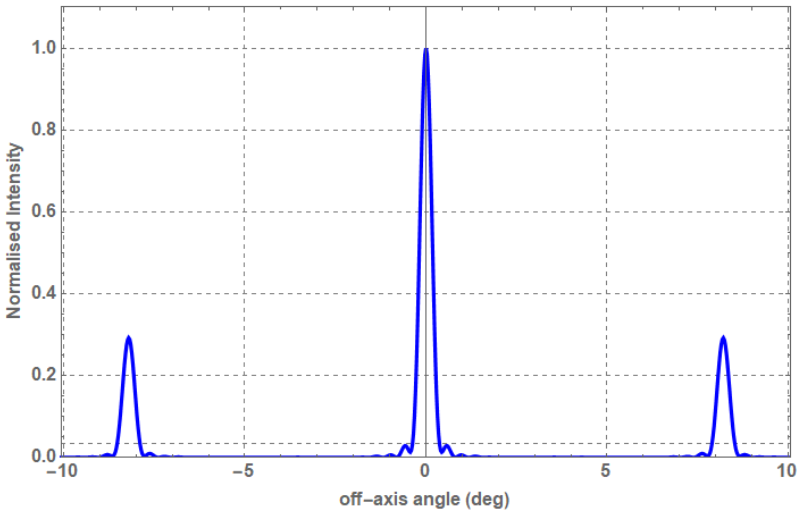

Figure 6.6: Diagonal cut of a synthetic beam on a screen 30 m away from the sky facing horn aperture, resulting from direct excitation (does not pass through the optical combiner) of the horn array by on-axis plane wave at 150 GHz.

To ensure that this asymmetry is inherent to the instrument design rather than a modelling limitation, comparisons to the TD synthetic beam (calculated from these FI simulations) were performed, as well as investigating the position of the screen and ensuring that the point source used was as close to a point source as possible.

6.3.1.1 *Comparison with TD results*

The synthetic beam has been shown for the TD (Section 3.6), and thus, this can be used as a comparison with the FI. Since MODAL outputs the data file for each horn beam separately, the horn beams corresponding to the TD horn positions can be extracted from the FI simulation and used to generate a synthetic beam for comparison with the full TD simulation (i.e. using the TD mirrors) carried out previously. Since the positions of the mirrors are the same for both instruments the synthetic beams are nearly identical as seen in Figure 6.7 (the FI mirrors are bigger). This indicates that there is no issue with the FI model in MODAL.

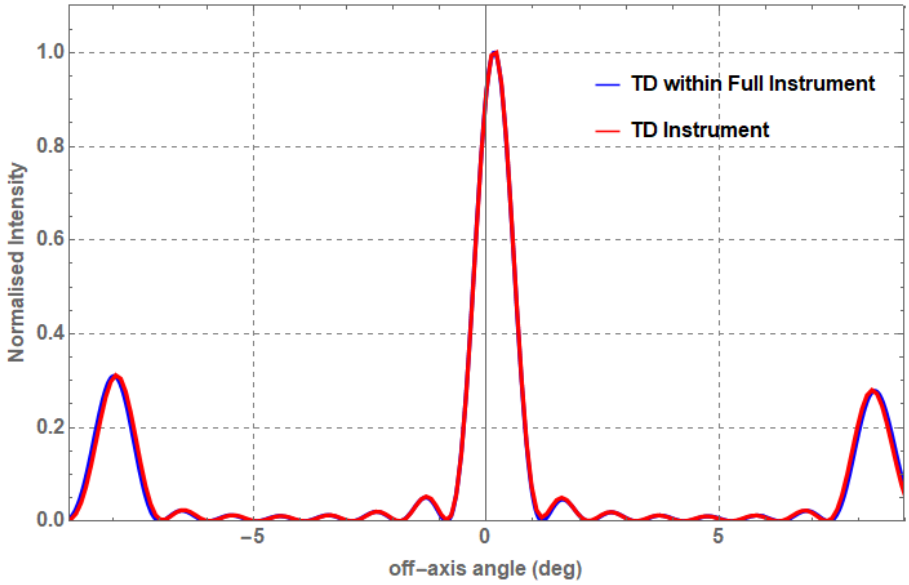

Figure 6.7: Comparison between the synthetic beam generated 30 m away from the sky facing horn aperture for the TD instrument in MODAL and the TD horns in the FI dataset for a 150 GHz point source located at (0 mm, 0 mm) on the ONAFP_RF.

6.3.1.2 *Source size*

A point source is not physical but, as explained in Chapter 2, in MODAL a uniformly illuminated small aperture can be used as a reasonable approximation. Initially an aperture of 0.05 mm radius was used (this was the size of the source used for the TD synthetic beams). Since the mirrors are bigger in the FI, it was theorised that there could be an issue with the mirrors not seeing this aperture as a point source. To investigate this, a full simulation was performed with an aperture that was reduced in size by a factor of 100. Figure 6.8 shows that the patterns are identical so the size of the aperture is not an issue.

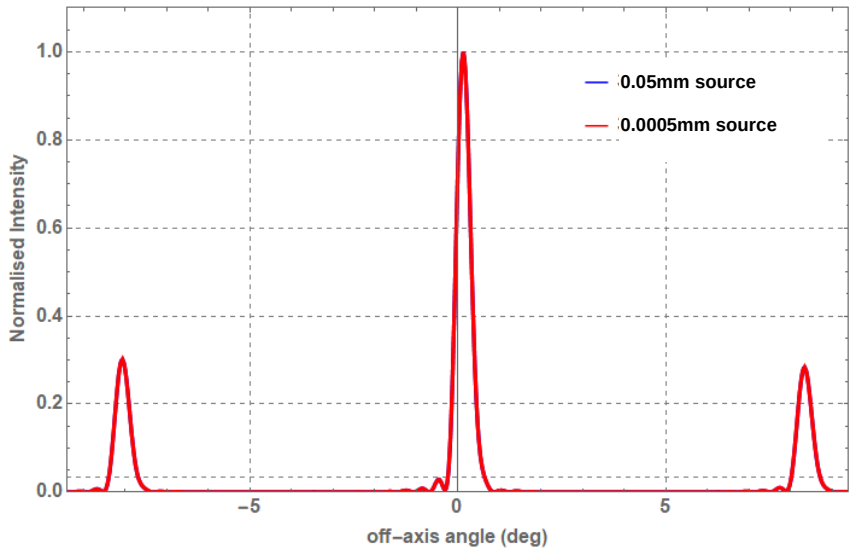

Figure 6.8: Comparison between the synthetic beam generated 30 m away from the sky facing horn aperture for the FI in MODAL calculated using a 150 GHz 'point source' approximation of aperture radius 0.05 mm (original) and 0.0005 mm located at (0 mm, 0 mm) on the ONAFP_RF.

6.3.1.3 Distance in the far-field

The next simulation was performed to investigate any effect due to the distance of the observation screen that the EM radiation from the horns was propagated on to and if it was far enough away to be in the far-field of the full instrument. For this, the screen was placed 40 m away from the horn apertures. This results in the essentially identical beam patterns seen in Figure 6.9. Since the screen was farther away than before the screen size had to be increased so that the angular extent remained the same, and to ensure that the simulations were not too computationally intensive the sampling size could not be increased proportionally with the size increase. Nevertheless, no significant differences can be seen so we can conclude that the 30 m screen was far enough into the far-field for the beam to have settled into a steady pattern.

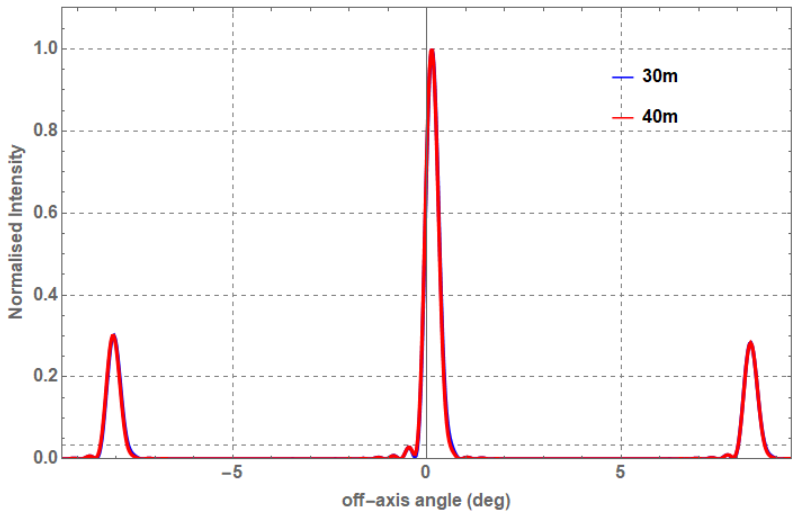

Figure 6.9: Comparison between the synthetic beams generated 30 m and 40 m away from the sky facing horn aperture for the FI in MODAL resulting from the excitation from a 150 GHz point source at (0 mm, 0 mm) on the ONAFP_RF.

The two obvious causes of errors in the simulation have been investigated. Another check is to use method 3 for generating the data (shown in Section 3.6.2). A PSF was generated with an on-axis plane wave at 150 GHz and from this a synthetic beam was generated for an on-axis FP point by imposing a phase slope on the PSF data. Comparing the two cuts of the synthetic beam (Figure 6.10) shows that the asymmetry is present in both of them though they are not identical, the main peaks match in position and in relative intensity.

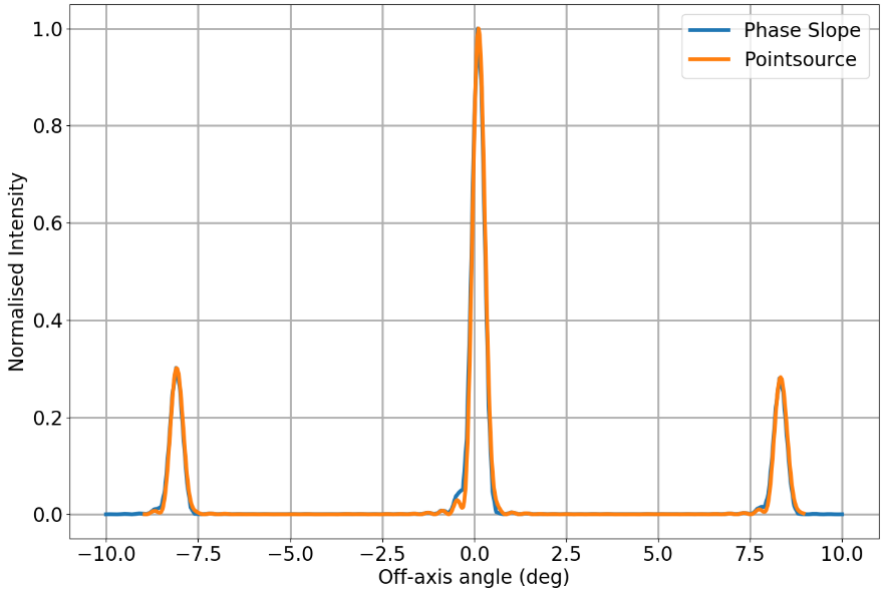

Figure 6.10: Cuts of the synthetic beam generated from the phase slope method and the point source method for a pixel centred on (0 mm, 0 mm) on the ONAFP_RF.

6.3.2 Inherent asymmetry due to combiner design

All of these tests point to the FI beam having some asymmetry present in it, inherent to the instrument design itself. This is to be expected from the off-axis nature of the design. To investigate this further the input radiation at two arbitrarily chosen horns (x14y06 and x14y22) was examined as in (Figure 6.11). This showed the intensity of the radiation was not uniform across the two horns, unlike what would be observed when exciting the horn of an ideal instrument with radiation from a true point source (plane wave and no combiner). The non-negligible intensity difference (10-15 %) arises due to aberrations and truncation introduced into the beam from the mirrors in the combiner. Note that this would be most notable for the horns on the outer edges of the array (i.e. horn x14y22).

Figure 6.12 shows that differences in the input field created a difference in the coupling between the radiation and the horns, causing the output beam to be different (in terms of intensity) for the selected horns. It is reasonable to assume that this difference can then cause the low level asymmetric features next to the main peak.

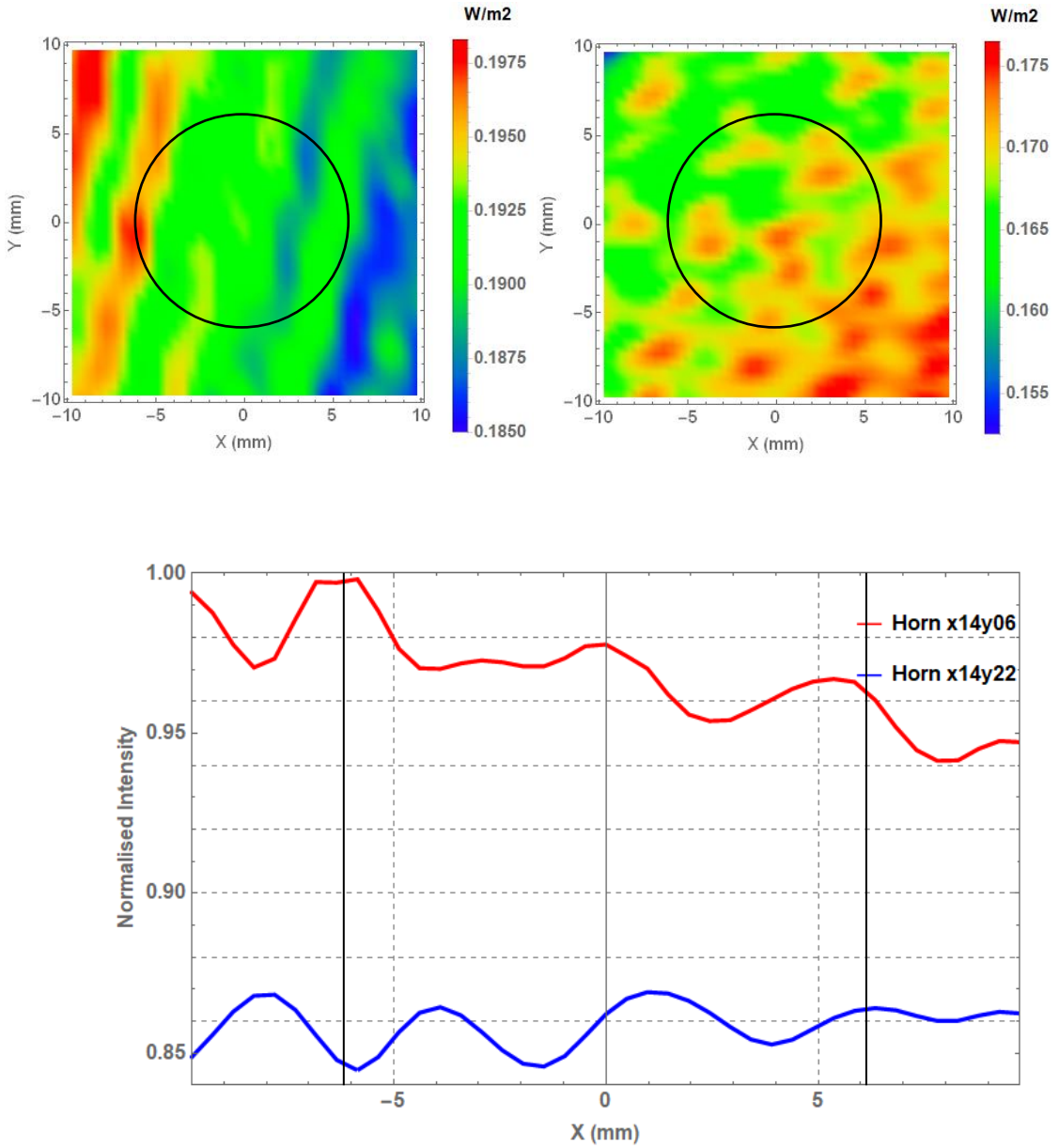

Figure 6.11: (top) Intensity of the field 1 cm from the input of horns x14y06 (left) and x14y22 (right) – the black circle indicates the size and position of the horn aperture. (bottom) Horizontal cuts across the centre of the patterns normalised relative to the peak of the pattern at the x14y06 horn – the black lines represent the size of the horn aperture.

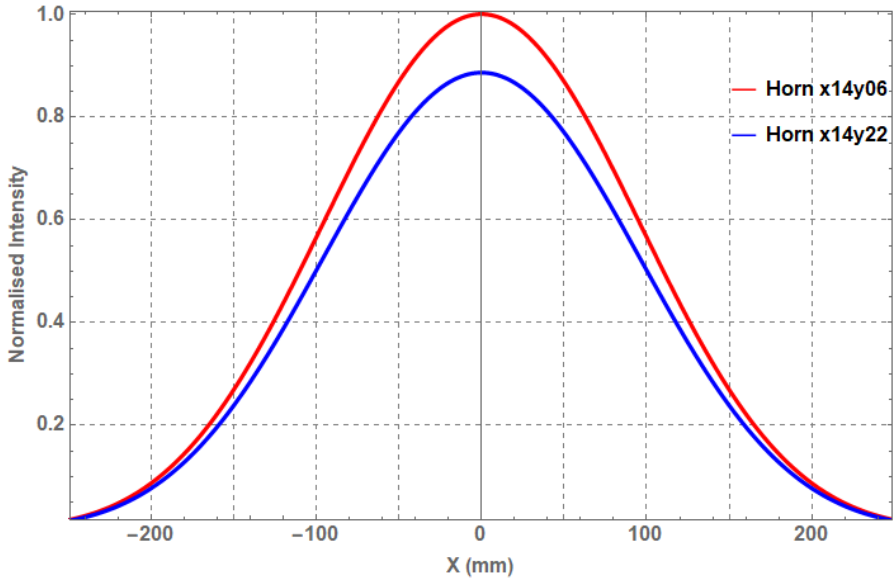

Figure 6.12: Horizontal cut of the output beam pattern from horns x14y06 and x14y22 normalised relative to the peak of the x14y06 beam on a screen 1 m away from the horns.

Figure 6.13 shows that the asymmetry in the synthetic beam peaks increases marginally for off-axis pixels. As well as this, it can be clearly seen that for off-axis pixels the asymmetry introduced by the combiner causes a further change in the coupling such that the synthetic beam peaks are below the nominal 12.9° Gaussian envelope (as seen in Chapter 4 with the TD instrument) rather than what would be expected for an idealised on-axis system as in Figure 6.14. This asymmetry itself should not affect the results and goals of the instrument, but it is useful to know this and take it into consideration for any potential future QUBIC like instruments.

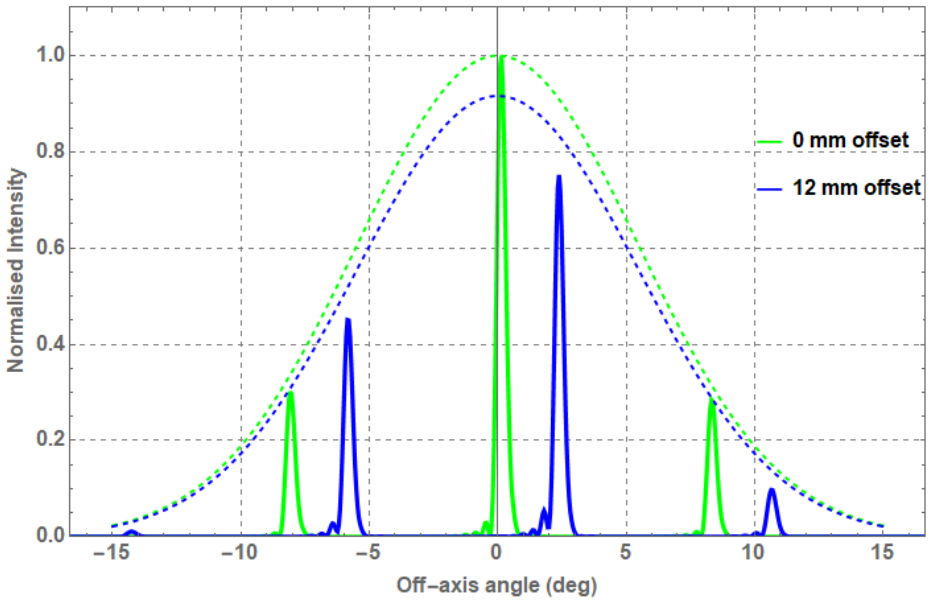

Figure 6.13: Synthetic beam for an on-axis pixel and a 12 mm (2.3°) off-axis pixel at (8.485 mm, 8.485 mm) on the ONAFP_RF, all normalised with respect to the peak of the on-axis synthetic beam.

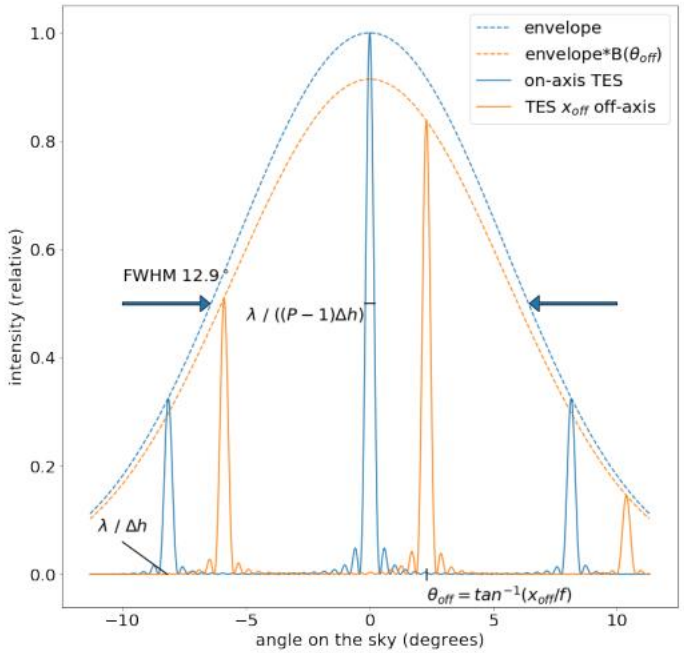

Figure 6.14: Synthetic beam for an on-axis pixel and a 2.3° off-axis pixel for an ideal QUBIC instrument (C. O'Sullivan *et al.*, 2020).

6.4 Upper band PO analysis

The multi-moded operation of the QUBIC horns was modelled with mode matching techniques in Chapter 5. The resulting scattering matrices contain the information for all the possible hybrid modes that exist at the aperture of the horn and the total far-field pattern is a result of the incoherent summation of these modes, essentially simulating the observation of a blackbody source. However, it is very difficult to get an incoherent black body source to use as a calibrator and as already stated the current test setup for QUBIC utilises a coherent calibrator source, which will not necessarily couple to all the modes in the horn, and thus will not provide the total far-field pattern for the upper band as seen in Figure 5.17. As a result, this section will use PO techniques to analyse the multi-moded response of the QUBIC feedhorns to a coherent source operating at 220 GHz (simulating what would be measured in the test laboratory with the current source), as well as presenting the incoherent observations of a non-blackbody source to provide a baseline for potential future measurements in the laboratory. MODAL also allows for the multi-moded beam to be propagated through the full optical combiner and the beam patterns to be observed on the focal plane of the instrument. The analysis in this section will be performed with the TD instrument.

The nature of the observed source will determine whether the modes should be combined incoherently or not. The sky is an incoherent source and that is how the modes of the QUBIC horns have been combined with the mode matching analysis shown in Chapter 5. However, since the calibrator source that will be used in the lab is coherent, the coherent combination of the horns must also be investigated. In MODAL, the datafiles of multi-moded beams can be exported in two ways: either as a coherent combination of the modes present, or, if there is more than one mode propagating, a separate datafile can be output for each mode present in the beam, allowing for an incoherent combination to be performed afterwards.

6.4.1 Exciting higher order modes in MODAL

A far-field source will be scanned across the FOV of QUBIC during calibration. The coupling between the horns and the incident radiation is different for on- and off-axis sources. For single-moded operating frequencies this results in a drop in intensity of the output beam (as seen in Chapter 4). At frequencies where higher-order modes can also propagate, changing the source angle of incidence can also cause different order modes to be excited. This is a real effect that has been verified with VNA measurements by Kalinauskaite (2018).

This can be investigated in MODAL by getting the field output for each individual mode which can later be recombined. To investigate this effect for the QUBIC horns, a plane wave input was tilted by various angles about the *x*-axis of the GRF (to simulate off-axis sources), with Table 6.1 showing that as the off-axis angle increases, the non HE_{11} modes also increase in relative power (note that the overall power will also drop with off-axis angle as was the case with the single moded operation). Figure 6.15 provides a visual representation for how these modes vary with the incident angle (it also shows that the shape of the modes is the same as when they are modelled with mode matching techniques as in Figure 5.16). Note that the plane wave is linearly polarised, and an unpolarised source would excite more orthogonal modes.

Table 6.1: Peak intensity of the far-field pattern of the three azimuthal orders in a QUBIC horn for a selection of off axis angles when excited with a 220 GHz incident plane wave source in MODAL. Note that the normalisation is with respect to the peak of primary $n = 1$ mode (i.e. the HE_{11} mode).

Off-axis angle (deg)	Azimuthal order	Peak Intensity (W/m^2)
0	0	1E-20
	1	1.00
	2	1E-18
1	0	0.004
	1	1.000
	2	0.004
2	0	0.017
	1	1.000
	2	0.018
5	0	0.127
	1	1.000
	2	0.130
7	0	0.314
	1	1.00
	2	0.323
10	0	1.034
	1	1.000
	2	1.131

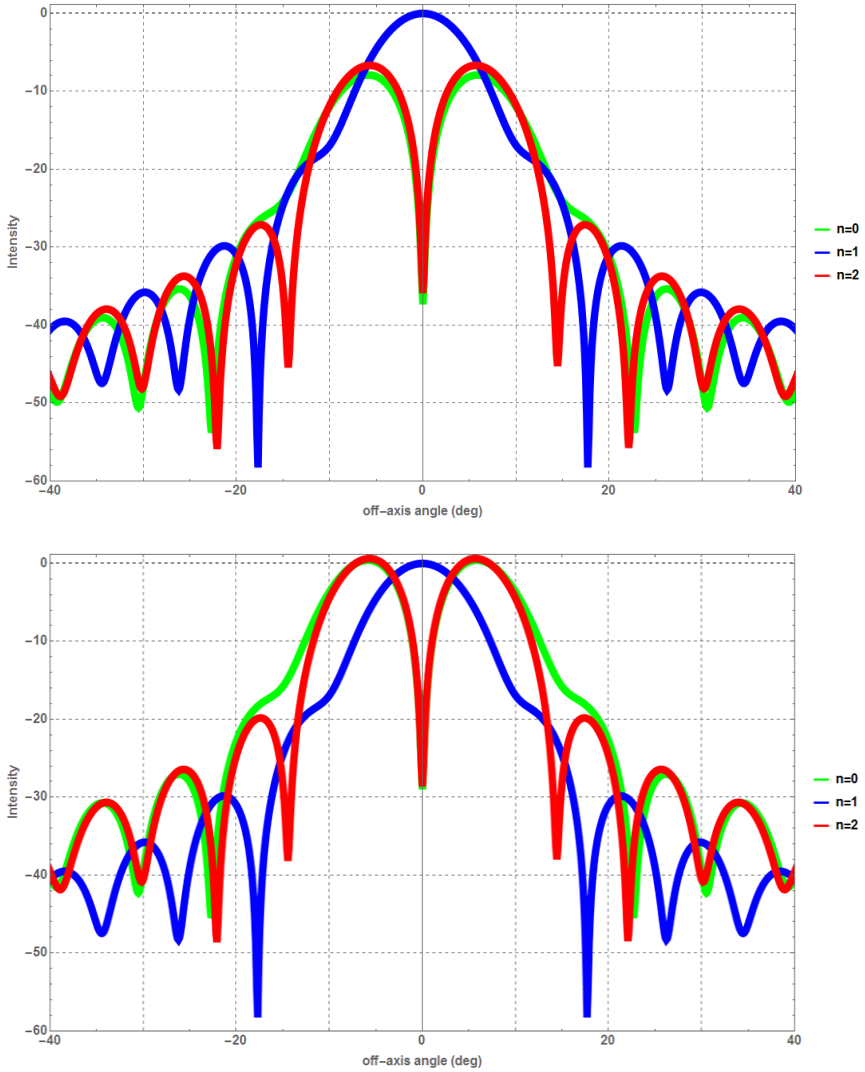

Figure 6.15: Normalised E-plane pattern of the hybrid modes (in dB) of the QUBIC horn excited by incident radiation at 5º (top) and 10º (bottom), all modes are normalised to the peak of the $n = 1$ hybrid mode (the HE_{11} mode) – no orthogonal modes included.

From Table 6.1 it can be seen that an incident on-axis plane wave will excite the HE_{11} mode in the horn, which can then be compared to the VNA test of the horns (which also could only excited a single mode in the horn) and Figure 6.16 shows that the far-field result of a MODAL simulation of the excitation of the nominal horn geometry match the single mode VNA observations well.

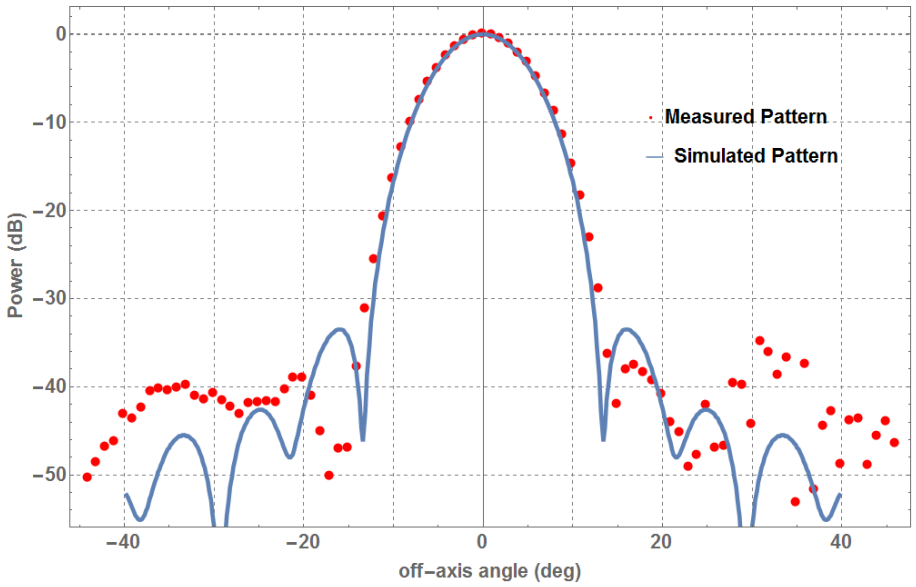

Figure 6.16: Comparison between the beam pattern simulated in MODAL for an observation of an on-axis co-polar plane wave at 220 GHz and VNA measurements of a horn at 220 GHz (performed by M. Zannoni of Università degli Studi di Milano-Bicocca in 2016).

6.4.2 Incoherent vs coherent addition of modes

Coherent

The coherent addition of the modes includes the phase relation between them, thus the resulting field will have some asymmetry present in it, even if it is propagated directly onto a far-field screen (i.e. there are no aberrations due to the QUBIC optical combiner) as in Figure 6.17.

Incoherent

The resulting incoherent far-field pattern (Figure 6.18) were all observed to be symmetric in shape, as expected. However, the cutting on of the higher order modes means that the overall patterns were very different in shape as the off-axis incident angle increased. This can be clearly seen in Figure 6.19, where the higher off-axis angles cause the higher modes to have more relative power, eventually causing the pattern to have an on-axis drop for a 10º off-axis source. These incoherent combinations can be compared with the patterns produced in the mode-matching software (as both use the incoherent combination of the modes) and it was found that an incident off-axis angle of 6º produced a pattern that was comparable to far-field resulting from a black body observation (all modes excited equally at the entrance of the horn) as seen in Figure 6.20.

The differences between the incoherent and coherent combinations will result in different envelopes for the PSF (and synthetic beam) which will be explored in the next section.

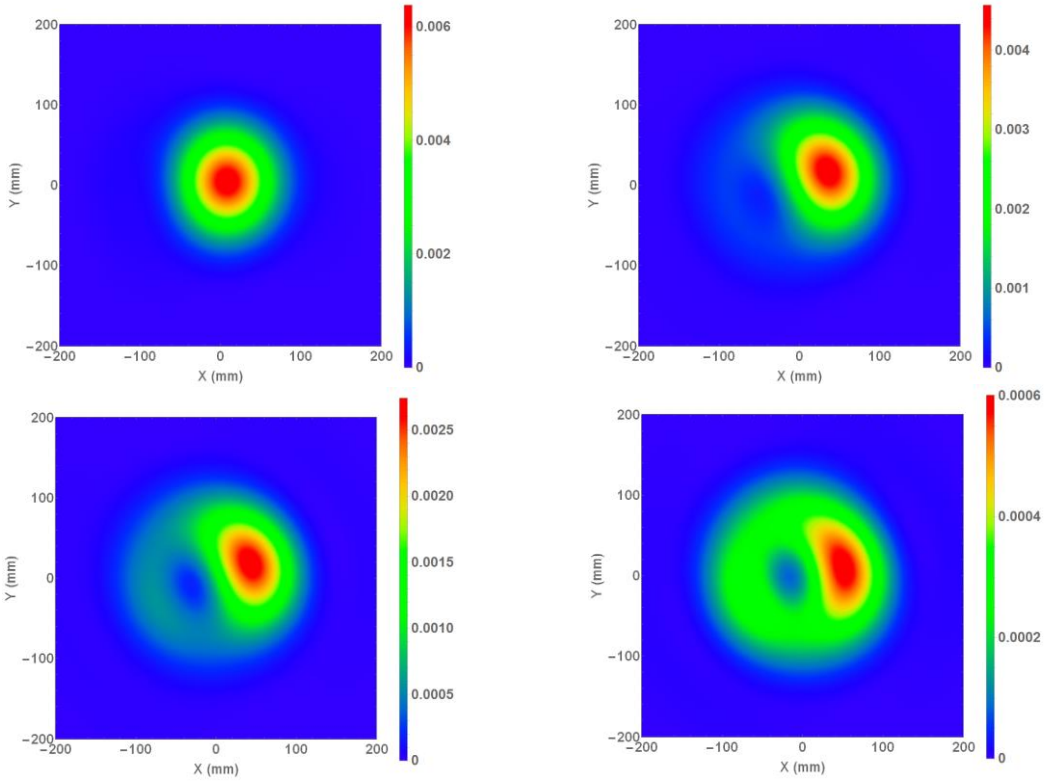

Figure 6.17: Intensity of the beam patterns resulting from a coherent combination of modes, observed 65 cm (in the far-field) from the horn when excited with a 220 GHz source at an incident angle of 1º (top left), 5º (top right) 7º (bottom left) and 10º (bottom right).

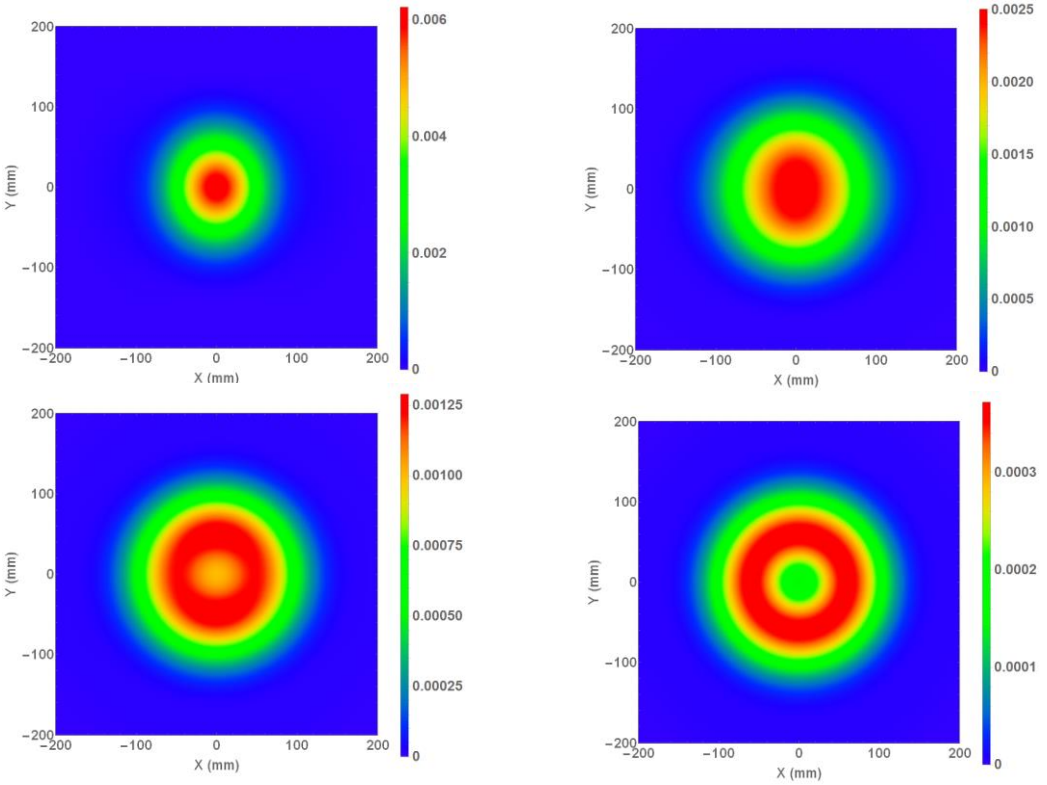

Figure 6.18: Intensity of the beam patterns resulting from an incoherent combination of modes, observed 65 cm from the horn when excited with a 220 GHz source at an incident angle of 1º (top left), 5º (top right) 7º (bottom left) and 10º (bottom right).

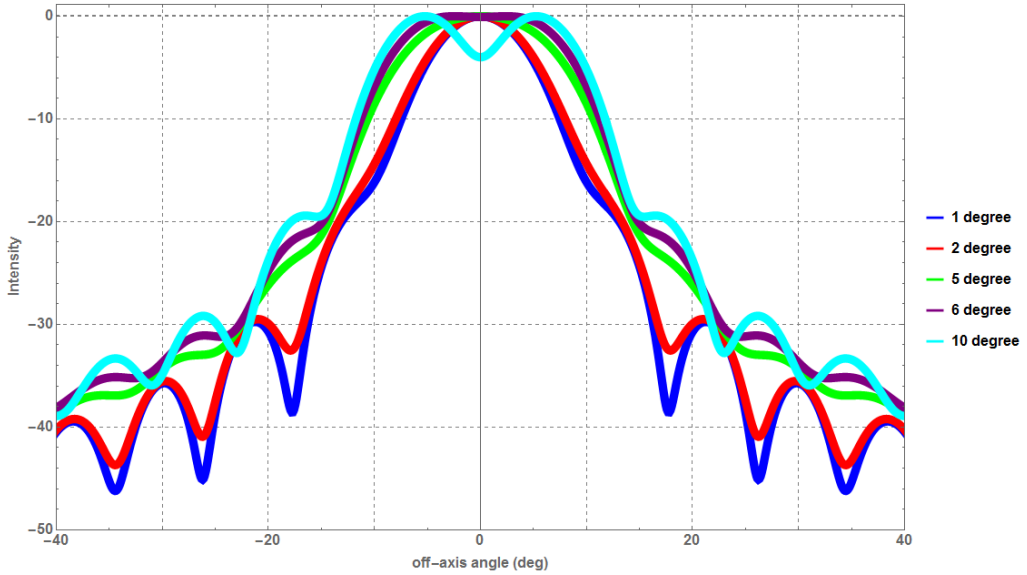

Figure 6.19: Normalised E-plane pattern (in dB) of a QUBIC horn excited with a plane wave at 220 GHz over a range of input angles. Each pattern is normalised to its own peak to show variation in the structure of the patterns – no orthogonal modes included.

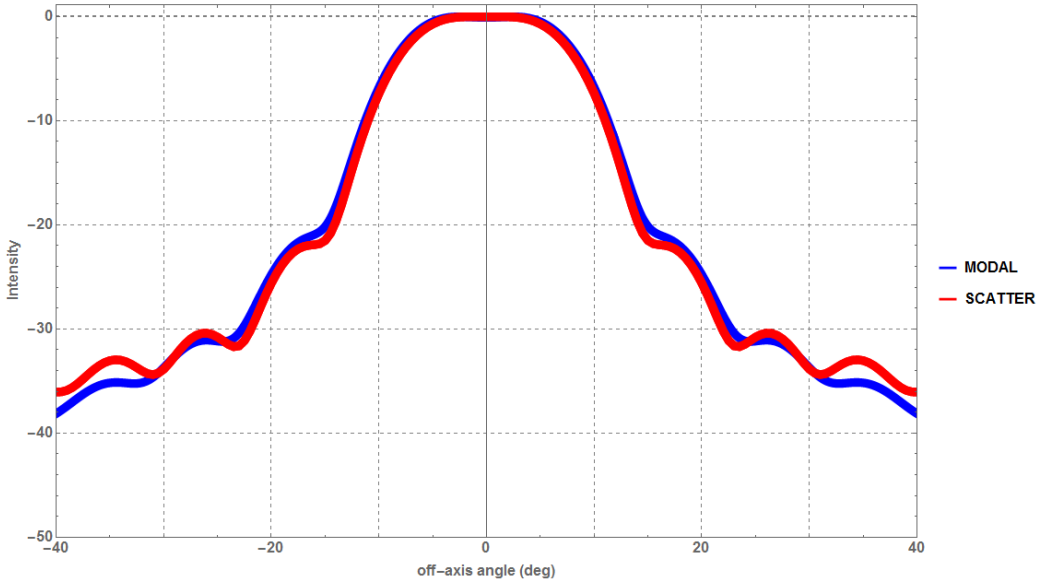

Figure 6.20: comparison between far-field pattern in MODAL from a 6º off axis source and the far-field produced by mode matching techniques when exciting all modes equally.

6.4.3 Beam patterns on the focal plane and effects on the PSF

As shown in Chapter 3, the aberrating optical combiner will introduce further asymmetries into the beam pattern regardless of whether or not they are combined coherently or incoherently (e.g. Figure 6.21 and Figure 6.22) on the focal plane.

Since MODAL outputs the field as a coherent combination of the modes the coherent PSF is obtained by modelling the instrument as before (Section 3.3.4). An incoherent PSF can be obtained by generating a separate PSF for each individual mode using the standard method. An incoherent combination is then obtained by simply summing up the intensities of each PSF. Figure 6.23 shows that the PSFs appeared somewhat as expected. However, the effect of the coherent vs incoherent envelope is evident, most noticeably on the 5° source, where the peaks at the top left are very faint in comparison to the peaks at the bottom left, agreeing with what is seen in Figure 6.21 and Figure 6.22. This being said, for testing purposes, the coherent source should be suitable, with the peaks agreeing with the expected separation (keeping in mind the systematic asymmetry introduced by the instrument).

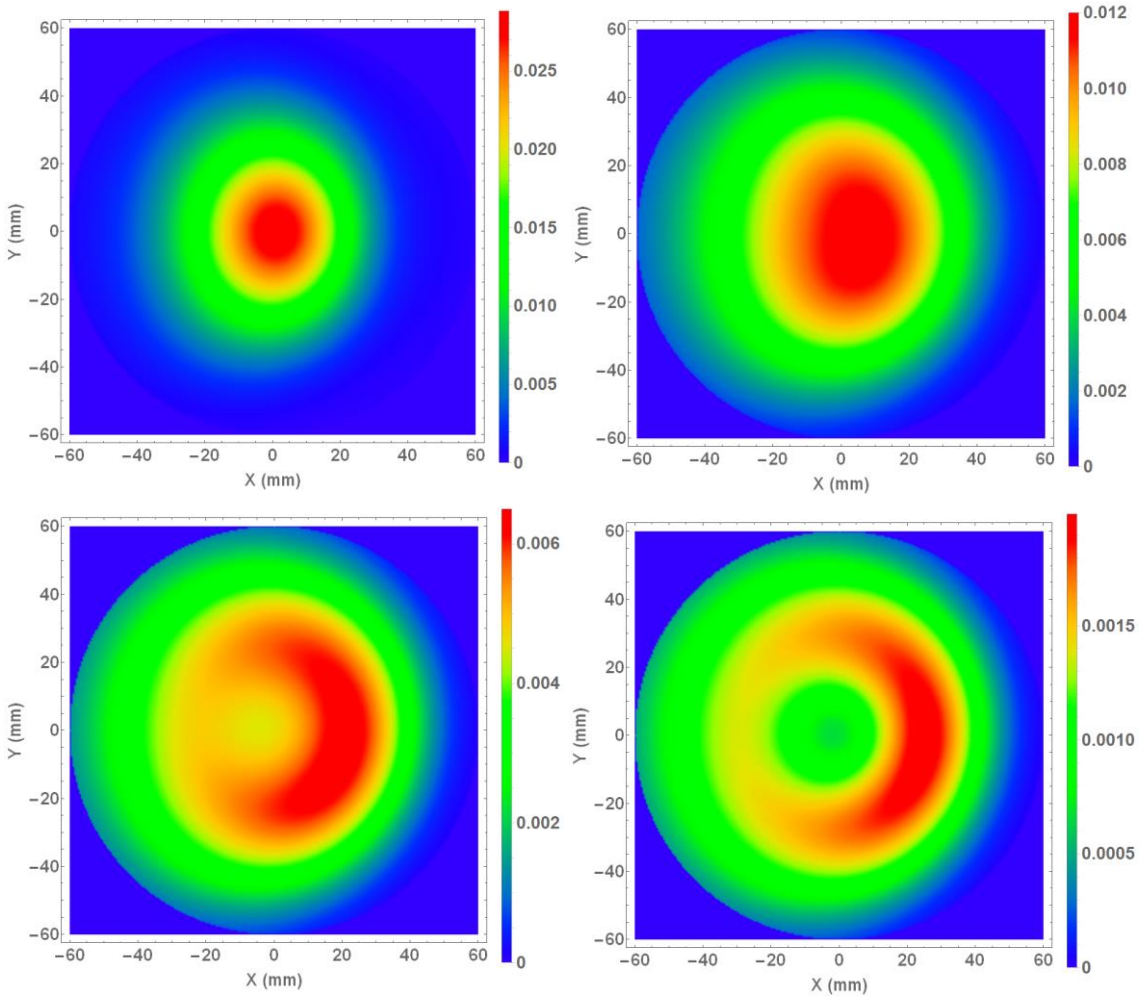

Figure 6.21: Intensity of the beam patterns resulting from an incoherent combination of modes on the focal plane when observing a 220 GHz source at an incident angle of 1º (top left), 5º (top right) 7º (bottom left) and 10º (bottom right).

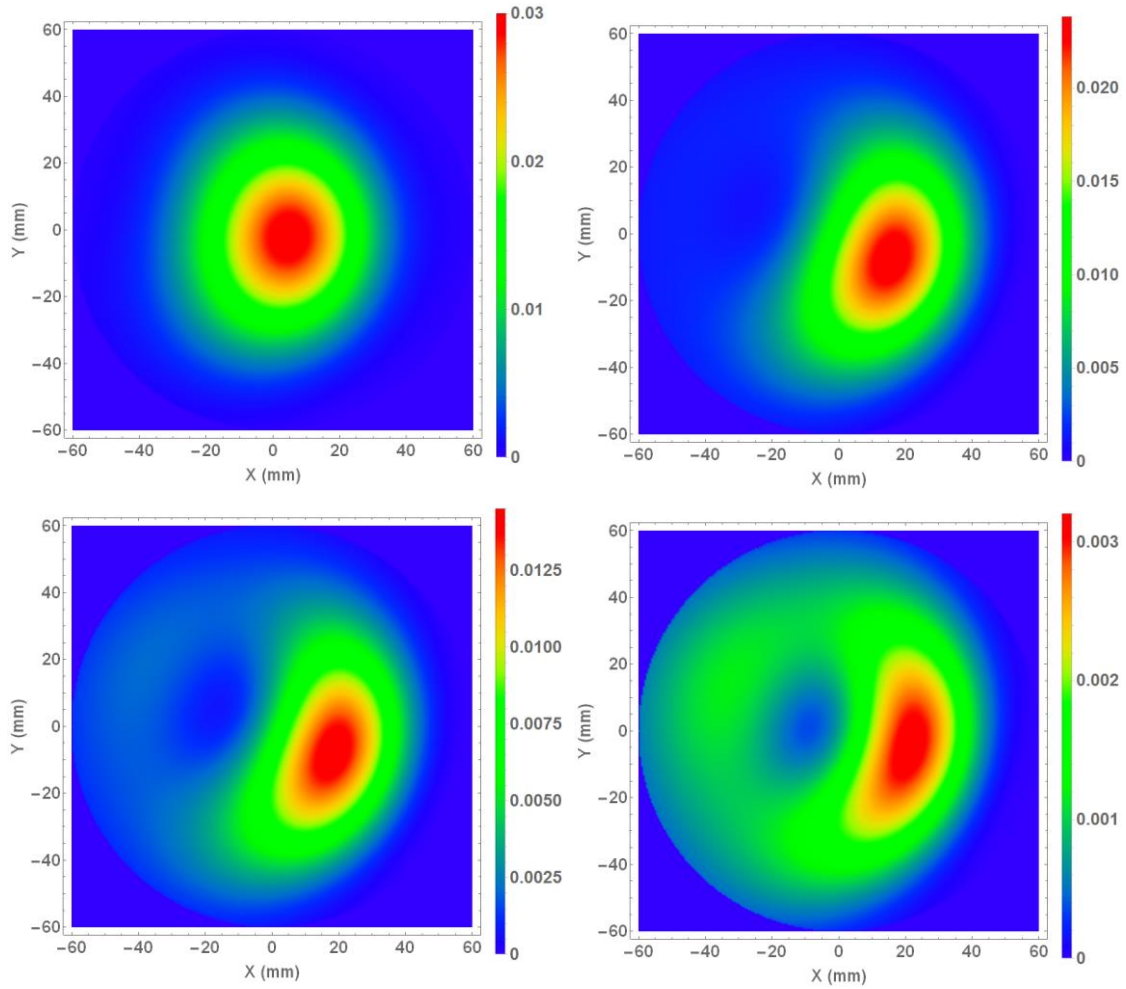

Figure 6.22: Intensity of the beam patterns resulting from a coherent combination of modes on the focal plane when observing a 220 GHz source at an incident angle of 1º (top left), 5º (top right) 7º (bottom left) and 10º (bottom right).

The beam patterns and PSFs in this section have been generated to illustrate the differences between coherent and incoherent observations and these should be borne in mind particularly when designing calibration schemes for future high-frequency upgrades to QUBIC.

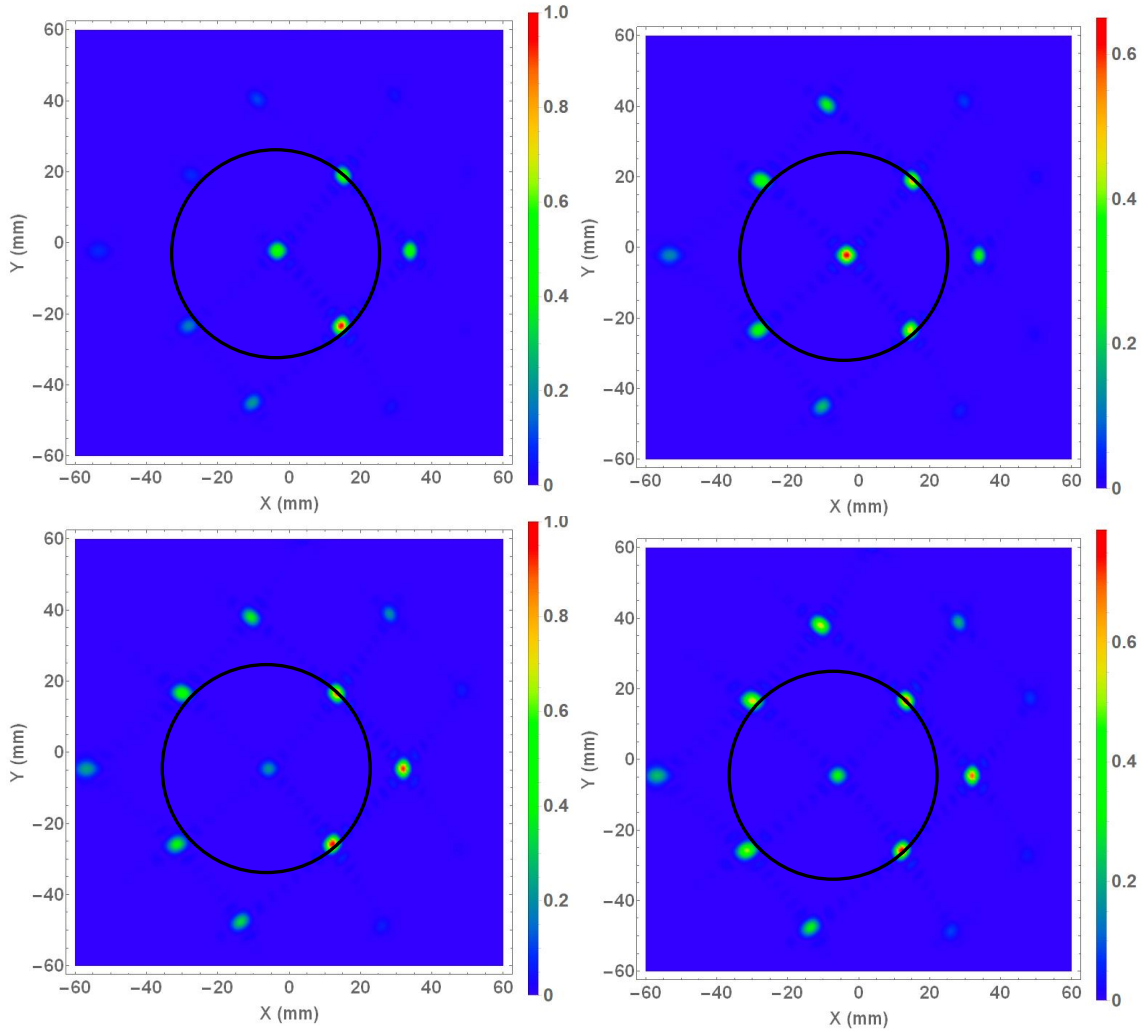

Figure 6.23: Normalised intensity PSF of the coherent (left) and incoherent (right) combination of modes for a 5° off-axis source (top) and 10° off axis source exciting the TD model. Note that each PSF is normalised to the peak of the coherent PSF for each off-axis angle. The black circles indicate an angular distance of 5.6°, the theoretical peak separation based on equation [37].

6.5 Spectro-Imaging

As has already been mentioned, there are difficulties with the manufacture of the dichroic. The current shape, which has been designed to capture all of the beams in the FI within the available space of the instrument, cannot be manufactured easily. The dichroic can only be constructed within the consortium as a disk with a maximum diameter of 300 mm (private communication, dichroic manufacturers in Cardiff), which is too large to fit into the instrument with its current housing structure. A disk of diameter 280 mm would be the maximum size that could fit in the current instrument (private communication, QUBIC collaboration). Figure 6.24 shows the footprint of the TD and FI beams on the dichroic with a 280 mm dichroic overlayed. While it would work for the smaller horn array of the TD, in the FI the beams are spread out over a large area and the disk cannot capture a large portion of the beams. This would mean that there would be a substantial loss in power as well as a reduction in the number of baselines in the FI, meaning that the desired synthetic beams could not be generated. When expansion to the full instrument takes place, the manufacturing techniques could have improved sufficiently so it would be possible to make an oval shaped dichroic in such a way that it could work with the current QUBIC layout. An alternative method for

simultaneous observation in the higher band was explored as it is still vital to observe at these frequencies, so that we can correct for the polarised foregrounds and not suffer from the same issues that affected previous CMB instruments. This technique known as spectro-imaging, offers additional benefits over the two-frequency observations originally envisioned.

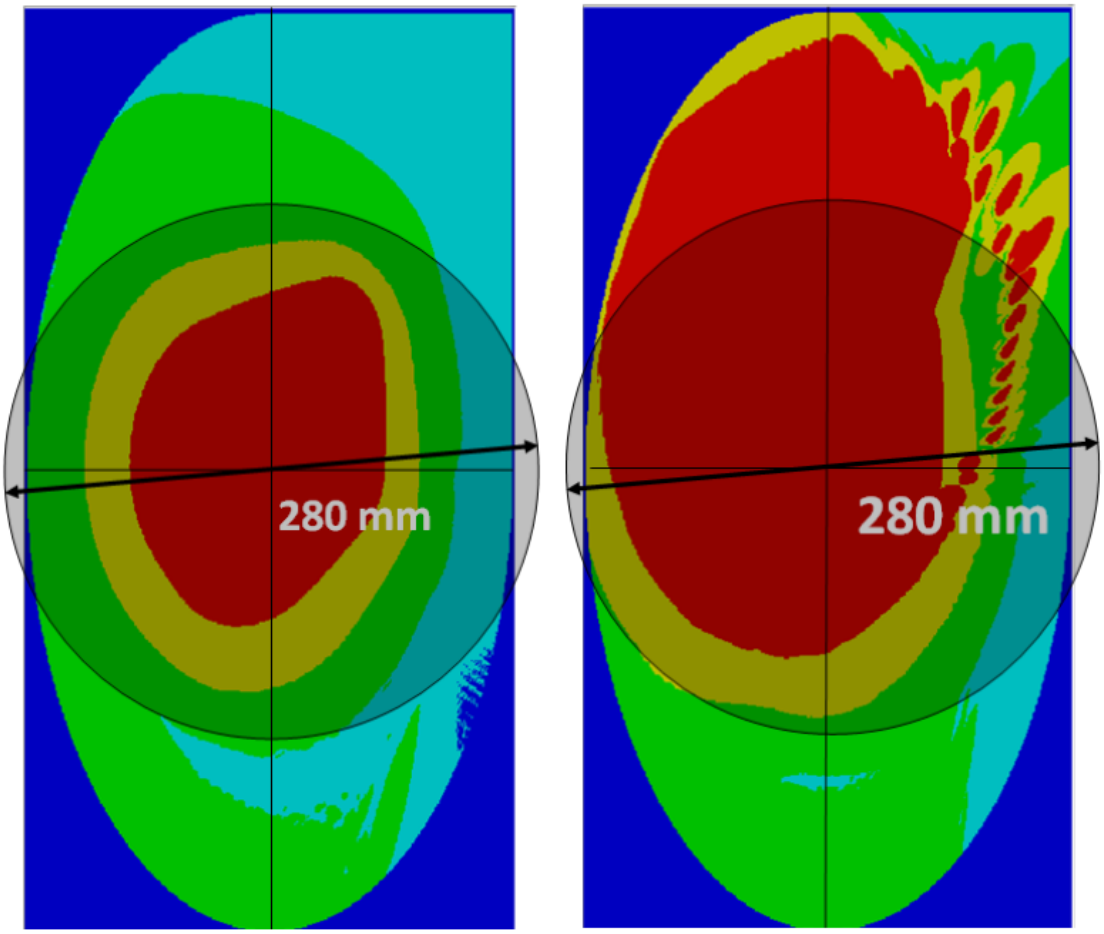

Figure 6.24: Footprint on the current dichroic from the 64 feedhorns beams of the TD (left) and the 400 feedhorns from the FI (right) with a 280 mm diameter dichroic roughly overlayed for display purposes (red shows $r = 1\ w$, yellow shows $r = 1.5\ w$ and green shows $r = 2\ w$ from equation [30]).

Spectro-imaging is a technique that takes advantage of the spectral resolution of the QUBIC interferometer to extract the synthetic image produced at different frequencies from a single focal plane. Since the TD is the only QUBIC instrument that exists right now, spectro-imaging is currently only being performed and tested across the lower operating band. The next section will give a brief overview of this technique, as well as exploring the idea of expanding it so that frequencies across both operating bands can be extracted from a single focal plane. Spectro-imaging means that there would be no need for a dichroic in the instrument.

6.5.1 Introduction to spectro-imaging

An excellent overview of using QUBIC as a spectro-imager is provided by Mousset *et al.* (2020) and its benefits for QUBIC by Hamilton *et al.* (2020); this section will merely provide an overview with some simulation results.

Chapter 6: Modelling for future instrument

The idea of spectral resolution was introduced in Chapter 4 which showed the angular position of the off-axis peaks changing with the frequency of the observed source. Using a simple example of a source which emits at two frequencies ν_1 and ν_2, the off-axis peaks of the two resulting synthetic beams on one focal can be distinguished from one another as long as the distance between the peaks ($\Delta\theta$) is greater than the average width of the peak (as in equation [89], from Mousset *et al.* (2020)).

$$\Delta\theta = \frac{c\Delta\nu}{\Delta h} \geq \frac{c\nu}{P\Delta h} \rightarrow \Delta\nu \geq \frac{\nu}{P} \qquad [89]$$

where $\nu = \sqrt{\nu_1\nu_2}$, $\Delta\nu = |\nu_2 - \nu_1|$, P is the maximum number of horns across the array (20 for the FI), and Δh is the inter-horn spacing (14 mm).

QUBIC is unique in that it is both an imager and an interferometer so it has a spatial resolution (FWHM_θ) on the sky and a spectral resolution (FWHM_ν) which is in the frequency domain. If the spatial resolution dictates the ability of an instrument to resolve separate objects on the sky, then the spectral resolution dictates the ability of an instrument to resolve separate frequencies from a single object on the sky. The spectral resolution can also be expressed as in equation [90] (Mousset *et al.*, 2020).

$$\mathrm{FWHM}_\nu = \frac{\Delta\nu}{\nu} = \frac{1}{P} \qquad [90]$$

Thus the limit of the spectral resolution is dependent on the size of the horn array (as is the spatial resolution), which means it has a value of 0.05 for the FI with the 20×20 horn array and 0.125 for the TD with the 8×8 horn array. As expected, the FI would perform better as a spectro-imager than the TD. Table 6.2 shows that neither the FI or the TD would be able to resolve the beam patterns for a difference of 5 GHz, however at a difference of 10 GHz the FI resolves the beam patterns, in fact the FWHM_ν value of 0.05 corresponds to a $\Delta\nu$ value of roughly 7.5 GHz. In essence this means that the synthetic beam from all frequencies (130-170 Ghz) across the lower band, can actually be resolved into five distinct sub-bands. A simple example is given in Figure 6.25, where it can be seen that the five different synthetic beams are clearly discernible and can be separated from each other. With the possibility of defining five sub-bands within the full lower band, the observed image could be essentially deconvolved into five separate image at the five frequencies sub-bands, allowing analysis to be performed on all of them. Some initial spectro-imaging results can be seen in Figure 6.26. It can be seen that there is some spill over between the bands, with faint images of the sources being observed in bands where they are not radiating. This is explained in detail in the paper by Mousset *et al.* (2020), and could due to the fact that the synthetic beams can overlap. This effect can be corrected for as long as the synthetic beams are accurately known, so it is important that accurate descriptions of the beams are known. Spectro-imaging will aid in the correction of images from foregrounds and allow the band in which the CMB peaks to be isolated.

Table 6.2: Calculating the $FWHM_\nu$ parameter to investigate feasibility of spectro-imaging for the QUBIC instrument at lower band frequencies.

ν_1(GHz)	ν_2(GHz)	$\Delta\nu$(GHz)	$\nu = \sqrt{\nu_1\nu_2}$(GHz)	$FWHM_\nu$
130	150	20	140	0.1432
130	140	10	135	0.0741
130	135	5	132.5	0.0377

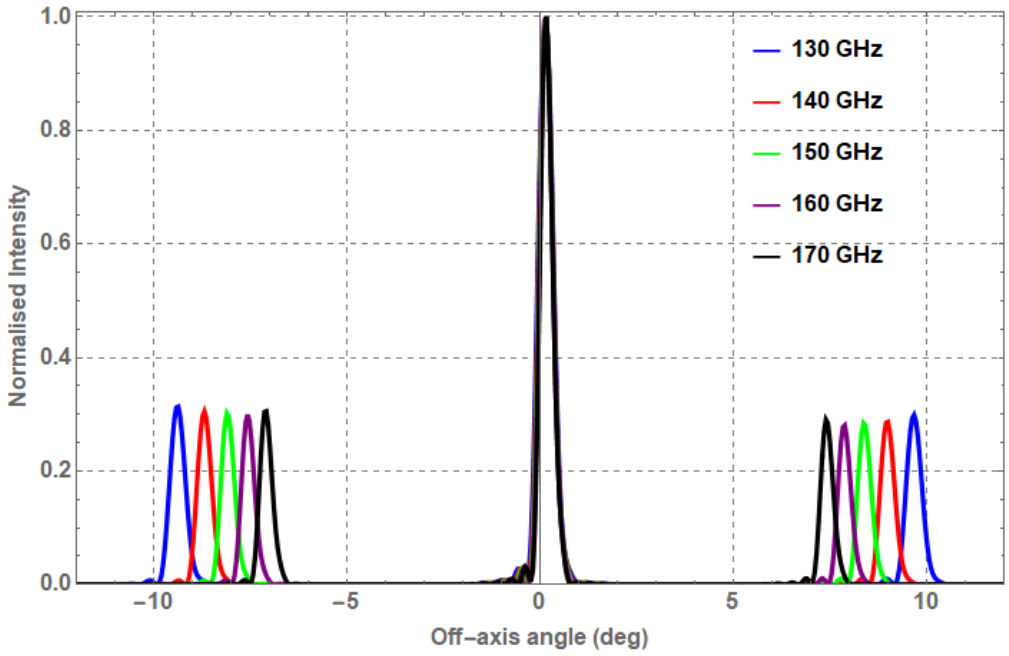

Figure 6.25: Incoherently combined synthetic beams for the FI across the lower band for a point source centred at (0 mm, 0 mm) modelled in MODAL. All beams are normalised to their respective peaks.

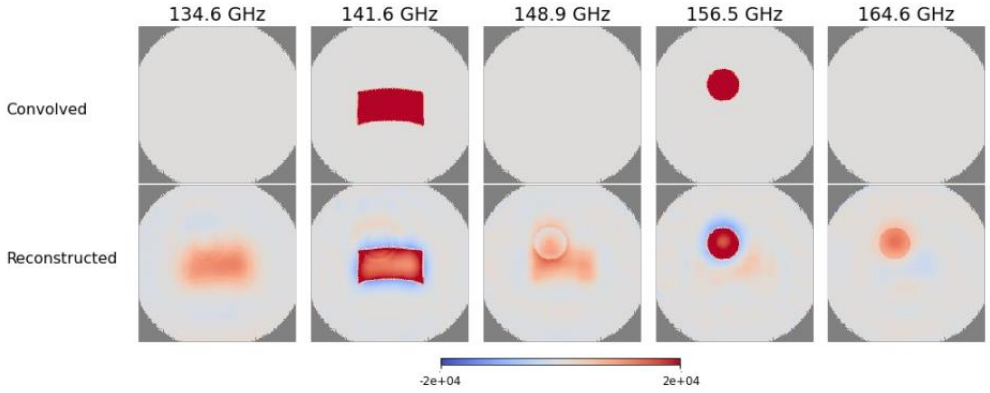

Figure 6.26: Mapmaking for a sky full of zeros with two extended, monochromatic regions centred at 141.6 GHz (square) and 156.5 GHz (disk). Each column corresponds to a single sub-band centred on the frequency listed above. The first row shows the input sky maps spatially convolved with the QUBIC resolution, and the reconstructed deconvolved images are in the second row (Image obtained from Mousset *et al.* (2020)).

6.5.2 Distinguishing between bands

Spectral imaging has proved to be quite promising, and a potential application of this process is to use it to distinguish between the two operating bands on a single focal plane, thus removing the need for a dichroic or even a second focal plane. As has been shown above, the peak separation for the central frequency of the higher operating band is much narrower than that of the the lower band. Spectro-imaging relies on the different values in the peak separation within the synthetic beam at differing frequencies. Figure 6.27 clearly shows that there is substantial difference in the peak separation at the central frequency of both bands (roughly 8.2° and 5.6° at 150 GHz and 220 GHz respectively) making spectro-imaging potentially an ideal solution. The higher band was observed with an on-axis source, thus exciting a single mode in the horn, but it has been shown that even with the higher order modes excited, they simply change the envelope with the peak separation remaining the same. Further real world testing will be required to investigate the viability of this application of spectro-imaging. It is planned that the spectro-imaging capabilities will be tested from sky observations.

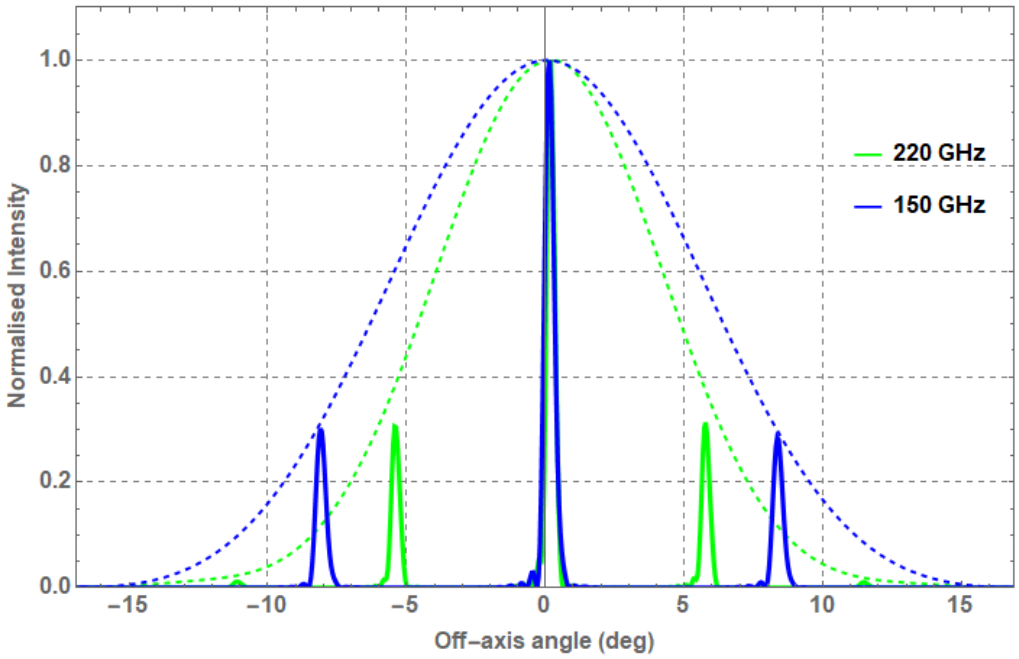

Figure 6.27: Synthetic beam for a theoretical on-axis pixel at (0 mm, 0 mm) when excited with a point source at the corresponding focal plane positions at 150 and 220 GHz. Note and the envelopes are the far-field beam patterns from MODAL.

6.6 Benefits of utilising multi-moded horns

Currently QUBIC operates as a multi-moded instrument out of necessity. It was required that the higher 220 GHz band be observed to account for the polarised foreground. There were then two options, have a separate module on the instrument that operates over these frequencies, considerably increasing the cost, or modify the current design to have a single module observe at both frequency bands. This method caused the least disruption and minimised costs. As a trade-off though the horns were operating at frequencies higher than they were designed. This results in the multiple propagating modes at this frequency as described above but it has been shown that the beam pattern is not adversely affected when operating in the multi-moded state. Another benefit of multi-mode operation is that the extra modes allow the horn to

transmit more power. There are ongoing discussions about exploiting this power gain to increase the sensitivity to the CMB signal by using multi-moded horns at 150 GHz on a QUBIC+ instrument. This will increase the sensitivity of the beam and will also generate a more top-hat like beam, thus increasing the spectro-imaging efficiency. This section will investigate the power gain obtained by operating the current horns in the multi-moded state (i.e. at 220 GHz) using mode matching techniques both with and without orthogonal mode pairs.

Since this is an investigation into the gains of multi-moded horns over single moded horns, for this analysis the primary HE_{11} mode (the only mode that propagates in a single moded corrugated horn) will be used as the baseline. The total power in the horn beam can be reasonably estimated by the area under the curve of the far-field pattern. There are 3 other modes propagating in the horn at 220 GHz (one mode at $n = 0$ and an orthogonal mode pair at $n = 2$), but this does not provide a corresponding integer increase in the power over the HE_{11} mode, which can be clearly seen in Figure 6.28 (how the modes are excited in practice will determine the relative power in the modes. Here all TE and TM modes were excited equally at the horn input). Table 6.3 shows that the non n =1 modes, contribute a substantial fractional increase to the total power in the field. With a total increase of nearly 70%. Table 6.4 shows the same analysis while only accounting for a single polarisation (i.e. no orthogonal mode pairs, which is more applicable to the QUBIC instrument when operating with the HWP and polariser) indicating that there was a higher gain in the power (nearly 90%), but it is still not a full integer multiple increase. In summary operating horns at multi-moded frequency will provide a noticeable gain in the throughput of the horn and this is an area that will be investigated further for future instruments.

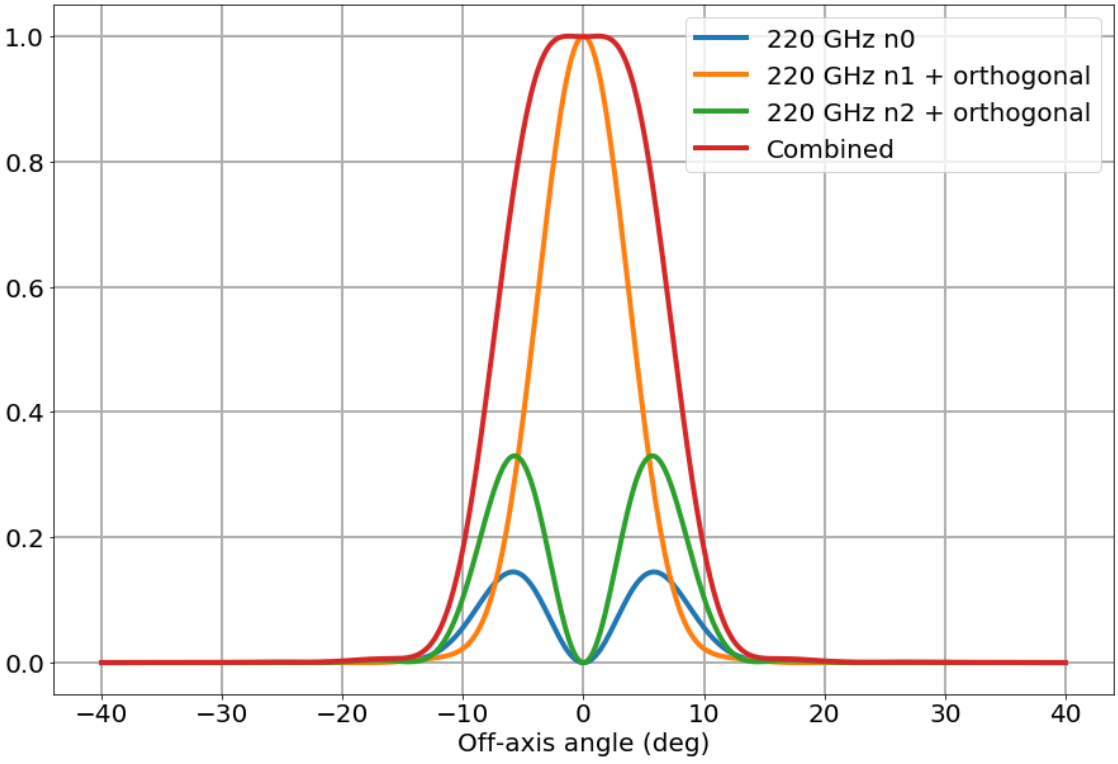

Figure 6.28: Far-field patterns of the modes propagating in the horn at 220 GHz, the power under the curves of the non $n = 1$ modes are much lower.

Table 6.3: Normalised power (relative to the total power for the $n = 1$ azimuthal order) including orthogonal mode pairs.

Azimuthal Order	Normalised power (under curve)
N + N1_orthogonal	1
N1 + N1_orthogonal +N0	1.216
N1 + N1_orthogonal +N2+ N2_orthogonal	1.465
N1 + N1_orthogonal + N2 + N2 _orthogonal+ N0	1.681

Table 6.4: Normalised power (relative to the total power for the $n = 1$ azimuthal order) not including orthogonal mode pairs

Azimuthal Order	Normalised power (under curve)
N1	1
N1 +N0	1.433
N1 +N2	1.465
N1 +N2 +N0	1.898

6.7 Summary

Up until this chapter, the performance of QUBIC had mostly been analysed with respect to the TD instrument, which – when commissioned – will be the first phase of the QUBIC science campaign. This chapter focussed on the FI (which will be phase 2), while comparing some of the results to those of the TD already presented.

It was found that the calibrator lamps that will be used as an aid in the intercalibration of the focal plane pixels will experience greater non-uniformity than was simulated for the TD. This is due to position of the calibrator lamps at the side of the wider horn array. The difference in the patterns is not necessarily a fault with the instrument, it simply highlights the importance of accurate modelling of these lamps.

The synthetic beam was shown for the FI, and it had a similar structure to the TD beam. The main differences were the size of the peaks (due to the size of the horn array) and there appeared to be some asymmetry present in the beam that was not seen in the TD. This was shown to be inherent to the instrument design and most likely occurred due to the size of the horn array, where the outer horns suffered from increased aberrations due to the combiner design.

The next section focussed on the modelling of upper band of the instrument in MODAL (up to that point only individual horns had been analysed at these frequencies). Higher order modes were excited with off-axis observations. The difference between coherent and incoherent summation of these modes (simulating observation of coherent or incoherent sources) was then shown and it was seen that the main result of the different methods of combination was a difference in the envelope of the PSF or synthetic beam, causing the peaks to suffer from varying levels of attenuations, but appearing in the same location for both methods.

Chapter 6: Modelling for future instrument

The idea of using the technique of spectro-imaging as an alternative to a dichroic (which is difficult to manufacture to a shape that is suitable for QUBIC) to differentiate between frequency bands was explored.

Finally the idea of using multi-moded horns as a source for an increase in the power of the throughput of the instrument was explored (potentially phase 3 of the campaign). Preliminary results show that there is a power gain for higher order modes, but further simulation and testing is required to investigate the exact level of the power gain.

The simulations presented in this chapter will be useful for future extensions and upgrades to QUBIC

7 Summary and conclusions

This thesis is concerned with the optical modelling of the QUBIC quasi-optical beam combiner. QUBIC aims to detect the primordial B-mode polarisation of the CMB for which an unprecedented level of sensitivity is required. It will achieve this sensitivity by combining the benefits of bolometric interferometry and imaging. QUBIC will observe in two frequency bands (centred at 150 and 220 GHz), to allow for separation of the CMB signal and the polarised foregrounds.

In Chapter 1 the history of Big Bang cosmology and CMB observation was summarised. It was shown that over the years, as technology became more sophisticated, the temperature of CMB was observed in ever greater detail culminating in the Planck satellite that extracted essentially all the temperature anisotropy information from the CMB.

It was shown that there were some 'problems' with the Big Bang theory that lead to the introduction of the concept of inflation, a very energetic short-lived period of cosmic expansion, in which gravitational waves would imprint a B-mode polarisation pattern on the CMB. Hence the primordial B-modes are known as the 'smoking gun' of inflation theory and are very sought after. Polarised foregrounds and their contamination of the CMB were also discussed. This contamination makes the B-modes even more difficult to detect. Finally this chapter finished with some examples of the current state-of-the-art in CMB instrumentation.

Chapter 2 introduced the modelling techniques of physical optics (PO) and Gaussian beam modes (GBM) that were used to analyse the QUBIC optical combiner in this thesis. The ABCD matrices technique, which is a simple yet powerful tool that allows for the analysis of an ideal instrument was detailed. The in house software MODAL utilises both PO and GBM and is very powerful software that can be used for initial instrument design (with GBM) and for a full vector analysis (with PO).

Some of the benefits of the MODAL software were explored. It allows for optical elements of complex shapes to be defined with its Constructive Solid Geometry (CSG) commands, and this proved very useful when modelling the primary mirror of the TD instrument. The different sources that can be used in MODAL were also shown, by simulating different types of observations (e.g. observation of a 10° Gaussian beam in the near field of the instrument). As well as this, one of the most powerful tools in MODAL is the ability to model the actual geometry of the QUBIC feedhorns and simulate their output, rather than having to a use a Gaussian approximation.

Use of the software and the importance of sampling choice was illustrated using multiple slit diffraction. The slits could also be used as a simple approximation of the QUBIC instrument that was later used as a reference. The results agreed very well with the theoretical model, providing a verification of the MODAL software (in addition to the verification against the commercially available GRASP software). To reduce the time taken for a simulation of the QUBIC combiner (a very optically complex instrument), the MODAL software was run on the computing cluster in MU, whose benefits were shown.

Finally it was shown that a very simple but effective model of QUBIC can be implemented with Fourier transforms. This allows for rapid investigation into the effects of some of properties of the optical combiner, such as the horn array size and inter-horn separation, on the focal plane pattern.

Chapter 7: Summary and conclusions

In Chapter 3 I introduced the QUBIC instrument, its predecessors MBI and BRAIN and its aims. After three years of observation a sensitivity of $r < 0.021$ is expected to be obtained. QUBIC will observe over relatively small multipoles to ensure that any B-modes detected will be primordial.

The idea of bolometric interferometry, which allows for the control over systematics, was described. It was shown that each baseline provides a Fourier component of the intensity distribution of an observed source meaning that, in the presence of a sufficiently large enough number of baselines, QUBIC can operate as an interferometer and an imager. The window function was introduced to describe the sensitivity of the instrument to different multipoles on the sky, and was used a figure-of-merit for a tolerance analysis of the instrument.

An overview each element in the optical combiner was provided. It was shown how the off-axis design of the instrument introduced aberrations into the beams as they passed through the combiner. The full instrument (FI) and the technological demonstrator (TD) were defined and I highlighted their differences. The modelling that went into resizing the mirrors and the cold stop (whose new smaller size will be used in the FI as well) was described.

Finally I detailed the differences between the PSF of the instrument and the synthetic beam of TES pixels (which did not suffer from the same levels of aberration). Both were used throughout this research to evaluate designs and in the testing phases of the instrument. I described three methods used to simulate the synthetic beam (one of which was used by collaborators in the generation of the window function of the instrument) and showed how their results are in excellent agreement.

In Chapter 4 I presented rigorous PO simulations of the QUBIC TD that are being used during the calibration campaign. The window function of the instrument was obtained using a PO analysis performed in MODAL, and subsequently used as the merit function for a tolerance analysis. It was found that the mirrors needed to be aligned to an accuracy of $\pm$ 0.1° and $\pm$ 1 mm.

The beam produced by internal calibrator lamps resembled a 50° Gaussian. The size of the beam meant it was susceptible to truncation from the optical elements, which provided a non-uniform illumination on the focal plane when simulated in MODAL. The pattern measured during the calibration can be compared with this prediction and used as a check of the inter-calibration of the TES pixels.

After simulation of the observation of an external far-field calibrator source (which had a 10° Gaussian far-field beam), it was found that a distance of 5 m or more from the QUBIC horn array was reasonable. In the lab, the source was placed off-axis using a plane mirror to redirect the source into the instrument. The truncation of the beam by the mirror and the QUBIC instrument was determined and it was found that the effects were negligible.

An analysis of the instrument synthetic beam was performed, including the effect of frequency, TES location and finite size. The synthetic beam for various on- and off-axis TESs were simulated in MODAL and were found to agree with the measured beams in terms of the peak locations. The measured peak heights in these early measurements were affected by saturation.

Chapter 7: Summary and conclusions

In Chapter 5, mode matching techniques were described and used to model the electromagnetic performance of the QUBIC horns across both frequency bands. The mode matching simulations resulted in a collection of four scattering matrices 'S_{AB}', which described the radiation at Port A scattered from Port B. In this thesis the throat of the horn was defined as Port 1 and the aperture of the horn was defined as Port 2. Performing an SVD analysis on S_{21} showed the hybrid modes supported by a horn, and whether the horn was single moded (only one hybrid mode supported) or multimoded (more than one hybrid mode supported). It was shown that the lower band of QUBIC was single moded and the upper band was multimoded. The multimoded nature of the upper band meant that the far-field pattern at the end of the band behaved undesirably, and thus the original bandwidth was reduced slightly.

Mode matching techniques were then used on horn geometries that were representative of the manufactured horns. It was found that cusps (a defect present on the corrugations of the horns due to the method of manufacture) did not have a significant effect on the beams. The performance of the horns was measured with a VNA by collaborators in Milan and when comparing the results with the simulated data it was found that the lower band and the lower end of the upper band agreed well. At the higher end of the upper band there were some discrepancies with the far-field pattern, however these could be explained by the multimoded nature of the horns. The discrepancies between the measured and simulated data for the reflected power were rectified after the lab measurements were refined. These discrepancies highlighted the importance of careful measurement with a VNA, particularly at frequencies where the horns are multi-moded. Overall there was good agreement between the simulations and the real performance of the horns.

There are three planned phases for the QUBIC instrument. Phase 1 is concerned with the TD instrument, while Phases 2 and 3 are concerned with the FI and the planned QUBIC+ instrument. These two phases were the focus of Chapter 6. The FI was modelled and it was shown that the calibrator lamps suffered from greater truncation due to their location on the larger horn array. This was not a fault in the instrument or the design, but merely highlighted the importance of accurate modelling of the lamps.

The FI synthetic beam was modelled and was as expected, with narrower peaks appearing in the same locations as for the TD. Asymmetry present in the synthetic beam due to the off-axis combiner was found to be small

Modelling of the upper band of the instrument in MODAL was also presented in this chapter. The higher order modes were investigated, particularly noting the difference between what is measured for coherent and incoherent sources. The main difference observed was in the envelope of the beam, resulting in varying levels of attenuation for the different observations, but the peaks appear in the same location in both cases.

The idea of using the technique of spectro-imaging to observe at multiple frequency bands was explored. It was shown that spectro imaging relies predominantly on the differences in synthetic beam peak separation. It should be a viable technique for QUBIC

The planned upgrade for QUBIC+ (Phase 3 of the campaign) is to use multimoded horns at all frequencies to obtain an increase in the power throughput of the instrument. Preliminary results showed that there was a power gain when including higher order modes, but further testing is required to investigate the exact level of this gain.

Chapter 7: Summary and conclusions

This research provided modelling results for the QUBIC instrument that have been used in the calibration and testing stages of the instrument as well as providing results that can be taken into consideration when future upgrades are planned. The results shown also provide an insight into the operation of bolometric interferometers at both single moded and multimoded operating frequencies, which could be beneficial for other instruments that aim to utilise these techniques.

Publications

This work presented in thesis has contributed to the following papers:

[1] QUBIC I: Overview and Science Program.

J.-Ch. Hamilton, L. Mousset, E.S. Battistelli, M.-A. Bigot-Sazy, P. Chanial, R. Charlassier, G. D'Alessandro, P. de Bernardis, M. De Petris, M.M. Gamboa Lerena, L. Grandsire, S. Lau, S. Marnieros, S. Masi, A. Mennella, C. O'Sullivan, M. Piat, G. Riccardi, C. Scóccola, M. Stolpovskiy, A. Tartari, S.A. Torchinsky, F. Voisin, M. Zannoni, P. Ade, J.G. Alberro, A. Almela, G. Amico, L.H. Arnaldi, D. Auguste, J. Aumont, S. Azzoni, S. Banfi, B. Bélier, A. Baù, D. Bennett, L. Bergé, J.-Ph. Bernard, M. Bersanelli, J. Bonaparte, J. Bonis, E. Bunn, **D. Burke**, D. Buzi, F. Cavaliere, C. Chapron, A.C. Cobos Cerutti, F. Columbro, A. Coppolecchia, G. De Gasperis, M. De Leo, S. Dheilly, C. Duca, L. Dumoulin, A. Etchegoyen, A. Fasciszewski, L.P. Ferreyro, D. Fracchia, C. Franceschet, K.M. Ganga, B. García, M.E. García Redondo, M. Gaspard, D. Gayer, M. Gervasi, M. Giard, V. Gilles, Y. Giraud-Heraud, M. Gómez Berisso, M. González, M. Gradziel, M.R. Hampel, D. Harari, S. Henrot-Versillé, F. Incardona, E. Jules, J. Kaplan, C. Kristukat, L. Lamagna, S. Loucatos, T. Louis, B. Maffei, W. Marty, A. Mattei, A. May, M. McCulloch, L. Mele, D. Melo, L. Montier, L.M. Mundo, J.A. Murphy, J.D. Murphy, F. Nati, E. Olivieri, C. Oriol, A. Paiella, F. Pajot, A. Passerini, H. Pastoriza, A. Pelosi, C. Perbost, M. Perciballi, F. Pezzotta, F. Piacentini, L. Piccirillo, G. Pisano, M. Platino, G. Polenta, D. Prêle, R. Puddu, D. Rambaud, P. Ringegni, G.E. Romero, E. Rasztocky, J.M. Salum, A. Schillaci, S. Scully, S. Spinelli, G. Stankowiak, A.D. Supanitsky, J.-P. Thermeau, P. Timbie, M. Tomasi, C. Tucker, G. Tucker, D. Viganò, N. Vittorio, F. Wicek, M. Wright, A. Zullo.

Submitted to Journal of Cosmology and Atroparticle Physics (2020).

ArXiv ID: 2010.15119.

[2] QUBIC II: Spectro-Polarimetry with Bolometric Interferometry.

L. Mousset, M.M. Gamboa Lerena, E.S. Battistelli, P. de Bernardis, P. Chanial, G. D'Alessandro, G. Dashyan, M. De Petris, L. Grandsire, J.-Ch. Hamilton, F. Incardona, S. Landau, S. Marnieros, S. Masi, A. Mennella, C. O'Sullivan, M. Piat, G. Ricciardi, C.G. Scóccola, M. Stolpovskiy, A. Tartari, J.-P. Thermeau, S.A. Torchinsky, F. Voisin, M. Zannoni, P. Ade, J.G. Alberro, A. Almela, G. Amico, L.H. Arnaldi, D. Auguste, J. Aumont, S. Azzoni, S. Banfi, B. Bélier, A. Baù, D. Bennett, L. Bergé, J.-Ph. Bernard, M. Bersanelli, M.-A. Bigot-Sazy, J. Bonaparte, J. Bonis, E. Bunn, **D. Burke**, D. Buzi, F. Cavaliere, C. Chapron, R. Charlassier, A.C. Cobos Cerutti, F. Columbro, A. Coppolecchia, G. De Gasperis, M. De Leo, S. Dheilly, C. Duca, L. Dumoulin, A. Etchegoyen, A. Fasciszewski, L.P. Ferreyro, D. Fracchia, C. Franceschet, K.M. Ganga, B. García, M.E. García Redondo, M. Gaspard, D. Gayer, M. Gervasi, M. Giard, V. Gilles, Y. Giraud-Heraud, M. Gómez Berisso, M. González, M. Gradziel, M.R. Hampel, D. Harari, S. Henrot-Versillé, E. Jules, J. Kaplan, C. Kristukat, L. Lamagna, S. Loucatos, T. Louis, B. Maffei, W. Marty, A.

Mattei, A. May, M. McCulloch, L. Mele, D. Melo, L. Montier, L.M. Mundo, J.A. Murphy, J.D. Murphy, F. Nati, E. Olivieri, C. Oriol, A. Paiella, F. Pajot, A. Passerini, H. Pastoriza, A. Pelosi, C. Perbost, M. Perciballi, F. Pezzotta, F. Piacentini, L. Piccirillo, G. Pisano, M. Platino, G. Polenta, D. Prêle, R. Puddu, D. Rambaud, E. Rasztocky, P. Ringegni, G.E. Romero, J.M. Salum, A. Schillaci, S. Scully, S. Spinelli, G. Stankowiak, A.D. Supanitsky, P. Timbie, M. Tomasi, G. Tucker, C. Tucker, D. Viganò, N. Vittorio, F. Wicek, M. Wright, A. Zullo.

Submitted to Journal of Cosmology and Atroparticle Physics (2020).

ArXiv ID: 2011.02213.

[3] QUBIC III: Laboratory Characterization.

S.A. Torchinsky, J.-Ch. Hamilton, M. Piat, E.S. Battistelli, C. Chapron, G. D'Alessandro, P. de Bernardis, M. De Petris, M.M. Gamboa Lerena, M. González, L. Grandsire, S. Masi, S. Marnieros, A. Mennella, L. Mousset, J.D. Murphy, D. Prêle, G. Stankowiak, C. O'Sullivan, A. Tartari, J.-P. Thermeau, F. Voisin, M. Zannoni, P. Ade, J.G. Alberro, A. Almela, G. Amico, L.H. Arnaldi, D. Auguste, J. Aumont, S. Azzoni, S. Banfi, B. Bélier, A. Baù, D. Bennett, L. Bergé, J.-Ph. Bernard, M. Bersanelli, M.-A. Bigot-Sazy, J. Bonaparte, J. Bonis, E. Bunn, **D. Burke**, D. Buzi, F. Cavaliere, P. Chanial, R. Charlassier, A.C. Cobos Cerutti, F. Columbro, A. Coppolecchia, G. De Gasperis, M. De Leo, S. Dheilly, C. Duca, L. Dumoulin, A. Etchegoyen, A. Fasciszewski, L.P. Ferreyro, D. Fracchia, C. Franceschet, K.M. Ganga, B. García, M.E. García Redondo, M. Gaspard, D. Gayer, M. Gervasi, M. Giard, V. Gilles, Y. Giraud-Heraud, M. Gómez Berisso, M. Gradziel, M.R. Hampel, D. Harari, S. Henrot-Versillé, F. Incardona, E. Jules, J. Kaplan, C. Kristukat, L. Lamagna, S. Loucatos, T. Louis, B. Maffei, W. Marty, A. Mattei, A. May, M. McCulloch, L. Mele, D. Melo, L. Montier, L.M. Mundo, J.A. Murphy, F. Nati, E. Olivieri, C. Oriol, A. Paiella, F. Pajot, A. Passerini, H. Pastoriza, A. Pelosi, C. Perbost, M. Perciballi, F. Pezzotta, F. Piacentini, L. Piccirillo, G. Pisano, M. Platino, G. Polenta, R. Puddu, D. Rambaud, P. Ringegni, G.E. Romero, E. Rasztocky, J.M. Salum, A. Schillaci, C. Scóccola, S. Scully, S. Spinelli, M. Stolpovskiy, A.D. Supanitsky, P. Timbie, M. Tomasi, G. Tucker, C. Tucker, D. Viganò, N. Vittorio, F. Wicek, M. Wright, A. Zullo

Submitted to Journal of Cosmology and Atroparticle Physics (2020).

ArXiv ID: 2008.10056.

[4] QUBIC IV: Performance of TES Bolometers and Readout Electronics.

M. Piat, G. Stankowiak, E.S. Battistelli, G. D'Alessandro, P. de Bernardis, M. De Petris, M. Gonzalez, L. Grandsire, J.-Ch. Hamilton, T.D. Hoang, S. Masi, S. Marnieros, A. Mennella, L. Mousset, C. O'Sullivan, D. Prele, A. Tartari, J.-P. Thermeau, S.A. Torchinsky, F. Voisin, M. Zannoni, P. Ade, J.G. Alberro, A. Almela, G. Amico, L.H. Arnaldi, D. Auguste, J. Aumont, S. Azzoni, S. Ban, B. Belier, A. Bau, D. Bennett, L. Berge, J.-Ph. Bernard, M. Bersanelli, M.-A. Bigot-Sazy, J. Bonaparte, J. Bonis, E. Bunn, **D. Burke**, D. Buzi, F. Cavaliere, P. Chanial, C. Chapron, R. Charlassier, A.C. Cobos Cerutti, F. Columbro, A. Coppolecchia, G. De Gasperis, M. De Leo, S. Dheilly, C. Duca, L. Dumoulin, A. Etchegoyen, A. Fasciszewski, L.P. Ferreyro, D. Fracchia, C. Franceschet, M.M. Gamboa Lerena, K.M. Ganga1 B. Garca, M.E. Garca Redondo, M. Gaspard, D. Gayer, M. Gervasi, M. Giard, V. Gilles, Y. Giraud-Heraud, M. Gomez Berisso, M. Gradziel, M.R. Hampel, D. Harari, S. Henrot-Versille, F. Incardona, E. Jules, J. Kaplan,

Chapter 7: Summary and conclusions

C. Kristukat, L. Lamagna, S. Loucatos, T. Louis, B. Maei, W. Marty, A. Mattei, A. May, M. McCulloch, L. Mele, D. Melo, L. Montier, L.M. Mundo, J.A. Murphy, J.D. Murphy, F. Nati, E. Olivieri, C. Oriol, A. Paiella, F. Pajot, A. Passerini, H. Pastoriza, A. Pelosi, C. Perbost, M. Perciballi, F. Pezzotta, F. Piacentini, L. Piccirillo, G. Pisano, M. Platino, G. Polenta, R. Puddu, D. Rambaud, P. Ringegni, G.E. Romero, E. Rasztocky, J.M. Salum, A. Schillaci, C. Scoccola, S. Scully, S. Spinelli, M. Stolpovskiy, A.D. Supanitsky, P. Timbie, M. Tomasi, G. Tucker, C. Tucker, D. Vigano, N. Vittorio, F. Wicek, M. Wright and A. Zullo.

In preparation for submission to Journal of Cosmology and Atroparticle Physics (2021).

[5] QUBIC V: Cryogenic system design and performance.

S. Masi, E.S. Battistelli, P. de Bernardis, C. Chapron, F. Columbro, G. D'Alessandro, M. De Petris, L. Grandsire, J.-Ch. Hamilton, S. Marnieros, L. Mele, A. May, A. Mennella, C. O'Sullivan, A. Paiella, F. Piacentini, M. Piat, L. Piccirillo, G. Presta, A. Schillaci, A. Tartari, J.-P. Thermeau, S.A. Torchinsky, F. Voisin, M. Zannoni, P. Ade, J.G. Alberro, A. Almela, G. Amico, L.H. Arnaldi, D. Auguste, J. Aumont, S. Azzoni, S. Banfi, B. Bélier, A. Baù, D. Bennett, L. Bergé, J.-Ph. Bernard, M. Bersanelli, M.-A. Bigot-Sazy, J. Bonaparte, J. Bonis, E. Bunn, **D. Burke**, D. Buzi, F. Cavaliere, P. Chanial, R. Charlassier, A.C. Cobos Cerutti, A. Coppolecchia, G. De Gasperis, M. De Leo, S. Dheilly, C. Duca, L. Dumoulin, A. Etchegoyen, A. Fasciszewski, L.P. Ferreyro, D. Fracchia, C. Franceschet, M.M. Gamboa Lerena, K.M. Ganga, B. García, M.E. García Redondo, M. Gaspard, D. Gayer, M. Gervasi, M. Giard, V. Gilles, Y. Giraud-Heraud, M. Gómez Berisso, M. González, M. Gradziel, M.R. Hampel, D. Harari, S. Henrot-Versillé, F. Incardona, E. Jules, J. Kaplan, C. Kristukat, L. Lamagna, S. Loucatos, T. Louis, B. Maffei, W. Marty, A. Mattei, M. McCulloch, D. Melo, L. Montier, L. Mousset, L.M. Mundo, J.A. Murphy, J.D. Murphy, F. Nati, E. Olivieri, C. Oriol, F. Pajot, A. Passerini, H. Pastoriza, A. Pelosi, C. Perbost, M. Perciballi, F. Pezzotta, G. Pisano, M. Platino, G. Polenta, D. Prêle, R. Puddu, D. Rambaud, E. Rasztocky, P. Ringegni, G.E. Romero, J.M. Salum, C.G. Scóccola, S. Scully, S. Spinelli, G. Stankowiak, M. Stolpovskiy, A.D. Supanitsky, P. Timbie, M. Tomasi, G. Tucker, C. Tucker, D. Viganò, N. Vittorio, F. Wicek, M. Wright, A. Zullo.

Submitted to Journal of Cosmology and Atroparticle Physics (2020).

ArXiv ID: 2008.10659.

[6] QUBIC VI: cryogenic half wave plate rotator, design and performances.

G. D'Alessandro, L. Mele, F. Columbro, G. Amico, E.S. Battistelli, P. de Bernardis, A. Coppolecchia, M. De Petris, L. Grandsire, J.-Ch. Hamilton, L. Lamagna, S. Marnieros, S. Masi, A. Mennella, C. O'Sullivan, A. Paiella, F. Piacentini, M. Piat, G. Pisano, G. Presta, A. Tartari, S.A. Torchinsky, F. Voisin, M. Zannoni, P. Ade, J.G. Alberro, A. Almela, L.H. Arnaldi, D. Auguste, J. Aumont, S. Azzoni, S. Banfi, B. Bélier, A. Baù, D. Bennett, L. Bergé, J.-Ph. Bernard, M. Bersanelli, M.-A. Bigot-Sazy, J. Bonaparte, J. Bonis, E. Bunn, **D. Burke**, D. Buzi, F. Cavaliere, P. Chanial, C. Chapron, R. Charlassier, A.C. Cobos Cerutti, G. De Gasperis, M. De Leo, S. Dheilly, C. Duca, L. Dumoulin, A. Etchegoyen, A. Fasciszewski, L.P. Ferreyro, D. Fracchia, C. Franceschet, M.M. Gamboa Lerena, K.M. Ganga, B. García, M.E. García Redondo, M. Gaspard, D. Gayer, M. Gervasi, M. Giard, V. Gilles, Y. Giraud-Heraud, M. Gómez Berisso, M. González, M. Gradziel, M.R. Hampel, D. Harari, S. Henrot-Versillé, F. Incardona, E. Jules, J. Kaplan, C. Kristukat, S. Loucatos, T. Louis, B. Maffei, W. Marty, A. Mattei, A. May, M. McCulloch, D. Melo, L. Montier, L.

Mousset, L.M. Mundo, J.A. Murphy, J.D. Murphy, F. Nati, E. Olivieri, C. Oriol, F. Pajot, A. Passerini, H. Pastoriza, A. Pelosi, C. Perbost, M. Perciballi, F. Pezzotta, L. Piccirillo, M. Platino, G. Polenta, D. Prêle, R. Puddu, D. Rambaud, E. Rasztocky, P. Ringegni, G.E. Romero, J.M. Salum, A. Schillaci, C.G. Scóccola, S. Scully, S. Spinelli, G. Stankowiak, M. Stolpovskiy, A.D. Supanitsky, J.-P. Thermeau, P. Timbie, M. Tomasi, G. Tucker, C. Tucker, D. Viganò, N. Vittorio, F. Wicek, M. Wright, A. Zullo.

Submitted to Journal of Cosmology and Atroparticle Physics (2020).

ArXiv ID: 2008.10667.

[7] QUBIC VII: The feedhorn-switch system of the technological demonstrator.

F. Cavaliere, A. Mennella, M. Zannoni, P. Battaglia, E.S. Battistelli, **D. Burke**, G. D'Alessandro, P. de Bernardis, M. De Petris, C. Franceschet, L. Grandsire, J.-Ch. Hamilton, B. Maffei, E. Manzan, S. Marnieros, S. Masi, C. O'Sullivan, A. Passerini, F. Pezzotta, M. Piat, A. Tartari, S.A. Torchinsky, D. Viganò, F. Voisin, P. Ade, J.G. Alberro, A. Almela, G. Amico, L.H. Arnaldi, D. Auguste, J. Aumont, S. Azzoni, B. Bélier, A. Baù, S. Banfi, D. Bennett, L. Bergé, J.-Ph. Bernard, M. Bersanelli, M.-A. Bigot-Sazy, J. Bonaparte, J. Bonis, E. Bunn, D. Buzi, P. Chanial, C. Chapron, R. Charlassier, A.C. Cobos Cerutti, F. Columbro, A. Coppolecchia, G. De Gasperis, M. De Leo, S. Dheilly, C. Duca, L. Dumoulin, A. Etchegoyen, A. Fasciszewski, L.P. Ferreyro, D. Fracchia, M. Gómez Berisso, M.M. Gamboa Lerena, K.M. Ganga, B. García, M.E. García Redondo, M. Gaspard, D. Gayer, M. Gervasi, M. Giard, V. Gilles, Y. Giraud-Heraud, M. González, M. Gradziel, M.R. Hampel, D. Harari, S. Henrot-Versillé, F. Incardona, E. Jules, J. Kaplan, C. Kristukat, L. Lamagna, S. Loucatos, T. Louis, W. Marty, A. Mattei, A. May, M. McCulloch, L. Mele, D. Melo, L. Montier, L. Mousset, L.M. Mundo, J.A. Murphy, J.D. Murphy, F. Nati, E. Olivieri, C. Oriol, E. Pagana, A. Paiella, F. Pajot, H. Pastoriza , A. Pelosi, C. Perbost, M. Perciballi, F. Piacentini, L. Piccirillo, G. Pisano, M. Platino, G. Polenta, D. Prêle, R. Puddu, D. Rambaud, E. Rasztocky, P. Ringegni, G.E. Romero, J.M. Salum, C. Scóccola, A. Schillaci, S. Scully, S. Spinelli, G. Stankowiak, M. Stolpovskiy, A.D. Supanitsky, J.-P. Thermeau, P. Timbie, M. Tomasi, G. Tucker, C. Tucker, N. Vittorio, F. Wicek, M. Wright, A. Zullo.

Submitted to Journal of Cosmology and Atroparticle Physics (2020).

ArXiv ID: 2008.12721.

[8] QUBIC VIII: Optical design and performance.

C. O'Sullivan, M. De Petris, **D. Burke**, D. Buzi, C. Chapron, L. Conversi, M. De Leo, D. Gayer, J.-Ch. Hamilton, L. Mousset, J.D. Murphy, A. Pelosi, M. Perciballi, S. Scully, M. Zannoni, A. Zullo, E.S. Battistelli, G. D'Alessandro, P. de Bernardis, L. Grandsire, M. Piat, S. Masi, S. Marnieros, A. Mennella, A. Tartari, S.A. Torchinsky, F. Voisin, P. Ade, J.G. Alberro, A. Almela, G. Amico, L.H. Arnaldi, D. Auguste, J. Aumont, S. Azzoni, S. Banfi, A. Baù, B. Bélier, D. Bennett, L. Bergé, J.-Ph. Bernard, M. Bersanelli, M.-A. Bigot-Sazy, J. Bonaparte, J. Bonis, A. Bottani, E. Bunn, F. Cavaliere, P. Chanial, R. Charlassier, A.C. Cobos Cerutti, A. Coppolecchia, F. Columbro, G. De Gasperis, S. Dheilly, C. Duca, L. Dumoulin, M.M. Gamboa Lerena, M. González, A. Etchegoyen, A. Fasciszewski, L.P. Ferreyro, D. Fracchia, C. Franceschet, K.M. Ganga, B. García, M.E. García Redondo, M. Gaspard, M. Gervasi, M. Giard, V. Gilles, Y. Giraud-Heraud, M. Gómez Berisso, M. Gradziel1 D. Harari, S. Henrot-Versillé, F.

Incardona, E. Jules, J. Kaplan, C. Kristukat, L. Lamagna, S. Loucatos, T. Louis, B. Maffei, W. Marty, A. Mattei, A. May, M. McCulloch, L. Mele, S. Melhuish, L. Montier, L. M. Mundo, J. A. Murphy, F. Nati, E. Olivieri, C. Oriol, A. Paiella, F. Pajot, A. Passerini, H. Pastoriza, C. Perbost, F. Pezzotta, F. Piacentini, L. Piccirillo, G. Pisano, M. Platino, G. Polenta, D. Prêle, R. Puddu, D. Rambaud, P. Ringegni, G. E. Romero, C. Scóccola, G. Stankowiak, J.M. Salum, A. Schillaci, S. Spinelli, M. Stolpovskiy, A.D. Supanitsky, P. Timbie, J.-P. Thermeau, M. Tomasi, G. Tucker, C. Tucker, D. Viganò, N. Vittorio, and F. Wicek.

Submitted to Journal of Cosmology and Atroparticle Physics (2020).

ArXiv ID: 2008.10119.

[9] QUBIC: the Q & U Bolometric Interferometer for Cosmology.

E.S. Battistelli, P. Ade, J.G. Alberro, A. Almela, G. Amico, L. H. Arnaldi, D. Auguste, J. Aumont, S. Azzoni, S. Banfi, P. Battaglia, A. Baù, B. Bèlier, D. Bennett, L. Bergè, J.-Ph. Bernard, M. Bersanelli, M.-A. Bigot-Sazy, N. Bleurvacq, J. Bonaparte, J. Bonis, A. Bottani, E. Bunn, **D. Burke**, D. Buzi, A. Buzzelli, F. Cavaliere, P. Chanial, C. Chapron, R. Charlassier, F. Columbro, G. Coppi, A. Coppolecchia, G. D'Alessandro, P. de Bernardis, G. De Gasperis, M. De Leo, M. De Petris, S. Dheilly, A. Di Donato, L. Dumoulin, A. Etchegoyen, A. Fasciszewski, L.P. Ferreyro, D. Fracchia, C. Franceschet, M.M. Gamboa Lerena, K. Ganga, B. Garcìa, M.E. Garcìa Redondo, M. Gaspard, A. Gault, D. Gayer, M. Gervasi, M. Giard, V. Gilles, Y. Giraud-Heraud, M. Gòmez Berisso, M. Gonzàlez, M. Gradziel, L. Grandsire, J.-Ch. Hamilton, D. Harari, V. Haynes, S. Henrot-Versillè, D.T. Hoang, F. Incardona, E. Jules, J. Kaplan, A. Korotkov, C. Kristukat, L. Lamagna, S. Loucatos, T. Louis, R. Luterstein, B. Maffei, S. Marnieros, W. Marty, S. Masi, A. Mattei, A. May, M. McCulloch, M.C. Medina, L. Mele, S. Melhuish, A. Mennella, L. Montier, L. Mousset, L. M. Mundo, J. A. Murphy, J.D. Murphy, F. Nati, E. Olivieri, C. Oriol, C. O'Sullivan, A. Paiella, F. Pajot, A. Passerini, H. Pastoriza, A. Pelosi , C. Perbost, M. Perciballi, F. Pezzotta, F. Piacentini, M. Piat, L. Piccirillo, G. Pisano, M. Platino, G. Polenta, D. Prèle, R. Puddu, D. Rambaud, P. Ringegni, G. E. Romero, M. Salatino, J.M. Salum, A. Schillaci, C. Scòccola, S. Scully, S. Spinelli, G. Stankowiak, M. Stolpovskiy, F. Suarez, A. Tartari, J.-P. Thermeau, P. Timbie, M. Tomasi, S. Torchinsky, M. Tristram, C. Tucker, G. Tucker, S. Vanneste, D. Viganò, N. Vittorio, F. Voisin, B. Watson, F. Wicek, M. Zannoni, A. Zullo

Journal of low temperature Physics (2020).

ArXiv ID: 2001.10272.

[10] Calibration of QUBIC: The Q and U bolometric interferometer for cosmology.

J. D. Murphy, **D. Burke**, M. M. Gamboa Lerena, J.-Ch. Hamilton, L. Mousset, M. De Petris, C. O'Sullivan, S. A. Torchinsky, P. Ade, J. G. Alberro, A. Almela, G. Amico, L. H. Arnaldi, D. Auguste, J. Aumont, S. Azzoni, S. Banfi, B. Bélier, E. S. Battistelli, A. Baù, D. Bennett, L. Bergé, J.-Ph. Bernard, M. Bersanelli, M.-A. Bigot-Sazy, J. Bonaparte, J. Bonis, E. Bunn, D. Buzi, F. Cavaliere, P. Chanial, C. Chapron, R. Charlassier, A. C. Cobos Cerutti, F. Columbro, A. Coppolecchia, G. D'Alessandro, G. De Gasperis, M. De Leo, S. Dheilly, C. Duca, L. Dumoulin, A. Etchegoyen, A. Fasciszewski, L. P. Ferreyro, D. Fracchia, C. Franceschet, K. M. Ganga, B. García, M. E. García Redondo, M. Gaspard, D. Gayer, M. Gervasi, M. Giard, V. Gilles, Y. Giraud-Heraud, L. Grandsire, M. Gómez Berisso, M. González, M. Gradziel, M. R. Hampel,

Chapter 7: Summary and conclusions

D. Harari, S. Henrot-Versillé, F. Incardona, E. Jules, J. Kaplan, C. Kristukat, L. Lamagna, S. Loucatos, T. Louis, B. Maffei, W. Marty, A. Mattei, A. May, M. McCulloch, L. Mele, D. Melo, A. Mennella, L. Montier, L. M. Mundo, J. A. Murphy, F. Nati, E. Olivieri, C. Oriol, A. Paiella, F. Pajot, A. Passerini, H. Pastoriza, A. Pelosi, C. Perbost, M. Perciballi, F. Pezzotta, F. Piacentini, L. Piccirillo, G. Pisano, M. Platino, G. Polenta, D. Prêle, R. Puddu, D. Rambaud, E. Rasztocky, P. Ringegni, G. E. Romero, J. M. Salum, C. Scóccola, A. Schillaci, S. Scully, S. Spinelli, G. Stankowiak, M. Stolpovskiy, A. D. Supanitsky, A. Tartari, J.-P. Thermeau, P. Timbie, M. Tomasi, G. Tucker, C. Tucker, D. Viganò, N. Vittorio, F. Voisin, F. Wicek, M. Wright, M. Zannoni, A. Zullo

Event: SPIE Astronomical Telescopes + Instrumentation, 2020.

Proceedings volume 11453, Millimeter, Submillimeter, and Far-Infrared Detectors and Instrumentation for Astronomy X.

DOI: 10.1117/12.2560172.

[11] QUBIC: the Q and U bolometric interferometer for cosmology.

C. O'Sullivan, P. Ade, G. Amico, D. Auguste, J. Aumont, S. Banfi, G. Barbarán, P. Battaglia, E. Battistelli, A. Baù, B. Bélier, D. Bennett, L. Bergé, J.-Ph. Bernard, M. Bersanelli, M.-A. Bigot-Sazy, N. Bleurvacq, J. Bonaparte, J. Bonis, G. Bordier, E. Bréelle, E. Bunn, **D. Burke**, D. Buzi, A. Buzzelli, F. Cavaliere, P. Chanial, C. Chapron, R. Charlassier, F. Columbro, G. Coppi, A. Coppolecchia, F. Couchot, R. D'Agostino, G. D'Alessandro, P. de Bernardis, G. de Gasperis, M. De Leo, M. De Petris, A. Di Donato, L. Dumoulin, A. Etchegoyen, A. Fasciszewski, C. Franceschet, M. M. Gamboa Lerena, B. García, X. Garrido, M. Gaspard, A. Gault, D. Gayer, M. Gervasi, M. Giard, Y. Giraud-Héraud, M. Gómez Berisso, M. González, M. Gradziel, L. Grandsire, E. Guerrard, J.-Ch. Hamilton, D. Harari, V. Haynes, S. Henrot-Versillé, D. T. Hoang, F. Incardona, E. Jules, J. Kaplan, A. Korotkov, C. Kristukat, L. Lamagna, S. Loucatos, T. Louis, A. Lowitz, V. Lukovic, R. Luterstein, B. Maffei, S. Marnieros, S. Masi, A. Mattei, A. May, M. McCulloch, M. C. Medina, L. Mele, S. Melhuish, A. Mennella, L. Montier, L. M. Mundo, J. A. Murphy, J. D. Murphy, E. Olivieri, A. Paiella, F. Pajot, A. Passerini, H. Pastoriza, A. Pelosi, C. Perbost, O. Perdereau, F. Pezzotta, F. Piacentini, M. Piat, L. Piccirillo, G. Pisano, G. Polenta, D. Prêle, R. Puddu, D. Rambaud, P. Ringegni, G. E. Romero, M. Salatino, A. Schillaci, C. G. Scóccola, S. Scully, S. Spinelli, M. Stolpovskiy, F. Suarez, A. Tartari, J.-P. Thermeau, P. Timbie, S. A. Torchinsky, M. Tristram, V. Truongcanh, C. Tucker, G. Tucker, S. Vanneste, D. Viganò, N. Vittorio, F. Voisin, B. Watson, F. Wicek, M. Zannoni, A. Zullo.

Event: SPIE Astronomical Telescopes + Instrumentation, 2018.

Proceedings volume10708, Millimeter, Submillimeter, and Far-Infrared Detectors and Instrumentation for Astronomy IX.

DOI: 10.1117/12.2313332.

[12] Optical modelling and analysis of the Q and U bolometric interferometer for cosmology.

D. Burke, D. Gayer, E. Kalinauskaite, C. O'Sullivan, J. D. Murphy, S. P. Scully, M. De Petris, M. De Leo, A. Mennella, S. A. Torchinsky, M. Zannoni, G. Amico, D. Auguste, J. Aumont, S. Banfi, G. Barbarán, P. Battaglia, E. Battistelli, A. Baù, B. Bélier, D. G. Bennett, L. Bergé, J.-Ph. Bernard, M. Bersanelli, M.-A. Bigot-Sazy, N. Bleurvac, J. Bonaparte, J. Bonis, G. Bordier, E. Bréelle, E. F. Bunn, D. Buzi, A. Buzzelli,

F. Cavaliere, P. Chanial, C. Chapron, R. Charlassier, F. Columbro, G. Coppi, A. Coppolecchia, F. Couchot, G. D'Alessandro, R. D'Agostino, P. de Bernardis, G. De Gasperis, A. Di Donato, A.-A. Drilien, Louis Dumoulin, A. Etchegoyen, A. Fasciszewski, C. Franceschet, M. Gamboa-Lerena, B. García, X. Garrido, M. Gaspard, A. Gault, M. Gervasi, M. Giard, Y. Giraud-Héraud, M. Gómez Berisso, M. González, M. L. Gradziel, L. Grandsire, E. Guerrard, J.-Ch. Hamilton, D. Harari, V. Haynes, S. Henrot-Versillé, D. T. Hoang, N. Holtzer, F. Incardona, E. Jules, J. Kaplan, A. L. Korotkov, C. Kristukat, L. Lamagna, J. Lande, S. Loucatos, T. Louis, A. Lowitz, V. Lukovic, R. Luterstein, Bruno Maffei, S. Marnieros, S. Masi, A. Mattei, A. J. May, M. A. McCulloch, M. C. Medina, L. Mele, S. J. Melhuish, L. Mundo, L. Montier, J. A. Murphy, D. Néel, E. Olivieri, A. Paiella, F. Pajot, A. Passerini, H. Pastoriza, A. Pelosi, C. Perbost, O. Perdereau, F. Pezzotta, F. Piacentini, M. R. Piat, L. Piccirillo, G. Pisano, G. Polenta, D. Prêle, R. Puddu, D. Rambaud, O. Rigaut, P. Ringegni, G. E. Romero, M. Salatino, A. Schillaci, C. G. Scóccola, S. M. Spinelli, M. Stolpovskiy, F. Suarez, A. Tartari, J.-P. Thermeau, P. T. Timbie, M. Tristram, V. Truongcanh, G. S. Tucker, C. E. Tucker, D. Viganò, N. Vittorio, F. Voisin, B. Watson, F. Wicek, A. Zullo

Event: SPIE Photonics west, 2018.

Proceedings Volume 10531, Terahertz, RF, Millimeter, and Submillimeter-Wave Technology and Applications XI.

DOI: 10.1117/12.2287158.

[13] Optical design and modelling of the QUBIC instrument, a next-generation quasi-optical bolometric interferometer for cosmology.

D. Burke, S. Scully, C. O'Sullivan, D. Gayer, M. Gradziel, J. A. Murphy, M. De Petris, D. Buzi, M. Zannoni, A Mennella, M. Gervasi, A. Tartari, B. Maffei, J. Aumont, S. Banfi, P. Battaglia, E. S. Battistelli, A. Baù, B. Bélier, D. Bennet, L. Bergé, J.-Ph. Bernard, M. Bersanelli, M.-A. Bigot-Sazy, N. Bleurvacq, G. Bordier, J. Brossard, E. F. Bunn, D. Cammileri, F. Cavaliere, P. Chanial, C. Chapron, A. Coppolecchia, F. Couchot, G. D'Alessandro, P. De Bernardis, T. Decourcelle, F. Del Torto, L. Dumoulin, C. Franceschet, A. Gault, A. Ghribi, M. Giard, Y. Giraud-Héraud, L. Grandsire, J. Ch. Hamilton, V. Haynes, S. Henrot-Versillé, N. Holtzer, J. Kaplan, A. Korotkov, J. Lande, A. Lowitz, S. Marnieros, J. Martino, S. Masi, Mark McCulloch, Simon Melhuish, L. Montier, D. Néel, M. W. Ng, F. Pajot, A. Passerini, C. Perbost, O. Perdereau, F. Piacentini, M. Piat, L. Piccirillo, G. Pisano, D. Prêle, R. Puddu, D. Rambaud, O. Rigaut, M. Salatino, A. Schillaci, M. Stolpovskiy, P. Timbie, M. Tristram, G. Tucker, D. Viganò, F. Voisin, B. Watson

Event: SPIE Astronomical Telescopes + Instrumentation, 2016.

Proceedings volume 9914, Millimeter, Submillimeter, and Far-Infrared Detectors and Instrumentation for Astronomy VIII.

DOI: 10.1117/12.2231717.

My work made a particularly significant contribution to papers [7], [8], [10], [12] and [13] which describe the optics and the horn array of QUBIC. I have also presented my work at the following conferences (in addition to giving an oral presentation of [12] and a poster presentation of [13] above):

[1] "Optical modelling of the QUBIC technical demonstrator", poster presentation at B-mode from space workshop in the Max-Planck-Institut für Astrophysik, Garching in 2019 (awarded third place in the best poster award).

[2] “QUBIC – The Q & U Bolometric Interferometer for Cosmology”, oral presentation at the Irish National Astronomy Meeting in Maynooth University in 2017.

[3] “Optimisation of the Optical Combiner for the QUBIC Technical Demonstrator”, poster presentation at the Institute of physics spring meeting in Belfast in 2016.

8 References

Abazajian, K. *et al.* (2019) 'CMB-S4 Decadal Survey APC White Paper'. Available at: http://arxiv.org/abs/1908.01062.

Ade, P. A. R. *et al.* (2015) 'Joint Analysis of BICEP2/Keck Array and Planck Data', *Physical Review Letters*, 114(10), pp. 1–17. doi: 10.1103/PhysRevLett.114.101301.

Ade, P. A. R. *et al.* (2018) 'Constraints on Primordial Gravitational Waves Using Planck, WMAP, and New BICEP2/ Keck Observations through the 2015 Season', *Physical Review Letters*, 121(22), pp. 1–23. doi: 10.1103/PhysRevLett.121.221301.

Alpher, R. A., Bethe, H. and Gamow, G. (1948) 'The Origin of Chemical Elements', *Physical Review*, 73(7), pp. 803–804. doi: 10.1103/PhysRev.73.803.

Alpher, R. A. and Herman, R. C. (1949) 'Remarks on the Evolution of the Expanding Universe', *Physical Review*. American Physical Society, 75(7), pp. 1089–1095. doi: 10.1103/PhysRev.75.1089.

Arnold, K. *et al.* (2010) 'The POLARBEAR CMB polarization experiment', in Holland, W. S. and Zmuidzinas, J. (eds) *Millimeter, Submillimeter, and Far-Infrared Detectors and Instrumentation for Astronomy V*. Journal of the Physical Society of Japan, p. 77411E. doi: 10.1117/12.858314.

Austermann, J. E. *et al.* (2012) 'SPTpol: an instrument for CMB polarization measurements with the South Pole Telescope', *Millimeter, Submillimeter, and Far-Infrared Detectors and Instrumentation for Astronomy VI*, 8452, p. 84521E. doi: 10.1117/12.927286.

Balanis, C. A. (2005) *Antenna Theory and Design*. 3rd edn, *IEEE Antennas and Propagation Society Newsletter*. 3rd edn. doi: 10.1109/MAP.1981.27568.

Battistelli, E. *et al.* (2011) 'QUBIC: The QU bolometric interferometer for cosmology', *Astroparticle Physics*, 34(9), pp. 705–716. doi: 10.1016/j.astropartphys.2011.01.012.

Baumann, D. *et al.* (2009) 'CMBPol Mission Concept Study: Probing Inflation with CMB Polarization', in *AIP Conference Proceedings*. AIP, pp. 10–120. doi: 10.1063/1.3160885.

Bélier, B. *et al.* (2018) 'Performance of NbSi transition-edge sensors readout with a 128 MUX factor for the QUBIC experiment', 1070845(July 2018), p. 140. doi: 10.1117/12.2312080.

Bennet, D. G. (2014) *Design and Analysis of a Quasi-Optical Beam Combiner For the QUBIC CMB Interferometer*. PhD thesis, NUI Maynooth.

Bigot-Sazy, M.-A. (2013) *Mesure des anisotropies de polarisation du fond diffus cosmologique avec l ' interféromètre bolométrique QUBIC*. Université Paris-Diderot.

Bigot-Sazy, M.-A. *et al.* (2013) 'Self-calibration: an efficient method to control systematic effects in bolometric interferometry', *Astronomy & Astrophysics*, 550, p. A59. doi: 10.1051/0004-6361/201220429.

Bracewell, R. (2000) *The Fourier Transform & Its Applications*. 3rd edn. McGraw-Hill Higher Education.

Chapter 8: References

Cahill, F. (2015) *Design and Analysis of Corrugated Conical Horn Antennas with Terahertz Applications*. MSc. Thesis, Maynooth Universtiy. Available at: http://eprints.maynoothuniversity.ie/7530/.

Carlstrom, J. E. *et al.* (2003) 'Status of CMB polarization measurements from DASI and other experiments', *New Astronomy Reviews*, 47(11–12), pp. 953–966. doi: 10.1016/j.newar.2003.09.007.

Carroll, B. W. and Ostlie, D. A. (2014) *An Introduction to Modern Astrophysics*. Second edi, *An Introduction to Modern Astrophysics*. Second edi. Pearson. doi: 10.1017/9781108380980.

Cavaliere, F. *et al.* (2020) 'QUBIC VII: The feedhorn-switch system of the technological demonstrator', *submitted to Journal of Cosmology and Astroparticle Physics*. Available at: http://arxiv.org/abs/2008.12721.

van Cittert, P. H. (1934) 'Die Wahrscheinliche Schwingungsverteilung in Einer von Einer Lichtquelle Direkt Oder Mittels Einer Linse Beleuchteten Ebene', *Physica*, 1(1–6), pp. 201–210. doi: 10.1016/S0031-8914(34)90026-4.

Clarricoats, P. J. B. and Olver, A. . (1984) *Corrugated Horns for Microwave Antennas*. IEEE.

Coles, P. and Lucchin, F. (2002) *Cosmology: The Origin and Evolution of Cosmic Structure, Classical and Quantum Gravity*. Wiley.

Colgan, R. (2001) *Electromagnetic and quasi-optical modelling of horn antennas for far-IR space applications*. PhD thesis, Maynooth Universtiy.

Collin, R. E. and Zucker, F. J. (1969) *Antenna Theory Part 1*. McGraw-Hill Book Company.

Curran, G. S. (2010) *Quasi-Optical Design and Analysis of Bolometric Interferometers for Cosmic Microwave Background Experiments*. PhD thesis, NUI Maynooth. Available at: http://eprints.nuim.ie/2583/.

D'Alessandro, G. *et al.* (2020) 'QUBIC VI: cryogenic half wave plate rotator, design and performances', *Submitted to Journal of Cosmology and Astroparticle Physics*. Available at: http://arxiv.org/abs/2008.10667.

Dicke, R. H. *et al.* (1965) 'Cosmic Black-Body Radiation.', *The Astrophysical Journal*, 142(9), p. 414. doi: 10.1086/148306.

Dickinson, C. (2016) 'CMB foregrounds - A brief overview', *Proceedings of the 51st Rencontres de Moriond on Cosmology 2016*, pp. 53–62.

Doherty, S. (2012) *Optical and Quasi-Optical Design and Analysis of Astronomical Instrumentation including a Prototype SAFARI Pixel*. PdD thesis, Maynooth Universtiy.

ESA and the Planck Collaboration (2013) *Planck CMB*. Available at: http://www.esa.int/spaceinimages/Images/2013/03/Planck_CMB (Accessed: 11 May 2017).

Chapter 8: References

Garc, B. *et al.* (2020) 'QUBIC : observing the polarized microwave sky over the Puna', *Science Reviews from the end of the world*, 1(September), pp. 47–65.

Gayer, D. (2020) *Thesis in preperation*. Maynooth University.

Gleeson, E. (2004) *Single and Multi-moded Corrugated horn Design for Cosmic Microwave Background Experiments*. PhD Thesis, Maynooth Universtiy.

Goldsmith, P. F. (1998) *Quasioptical Systems: : Gaussian Beam Quasioptical Propagation and Applications*. IEEE Press.

Gradziel, M. L. *et al.* (2007) 'Modelling of the optical performance of millimeter-wave instruments in MODAL', in *SPIE*. International Society for Optics and Photonics, p. 64720D. doi: 10.1117/12.700680.

Grayson, J. A. *et al.* (2016) 'BICEP3 performance overview and planned Keck Array upgrade', *Millimeter, Submillimeter, and Far-Infrared Detectors and Instrumentation for Astronomy VIII*, 9914, p. 99140S. doi: 10.1117/12.2233894.

Gualtieri, R. *et al.* (2018) 'SPIDER: CMB Polarimetry from the Edge of Space', *Journal of Low Temperature Physics*, 193(5–6), pp. 1112–1121. doi: 10.1007/s10909-018-2078-x.

Guth, A. H. (1981) 'Inflationary universe: A possible solution to the horizon and flatness problems', *Physical Review D*, 23(2), pp. 347–356. doi: 10.1103/PhysRevD.23.347.

Haas, R. W. *et al.* (1993) 'Fabrication and performance of MMW and SMMW platelet horn arrays', *International Journal of Infrared and Millimeter Waves*, 14(11), pp. 2289–2294. doi: 10.1007/BF02085698.

Hamilton, J.-C. *et al.* (2008) 'Sensitivity of a bolometric interferometer to the cosmic microwave backgroud power spectrum', *Astronomy and Astrophysics*, 491(3), pp. 923–927. doi: 10.1051/0004-6361:200810504.

Hamilton, J.-C. *et al.* (2020) 'QUBIC I: Overview and ScienceProgram', *submitted to Journal of Cosmology and Astroparticle Physics*. Available at: http://arxiv.org/abs/2011.02213.

Hamilton, J.-C. and Charlassier, R. (2010) 'QUBIC, a bolometric interferometer to measure the B-modes of the CMB', *EAS Publications Series*, 40, pp. 399–404. doi: 10.1051/eas/1040055.

Hinderks, J. R. *et al.* (2009) 'QUaD: A HIGH-RESOLUTION COSMIC MICROWAVE BACKGROUND POLARIMETER', *The Astrophysical Journal*, 692(2), pp. 1221–1246. doi: 10.1088/0004-637X/692/2/1221.

Hinshaw, G. *et al.* (2007) ' Three-Year Wilkinson Microwave Anisotropy Probe (WMAP) Observations: Temperature Analysis ', *The Astrophysical Journal Supplement Series*, 170(2), pp. 288–334. doi: 10.1086/513698.

Hinshaw, G. *et al.* (2013) 'Nine-Year Wilkinson Microwave Anisotropy Probe (WMAP) Observations: Cosmological Parameter Results', *The Astrophysical Journal Supplement Series*, 208(2), p. 19. doi: 10.1088/0067-0049/208/2/19.

Chapter 8: References

Holmes, W. A. *et al.* (2008) 'Initial test results on bolometers for the Planck high frequency instrument', *Applied Optics*, 47(32), pp. 5996–6008. doi: 10.1364/AO.47.005996.

Hu, W. (2001) *Intermediate Guide to the Acoustic Peaks and Polarization*. Available at: http://background.uchicago.edu/~whu/intermediate/score1.html (Accessed: 27 July 2020).

Hu, W. and Dodelson, S. (2002) 'Cosmic Microwave Background Anisotropies', *Annual Review of Astronomy and Astrophysics*, 40(1), pp. 171–216. doi: 10.1146/annurev.astro.40.060401.093926.

Hu, W. and White, M. (1997) 'A CMB Polarization Primer', *New Astronomy*, 2(4), pp. 323–344. doi: 10.1016/S1384-1076(97)00022-5.

Hubble, E. (1929) 'A relation between distance and radial velocity among extra-galactic nebulae', *Proceedings of the National Academy of Sciences*, 15(3), pp. 168–173. doi: 10.1073/pnas.15.3.168.

Irwin, K. D., Hilton, G. C. and Ed, C. E. (2005) *Transition-Edge Sensors Preprint of chapter in Cryogenic Particle Detection Transition-Edge Sensors, Topics Appl. Phys.* doi: 10.1007/10933596_3.

Johansen, P. M. (1996) 'Uniform physical theory of diffraction equivalent edge currents for implementation in general computer codes', in *IEEE Antennas and Propagation Society International Symposium. 1996 Digest*. IEEE, pp. 784–787. doi: 10.1109/APS.1996.549713.

Kalinauskaite, E. (2018) *Electromagnetic and Quasi-Optical Analysis of Cavity Coupled Bolometers for Far-Infrared and Terahertz Receivers*. PhD thesis, Maynooth Universtiy. Available at: http://eprints.maynoothuniversity.ie/10049/ (Accessed: 12 January 2019).

Kovac, J. *et al.* (2002) 'Detection of Polarization in the Cosmic Microwave Background using DASI', *Nature*, 420(6917), pp. 772–787. doi: 10.1038/nature01269.

Lahav, O. and Liddle, A. R. (2004) 'The Cosmological Parameters', *Unsolved Problems in Astrophysics*. Princeton University Press, 1, pp. 1–24. doi: 10.2307/j.ctv301fr4.4.

Lemaitre, G. (1927) 'Un univers homogène de masse constante et de rayon croissant, rendant compte de la vitesse radiale des nébuleuses extra-galactiques', *Annales de la Societe Scietifique de Bruxelles*, 47, pp. 49–59. Available at: http://articles.adsabs.harvard.edu/full/1927ASSB...47...49L.

Lesurf, J. (1990) *Millimetre-Wave Optics, Devices and Systems*. IOP Publishing ltd.

Li, H. *et al.* (2019) 'Probing primordial gravitational waves: Ali CMB Polarization Telescope', *National Science Review*, 6(1), pp. 145–154. doi: 10.1093/nsr/nwy019.

Liddle, A. (2015) *An Introduction to Modern Cosmology*. third edit. Wiley.

López-Caniego, M. *et al.* (2014) 'The QUIJOTE CMB Experiment: status and first results with the multi-frequency instrument'. Available at: http://arxiv.org/abs/1401.4690.

Masi, S. *et al.* (2005) 'Precision CMB Polarization from Dome-C: the BRAIN experiment', *EAS Publications Series*, 14, pp. 87–92. doi: 10.1051/eas:2005014.

Chapter 8: References

Masi, S. *et al.* (2020) 'QUBIC V: Cryogenic system design and performance', *submitted to Journal of Cosmology and Astroparticle Physics*. Available at: http://arxiv.org/abs/2008.10659.

May, A. *et al.* (2018) 'Thermal architecture for the QUBIC cryogenic receiver', p. 130. doi: 10.1117/12.2312085.

McCarthy, D. (2014) *Investigation of Horn Optimisation, Simulation and Measurement Techniques, with Application to Integrating Cavity Based Pixel Design*. PhD Thesis, Maynooth Universtiy.

Mele, L. *et al.* (2020) 'The QUBIC instrument for CMB polarization measurements', *Journal of Physics: Conference Series*, 1548(1), pp. 1–6. doi: 10.1088/1742-6596/1548/1/012016.

Mousset, L. *et al.* (2020) 'QUBIC II: Spectro-Polarimetry with Bolometric Interferometry', *submitted to Journal of Cosmology and Astroparticle Physics*. Available at: http://arxiv.org/abs/2010.15119.

Murphy, J. (2021) *Thesis in preperation*. Maynooth University.

Netterfield, C. B. *et al.* (1997) 'A Measurement of the Angular Power Spectrum of the Anisotropy in the Cosmic Microwave Background', *The Astrophysical Journal*, 474(1), pp. 47–66. doi: 10.1086/303438.

O'Sullivan, C. *et al.* (2020) 'QUBIC VIII: Optical design and performance', *submitted to Journal of Cosmology and Astroparticle Physics*. Available at: http://arxiv.org/abs/2008.10119.

O'Sullivan, C *et al.* (2020) 'The Optical Combiner of QUBIC : the Q & U Bolometric Interferometer for Cosmology', in *14th European Conference on Antennas and Propagation*, pp. 8–11.

Ogburn IV, R. W. *et al.* (2010) 'The BICEP2 CMB polarization experiment', in Holland, W. S. and Zmuidzinas, J. (eds) *Millimeter, Submillimeter, and Far-Infrared Detectors and Instrumentation for Astronomy V*, p. 77411G. doi: 10.1117/12.857864.

Oguri, S. *et al.* (2016) 'GroundBIRD: Observing Cosmic Microwave Polarization at Large Angular Scale with Kinetic Inductance Detectors and High-Speed Rotating Telescope', *Journal of Low Temperature Physics*, 184(3–4), pp. 786–792. doi: 10.1007/s10909-015-1420-9.

Olver, A. . *et al.* (1994) *Microwave Horns and Feeds*. IEEE Press.

Penzias, A. a. and Wilson, R. W. (1965) 'A Measurement of Excess Antenna Temperature at 4080 Mc/s.', *The Astrophysical Journal*, 142, p. 419. doi: 10.1086/148307.

Piat, M. *et al.* (2021) 'QUBIC IV: Performance of TES Bolometers and Readout Electronics', *submitted to Journal of Cosmology and Astroparticle Physics*. Available at: http://arxiv.org/abs/2101.06787.

Planck Collaboration, Ade, P. A. R., Aghanim, N., Alves, M. I. R., *et al.* (2014) 'Planck 2013 results. I. Overview of products and scientific results', *Astronomy & Astrophysics*, 571, p. A1. doi: 10.1051/0004-6361/201321529.

Chapter 8: References

Planck Collaboration, Ade, P. A. R., Aghanim, N., Armitage-Caplan, C., *et al.* (2014) 'Planck 2013 results. XVI. Cosmological parameters', *Astronomy & Astrophysics*, 571, p. A16. doi: 10.1051/0004-6361/201321591.

Planck Collaboration *et al.* (2016) 'Planck 2015 results. XX. Constraints on inflation', *Astronomy & Astrophysics*, 594, p. A20. doi: 10.1051/0004-6361/201525898.

Planck Collaboration *et al.* (2018) 'Planck 2018 results. IV. Diffuse component separation', *Astronomy & Astrophysics*. doi: 10.1051/0004-6361/201833881.

Polenta, G. *et al.* (2007) 'The BRAIN CMB polarization experiment', *New Astronomy Reviews*, 51(3–4), pp. 256–259. doi: 10.1016/j.newar.2006.11.065.

Ramo, S., Whinnery, J. R. and Van Duzer, T. (1994) *Fields and Waves in Communication Electronics*. 3rd edn. Wiley.

Sachs, R. K. and Wolfe, A. M. (1967) 'Perturbations of a Cosmological Model and Angular Variations of the Microwave Background', *The Astrophysical Journal*, 147, p. 73. doi: 10.1086/148982.

Schillaci, A. *et al.* (2020) 'Design and Performance of the First BICEP Array Receiver', *Journal of Low Temperature Physics*, 199(3–4), pp. 976–984. doi: 10.1007/s10909-020-02394-6.

Scully, S. (2015) *Quasi-Optical Design and Analysis of a Bolometric Interferometer for Cosmic Microwave Background Radiation Experiments*, *Department of Experimental Physics*. PhD thesis, Maynooth Universtiy. Available at: http://eprints.nuim.ie/2583/.

Scully, S. *et al.* (2016) 'Optical design and modelling of the QUBIC instrument, a next-generation quasi-optical bolometric interferometer for cosmology', in *SPIE Astronomical Telescopes + Instrumentation, 2016, Edinburgh, United Kingdomm*, p. 99142S. doi: 10.1117/12.2231717.

Sheehy, C. D. *et al.* (2010) 'The Keck Array: a pulse tube cooled CMB polarimeter', in Holland, W. S. and Zmuidzinas, J. (eds) *Millimeter, Submillimeter, and Far-Infrared Detectors and Instrumentation for Astronomy V*, p. 77411R. doi: 10.1117/12.857871.

Siegman, A. E. (1986) 'Lasers'. University Science Books.

Slipher, V. M. (1913) 'The radial velocity of the Andromeda nebula', *Lowell Observatory Bulletin no. 58*, 2(2301), p. 56.

Smoot, G. F. *et al.* (1992) 'Structure in the COBE differential microwave radiometer first-year maps', *The Astrophysical Journal, Part 2 - Letters*, 396, pp. L1–L5. doi: 10.1086/186504.

Smoot, G. F. and Scott, D. (1998) 'Cosmic background radiation', *European Physical Journal C*, 3(1–4), pp. 127–130. doi: 10.1119/1.17126.

Spencer, R. (2013) *Global Warming*. Available at: http://www.drroyspencer.com/2013/12/ (Accessed: 17 March 2020).

Chapter 8: References

Spergel, D. N. *et al.* (2007) 'Three-Year Wilkinson Microwave Anisotropy Probe (WMAP) Observations: Implications for Cosmology', *The Astrophysical Journal Supplement Series*, 170(2), pp. 377–408. doi: 10.1086/513700.

Stebor, N. *et al.* (2016) 'The Simons Array CMB polarization experiment', *Millimeter, Submillimeter, and Far-Infrared Detectors and Instrumentation for Astronomy VIII*, 9914(July), p. 99141H. doi: 10.1117/12.2233103.

Stokes, G. G. (1880) 'On the Composition and Resolution of Streams of Polarized Light from different Sources', in *Mathematical and Physical Papers*. Cambridge: Cambridge University Press, pp. 233–258. doi: 10.1017/CBO9780511702266.010.

Sugai, H. *et al.* (2020) 'Updated Design of the CMB Polarization Experiment Satellite LiteBIRD', *Journal of Low Temperature Physics*, 199(3–4), pp. 1107–1117. doi: 10.1007/s10909-019-02329-w.

Sugiyama, N. (1995) 'Cosmic Background Anisotropies in Cold Dark Matter Cosmology', *The Astrophysical Journal Supplement Series*, 100, p. 281. doi: 10.1086/192220.

Tartari, A. *et al.* (2016) 'QUBIC: A Fizeau Interferometer Targeting Primordial B-Modes', *Journal of Low Temperature Physics*, 184(3–4), pp. 739–745. doi: 10.1007/s10909-015-1398-3.

Tegmark, M. (1996) 'The Angular Power Spectrum of the Four-Year [ITAL]COBE[/ITAL] Data', *The Astrophysical Journal*, 464(1), pp. L35–L38. doi: 10.1086/310079.

The POLARBEAR Collaboration *et al.* (2017) 'A Measurement of the Cosmic Microwave Background B -mode Polarization Power Spectrum at Subdegree Scales from Two Years of polarbear Data', *The Astrophysical Journal*, 848(2), p. 121. doi: 10.3847/1538-4357/aa8e9f.

The QUBIC collaboration *et al.* (2016) 'QUBIC Technical Design Report'. Available at: http://arxiv.org/abs/1609.04372 (Accessed: 23 September 2016).

Thomas Keating ltd. (2019) *Ultra Gaussian Corrugated Horns*. Available at: http://www.terahertz.co.uk/tk-instruments/products/corrugatedhorns/ultra (Accessed: 18 March 2020).

TICRA (2005) *GRASP Technical Description*. Edited by 9. Copenhagen: TICRA Engineering Consultants.

Torchinsky, S. A. *et al.* (2020) 'QUBIC III: Laboratory characterization', *submitted to Journal of Cosmology and Astroparticle Physics.*

Tucker, G. S. *et al.* (2003) 'Bolometric interferometry: The millimeter-wave bolometric interferometer', *New Astronomy Reviews*, 47(11–12), pp. 1173–1176. doi: 10.1016/j.newar.2003.09.024.

White, M. *et al.* (1999) 'Interferometric Observation of Cosmic Microwave Background Anisotropies', *The Astrophysical Journal*, 514(1), pp. 12–24. doi: 10.1086/306911.

White, M. and Cohn, J. D. (2002) 'TACMB-1: The Theory of Anisotropies in the Cosmic Microwave Background (Bibliographic Resource Letter)', *American Journal of Physics*, 70(2), pp. 106–118. doi: 10.1119/1.1380381.

Chapter 8: References

Wilson, D. (2014) *Quasi-Optical Modelling of Telescope Systems for Planck and STEAMR*. PhD thesis, Maynooth Universtiy.

Yoon, K. W. *et al.* (2006) 'The Robinson Gravitational Wave Background Telescope (BICEP): a bolometric large angular scale CMB polarimeter', in Zmuidzinas, J. et al. (eds) *Millimeter and Submillimeter Detectors and Instrumentation for Astronomy III*, p. 62751K. doi: 10.1117/12.672652.

Zaldarriaga, M. and Seljak, U. (1997) 'All-sky analysis of polarization in the microwave background', *Physical Review D - Particles, Fields, Gravitation and Cosmology*, 55(4), pp. 1830–1840. doi: 10.1103/PhysRevD.55.1830.